

AD-A066 086

OKLAHOMA STATE UNIV STILLWATER DEPT OF PHYSICS

F/G 20/5

MULTISTEP ENERGY MIGRATION AND RADIATIONLESS RELAXATION PROCESS--ETC(U)

DEC 78 R C POWELL

DAA629-76-G-0099

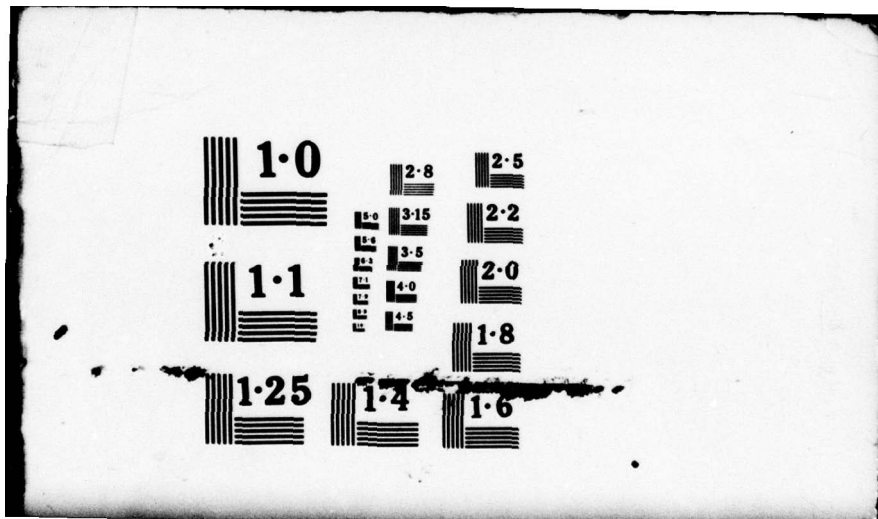
UNCLASSIFIED

ARO-13318.8-P

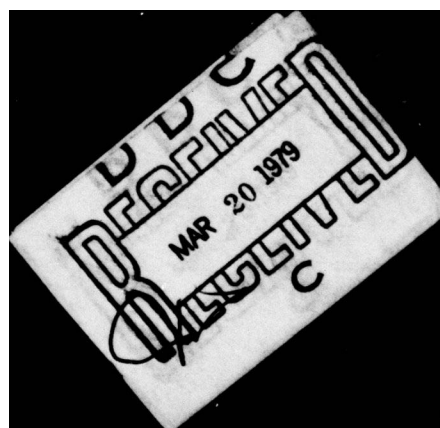
NL

1 OF 4  
ADA  
066086









Unclassified

SECURITY CLASSIFICATION OF THIS PAGE (When Data Entered)

REPORT DOCUMENTATION PAGE		READ INSTRUCTIONS BEFORE COMPLETING FORM
1. REPORT NUMBER <b>19</b> 13318.8-P	2. GOVT ACCESSION NO. <b>18</b> ARD	3. RECIPIENT'S CATALOG NUMBER
4. TITLE (and Subtitle) <b>6</b> Multistep Energy Migration and Radiationless Relaxation Processes in Phosphor and Laser Crystals		5. TYPE OF REPORT & PERIOD COVERED <b>9</b> Final Report 1 Jan 76 - 31 Dec 78
7. AUTHOR(s) <b>10</b> Richard C. Powell		6. PERFORMING ORG. REPORT NUMBER
9. PERFORMING ORGANIZATION NAME AND ADDRESS Oklahoma State University Stillwater, Oklahoma 74074		8. CONTRACT OR GRANT NUMBER(s) <b>15</b> DAAG29-76-G-4499
11. CONTROLLING OFFICE NAME AND ADDRESS U. S. Army Research Office P. O. Box 12211 Research Triangle Park, NC 27709		10. PROGRAM ELEMENT, PROJECT, TASK AREA & WORK UNIT NUMBERS <b>11</b> 34 Dec 78
14. MONITORING AGENCY NAME & ADDRESS (if different from Controlling Office) <b>12</b> 298 P		12. REPORT DATE Dec 31, 1978
		13. NUMBER OF PAGES 291
		15. SECURITY CLASS. (of this report) Unclassified
		15a. DECLASSIFICATION/DOWNGRADING SCHEDULE
16. DISTRIBUTION STATEMENT (of this Report) Approved for public release; distribution unlimited.		
17. DISTRIBUTION STATEMENT (of the abstract entered in Block 20, if different from Report)		
18. SUPPLEMENTARY NOTES The view, opinions, and/or findings contained in this report are those of the author(s) and should not be construed as an official Department of the Army position, policy, or decision, unless so designated by other documentation.		
19. KEY WORDS (Continue on reverse side if necessary and identify by block number) Energy migration Radiationless relaxation processes Relaxation processes Phosphor crystals Laser crystals Laser techniques Photoacoustic spectroscopy Neodymium ions Garnet crystals		
20. ABSTRACT (Continue on reverse side if necessary and identify by block number) This report covers the work supported by the US Army Research Office. The research involves the utilization of new laser techniques such as time-resolved site-selection spectroscopy and photoacoustic spectroscopy to characterize multistep energy transfer and radiationless relaxation processes in phosphor and laser materials. The materials investigated include $\text{CaWO}_4$ , $\text{YVO}_4$ , $\text{LiNbO}_3$ , $\text{Bi}_3\text{Ge}_4\text{O}_{12}$ , $\text{KCl}$ , $\text{Al}_2\text{O}_3$ , and $\text{Y}_3(\text{Al}_{1-x}\text{Ga}_x)_5\text{O}_{12}$ crystals doped with various rare earth and transition		

DDC  
RECEIVED  
MAR 20 1979  
C

DD FORM 1 JAN 73 1473

EDITION OF 1 NOV 65 IS OBSOLETE

Unclassified

20. ABSTRACT CONTINUED

metal ions and also the  $\text{Nd}_{1-x}\text{Y}_x\text{P}_{0.5}\text{O}_{1.5}$  system. Important results include the development of models for explaining energy migration among  $\text{Nd}^{3+}$  ions in disordered garnet crystals and concentration quenching in stoichiometric laser materials.

1. REPORT NUMBER 13318.8-P		2. PERFORMING ORGANIZATION NAME AND ADDRESS Oklahoma State University Stillwater, Oklahoma 74074	
3. REPORT DATE Dec 31, 1978		4. CONTROLLING OFFICE NAME AND ADDRESS U. S. Army Research Office F. O. Box 12211 Research Triangle Park, NC 27709	
5. NUMBER OF PAGES 291		6. SECURITY CLASS (of this report) Unclassified	
7. DISTRIBUTION STATEMENT (of this report) Approved for public release; distribution unlimited.		8. DISTRIBUTION STATEMENT (of this abstract entered in Block 10) (if different from Report) Approved for public release; distribution unlimited.	
9. SUPPLEMENTARY NOTES The view, opinions, author, findings contained in this report are those of the author(s) and should not be construed as an official position of the Army or Department of Defense, or be used to endorse or recommend products or to be used for official policy, or be used for official documentation.			
10. KEY WORDS (Continue on reverse side if necessary and identify by block number) Energy migration Radiationless relaxation processes Relaxation processes Phosphor crystals Laser crystals Garnet crystals Neodymium ions Photonic spectroscopy Laser techniques			
11. ABSTRACT (Continue on reverse side if necessary and identify by block number) This report covers the work supported by the US Army Research Office. The research involves the utilization of new laser techniques such as time-resolved spectroscopy and photonic spectroscopy to characterize multiphonon energy transfer and radiationless relaxation processes in phosphor and laser materials. The materials investigated include $\text{CaWO}_4$ , $\text{YVO}_4$ , $\text{LiNbO}_3$ , $\text{Bi}_2\text{GeO}_5$ , $\text{Al}_2\text{O}_3$ , and $\text{Y}(\text{Al}_{1-x}\text{Ga}_x)_3\text{O}_{12}$ crystals doped with various rare earth and transition			



OKLAHOMA STATE UNIVERSITY

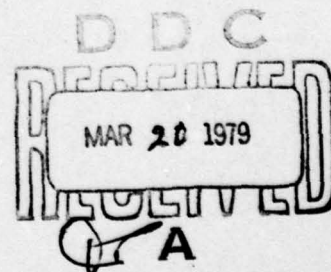
Department of Physics

LEVEL #  
(12)

MULTISTEP ENERGY MIGRATION AND RADIATIONLESS RELAXATION  
PROCESSES IN PHOSPHOR AND LASER CRYSTALS

Richard C. Powell, Principal Investigator

FINAL REPORT  
Grant Number DAAG29-76-G-0099  
U. S. Army Reserach Office  
Research Triangle Park, North Carolina



December 31, 1978

# ABSTRACT

This report covers the work done in the Department of Physics of Oklahoma State University under grant number BAAG29-76-G-0099 supported by the U. S. Army Research Office, Research Triangle Park, North Carolina from 1 January 1976 through 31 December 1978. The research involves the utilization of new laser techniques such as time-resolved site-selection spectroscopy and photo-acoustic spectroscopy to characterize multistep energy transfer and radiationless relaxation processes in phosphor and laser materials. The materials investigated include  $\text{CaWO}_4$ ,  $\text{YVO}_4$ ,  $\text{LiNbO}_3$ ,  $\text{Bi}_3\text{Ge}_4\text{O}_{12}$ ,  $\text{KCl}$ ,  $\text{Al}_2\text{O}_3$ , and  $\text{Y}_3(\text{Al}_{1-x}\text{Ga}_x)_5\text{O}_{12}$  crystals doped with various rare earth and transition metal ions and also the  $\text{Nd}_{1-x}\text{Y}_x\text{P}_5\text{O}_{14}$  system. Important results include the development of models for explaining energy migration among  $\text{Nd}^{3+}$  ions in disordered garnet crystals and concentration quenching in stoichiometric laser materials.

ACCESSION for	
NTIS	White Section <input checked="" type="checkbox"/>
DDC	Buff Section <input type="checkbox"/>
UNANNOUNCED	<input type="checkbox"/>
J. S. LOCATION	
DISTRIBUTION PRIORITY CODES	
SPECIAL	
A	

## CONTENTS

- I. INTRODUCTION
  - I.1 Summary of Research Accomplishments
  - I.2 Publications and Personnel
- II. PHOTOACOUSTIC SPECTROSCOPY OF SOLIDS
  - II.1 Experimental Apparatus
  - II.2 Theory of Signal Generation
  - II.3 Application to Radiationless Relaxation Processes
- III. ENERGY TRANSFER IN SOLIDS
  - III.1 Combined Energy Transfer Theory
  - III.2 Phonon Assisted Energy Transfer
- IV. HOST-SENSITIZED ENERGY TRANSFER RESULTS
  - IV.1 Energy Transfer in Rare Earth-Doped  $\text{CaWO}_4$  After Red Edge Excitation
    - A. Introduction
    - B. Experimental
    - C. Results
    - D. Discussion
  - IV.2 Laser Time-Resolved Spectroscopy: Investigations of Energy Transfer in  $\text{Eu}^{3+}$  and  $\text{Er}^{3+}$  Doped  $\text{YVO}_4$ 
    - A. Introduction
    - B. Results and Interpretation of Undoped  $\text{YVO}_4$  Data
    - C. Results and Interpretation of  $\text{YVO}_4:\text{Eu}^{3+}$  Data
    - D. Results and Interpretation of  $\text{YVO}_4:\text{Er}^{3+}$  Data
    - E. Discussions and Conclusions
  - IV.3 Laser Time-Resolved Spectroscopy Studies of Host-Sensitized Energy Transfer in  $\text{Bi}_4\text{Ge}_3\text{O}_{12}:\text{Er}^{3+}$  Crystals
    - A. Introduction
    - B. Experimental
    - C. Interpretation
    - D. Discussion and Conclusion
  - IV.4 Laser Time-Resolved Studies of Exciton Migration in Doped Lithium Niobate
    - A. Introduction
    - B. Experimental Results
    - C. Interpretation of Results
- V. SITE-SELECTION SPECTROSCOPY RESULTS
  - V.1 Laser Site-Selection Investigation of  $\text{Eu}^{3+}$  Ions in  $\text{YVO}_4$  Crystals
    - A. Introduction
    - B. Experimental
    - C. Interpretation
    - D. Discussion



- V.2 Energy Transfer Among  $\text{Nd}^{3+}$  Ions in  $\text{Y}_3\text{Al}_5\text{O}_{12}$  and  $\text{Y}_3\text{Ga}_5\text{O}_{12}$  Crystals
  - A. Introduction
  - B. Theoretical Background
  - C. Experimental
  - D. Analysis
  - E. Interpretation
  - F. Discussion and Conclusions
- V.3 Time-Resolved Site-Selection Spectroscopy of  $\text{Nd}^{3+}$  Ions in Mixed Garnet Crystals
  - A. Introduction
  - B. Mixed Crystal Spectroscopy
  - C. Time-Resolved Spectroscopy
  - D. Discussion and Conclusions

#### VI. CONCENTRATION QUENCHING IN $\text{Nd}_{x-1}\text{Y}_x\text{P}_5\text{O}_{14}$ Crystals

- A. Introduction
- B. Samples and Experimental Equipment
- C. General Spectroscopy and Concentration Quenching Results
- D. Time-Resolved Site-Selection Spectroscopy Results
- E. Interpretation of Results
- F. Photoacoustic Spectroscopy Results
- G. Discussion and Conclusions

#### VII. RESULTS ON THE CHARACTERIZATION OF RADIATIONLESS PROCESSES

##### VII.1 Radiationless Processes in $\text{KCl:Eu}^{2+}$

- A. Introduction
- B. Sample Growth and Properties
- C. Energy Transfer Between  $\text{Eu}^{2+}$  Ions
- D. Analysis of the Vibronic Spectrum of  $\text{Eu}^{2+}$  in KCl
- E. Width and Position of the Zero-Phonon Line
- F. Radiationless Relaxation
- G. Discussion and Conclusions

##### VII.2 Photoacoustic Spectroscopy Investigation of Radiationless Relaxation Processes of $\text{Cr}^{3+}$ in Crystals

#### VIII. MISCELLANEOUS STUDIES

## I. INTRODUCTION

The purpose of this research was to enhance our understanding of some of the physical properties of optical materials with potentially important practical applications. The research goals stated in the original proposal have all be accomplished and an additional investigation was carried out on a material of interest to the Army Electronics Laboratory. The work accomplished during the period of this grant is briefly outlined in this section and presented in detail in the remainder of the report.

### I.1 Summary of Research Accomplishments

There are three main thrust areas to our research program. These are listed in Table I. The first is characterizing the properties of specific materials having interesting possibilities for applications in optical systems such as those involving lasers, phosphors for display screens and lighting, frequency upconverters, optical storage and printing, fiber optics communication, etc. The field of electro-optics devices is one of the most rapidly advancing areas of technology today, and it has a significant impact on a wide variety of applications. These advances have resulted in requirements for materials with specific optical properties. Since there is a lag of several years between the time that basic research is done on the properties of a new material in the laboratory and the time it is incorporated into some new technological system, it is important to compile as much information as possible on the properties of potentially interesting materials to be available when specific material design requirements are generated. Similarly, in order to develop materials having specific physical properties, it is necessary to gain an understanding of the basic phenomena affecting these properties. This is the second thrust area of our research project. Finally, it is important to develop new experimental techniques to probe the optical properties of



**TABLE I**  
**RESEARCH THRUST AREAS**

CHARACTERIZATION OF MATERIALS	UNDERSTANDING OF PHYSICAL PHENOMENA	DEVELOPMENT OF EXPERIMENTAL TECHNIQUES
$\text{Nd}_{x-1}\text{Y}_x\text{P}_2\text{O}_7$ $\text{Y}_3(\text{Al}_{1-x}\text{Ga}_x)_5\text{O}_{12}:\text{Nd}^{3+}$ $\text{YVO}_4:\text{Eu}^{3+};\text{Er}^{3+}$ $\text{CaWO}_4:\text{Sm}^{3+};\text{Eu}^{3+}$ $\text{Bi}_4\text{Ge}_3\text{O}_{12}:\text{Mn}^{4+}$ $\text{LiNbO}_3:\text{Eu}^{3+}$	<p>Exciton dynamics</p> <p>Ion-ion interaction</p> <p>Radiationless and Vibronic decay processes</p> <p>Concentration quenching</p>	<p>Time-resolved spectroscopy</p> <p>Site-selection spectroscopy</p> <p>Photoacoustic spectroscopy</p>

materials both for the purpose of sample characterization and for understanding basic phenomena. This is the third thrust area. Using new investigative techniques is a critically important part of obtaining new knowledge about materials and physical properties.

The development of new types of experimental techniques has centered around the three spectroscopic methods listed in Table I. Time-resolved spectroscopy allows direct monitoring of the time evolution of dynamical physical processes. This adds an important new dimension to the more conventional steady state spectroscopy methods. Our current capabilities have a time resolution of about 1 ns. Site-selection spectroscopy relies on the high resolution capabilities of lasers to selectively excite impurity ions in nonequivalent crystal field sites. This allows microscopic inhomogeneities in the system to be probed. Our current equipment is limited in resolution by the width of the laser line which is about  $0.20 \text{ cm}^{-1}$ . Photoacoustic spectroscopy is a method of directly measuring the heat given off in radiationless decay processes. It is a well known technique for gas phase research but its application to solid state physics is relatively new. There is still a great deal of work to do on this technique in optimizing the signal to noise ratio, understanding all of the contributions to the PAS signal, and extending the capabilities to low temperatures. Although a detailed interpretation of the absolute magnitude of the signal in a PAS spectrum is extremely difficult, we have found that PAS is still a powerful tool when used by comparing the relative peak heights of bands in the absorption, fluorescence excitation and photoacoustic spectra. This gives added information on the relaxation dynamics of a system which cannot be obtained from standard optical methods.

Our investigation of physical phenomena has focused on energy transfer and radiationless decay. Both of these types of processes are extremely important



in determining the optical characteristics of a material useful in practical applications. Radiationless decay processes determine the efficiency of pumping fluorescing levels after exciting into higher absorption bands. They also directly effect the radiative quantum efficiency of a metastable level. Energy transfer processes can be effective either in enhancing the pumping of a specific species of fluorescing ions or in causing concentration quenching of the fluorescence. There are many aspects of these processes which are still not well understood and they have not been well characterized in most materials.

The new experimental techniques discussed previously are especially useful in obtaining new knowledge concerning these specific types of processes. Photo-acoustic spectroscopy has yielded important information about decay modes of ions in crystals and about concentration quenching of the fluorescence. Time-resolved spectroscopy has been most helpful in developing models for excitation migration in materials exhibiting intrinsic fluorescence. Site-selection spectroscopy has elucidated microscopic differences in the local environments of impurity ions in host crystals and, coupled with time-resolved techniques, has been a powerful tool for studying energy transfer between ions in nonequivalent sites. The ability to probe the details of energy transfer with the spectral and temporal resolution now available has necessitated the development of new theoretical models for explaining the observed results.

The materials characterization part of this program has centered around the systems listed in Table I which all exhibit useful properties for applications as lasers or phosphors. Host-sensitized energy transfer is being characterized in the tungstate, vanadate, germanate, and niobate hosts doped with rare earth or transition metal impurity ions. The interaction and energy transfer between impurity ions has been characterized in some of these materials as well as in

the mixed garnet and mixed pentaphosphate hosts. The characterization of the radiationless quenching of the fluorescence in neodymium pentaphosphate crystals have proven especially important.

One important result of this work has been the development of a model to quantitatively characterize the transfer of electronic excitation energy from "molecular" host crystals to impurity ions. This model is based on the migration and trapping of localized exciton and has now been employed by several different laboratories in interpreting results obtained on a variety of materials of this type. In our laboratory laser excited time-resolved spectroscopy techniques have been used to study  $\text{CaWO}_4$  with  $\text{Sm}^{3+}$  and  $\text{Eu}^{3+}$  activator ions,  $\text{YVO}_4$  with  $\text{Eu}^{3+}$  and  $\text{Er}^{3+}$  activator ions,  $\text{LiNbO}_3$  double doped with  $\text{Eu}^{3+}$  and  $\text{Cr}^{3+}$  ions and  $\text{Bi}_4\text{Ge}_3\text{O}_{12}$  with  $\text{Er}^{3+}$  activators. The exciton migration and trapping parameters determined for these systems are discussed in Chapter IV.

A second important result of this work has been the characterization of energy transfer between similar ions in different types of sites in an inhomogeneous crystal host. Our previous work utilizing laser time-resolved site-selection spectroscopy techniques to study  $\text{Sm}^{3+}$  ions in  $\text{CaWO}_4$  was extended to  $\text{Eu}^{2+}$  ions in KCl crystals,  $\text{Eu}^{3+}$  ions in  $\text{YVO}_4$  crystals and  $\text{Nd}^{3+}$  ions in pure and mixed garnet crystals. These results are presented in detail in Chapter V. The Nd-garnet system yielded the most interesting results since the energy transfer was found to be consistent with a two phonon assisted process as predicted by recent theoretical work. The transfer efficiency was found to be greatly enhanced by increasing the inhomogeneities in the system due to the change in the transition matrix elements.

A third important result of this work was the development of a model to explain concentration quenching in neodymium pentaphosphate ( $\text{NdP}_5\text{O}_{14}$ ). This is an important new material having the low threshold and high gain characteristics



ideal for miniature optically pumped laser which maybe the key elements in the new fiber optics communication technology. The model is based on efficient spatial but non-spectral energy migration to surface quenching sites. This is substantiated by time-resolved site-selection spectroscopy and photoacoustic spectroscopy results as well as the results of standard optical spectroscopy measurements. The details of this work are presented in Chapter VI.

A final important result was the demonstration of the usefulness of photoacoustic spectroscopy as a technique for characterizing radiationless relaxation processes of ions in crystals. This was done in three separate investigations. The first involved  $\text{Eu}^{2+}$  in KCl where the phase of the PAS signal was used to show the importance of  $4f^7$  levels acting as bottlenecks in the decay from the  $4f^6 5d(e_g)$  level. The second was a comparison of the PAS spectra of  $\text{Cr}^{3+}$  ions in various host crystals. The differences in the spectra observed for MgO and  $\text{Al}_2\text{O}_3$  hosts showed the usefulness of PAS in determining dominant decay modes. The third was the investigation of  $\text{NdP}_5\text{O}_{14}$  which helped lead to the proposed model for concentration quenching in this system as discussed in the preceeding paragraph. The details of this work are given in Chapter VII.

The following two chapter present background material in the areas of photoacoustic spectroscopy and energy transfer while the final chapter summarize plans for the continuation of this research project.

## I.2 Publications and Personnel

The work performed during the three years of this grant resulted in the 14 publications listed in Table II along with numerous unpublished presentation and colloquia. Four graduate students were supported by this grant and their doctoral theses are listed in Table II. Also two undergraduate students E. W. Freed and D. P. Neikirk participated in this research project.

TABLE II  
PUBLICATIONS, THESES, AND PRESENTATIONS

- I. Publications:
1. PHOTOACOUSTIC SPECTROSCOPY INVESTIGATION OF RADIATIONLESS TRANSITIONS IN  $\text{Eu}^{2+}$  IONS IN KCl CRYSTALS, L.D. Merkle and R.C. Powell. Chem. Phys. Letters, 46, 303 (1977).
2. LASER TIME-RESOLVED SPECTROSCOPY INVESTIGATIONS OF ENERGY TRANSFER IN  $\text{Eu}^{3+}$  AND  $\text{Er}^{3+}$  DOPED  $\text{YVO}_4$ , G.E. Venikouas and R.C. Powell, J. Lumin, 16, 29 (1978).
3. PHOTOACOUSTIC SPECTROSCOPY INVESTIGATION OF RADIATIONLESS RELAXATION PROCESSES OF  $\text{Cr}^{3+}$  IN CRYSTALS, R.G. Peterson and R.C. Powell, Chem. Phys. Letters, 53, 366 (1978).
4. LASER SITE-SELECTION SPECTROSCOPY INVESTIGATION OF  $\text{Eu}^{3+}$  IONS IN  $\text{YVO}_4$  CRYSTALS, G.E. Venikouas and R.C. Powell, Phys. Rev. B. 17, 3456 (1978) to be published.
5. ENERGY TRANSFER IN RARE EARTH-DOPED  $\text{CaWO}_4$  AFTER RED EDGE EXCITATION, R.G. Peterson and R.C. Powell, J. Lumin 16, 285 (1978).
6. LASER SITE-SELECTION TIME-RESOLVED SPECTROSCOPY OF  $\text{NdP}_5\text{O}_{14}$ , J.M. Flaherty and R.C. Powell, Solid State Comm., 26, 503 (1978).
7. RADIATIONLESS PROCESSES IN  $\text{KCl:Eu}^{2+}$ , L.D. Merkle, R.C. Powell and T.M. Wilson, J. Phys. C. 11, 3103 (1978).
8. CONCENTRATION QUENCING IN  $\text{Nd}_x\text{Y}_{1-x}\text{P}_5\text{O}_{14}$  CRYSTALS, J.M. Flaherty and R.C. Powell, Phys. Rev. B. to be published.
9. ENERGY TRANSFER AND RADIATIONLESS RELAXATION IN Nd-DOPED MIXED CRYSTALS, R.C. Powell, J.M. Flaherty, and M. Zokai, J. Lumin, to be published.
10. PHOTOACOUSTIC AND PIEZOSPECTROSCOPIC MEASUREMENTS ON NEODYMIUM PENTAPHOSPHATE CRYSTALS, R.C. Powell, and J.M. Flaherty, submitted to Optics Letters.
11. LASER TIME-RESOLVED SPECTROSCOPY STUDIES OF HOST-SENSITIZED ENERGY TRANSFER IN  $\text{Bi}_4\text{Ge}_3\text{O}_{12}:\text{Er}^{3+}$  CRYSTAL, D.P. Neikirk and R.C. Powell, submitted to J. Luminescence.
12. LASER TIME-RESOLVED STUDIES OF EXCITON MIGRATION IN DOPED LITHIUM NIOBATE, R.C. Powell, and E.E. Freed, submitted to J. Chem. Phys.
13. ENERGY TRANSFER AMONG  $\text{Nd}^{3+}$  IONS IN GARNET CRYSTALS, L.D. Merkle and R.C. Powell, submitted to Phys. Rev.



TABLE II (continued)

14. TIME-RESOLVED SITE-SELECTION SPECTROSCOPY INVESTIGATION OF  $Y_3(Al_{1-x}Ga_x)_5O_{12}:Nd^{3+}$  CRYSTALS, M. Zokai, R.C. Powell, G.F. Imbusch, and B. DiBartolo, submitted to J. Appl. Phys.
- II. Doctoral Theses:
1. LASER SPECTROSCOPY STUDIES OF ENERGY TRANSFER IN  $YVO_4:Eu^{3+}, Er^{3+}$ , G. Venikouas, May, 1978.
  2. ENERGY TRANSFER AND DISSIPATION PROCESSES IN DOPED CRYSTALS, R.G. Peterson, December, 1977.
  3. OPTICAL SPECTROSCOPIC STUDIES OF  $KCl:Eu^{2+}$  AND  $Nd^{3+}$  DOPED GARNET CRYSTALS, L.D. Merkle, December, 1978.
  4. DYE LASER SPECTROSCOPY INVESTIGATIONS OF  $Nd^{3+}$  IONS IN MIXED GARNET CRYSTALS, M. Zokai, May, 1979.
- III. Presentations:
1. ENERGY MIGRATION IN CRYSTALS, R.C. Powell, Invited talk, March, 1976, American Physical Society Meeting, Atlanta, GA. Bull. Am. Phys. Soc. 21, 248 (1976).
  2. LASER TIME-RESOLVED ENERGY TRANSFER STUDIES OF  $CaWO_4$  DOPED WITH  $Sm^{3+}$  AND  $Eu^{3+}$  IONS, R.G. Peterson and R.C. Powell, March 1977, American Physical Society Meeting, San Diego, California, Bull. Am. Phys. Soc. 22, 464 (1977).
  3. DYE LASER SPECTROSCOPY OF  $Eu^{3+}$  IONS IN  $YVO_4$  CRYSTALS, G.E. Venikouas and R.C. Powell, March 1977, American Physical Society Meeting, San Diego, California, Bull. Am. Phys. Soc. 22, 464 (1977).
  4. PHOTOACOUSTIC SPECTROSCOPY OF IONS IN CRYSTALS, L.D. Merkle, R.G. Peterson, and R.C. Powell, Midwest Solid State Conference, Oct. 1977, Columbia, Mo., paper 11.
  5. TIME-RESOLVED SITE-SELECTION SPECTROSCOPY IN  $Nd:Y_3B_5O_{14}$ , J.M. Flaherty and R.C. Powell, March 1978, American Physical Society Meeting, Washington, D.C., Bull. Am. Phys. Soc. 23, 203 (1978).
  6. ENERGY TRANSFER IN  $Y_3(Al_{1-x}Ga_x)_5O_{12}:Nd$ , M. Zokai and R.C. Powell, March, 1978, American Physical Society Meeting, Washington, D.C., Bull. Am. Phys. Soc. 23, 203 (1978).
  7. RADIATIONLESS PROCESSES IN  $KCl:Eu^{2+}$ , R.D. Merkle, R.C. Powell, and T.M. Wilson, March, 1978, American Physical Society Meeting, Washington, D.C., Bull. Am. Phys. Soc. 23, 202 (1978).

TABLE II (continued)

8. ENERGY MIGRATION AMONG  $\text{Nd}^{3+}$  IONS IN MIXED CRYSTAL HOSTS, R.C. Powell, CONFERENCE ON DYNAMICAL PROCESSES IN THE EXCITED STATES OF IONS AND MOLECULES IN SOLIDS, June 1978, Athens, Georgia.
9. ENERGY TRANSFER AND RADIATIONLESS RELAXATION IN Nd-DOPED MIXED CRYSTALS, R.C. Powell, J.M. Flaherty, and M. Zokai, International Conference on Luminescence, Paris, France, July 1978.
10. ENERGY TRANSFER AND CONCENTRATION IN Nd-DOPED LASER CRYSTALS, R.C. Powell, Physical Chemistry Colloquium, University of Utrecht, Netherlands, July, 1978.
11. LASER SPECTROSCOPY STUDIES OF SOLIDS, R.C. Powell, Colloquium at the Laboratory for Luminescence Research, University of Lyon, Lyon, France, July 1978.
12. PHOTOACOUSTIC SPECTROSCOPY OF SOLIDS, R.C. Powell, Quantum Electronics, Colloquium, University of Southern California, November 1978.
13. DYNAMICS OF ENERGY TRANSFER IN SOLIDS, R.C. Powell, Physics Department Colloquium, UCLA, November 1978.
14. ENERGY TRANSFER IN LASER MATERIALS, R.C. Powell, Chemical Physics Colloquium, California Institute of Technology, November 1978.
15. LASER SPECTROSCOPY OF Nd-LASER MATERIALS, R.C. Powell, Research Colloquium, Lawrence Livermore Laboratory, November 1978.



It was a pleasure to have the opportunity to collaborate with Profs. B. DiBartolo of Boston College and G. F. Imbusch of University College in Galway Ireland. Both spent one month in our laboratory working on the Nd-mixed garnet system with us. Prof. Imbusch was sponsored by the Middle America State University Association as a MASUA Visiting Foreign Scientist. Three other scientists also worked on this project. J. M. Flaherty, a visiting assistant professor at Oklahoma State University spent one year working on the  $\text{NdP}_{50}\text{O}_{14}$  research and B. J. Ackerson, an assistant professor at Oklahoma State, spent one month initiating preliminary experiments on antistokes excitation studies in our laboratory. Also Prof. T. M. Wilson of our faculty assisted us with the computer program involved in analyzing vibronic sidebands.

Supplemental support for our laboratory was received in the form of an equipment grant from the National Science Foundation. This allowed us to expand our laboratory capabilities to include a CW dye laser system which has been used in some of our photoacoustic work.

## II. PHOTOACOUSTIC SPECTROSCOPY OF SOLIDS

Photoacoustic spectroscopy (PAS) is a technique for measuring the amount of heat generated in a sample after the absorption of light.<sup>1</sup> Although it has been used successfully for years in gas studies, its application to solid state physics is relatively new. In this section we review the experimental apparatus and the theory of PAS signal generation. Results obtained using this technique to investigate radiationless relaxation processes of ions in solids are discussed in later sections.

### II.1 Experimental Apparatus

Photoacoustic spectroscopy is based on the periodic illumination of a sample in an acoustical cell containing a microphone detector. A block diagram of our PAS experimental apparatus is shown in Fig. 1. For spectral scans a

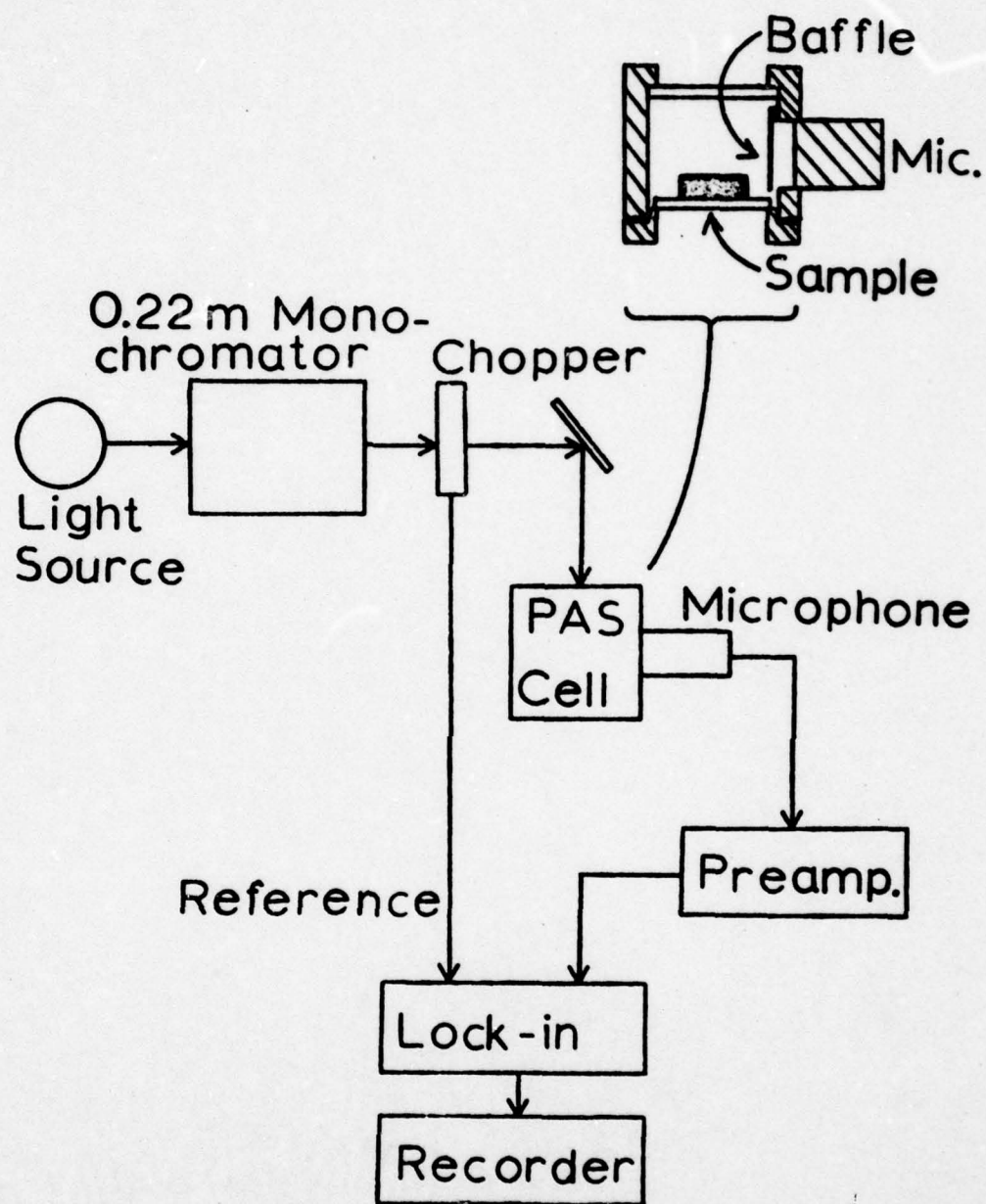


Figure 1. PAS Apparatus

1000 W high pressure mercury or tungsten-halogen lamp focused onto the entrance slit of a Spex 0.22 meter Czerny-Turner monochromator with grating blazed at 300 nm and typically used with 5 mm slit widths to give a 20 nm bandpass. For chopping frequency studies argon ion or tunable dye lasers were used as excitation sources. The light was modulated by a mechanical chopper capable of numerous discrete frequency settings between 100 Hz and 2000 Hz.

The excitation light was focused onto the sample inside the PAS cell which is also shown in Fig. 1. This consisted of an aluminum chamber with a quartz input window and a microphone mounted at the side. An aluminum foil baffle kept scattered light from the microphone, a General Radio 1961 one inch electret. The sample was mounted on a quartz exit window. The chamber was backed by a piece of black cloth to eliminate back scattered light, and mounted in a styrofoam holder to minimize coupling of outside vibrations to the cell. The signal from the microphone was amplified by a current sensitive preamplifier and a PAR Model 128 lock-in amplifier. The lock-in received its reference signal from the light chopper, and the phase of detection relative to this reference could be chosen manually. Output from the lock-in was recorded on a strip chart recorder. When signal to noise improvement was necessary the signal was sent through a voltage to frequency convertor to a multichannel analyzer and the spectral scans repeated several times and averaged.

To correct the spectra for variations of the excitation intensity with wavelength, a piece of charcoal was substituted for the sample. Charcoal has sufficiently strong absorption at all wavelengths of interest to give a PAS signal which directly indicates the power of the input beam, that is its optical penetration depth is much less than its thermal diffusion length and its radiationless relaxation probability is practically unity.



## II.2 Theory of PAS Signal Generation

Several theoretical developments have been given for the signal generation in solid state PAS. The theory outlined in this section is due mainly to Rosencwaig and Gersho.<sup>2</sup>

Typically, the derivation of an expression for the PAS signal considers a simple cell geometry such as depicted in Fig. 2. The problem is treated as one-dimensional, with incident light passing through a front window, a length of gas,  $l_g$ , a sample of thickness  $l$ , and a backing material of thickness  $l_b$  upon which the sample is mounted. Various optical and thermal parameters are required. These include thermal conductivity  $k_i$ , density  $\rho_i$ , specific heat  $c_i$ , where in each case the subscript  $i$  may take the values  $g$ ,  $s$  and  $b$  for the gas, sample and backing, respectively. From these may be derived the thermal diffusivity  $\alpha_i = k_i / \rho_i c_i$ , the thermal diffusion coefficient  $a_i = (\omega / 2\alpha_i)^{1/2}$ , and the thermal diffusion length  $\mu_i = 1/a_i$ , where  $\omega/2\pi$  is the modulation frequency of the excitation light. This modulation is assumed to be sinusoidal, of intensity

$$I = \frac{1}{2} I_0 (1 + \cos \omega t) \quad (1)$$

in units of power per unit area. The gas and backing are assumed to be transparent, whereas the sample has optical absorption coefficient  $\beta$ , and may convert a fraction  $\eta$  of the absorbed energy of heat, where both these quantities are dependent upon the wavelength of the incident light.

The method of solution proceeds by setting up equations for the temperature in the three regions, gas, sample, and backing. For the gas and backing these are simply diffusion equations, where  $\phi$  is the temperature relative to room temperature:

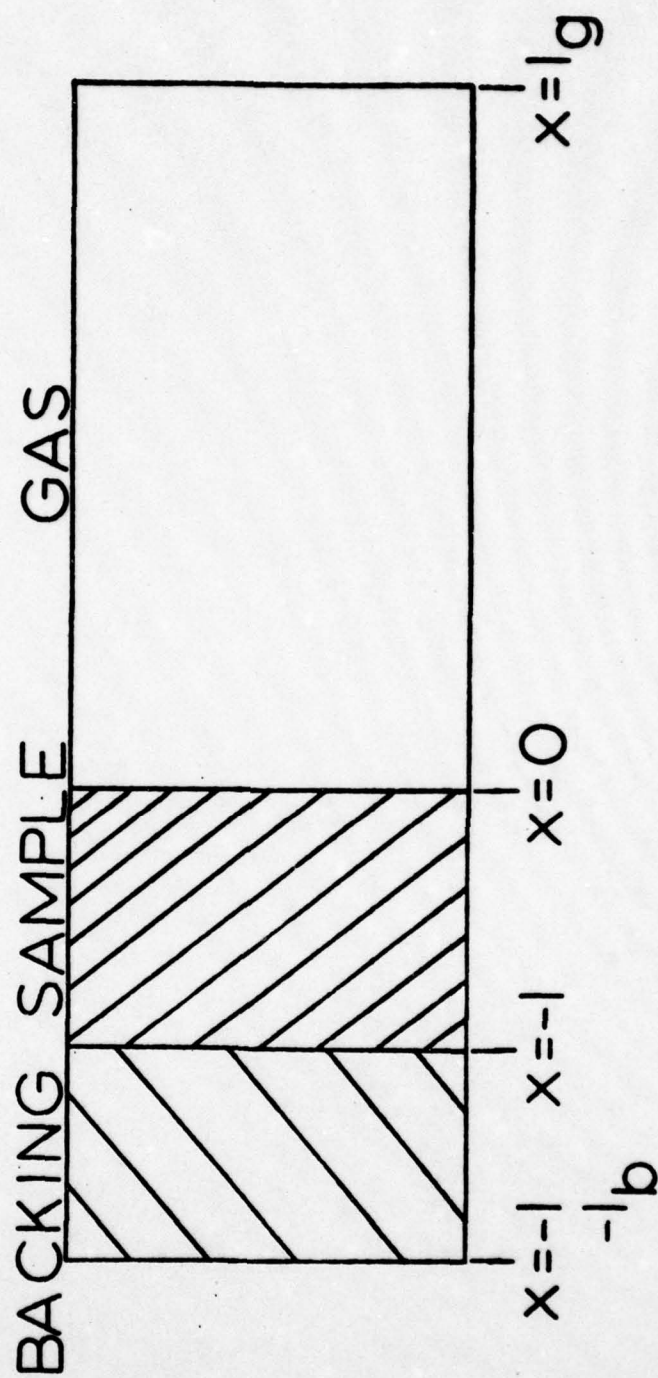


Figure 2. One Dimensional Model of PAS Cell

$$\alpha_g \frac{\partial^2 \phi}{\partial x^2} = \frac{\partial \phi}{\partial t}, \quad 0 \leq x \leq l_g \quad (2)$$

$$\alpha_b \frac{\partial^2 \phi}{\partial x^2} = \frac{\partial \phi}{\partial t}, \quad -l-l_b \leq x \leq -l. \quad (3)$$

In the sample a source term is required to account for heat production due to light absorption:

$$\alpha_s \frac{\partial^2 \phi}{\partial x^2} = \frac{\partial \phi}{\partial t} - \frac{\tau_0 \beta n}{2\rho_s C_s} e^{\beta x} [1 + e^{i\omega t}], \quad -l \leq x \leq 0. \quad (4)$$

The boundary conditions are that the temperature at the cell ends equal room temperature, and continuity of temperature and heat flux at the gas-sample and sample-backing boundaries. The solution of this set of equations will not be carried through here, but may be found in Rosencwaig and Gersho.<sup>2</sup>

These workers then use the solution for the time-dependent gas temperature to estimate the pressure fluctuation as follows. It is first noted that for the gas beyond  $2\pi \mu_g$  the temperature fluctuation is nearly zero. Thus the volume change in the layer  $0 \leq x \leq 2\pi \mu_g$  is calculated using the spatial average of temperature over this layer and the ideal gas law, assuming constant pressure. This latter assumption is clearly not true, and represents a rough approximation. The pressure fluctuation in the remaining gas,  $2\pi \mu_g \leq x \leq l$ , is then calculated assuming adiabatic compression of this region by the "piston" formed by the layer in which temperature fluctuations were found to be significant. If the PAS cell's microphone senses the pressure fluctuation in this region the result is<sup>1</sup>

$$\delta P(t) = Q \exp[i(\omega t - \pi/4)] \quad (5)$$



where Q is given by

$$\begin{aligned}
 Q = & \frac{I_0 \gamma P_0 \beta \eta}{2\sqrt{2} \kappa_s l a_g T_0 [\beta^2 - (1+i)^2 a_s^2]} \\
 & \times \left[ \left( \frac{(1-i)\beta}{2a_s} - 1 \right) \left( \frac{k_b a_b}{k_s a_s} + 1 \right) e^{(1+i)a_s l} \right. \\
 & \quad - \left( \frac{(1-i)\beta}{2a_s} + 1 \right) \left( \frac{k_b a_b}{k_s a_s} - 1 \right) e^{-(1+i)a_s l} \\
 & \quad \left. + 2 \left( \frac{k_b a_b}{k_s a_s} - \frac{(1-i)\beta}{2a_s} e^{-\beta l} \right) \right. \\
 & \quad + \left[ \left( \frac{k_a a_g}{k_s a_s} + 1 \right) \left( \frac{k_a a_g}{k_s a_s} + 1 \right) e^{(1+i)a_s l} \right. \\
 & \quad \left. \left. - \left( \frac{k_a a_g}{k_s a_s} - 1 \right) \left( \frac{k_b a_b}{k_s a_s} - 1 \right) e^{-(1+i)a_s l} \right] . \quad (6)
 \end{aligned}$$

Here  $P_0$  and  $T_0$  are the ambient pressure and temperature, and  $\gamma$  is the ratio of specific heats of the gas. The real part of Eq. (5) represents the actual signal to be measured.

The rather difficult general expression for the photoacoustic signal may be greatly simplified in certain special cases. These consist of combinations of thermally thick or thin sample, and optically thick or thin sample. Again following the work of Rosencwaig and Gersho, six cases suggest themselves. Definition of an optical penetration length  $\mu_\beta = 1/\beta$  will facilitate identification of these cases, and it will always be assumed that  $k_g a_g < k_b a_b$  due to the low thermal conductivity of gases.

First let us consider the case of an optically thin solid, one for which  $\mu_\beta > l$ . If  $\mu_s \gg l$  and  $\mu_s > \mu_\beta$ , that is the sample is even more transparent to the passage of heat than of light, one would expect the amount of light absorbed to be roughly proportional to  $\beta$ , and that virtually all the heat generated is able to diffuse out of the sample. Indeed, using the approximations  $\exp(-\beta l) \doteq 1 - \beta l$  and  $\exp(\pm(1+i)a_s l) \doteq 1$ , Eq. (6) becomes

$$\begin{aligned}
 Q &\doteq \frac{I_{\text{O O}} P \gamma \beta \eta}{2\sqrt{2} l \frac{T}{g} k_s a_g \beta^2} \frac{\frac{1-i}{a_s} \beta - \frac{2k_b a_b}{k_s a_s} + \frac{2k_b a_b}{k_s a_s} (1-\beta l) - \frac{(1-i)\beta}{a_s} (1-\beta l)}{\frac{2k_b a_b}{k_s a_s} + \frac{2k_b a_b}{k_s a_s}} \\
 &= \frac{I_{\text{O O}} P \gamma \eta}{2\sqrt{2} l \frac{T}{g} k_s a_g} \left( \frac{k_s (1-i)\beta l}{2k_b a_b} - l \right) \\
 &= \frac{I_{\text{O O}} P \gamma l (1-i)}{4\sqrt{2} l \frac{T}{g} k_s a_g} \eta \beta, \tag{7}
 \end{aligned}$$

since it is reasonable to assume  $k_s \doteq k_b$  and  $a_b \doteq a_s < \beta$ . Thus the PAS signal is proportional to  $\beta \eta$ , since  $a_b a_g = \omega/2 \sqrt{\alpha_b \alpha_g}$  the signal varies as  $\omega^{-1}$ .

If again the sample is optically and thermally thin, but with  $\mu_s < \mu_\beta$ , the result is similar. In this case  $\exp(-\beta l) \doteq 1 - \beta l$  but we will keep  $\exp(\pm(1+i)a_s l) \doteq 1 \pm (1+i)a_s l$ , so that

$$\begin{aligned}
 Q &\doteq \frac{I_{\text{O O}} P \gamma \beta \eta}{-2\sqrt{2} k_s l \frac{T}{g} a_g (1+i)^2 a_s^2} \frac{-2(1+i)a_s l + (1-i)\beta^2 l/a_s}{2k_b a_b/k_s a_s} \\
 &\doteq \frac{I_{\text{O O}} P \gamma (1-i)}{4\sqrt{2} l \frac{T}{g} k_s a_g} \eta \beta, \tag{8}
 \end{aligned}$$



just as in the previous case, since  $a_s^2 \gg \beta^2$ , so that the PAS signal is proportional to  $\eta\beta/\omega$ .

The result is slightly different if the sample, still regarded as optically thin, is taken to be thermally thick so that  $\mu_s \ll \mu_\beta$  and  $\mu_s < \ell$ . In this case only a layer of the sample of thickness  $\mu_s$  near the surface contributes to the signal, due to the limited thermal diffusivity. We may still expect a signal proportional to  $\beta\eta$ , but with a somewhat different dependence on the thermal parameters. Indeed, taking  $\exp(-\beta\ell) \doteq 1 - \beta\ell$  and  $\exp(-(1+i)a_s\ell) \doteq 0$ , the result is

$$Q \doteq \frac{I_{OO} P_Y \beta \eta}{-2\sqrt{2} k_{sg} \ell a_{go} T_o (1+i)^2 a_s^2} \frac{(-1 - k_{bb} a_{bs}/k_{ss} a_s) e^{(1+i)a_s \ell}}{(1 + k_{bb} a_{bs}/k_{ss} a_s) e^{(1+i)a_s \ell}}$$

$$\doteq -i \frac{I_{OO} P_Y}{4\sqrt{2} k_{sg} \ell a_{gs} a_s^2 T_o} \beta \eta. \quad (9)$$

Thus the signal is indeed proportional to  $\beta\eta$ , but due to the factor  $a_{gs} a_s^2$  in the denominator it is now proportional to  $\omega^{-3/2}$ .

The three cases considered thus far have involved samples sufficiently transparent that the amount of light absorbed, and thus the signal, could be taken as approximately proportional to  $\beta$ , regardless of thermal properties of the sample. In the following three cases the sample is taken to be optically dense, so that effectively all the light incident upon the sample is absorbed. In such a case the sample's thermal properties are found to be critical in determining what, if any, dependence upon absorption coefficient the sample displays.

If the optically thick sample,  $\mu_\beta \ll \ell$ , is thermally very thin such that  $\mu_s \gg \ell \gg \mu_\beta$ , we may intuitively suspect that since all the light is absorbed and all the heat produced is efficiently carried out of the sample, the PAS signal will show no dependence upon  $\beta$ . Taking  $\exp(-\beta\ell) \doteq 0$  and  $\exp(\pm(1+i)a_s\ell) \doteq 1$ , we find

$$Q \doteq \frac{I_{oo} P \gamma \beta \eta}{2\sqrt{2} k_{sg} \ell a_g T_o \beta^2} \frac{(1-i)\beta/a_s - 2k_{ba}/k_{sa}}{2k_{ba}/k_{sa} + 2k_{ga}/k_{sa}}$$

$$= \frac{I_{oo} P \gamma (1-i)}{4\sqrt{2} \ell a_g k_{gb} T_o} \eta, \quad (10)$$

where we note that  $\beta \gg a_s$  whereas it is reasonable to assume that  $k_{ba}$  and  $k_{sa}$  are of the same order of magnitude, both these components being solids. Also, recall that we take  $k_{ga} \ll k_{sa}$ , as stated earlier. The resultant PAS signal is proportional  $\eta$ , and due to the  $a_g a_b$  factor, to  $\omega^{-1}$ , but as expected is independent of  $\beta$ .

If the opaque sample is thermally thick, so that  $\mu_s < \ell$ , two cases may arise. The first occurs if the thermal diffusion length is longer than the optical penetration depth,  $\mu_s > \mu_\beta$ . In this case, although only a small portion of the sample may thermally "communicate" with the surface, this small region is sufficient to contain the region in which the light is fully absorbed. We thus may expect a result similar to the preceding case. Taking  $\exp(-\beta\ell) \doteq 0$  and  $\exp(-(1+i)a_s\ell) \doteq 0$ , we have

$$Q \doteq \frac{I_{oo} P \gamma \beta \eta}{2\sqrt{2} k_{sg} \ell a_g T_o \beta^2} \frac{((1-i)\beta/2a_s - 1)(k_{ba}/k_{sa} + 1)e^{(1+i)a_s\ell}}{(k_{ba}/k_{sa} + 1)e^{(1+i)a_s\ell}}$$

$$\dot{=} \frac{I_o P_o \gamma (1-i)}{4\sqrt{2} \ell_a k_{gs} a_s T_o} \eta, \quad (11)$$

the same result as the optically thick and thermally thin case, except that the thermal parameters of the backing are replaced by those of the sample since the short diffusion length allows no communication of backing properties to the gas. Again the signal is proportional to  $\eta \omega^{-1}$ .

It may be observed that the insensitivity of these two cases to the absorption coefficient, and the strength of signal expected in a case in which all light is absorbed and efficient thermal diffusion occurs, are well-suited for production of a signal proportional only to  $I_o(\lambda)$ . If  $\eta$  is also near unity for all wavelengths, as in the case of charcoal and similar carbon materials, a good material for calibration of the excitation source spectrum results.

The final case to be considered is that of an optically and thermally thick sample in which the thermal diffusion length is much shorter than the optical penetration depth,  $\mu_s \ll \mu_\beta \ll \ell$ . Since now only a small portion of the region in which the light is absorbed can contribute to the PAS signal we may expect to recover a dependence upon  $\beta$ . If  $\exp(-\beta\ell) \doteq 0$  and  $\exp(-(1+i)a_s\ell) \doteq 0$ , we have

$$Q \doteq \frac{I_o P_o \gamma \beta \eta}{-2\sqrt{2} k_s \ell_a T_o (1+i)^2 a_s^2} \frac{\left(\frac{(1-i)\beta}{2a_s} - 1\right) \left(\frac{k_b a_b}{k_s a_s} + 1\right) e^{(1+i)a_s \ell}}{\left(\frac{k_b a_b}{k_s a_s} + 1\right) e^{(1+i)a_s \ell}}$$

$$\dot{=} -i \frac{I_o P_o \gamma}{4\sqrt{2} \ell_a k_{gs} a_s^2 T_o} \beta \eta, \quad (12)$$



which is proportional to  $\beta\eta\omega^{-3/2}$ , and is exactly the result (9), in which also the short thermal diffusion length controlled the behavior.

Some comments as to phase of the PAS signal are appropriate. The  $\pi/4$  phase factor in Eq. (5) together with the complex numbers in the various special case forms of  $Q$  indicate the phase of the PAS signal relative to the excitation source modulation. It is not surprising that these vary among the cases, since in those cases where the thermal diffusion length is much greater than the depth of the illuminated region little time is required for the bulk of the generated heat to diffuse to the surface, whereas in the opposite case considerable heat is still reaching the surface long after the peak light intensity has passed. Another source of phase shift, the lifetime of the radiationless transition giving rise to the heat signal, has been neglected in this derivation. It will be treated in an approximate manner in the next section.

The limited usefulness of these special case results should be noted. In many cases it is possible to control the sample thickness and, by means of chopping frequency, the thermal diffusion length to a degree, thus choosing conditions consistent with a particular special case. However, as the excitation source is scanned in wavelength to obtain a photoacoustic spectrum the optical absorption coefficient may change considerably. In the case of very strong absorption bands separated by transparent regions one may vary from a small  $-\beta$  case with signal proportional to  $\beta$  to a large- $\beta$  case independent of  $\beta$ .

### II.3 Application to Radiationless Relaxation Processes

An excited electronic state of an ion in a solid may deexcite by, among other processes, radiationless relaxation. In this process the energy of the excited electron is dissipated by the emission of one or more quanta of lattice vibrational energy, requiring some interaction between the electronic states and the atomic vibrations.

The consequent electron-phonon interaction makes possible radiationless transitions between electronic states, the probability of which depends upon the strength of the interaction between the excited electron and the neighboring ions. For the purpose of this work it is simply necessary to note that any given excited state may have radiationless as well as radiative decay channels available to it. The probabilities of these various decays sum to give the total decay probability of the level, dictating the lifetime of the decay of the level. If one radiationless transition is to be detected by photoacoustic spectroscopy the excited level will contribute to the signal an amount proportional to the probability of excitation of the level and to the fractional probability of decay by that radiationless mode multiplied by the quantity of energy dissipated by phonon emission in the decay process. Further, the lifetime of excited level will affect the phase lag of the PAS signal behind the modulation of the excitation source.

The relation of the PAS phase to the decay lifetime may be simply expressed if this lifetime is regarded as the only factor causing a phase difference between the excitation and the signal. In this case the signal observed is proportional to the convolution of the time-varying excitation intensity function with the exponential decay term. Only the sinusoidal portion of the intensity need be considered, giving

$$\int_0^{\infty} e^{-s/\tau} \cos \omega(s-t) ds = \frac{\cos (\omega t - \alpha)}{\sqrt{\omega^2 + \tau^{-2}}} \quad (13)$$

where  $\omega$  is the angular frequency of the light modulation,  $\tau$  is the lifetime of the decay, and the phase shift  $\alpha$  is related to the other parameters by

$$\tau = (\tan \alpha)/\omega . \quad (14)$$

This relation may be used to estimate the lifetime of the decay by the phase shift of the signal.

In general an excited electronic state may have more than one radiationless channel of decay available to it terminating on various lower energy levels, each of which may also have more than one decay channel. The signal due to the  $i^{\text{th}}$  decay mode of the  $j^{\text{th}}$  level will be proportional to the probability of that decay relative to the total level decay probability, the fraction  $\phi_{ji}^{\text{nr}}$ , and to the energy dissipated in the transition,  $h\nu_{ji}$ .

Since each decay process is driven, directly or indirectly, by the periodic illumination, each will contribute a signal with a phase shift  $\alpha_j$  related to the lifetime of the  $j^{\text{th}}$  level by Eq. (14). The signal due to the  $ji$  decay is thus proportional to

$$\phi_{ji}^{\text{nr}} h\nu_{ji} \cos(\alpha_j - \theta) \quad (15)$$

where  $\theta$  is the phase angle of detection. For a total signal involving several such transitions a summation is required. Also, the signal is proportional to the number of photons absorbed,  $N_a$ , and will be normalized by the number and energy of photons  $N_o h\nu_o$  available to excite the ions in the sample to a particular initial energy level. Thus, the PAS signal may be written as

$$I_{\text{PAS}}(\theta) \propto N_a \sum_i \sum_j \phi_{ji}^{\text{nr}} h\nu_{ji} \cos(\alpha_j - \theta) / (N_o h\nu_o). \quad (16)$$

This formula allows a simple means of interpreting PAS data arising from multiple decays and of estimating radiationless decay parameters from these data.

#### REFERENCES

1. A. Rosencwaig, Adv. Electronics and Electron Physics 46, 207, (1978).
2. A. Rosencwaig and A. Gersho, J. Appl. Phys. 47, 64 (1976).



### III. ENERGY TRANSFER IN SOLIDS

In the final reports on our two previous Army grants the basic theories of single-step and multistep energy transfer processes were outlined. In this section we discuss two further aspects of energy transfer, the treatment of combined long range resonance interaction and diffusion processes and the treatment of phonon assisted energy transfer. The application of these theories to the interpretation of results are discussed further in later sections.

#### III.1 Combined Energy Transfer Theory

Several approaches have been presented for treating the combined effects of energy migration and trapping at an activator site. The one most appropriate for most of the investigations of interest here were developed by Yokota and Tanimoto<sup>1</sup> and is outlined in the following paragraphs.

If the distribution function for excited sensitizers is  $n_s(\vec{r}, t)$ , then under the influence of diffusion among sensitizers and dipole-dipole transfer to activators,

$$\frac{\partial n_s}{\partial t} = -\frac{1}{\tau} n_s + D \nabla^2 n_s - \sum_i \frac{\alpha}{r_i^6} n_s \quad (1)$$

where  $D$  is the diffusion constant,  $\tau$  is the sensitizer lifetime,  $r_i$  is the separation between a given sensitizer-activator pair and  $\alpha$  is the interaction strength. Upon summing over all sensitizers, assuming a uniform distribution of donors and averaging over all activator positions, which are assumed to be random, we may write

$$N_s(t) = N_s(0) e^{-t/\tau} \langle e^{t(D\nabla^2 - \sum_i \alpha/r_i^6)} \rangle_{av} \quad (2)$$

where  $N_s$  is the total number of excited sensitizers and  $\langle \rangle_{av}$  represents the activator averaging. To evaluate this we first assume a sufficiently low activator concentration that each is unaffected by the others, so that the sensitizer decay term due to transfer to one activator may simply be taken to the  $N_a$  power, where  $N_a$  is the total number of activators. Due to the assumption of uniform sensitizer distribution, the average transfer rate to a single activator is found by converting the sum over all s-a separations to an integral over the crystal volume,  $V = 4\pi R_V^3/3$ . Therefore,

$$N_s(t) = N_s(0)e^{-t/\tau} \left\{ \frac{1}{V} \int_0^{R_V} 4\pi r^2 \exp(tD\nabla_r^2 - \frac{\alpha t}{r^6}) dr \right\}^{N_a}. \quad (3)$$

Now since  $\nabla_r^2$  and  $r^{-6}$  are Hermitian we may use the expansion

$$\begin{aligned} \exp(tD\nabla_r^2 - \frac{\alpha t}{r^6}) &= \exp(-\frac{\alpha t}{r^6}) \left\{ 1 + \sum_{n=1}^{\infty} (-1)^n \int_0^t dt_1 \dots \int_0^{t_{n-1}} dt_n \right. \\ &\quad \times U(t_1) \dots U(t_n) \} \end{aligned} \quad (4)$$

where

$$U(t) = e^{\alpha/r^6} (-D\nabla_r^2) e^{-\alpha/r^6}. \quad (5)$$

If  $D$  is assumed to be rather small it will suffice to keep only a few terms of the sum. Therefore,

$$N_s(t) = N_s(0)e^{-t/\tau} \left[ \frac{4\pi}{V} \int_0^{R_V} dr r^2 e^{-\alpha/r^6} \left\{ 1 + \int_0^t dt_1 e^{t_1 \alpha/r^6} D\nabla_r^2 e^{-t_1 \alpha/r^6} \right\} \right]^{N_a}$$



$$\begin{aligned}
& + \int_0^t dt_1 \int_0^{t_1} dt_2 (e^{t_1 \alpha/r^6} Dv_r^2 e^{-t_1 \alpha/r^6}) (e^{t_2 \alpha/r^6} Dv_r^2 e^{-t_2 \alpha/r^6}) \\
& + \int_0^t dt_1 \int_0^{t_1} dt_2 \int_0^{t_2} dt_3 (e^{t_1 \alpha/r^6} Dv_r^2 e^{-t_1 \alpha/r^6}) (e^{t_2 \alpha/r^6} Dv_r^2 e^{-t_2 \alpha/r^6}) \\
& \times (e^{t_3 \alpha/r^6} Dv_r^2 e^{-t_3 \alpha/r^6}) + \dots \}^N \\
& = N_s(0) e^{-t/\tau} [T_0 + T_1 + T_2 + T_3 + \dots]^N, \tag{6}
\end{aligned}$$

where  $T_n$  is the term dependent on  $D^n$ . Let us now evaluate these terms through  $T_3$ .

The term  $T_0$  is

$$\begin{aligned}
T_0 &= \frac{4\pi}{V} \int_0^{R_v} e^{-t\alpha/r^6} r^2 dv \\
&= -\frac{4\pi(\alpha t)^{1/2}}{6V} \int_0^{y_v} e^{-y} y^{-3/2} dy \tag{7}
\end{aligned}$$

where  $y = \alpha t/r^6$  and  $y_v = \alpha t/R_v^6 = tR_0^6/\tau R_v^6$ . Integrating by parts and noting that for all times of interest,  $t$  less than several  $\tau$ , we may assume  $y_v \ll 1$ , we have

$$\begin{aligned}
T_0 &= \frac{4\pi(\alpha t)^{1/2}}{6V} \{ 2e^{-y_v} y_v^{-1/2} - 2 \int_{y_v}^{\infty} e^{-y} y^{-1/2} dy \} \\
&= \frac{4\pi(\alpha t)^{1/2}}{3V} \{ e^{-y_v} y_v^{-1/2} + \int_0^{y_v} e^{-y} y^{-1/2} dy - \int_0^{\infty} e^{-y} y^{-1/2} dy \} \\
&= \frac{4\pi(\alpha t)^{1/2}}{3V} \{ y_v^{-1/2} - y_v^{+1/2} + \dots + \int_0^{y_v} (y^{-1/2} - y^{+1/2} + \dots)
\end{aligned}$$

$$x \, dy - \Gamma(\frac{1}{2})\}$$

$$\doteq \frac{4\pi}{3V} (at)^{\frac{1}{2}} \{y_v^{-\frac{1}{2}} - \Gamma(\frac{1}{2}) + \text{higher order terms}\} \quad (8)$$

Noting that  $\Gamma(\frac{1}{2}) = \sqrt{\pi}$  and that  $V = 4\pi R_v^3/3$ , we find

$$T_o \doteq 1 - \frac{4\pi^{3/2} (at)^{1/2}}{3V} . \quad (9)$$

In evaluating the term linear in  $D$  the time integration must first be done. It is

$$\begin{aligned} \int_0^t dt_1 e^{t_1 a/r^6} D \nabla_r^2 e^{-t_1 a/r^6} &= \int_0^t dt_1 e^{t_1 a/r^6} D \left( \frac{36t_1^2 a^2}{r^{14}} - \frac{30t_1 a}{r^8} \right) \\ &\quad e^{-t_1 a/r^6} \\ &= \int_0^t dt_1 D \left( \frac{36t_1^2 a^2}{r^{14}} - \frac{30t_1 a}{r^8} \right) \\ &= D \left( \frac{12a^2 t^3}{r^{14}} - \frac{15at^2}{r^8} \right) . \end{aligned} \quad (10)$$

Therefore, with  $y = at/r^6$  as before,

$$\begin{aligned} T_1 &= \frac{4\pi D}{V} \int_0^{R_v} \left( \frac{12a^2 t^3}{r^{12}} - \frac{15at^2}{r^6} \right) e^{-ta/r^6} dr \\ &= \frac{4\pi D}{V} (at)^{1/6} \int_{y_v}^{\infty} \left( 2ty^{5/6} - \frac{5}{2} ty^{-1/6} \right) e^{-y} dy \\ &= \frac{4\pi D}{V} (at)^{1/6} \left\{ 2\Gamma\left(\frac{11}{6}\right) - 2\int_0^{y_v} (y^{5/6} - y^{11/6} + \dots) dy \right. \\ &\quad \left. - \frac{5}{2} \Gamma\left(\frac{5}{6}\right) + \frac{5}{2} \int_0^{y_v} (y^{-1/6} - y^{5/6} + \dots) dy \right\} \end{aligned}$$

$$\begin{aligned}
&= \frac{4\pi D}{V} \alpha^{1/6} t^{7/6} \left\{ \frac{10}{6} \Gamma\left(\frac{5}{6}\right) - \frac{5}{2} \Gamma\left(\frac{5}{6}\right) + \text{terms of order } (y_v)^{5/6} \right. \\
&\quad \left. \text{and higher} \right\} \\
&\doteq \frac{4\pi}{V} D \alpha^{1/6} t^{7/6} \left\{ \frac{5}{6} \Gamma\left(\frac{5}{6}\right) \right\},
\end{aligned} \tag{11}$$

again noting that  $y_v \ll 1$  for times of interest. The term quadratic in  $D$  follows similarly. The time integrations are, using Eq. (10),

$$\begin{aligned}
&\int_0^t dt_1 \int_0^{t_1} dt_2 (e^{t_1 \alpha/r^6} D \nabla_r^2 e^{-t_1 \alpha/r^6}) (e^{t_2 \alpha/r^6} D \nabla_r^2 e^{-t_2 \alpha/r^6}) \\
&= D^2 \int_0^t dt_1 \int_0^{t_1} dt_2 (e^{t_1 \alpha/r^6} \nabla_r^2 e^{-t_1 \alpha/r^6}) \left( \frac{36\alpha^2}{r^{14}} t_2^2 - \frac{30\alpha}{r^8} t_2 \right) \\
&= D^2 \int_0^t dt_1 \int_0^{t_1} dt_2 \left\{ \frac{36 \cdot 36\alpha^4}{r^{28}} t_1^2 t_2^2 - \frac{(6 \cdot 14 \cdot 36 + 6 \cdot 19 \cdot 36)\alpha^3}{r^{22}} t_1 t_2^2 \right. \\
&\quad \left. - \frac{30 \cdot 36\alpha^3}{r^{22}} t_1^2 t_2 + \frac{(6 \cdot 8 \cdot 30 + 6 \cdot 13 \cdot 30)\alpha^2}{r^{16}} t_1 t_2 \right. \\
&\quad \left. + \frac{13 \cdot 14 \cdot 36\alpha^2}{r^{16}} t_2^2 - \frac{7 \cdot 8 \cdot 30\alpha}{r^{10}} t_2 \right\} \\
&= D^2 \left\{ \frac{72\alpha^4 t^6}{r^{28}} - \frac{36 \cdot 81\alpha^3 t^5}{5r^{22}} + \frac{21 \cdot 97\alpha^2 t^4}{2r^{16}} - \frac{7 \cdot 40\alpha t^3}{r^{10}} \right\}.
\end{aligned} \tag{12}$$

Therefore, with the same substitution as previously,

$$\begin{aligned}
T_2 &= \frac{4\pi D^2}{6V} (\alpha t)^{-1/6} t^2 \int_{y_v}^{\infty} dy e^{-y} \left\{ 72y^{19/6} - \frac{36 \cdot 81}{5} y^{13/6} \right. \\
&\quad \left. + \frac{21 \cdot 97}{2} y^{7/6} - 7 \cdot 40 y^{1/6} \right\}
\end{aligned}$$



$$\begin{aligned}
&= \frac{4\pi D^2}{6V} \alpha^{-1/6} t^{11/6} \left\{ 72 \Gamma\left(\frac{25}{6}\right) - \frac{36 \cdot 81}{5} \Gamma\left(\frac{19}{6}\right) \right. \\
&\quad \left. + \frac{21 \cdot 97}{2} \Gamma\left(\frac{13}{6}\right) - 7.40 \Gamma\left(\frac{7}{6}\right) + \int_0^y v dy (\text{terms of order } y^{1/6}) \right\} \quad (13) \\
&\approx \frac{4\pi}{V} D^2 \alpha^{-1/6} t^{11/6} \left\{ \frac{89}{60} \Gamma\left(\frac{13}{6}\right) \right\}.
\end{aligned}$$

The final term to be calculated explicitly in this treatment will be the cubic term.

The time integral is, using Eq. (12),

$$\begin{aligned}
&\int_0^t dt_1 \int_0^{t_1} dt_2 \int_0^{t_2} dt_3 (e^{t_1 \alpha/r^6} D V_r^2 e^{-t_1 \alpha/r^6}) (e^{t_2 \alpha/r^6} D V_r^2 e^{-t_2 \alpha/r^6}) \\
&\times (e^{t_3 \alpha/r^6} D V_r^2 e^{-t_3 \alpha/r^6}) \\
&= D^3 \int_0^t dt_1 \int_0^{t_1} dt_2 \int_0^{t_2} dt_3 (e^{t_1 \alpha/r^6} V_r^2 e^{-t_1 \alpha/r^6}) \left( \frac{36 \cdot 36 \alpha^4}{r^{28}} t_2^2 t_3^2 \right. \\
&\quad - \frac{6 \cdot 33 \cdot 36 \alpha^3}{r^{16}} t_2^2 t_3^2 - \frac{30 \cdot 36 \alpha^3}{r^{22}} t_2^2 t_3^2 + \frac{6 \cdot 21 \cdot 30 \alpha^2}{r^{16}} t_2^2 t_3^2 \\
&\quad \left. + \frac{13 \cdot 14 \cdot 36 \alpha^2}{r^{16}} t_3^2 - \frac{7 \cdot 8 \cdot 30 \alpha}{r^{10}} t_3 \right) \\
&= D^3 \int_0^t dt_1 \int_0^{t_1} dt_2 \int_0^{t_2} dt_3 \left\{ \frac{36 \cdot 36 \cdot 36 \alpha^6}{r^{42}} t_1^2 t_2^2 t_3^2 - \frac{6 \cdot 36 \cdot 36 \cdot 61 \alpha^5}{r^{36}} t_1^2 t_2^2 t_3^2 \right. \\
&\quad - \frac{6 \cdot 33 \cdot 36 \cdot 36 \alpha^5}{r^{36}} t_1^2 t_2^2 t_3^2 - \frac{30 \cdot 36 \cdot 36 \alpha^5}{r^{36}} t_1^2 t_2^2 t_3^2 \\
&\quad + \frac{27 \cdot 28 \cdot 36 \cdot 36 \alpha^4}{r^{30}} t_2^2 t_3^2 + \frac{33 \cdot 36 \cdot 36 \cdot 49 \alpha^4}{r^{30}} t_1^2 t_2^2 t_3^2 + \frac{6 \cdot 30 \cdot 36 \cdot 49 \alpha^4}{r^{30}} t_1^2 t_2^2 t_3^2 \\
&\quad \left. + \frac{6 \cdot 21 \cdot 30 \cdot 36 \alpha^4}{r^{30}} t_1^2 t_2^2 t_3^2 + \frac{13 \cdot 14 \cdot 36 \cdot 36 \alpha^4}{r^{30}} t_1^2 t_3^2 - \frac{6 \cdot 21 \cdot 22 \cdot 33 \cdot 36 \alpha^3}{r^{24}} t_2^2 t_3^2 \right\}
\end{aligned}$$

$$\begin{aligned}
& - \frac{21 \cdot 22 \cdot 30 \cdot 36 \alpha^3}{r^{24}} t_2^2 t_3 - \frac{21 \cdot 30 \cdot 36 \cdot 37 \alpha^3}{r^{24}} t_1 t_2 t_3 - \frac{6 \cdot 13 \cdot 14 \cdot 36 \cdot 37 \alpha^3}{r^{24}} t_1^2 t_3 \\
& - \frac{7 \cdot 8 \cdot 30 \cdot 36 \alpha^3}{r^{24}} t_1^2 t_3 + \frac{16 \cdot 21 \cdot 30 \cdot 90 \alpha^2}{r^{18}} t_2 t_3 + \frac{13 \cdot 14 \cdot 15 \cdot 16 \cdot 36 \alpha^2}{r^{18}} t_3^2 \\
& + \frac{8 \cdot 25 \cdot 30 \cdot 42 \alpha^2}{r^{18}} t_1 t_3 - \frac{30 \cdot 56 \cdot 90 \alpha}{r^{12}} t_3 \} \\
& = D^3 \left\{ \frac{288 \alpha^6 t^9}{r^{42}} - \frac{29,592 \alpha^5 t^8}{5r^{36}} + \frac{187,542 \alpha^4 t^7}{5r^{30}} - \frac{842,709 \alpha^3 t^6}{10r^{24}} \right. \\
& \quad \left. + \frac{57,288 \alpha^2 t^5}{r^{18}} - \frac{6300 \alpha t^4}{r^{12}} \right\} .
\end{aligned} \tag{14}$$

By the usual technique we get

$$\begin{aligned}
T_3 &= \frac{4\pi D^3}{6V} (\alpha t)^{-1/2} t^3 \int_{y_v}^{\infty} dy e^{-y} \left\{ 288 y^{11/2} - \frac{29,592}{5} y^{9/2} \right. \\
& \quad \left. + \frac{187,542}{5} y^{7/2} - \frac{842,709}{10} y^{5/2} + 57,288 y^{3/2} - 6300 y^{1/2} \right\} \\
&= \frac{4\pi D^3}{6V} \alpha^{-1/2} t^{5/2} \left\{ 288 \Gamma\left(\frac{13}{2}\right) - \frac{29,592}{5} \Gamma\left(\frac{11}{2}\right) + \frac{187,542}{5} \Gamma\left(\frac{9}{2}\right) \right. \\
& \quad \left. - \frac{842,709}{10} \Gamma\left(\frac{7}{2}\right) + 57,288 \Gamma\left(\frac{5}{2}\right) - 6300 \Gamma\left(\frac{3}{2}\right) + \int_0^{y_v} dy \text{ (terms of order } y^{1/2}) \right\} \\
&\approx \frac{4\pi}{6V} D^3 \alpha^{-1/2} t^{5/2} \left\{ -\frac{693}{8} \Gamma\left(\frac{3}{2}\right) \right\} = -\frac{4\pi^{3/2}}{V} D^3 \alpha^{-1/2} t^{5/2} \left\{ \frac{693}{96} \right\} .
\end{aligned}$$

From these calculations the time dependent excited sensitizer population,

Eq. (16), becomes

$$\begin{aligned}
 N_s(t) &\doteq N_s(0) e^{-t/\tau} \left[ 1 - \frac{4\pi^{3/2}}{3V} \alpha^{1/2} t^{1/2} \left\{ 1 + \frac{5}{2} \pi^{-1/2} \Gamma\left(\frac{5}{6}\right) D \alpha^{-1/3} t^{2/3} \right. \right. \\
 &\quad \left. \left. - \frac{89}{20} \pi^{-1/2} \Gamma\left(\frac{13}{6}\right) D^2 \alpha^{-2/3} t^{4/3} + \frac{693}{32} D^3 \alpha^{-1} t^2 \right\} \right]^{N_a} \\
 &\doteq N_s(0) \exp\left[-\frac{t}{\tau} - \frac{4\pi^{3/2}}{3} n_a \alpha^{1/2} t^{1/2} \left\{ 1 + \frac{5}{2} \pi^{-1/2} \Gamma\left(\frac{5}{6}\right) D \alpha^{-1/3} t^{2/3} \right. \right. \\
 &\quad \left. \left. - \frac{89}{20} \pi^{-1/2} \Gamma\left(\frac{13}{6}\right) D^2 \alpha^{-2/3} t^{4/3} + \frac{693}{32} D^3 \alpha^{-1} t^2 \right\} \right]
 \end{aligned} \tag{16}$$

where  $n_a = N_a/V$ . The final step relies upon the fact that  $\alpha^{1/2}/V$  is proportional to  $(R_o^3/R_v^3) \ll 1$ . It should be noted that the term linear in  $D$  in Eq. (18) of reference 1 has a misprint, showing the wrong exponent for  $\pi$ . Also note that for  $D = 0$  the standard single step dipole-dipole energy transfer rate equation results.

Since the long-term behavior of Eq. (16) is not evident it is convenient to reexpress the result by use of the [1,2] Padé approximant. The three coefficients of this approximant may be fit to the coefficients of  $D$ ,  $D^2$  and  $D^3$ , and if the expression is raised to the appropriate power a physically reasonable time dependence at long times will result. Specifically, we expect that at short times after excitation both diffusion to traps and single step transfer from randomly positioned sensitizers will contribute to the total energy transfer rate, resulting in a complicated time dependence. At sufficiently long times, however, those originally excited sensitizers near enough to activators to have significant sensitizer to activator transfer probability will have been depleted, so that the transfer rate is limited by diffusion of excitation quanta, excitons, into the vicinity of activators. Thus the long time behavior should be similar to that of the simple



diffusion model, a purely exponential decay. Noting that the exponent of Eq. (16) is an expansion in powers of  $x = D\alpha^{-1/3} t^{2/3}$ , we may therefore write

$$N_s(t) \doteq N_s(0) \exp\left[-\frac{t}{\tau} - \frac{4\pi^{3/2}}{3} n_a^{1/2} t^{1/2} \left(\frac{1+ax+bx^2}{1+cx}\right)^{3/4}\right]. \quad (17)$$

The three quarters exponent is chosen so that as  $x$  grows large the energy transfer contribution to the decay has a time dependence controlled by  $t^{1/2} x^{3/4}$  which is proportional to  $g$ , as desired.

The coefficients  $a$ ,  $b$  and  $c$  in Eq. (17) are determined by a Maclaurin expansion of the Padé approximant

$$\begin{aligned} \left(\frac{1+ax+bx^2}{1+cx}\right)^{3/4} &= 1 + \frac{3(a-c)}{4} x - \frac{3}{8} \left\{ \frac{(a-c)^2}{4} - 2b - 2c(a-c) \right\} x^2 \\ &\quad + \frac{1}{8} \left\{ \frac{5}{16}(a-c)^3 + \left[ \frac{3}{2}(a-c) + 6c \right] [c(a-c)-b] \right\} x^3 \end{aligned} \quad (18)$$

where only terms up to  $x^3$  need be kept to determine the constants. The coefficients of each power of  $x$  may be equated to the corresponding coefficients in Eq. (17). Solution of the resulting set of equations gives the coefficients

$$\begin{aligned} a &= 10.87 \\ b &= 15.51 \\ c &= 8.745 \end{aligned} \quad (19)$$

in close agreement with the results of Yokota and Tanimoto.<sup>1</sup> To assure agreement with the literature, their calculated values will be used in the final expression

$$N_s(t) \doteq N_s(0) \exp \left[ -\frac{t}{\tau} - \frac{4\pi^{3/2}}{3} n_a \alpha^{1/2} t^{1/2} \left( \frac{1+10.87x + 15.50x^2}{1+8.743x} \right)^{3/4} \right] \quad (22)$$

where  $x = D\alpha^{-1/3} t^{2/3}$ .

In the case of long times after excitation, or equivalently of small sensitizer to activator transfer rate coefficient  $\alpha$ , it has been seen that a diffusion-like exponential decay is expected. More precisely, for  $x \gg 1$ ,

$$\begin{aligned} N_s(t) &\doteq N_s(0) \exp \left[ -\frac{t}{\tau} - \frac{4\pi^{3/2}}{3} n_a \alpha^{1/2} t^{1/2} (1.773x)^{3/4} \right] \\ &\doteq N_s(0) \exp \left[ -\frac{t}{\tau} - 4\pi n_a (0.908 \alpha^{1/4} D^{3/4}) t \right]. \end{aligned} \quad (21)$$

comparison with the standard diffusion theory result shows that we have simply replaced the somewhat arbitrary trapping radius  $R$  by the quantity  $0.908 (\alpha/D)^{1/4}$ .

The numerical coefficient in this transfer rate varies somewhat, depending upon the method used to estimate it. Indeed, the number most widely used in the literature appears to be 0.676, derived by a rather difficult scattering length method by Yokota and Tanimoto.<sup>1</sup> Therefore the long time transfer rate may be written

$$W = 4\pi n_a D (0.676 \alpha^{1/4} D^{-1/4}), \quad (22)$$

the result to be used in this work.

#### REFERENCES

1. M. Yokota and O. Tanimoto, J. Phys. Soc. Japan 22, 779 (1967).

### III.2 Phonon Assisted Energy Transfer

The resonant energy transfer process requires that transfer take place only between ions for which the sensitizer deexcitation transition and the activator excitation transition are of equal energy. It is possible, however, for energy transfer to occur by a process involving electron-phonon interaction so that emission or absorption of one or more phonons allows energy conservation in a transfer between non-resonant ions. Several types of "phonon assisted" energy transfer processes are possible, depending upon the number of phonons emitted or absorbed, the energy mismatch between the ions and the participation of other excited states of either ion in the process. Such processes may involve any of the standard multipole or exchange interactions as the mechanism for ion-ion interaction. However, it is possible to discuss the electron-phonon interaction and its impact upon the transfer rate without assuming a form for the ion-ion interaction.

Recently Orbach and coworkers have developed theoretical expressions for the energy transfer rate to be expected due to various one phonon and two phonon processes.<sup>1</sup> The one phonon rate may be developed as follows. The relevant energy levels may be modeled as shown in Fig. 1, where  $\Delta E$  is the energy mismatch between the sensitizer and activator transitions. If an asterisk is used to represent an excited state, the initial and final states including sensitizer and activator electronic states and the occupation number of the phonon mode involved in the process, with wave vector  $\vec{k}$  and polarization  $s$ , may be written

$$|i\rangle = |s^*a, n_{sk}\rangle \quad (1)$$

$$|f\rangle = |sa^*, n_{sk}\rangle \quad (2)$$

The transition rate is

$$W_{sa} = \frac{2\pi}{\hbar} \sum_{sk} |M_{if}|^2 \delta(\hbar\omega_{sk} \mp \Delta E) \quad (3)$$



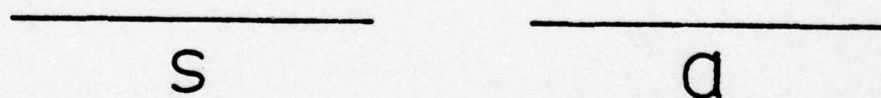


Figure 1. Diagram for Phonon Assisted Energy Transfer

where the upper sign holds for phonon emission,  $\Delta E > 0$ , and the lower for phonon absorption. The transfer matrix element is

$$M_{if} = \langle f|H|i \rangle + \sum_j \frac{\langle f|H|j \rangle \langle j|H|i \rangle}{E_i - E_j} + \sum_{j\ell} \frac{\langle f|H|\ell \rangle \langle \ell|H|j \rangle \langle j|H|i \rangle}{(E_i - E_j)(E_i - E_\ell)} + \dots \quad (4)$$

where  $H$  is the interaction Hamiltonian and  $j$  and  $\ell$  are intermediate states. The first term in (4) is applicable to no phonon transfer processes, the second term to one and two phonon two-state processes, and so on. The interaction Hamiltonian consists of the multipole or other interaction by which the energy transfer occurs,  $H_t$ , and the electron-phonon interaction,  $H_v$ . Thus the matrix element for one-phonon assisted energy transfer is

$$M_{if} = \sum_{m=s,a} \frac{\langle s^*a, n_{sk} \pm 1 | H_t | s^*a, n_{sk} \pm 1 \rangle \langle s^*a, n_{sk} \pm 1 | H_v(m) | s^*a, n_{sk} \rangle}{E_s - (E_s \pm \hbar\omega_{sk})} + \sum_{m=s,a} \frac{\langle s^*a, n_{sk} \pm 1 | H_v(m) | s^*a, n_{sk} \rangle \langle s^*a, n_{sk} | H_t | s^*a, n_{sk} \rangle}{E_s - E_a} \quad (5)$$

where the argument of  $H_v(m)$  denotes that the phonon emission or absorption may occur at the sensitizer or activator site. If we regard the  $H_t$  matrix elements to be the same regardless of  $n_{sk}$  then

$$\langle s^*a, n_{sk} \pm 1 | H_t | s^*a, n_{sk} \pm 1 \rangle = \langle s^*a, n_{sk} | H_t | s^*a, n_{sk} \rangle = J. \quad (6)$$

Also the electron-phonon matrix element may be expressed in terms of the strain parameter  $\epsilon$  in the standard way.<sup>2</sup> In a notation compatible with Orbach,

$$\begin{aligned} \langle \ell^*m, n_{sk} \pm 1 | H_v(\ell) | \ell^*m, n_{sk} \rangle &= f(\ell) \langle n_{sk} \pm 1 | \epsilon(\ell) | n_{sk} \rangle \\ \langle \ell^*m, n_{sk} \pm 1 | H_v(m) | \ell^*m, n_{sk} \rangle &= g(m) \langle n_{sk} \pm 1 | \epsilon(m) | n_{sk} \rangle \end{aligned} \quad (7)$$

where  $\ell, m = s, a$   $f(m)$  is the electron-phonon coupling strength in the excited state of ion  $m$  and  $g(m)$  is that coupling strength in the ground state of site  $m$ . Then

$$\langle n_{sk} \pm 1 | \epsilon(m) | n_{sk} \rangle = \langle n_{sk} \pm 1 | \epsilon | n_{sk} \rangle e^{\pm i \vec{k} \cdot \vec{r}_m} \quad (8)$$

where  $\vec{r}_m$  is the position of ion  $m$  and  $\epsilon = \epsilon(r=0)$ . If  $\vec{r} = \vec{r}_a - \vec{r}_s$  and if the difference  $f-g$  is equal for  $s$  and  $a$  we may write, noting that

$$\pm \hbar \omega_k = \Delta E,$$

$$\begin{aligned} M_{if} &= J \langle n_{sk} \pm 1 | \epsilon | n_{sk} \rangle \left\{ \frac{f(s) \exp(\pm i \vec{k} \cdot \vec{r}_s) + g(a) \exp(\pm i \vec{k} \cdot \vec{r}_a)}{-\Delta E} \right. \\ &\quad \left. + \frac{g(s) \exp(\pm i \vec{k} \cdot \vec{r}_s) + f(a) \exp(\pm i \vec{k} \cdot \vec{r}_a)}{\Delta E} \right\} \\ &= J \frac{\langle n_{sk} \pm 1 | \epsilon | n_{sk} \rangle}{-\Delta E} (f-g) e^{\pm i \vec{k} \cdot \vec{r}_a} [e^{\pm i \vec{k} \cdot \vec{r}_s} - 1] . \end{aligned} \quad (9)$$

Therefore,

$$\begin{aligned} W_{sa} &= \frac{2\pi}{\hbar} \frac{J^2 (f-g)^2}{\Delta E^2} \sum_{sk} |\langle n_{sk} \pm 1 | \epsilon | n_{sk} \rangle|^2 \\ &\quad \times |e^{\pm i \vec{k} \cdot \vec{r}_s} - 1|^2 \delta(\hbar \omega_{sk} \mp \Delta E) . \end{aligned} \quad (10)$$

The factor

$$h(\vec{k}, \vec{r}) = |e^{\pm i \vec{k} \cdot \vec{r}} - 1|^2 \quad (11)$$

is called the coherence factor, as it measures the degree to which a phonon mode causes the sensitizer and activator to move in or out of phase, and plays an important role in determining the energy transfer rate.



The energy mismatch between the ions between which energy transfer is to be studied in this work is relatively small, particularly in the Nd doped garnets where  $\Delta E$  is about  $20 \text{ cm}^{-1}$  whereas the phonon density of states extends to several hundred wave numbers. In such a case the relevant phonon modes tend to be those of small wave vector, so that  $\vec{k} \cdot \vec{r} \ll 1$ , that is the phonon wavelength is much greater than  $r$ .

Upon averaging the coherence factor over all angles we then have

$$\langle h(\vec{k}, \vec{r}) \rangle_{\Omega} = \frac{k^2 r^2}{3}. \quad (12)$$

The sum over phonon modes may be approximated by use of the Debye approximation

$$\sum_{\vec{k}} = \frac{V}{2\pi^2} \sum_s \frac{1}{v_s^3} \int_0^{\omega_D} d\omega_s \omega_s^2 \langle \rangle_{\Omega} \quad (13)$$

where  $V$  is the crystal volume,  $\omega_D$  the Debye frequency, and  $v_s$  the velocity of sound in the crystal. In each of the previous two equations  $\langle \rangle_{\Omega}$  represents the average over all angles. Noting that the strain parameter is more accurately expressed  $\epsilon_{ij} = (\partial u_i / \partial r_j + \partial u_j / \partial r_i) / 2$ , and writing the polarization vector as  $(e_{sx}, e_{sy}, e_{sz})$ ,

$$\epsilon_{ij} = \sum_{\vec{k}} \frac{1}{2} \left( \frac{\hbar}{2M\omega_{\vec{k}}} \right)^{1/2} (b_{s,\vec{k}}^+ + b_{s,-\vec{k}}) (e_{si} k_j + e_{sj} k_i). \quad (14)$$

Therefore, Eq. (10) becomes

$$W_{sa} = \frac{2\pi}{\hbar} \frac{J^2 (f-g)^2}{\Delta E^2} \frac{V}{2\pi^2} \sum_s \frac{\hbar}{8Mv_s^3} \int_0^{\omega_D} d\omega_s \frac{\omega_s^2}{\omega_s} \frac{k^2 r^2}{3} \langle (e_{si} k_j + e_{sj} k_i)^2 \rangle_{\Omega}$$

$$\begin{aligned}
& \left\{ \begin{array}{c} n(\omega_s)+1 \\ n(\omega_s) \end{array} \right\} \frac{1}{\hbar} \delta(\omega_s \mp \Delta E/\hbar) \\
& = \frac{J^2 (f-g)^2 |\Delta E|^3 r^2}{6\pi \rho \hbar^6} \left( \sum_s \frac{\alpha_s}{v_s^7} \right) \left\{ \begin{array}{c} n(|\Delta E|+1) \\ n(|\Delta E|) \end{array} \right\}
\end{aligned} \tag{15}$$

where  $\rho = M/V$ ,  $k = v_s \omega_s$  and

$$\alpha_s k^2 = \frac{1}{4} \langle (e_{si} k_j + e_{sj} k_i)^2 \rangle_\Omega . \tag{16}$$

For  $k_B T \gg |\Delta E|$ ,  $n+1 \approx n \approx k_B T/|\Delta E|$  so that

$$W_{sa} = \frac{J^2 (f-g)^2 |\Delta E|^2 r^2}{6\pi \rho \hbar^6} \left( \sum_s \frac{\alpha_s}{v_s^7} \right) k_B T . \tag{17}$$

The positive exponent of the  $\Delta E$  dependence is a consequence of the density of states and of the coherence factor. Their combined effect is to make  $W_{sa}$  very small as  $\Delta E$  goes to zero, so that one-phonon assisted energy transfer in this case is very weak.

It is possible in the small energy mismatch case that two-phonon assisted transfer processes may be much more important than the one-phonon process. The disadvantage of a two-phonon process lies in its second order dependence on the electron-phonon coupling, which is usually small. However, a process in which one high energy phonon is emitted and another of energy different by  $\Delta E$  is

absorbed gives the advantages of the much larger density of states and coherence factor associated with a high energy phonon of appropriate frequency. The Orbach theory considers several processes by which such transfer may take place.<sup>1</sup> These are too numerous and lengthy to present in detail here, but the results will be listed. The first case involves use of the one-phonon-electron coupling Hamiltonian to second order, with the result for  $k_B T \gg |\Delta E|$

$$W_{sa}^{2a} = \frac{J^2 (f-g)^4}{2\pi^3 \rho^2 \hbar^7} \left( \sum_s \frac{\alpha_s}{v_s^5} \right)^2 I_2 (k_B T)^3 \quad (18)$$

where

$$I_n = \int_0^{T_D/T} \frac{x^n dx}{(e^x - 1)(1 - e^{-x})} \quad (19)$$

which enters upon use of the Debye approximation. For  $|\Delta E| \ll k_B T \ll k_B T_D$ ,  $W_{sa}^{2a}$  is roughly proportional to  $T^3$ . A second case of the two-phonon assisted transfer is found by treating the two-phonon-electron coupling Hamiltonian to first order. The result here, for  $k_B T \gg |\Delta E|$ , is

$$W_{sa}^{2b} = \frac{J^2 (f_2 - g_2)^2}{4\pi^3 \rho^2 \hbar^7 \Delta E^2} \left( \sum_s \frac{\alpha_s}{v_s^5} \right)^2 I_6 (k_B T)^7, \quad (20)$$

so that for  $|\Delta E|/k_B \ll T \ll T_D$  a  $T^7$  law results. It should be noted that Eqs. (18)-(20) were obtained by assuming  $kr > 1$  so that the coherence factor becomes much larger than in Eq. (12) and only weakly dependent on  $kr$ . Specifically it is assumed that  $h(\vec{k}, \vec{r}) \approx 2$ . If it should be that  $kr \ll 1$ , for instance at such low temperatures that only low energy phonon modes are populated, these expressions must be adjusted accordingly.



Rather different processes may occur if another excited state lies sufficiently close to one of the states considered so that the energy difference, say  $\delta$ , may be spanned by a lattice phonon. In this case one phonon radiationless transitions such as those discussed in the treatment of lifetime broadening may play an important role in the energy transfer. Additional parameters appear in such a case, particularly  $J_2$ , the ion-ion interaction involving the new excited state, and  $\Gamma_2$ , the width of the new excited state resulting from lifetime broadening due to phonon emission. Two general types of processes occur. The first is a resonant process in which the phonon absorption and emission cause changes of electronic state, the second is a nonresonant process as were those listed in the preceding paragraph but involving the second excited state. Again simply stating the results of Orbach,<sup>1</sup> the resonant process gives

$$w_{sa}^{2c} = \left[ J^2 + \frac{2 \Delta E^2 J_2^2}{\Delta E^2 + 8 \Gamma_2^2} \right] \frac{1 + e^{\Delta E/k_B T}}{\Delta E^2} \frac{2}{\hbar} \Gamma_2 e^{-\delta/k_B T} \quad (21)$$

where it has been assumed that  $|\Delta E| \ll \delta$  and  $\Gamma_2 \ll k_B T \ll \delta \pm \Delta E$ . In the case  $|\Delta E| \ll k_B T$  this is very similar to the simple model in which spectral overlap of the second excited states of the two ions controls the energy transfer rate. Finally, the nonresonant process gives, for  $k_B T \gg |\Delta E|$ ,

$$w_{sa}^{2d} = \frac{16 \Gamma_2^2 I_6 k_B^7 T^9}{\pi \hbar \delta^8 \Delta E^2} \quad (22)$$

A wide variety of dependence upon temperature and energy mismatch is thus seen to be possible for various two-phonon-assisted energy transfer processes.

## REFERENCES

1. T. Holstein, S. K. Lyo and R. Orbach, Phys. Rev. Lett. 36, 891 (1976).
2. B. DiBartolo, Optical Interactions in Solids, (John Wiley, New York, 1968).

## IV. HOST-SENSITIZED ENERGY TRANSFER RESULTS

### IV.1 Energy Transfer in Rare Earth-Doped $\text{CaWO}_4$ After Red Edge Excitation

#### A. Introduction

Calcium tungstate is an important material in applications as a phosphor and a laser host for trivalent rare earth ions. However, the optical properties of this material are still not completely understood. In this paper we address ourselves to the question of the importance of tungstate defect sites in the absorption, emission, and host-sensitized energy transfer processes in  $\text{CaWO}_4$  crystals.

There is still a question as to whether tungstate ions near to crystal defects are the dominant emitting centers in calcium tungstate and the centers responsible for the low energy absorption band of this material [1-6]. Also tungstate ions next to activator impurities have been suggested as exciton traps playing an important role in host-sensitized energy transfer to rare earth impurity ions [7,8]. Here we employ time-resolved spectroscopy (TRS) techniques after pulsed laser excitation into the long wavelength tail of the host absorption edge to better characterize the effect of defects on these processes. The results indicate that this "red edge" excitation does selectively excite defect tungstate ions next to activator impurity ions and that energy transfer takes place very efficiently to the nearest neighbor activators. These results are quite different from those obtained by higher excitation into the major host absorption bands [8]. In this case, at low temperatures energy transfer was found to be consistent with a single step process from randomly distributed self-trapped excitons to randomly distributed activators. At high temperatures the host-sensitized energy transfer was

found to be consistent with a multistep exciton diffusion process where the activators act as exciton traps. However, the results indicated that extended trapping regions exist around each activator and the results obtained in the present study are important in verifying this conclusion.

#### B. Experimental

The samples investigated were good optical quality single crystals of  $\text{CaWO}_4$  containing 0.5%  $\text{Sm}^{3+}$  or 0.5%  $\text{Eu}^{3+}$  impurity ions which go into the lattice substitutionally for the host  $\text{Ca}^{2+}$  ions and are charge compensated by an equal concentration of  $\text{Na}^+$  ions.

Absorption spectra were obtained on a Cary 14 spectrophotometer. The fluorescence lifetimes and time-resolved emission spectra were obtained by exciting the samples with an Avco-Everett 20 KW pulsed nitrogen laser. This emits a 10 ns pulse at  $3371 \text{ }^{\circ}\text{A}$ . The sample temperature was controlled by a cryogenic refrigerator. The fluorescence was analyzed by a one meter Spex Czerny-Turner Monochromator and detected by a cooled RCA C31034 photomultiplier tube. The signal was processed by a boxcar averager triggered by the laser pulse and having a time resolution of the order of 75 ns.

Fig. 1 shows the absorption spectrum of undoped calcium tungstate. The absorption edge occurs at about  $3000 \text{ }^{\circ}\text{A}$  and excitation spectra indicate the existence of several overlapping bands at higher energies [3]. These are due to transitions in  $\text{WO}_4^{2-}$  molecular ions to excited states split by the crystal field of  $S_4$  symmetry. As indicated in the figure, the nitrogen laser excites the crystal in the long wavelength tail (red edge) of the absorption band.

#### C. Results

Figs. 2 and 3 show the fluorescence spectra of samarium-doped calcium tungstate and europium-doped calcium tungstate, respectively, at two different times



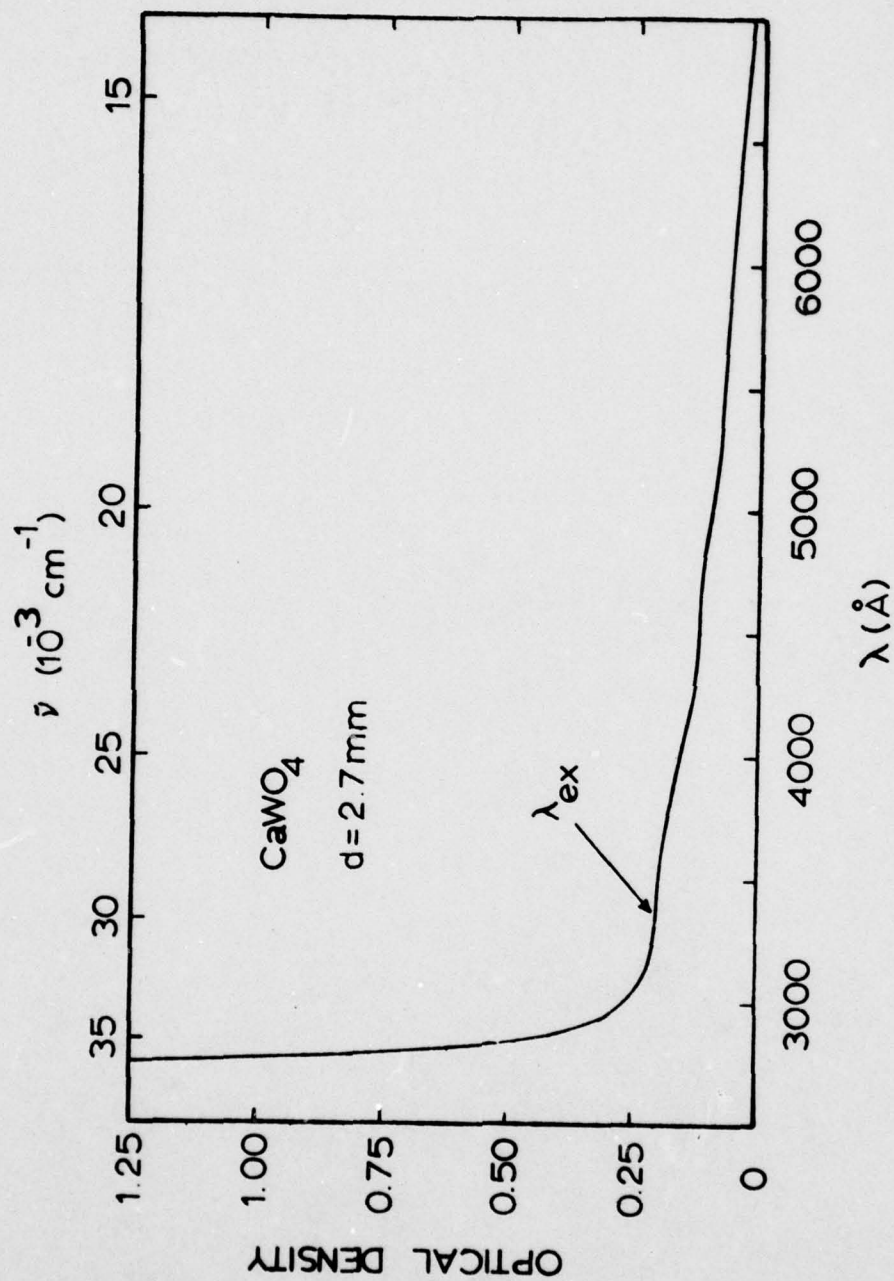


Figure 1. Absorption Spectrum of CaWO<sub>4</sub> at Room Temperature. Crystal Thickness is 2.8 mm. The Arrow Indicates the Wavelength of the Nitrogen Laser Excitation at 3371 Å

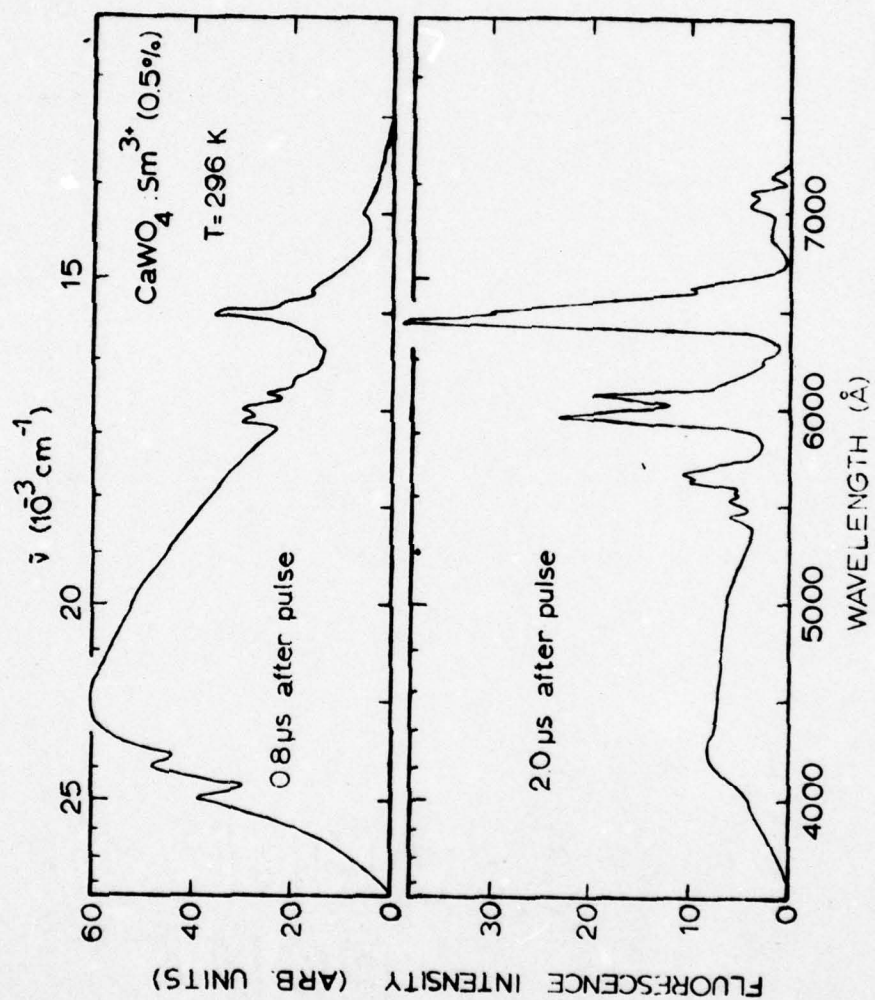


Figure 2. Fluorescence Spectra of  $\text{CaWO}_4:\text{Sm}^{3+}$  at Room Temperature, 0.8  $\mu\text{s}$  and 20  $\mu\text{s}$  After Laser Excitation

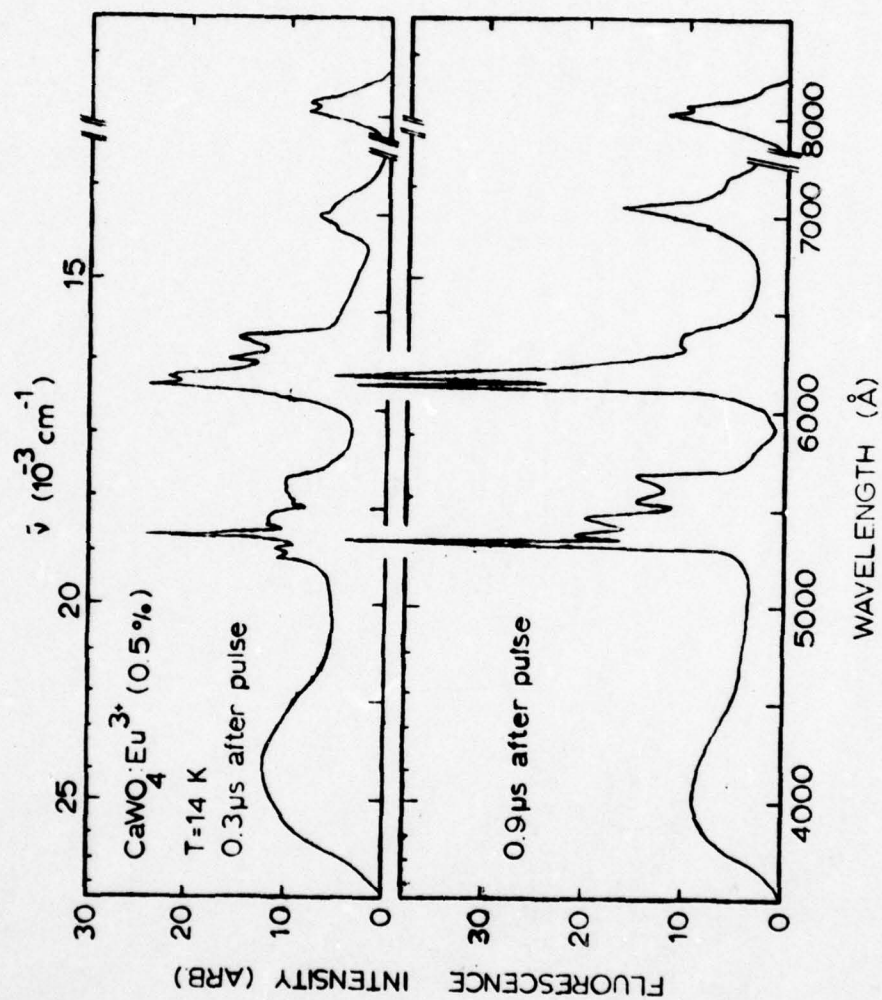


Figure 3. Fluorescence Spectra of  $\text{CaWO}_4:\text{Eu}^{3+}$  at 14K, 0.3 $\mu\text{s}$  and 0.9 $\mu\text{s}$  After the Laser Pulse



after the laser pulse. The broad band with a peak near  $4200 \text{ \AA}$  is the intrinsic host emission and the sharper lines at long wavelengths are due to transitions of the activator ions. The relative intensity of the tungstate fluorescence decreases immediately after the excitation pulse while activator fluorescence initially increases. This is due to energy transfer from the directly excited host to the impurity ions.

The  $\text{Sm}^{3+}$  fluorescence spectra are due to transitions originating in the  $^4\text{F}_{5/2}$  state and terminating on various levels of the  $^6\text{H}_J$  multiplets. All of these transitions exhibit the same time dependence. Fig. 4 shows the TRS results obtained at room temperature and 14 K. The integrated fluorescence intensity of the  $\text{Sm}^{3+}$  transition terminating on the  $^6\text{H}_{9/2}$  level divided by the integrated tungstate emission is plotted as a function of time after the laser pulse. For both temperatures this ratio increases by an order of magnitude in less than  $2 \mu\text{s}$ . Fig. 5 shows similar results for the  $\text{Eu}^{3+}$  doped sample. In this case emission from both the  $^5\text{D}_0$  and  $^5\text{D}_1$  levels can be observed and are monitored separately. The increases in the relative intensity ratios are generally not as great as they are for the samarium activators. Tables I-IV list the TRS data.

Figs. 6 and 7 show the temperature dependences of the fluorescence lifetimes of the observed transitions. These data are listed in Table V. The tungstate fluorescence decay time in the undoped sample was approximately  $1.2 \mu\text{s}$  and independent of temperature for this wavelength of excitation. The host lifetime is quenched to about  $0.52 \mu\text{s}$  in the samarium-doped sample and about  $0.6 \mu\text{s}$  in the europium-doped sample. The  $\text{Sm}^{3+}$  fluorescence has a decay time of about  $800 \mu\text{s}$  at room temperature and decreases slightly to a little more than  $700 \mu\text{s}$  at low temperature. The  $^5\text{D}_0 \text{ Eu}^{3+}$  fluorescence lifetime increases from  $338 \mu\text{s}$  at room temperature to around  $535 \mu\text{s}$  at low temperature whereas the  $^5\text{D}_1$  lifetime increases from about  $1.3 \mu\text{s}$  at  $290 \text{ K}$  to slightly over  $4 \mu\text{s}$  at  $14 \text{ K}$ .

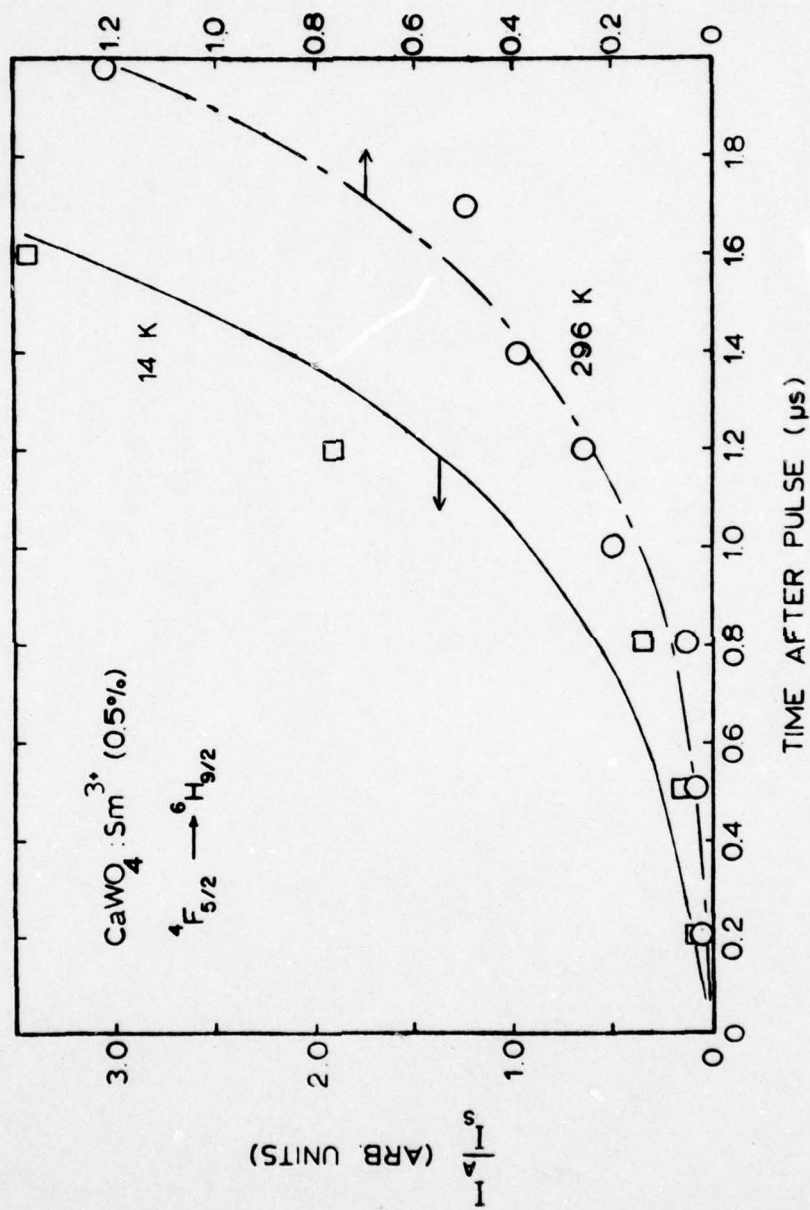


Figure 4. Time-Resolved Spectroscopy Results for CaWO<sub>4</sub>:Sm<sup>3+</sup> at 296 K and 14 K. The  $4F_{5/2}$  to  $6H_{9/2}$  Transition is Monitored

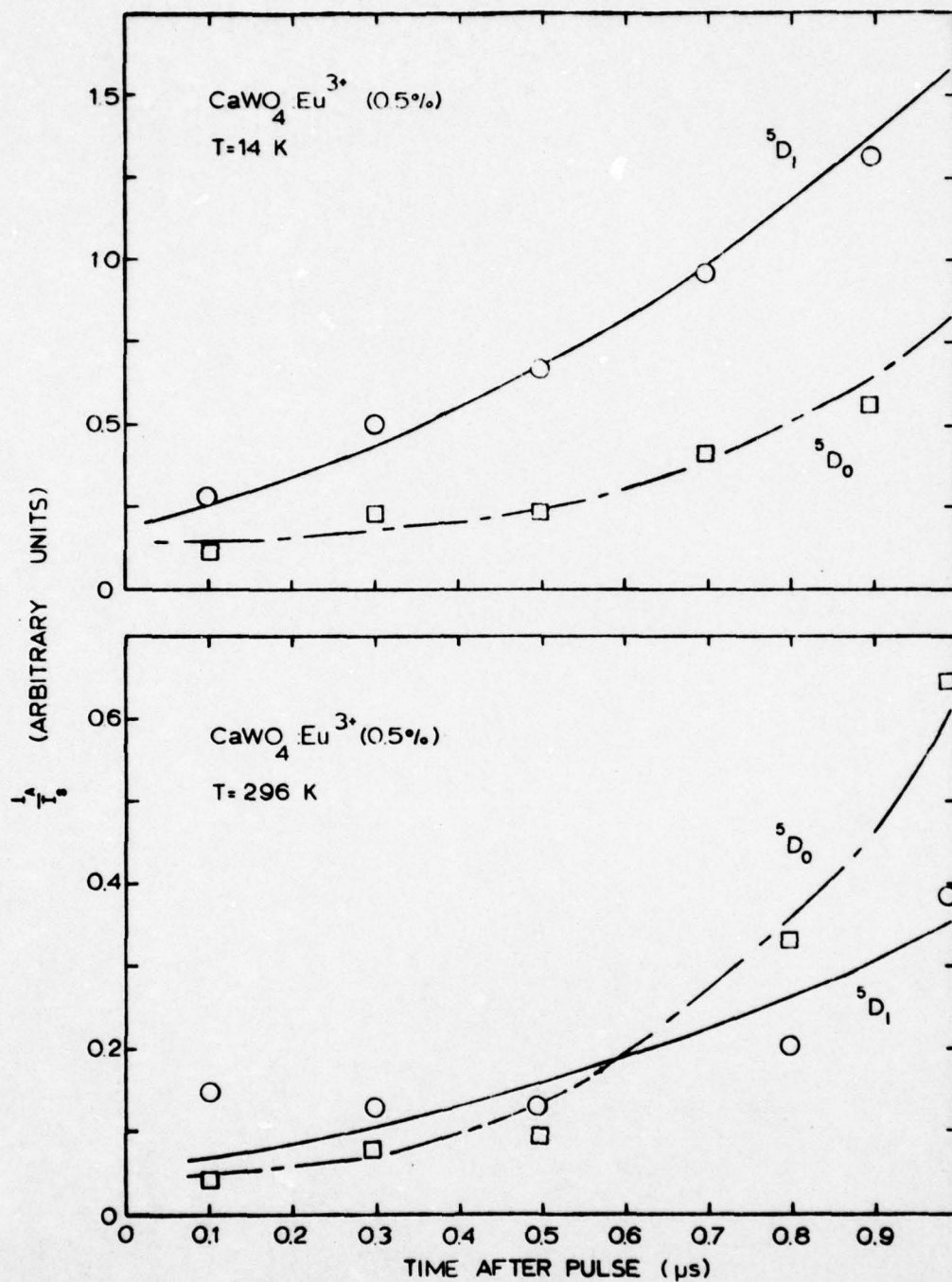


Figure 5. Time-Resolved Spectroscopy Results for  $\text{CaWO}_4:\text{Eu}^{3+}$  at 296K and 14K. Both  $^5\text{D}_0$  and  $^5\text{D}_1$  to  $^7\text{F}_J$  Transitions are Monitored



TABLE I  
TIME-RESOLVED SPECTROSCOPY RESULTS FOR  $\text{CaWO}_4:\text{Sm}^{3+}$  AT 296K\*

Time After Pulse ( $\mu\text{s}$ )	Integrated Host Fluorescence Intensity, $I_S$ (arb. units)	Integrated Impurity Fluorescence Intensity, $I_A$ (arb. units)	$\frac{I_A}{I_S}$
0.2	8830	162	0.0183
0.5	5145	187	0.0363
0.8	6711	339	0.0505
1.0	3617	737	0.204
1.2	2355	630	0.268
1.4	2030	797	0.393
1.7	1331	660	0.496
2.0	686	842	1.23

\*  $\text{Sm}^{3+}$   $^4F_{5/2}$  to  $^6H_{9/2}$  transition monitored.

TABLE II  
TIME-RESOLVED SPECTROSCOPY RESULTS FOR  $\text{CaWO}_4:\text{Sm}^{3+}$  AT 14K

Time After Pulse ( $\mu\text{s}$ )	Integrated Host Fluorescence Intensity, $I_S$ (arb. units)	Integrated Impurity Fluorescence Intensity, $I_A$ (arb. units)	$\frac{I_A}{I_S}$
0.2	6095	440	0.0722
0.5	7778	1012	0.130
0.8	4506	1495	0.332
1.2	955	1824	1.91
1.6	570	1962	3.44

\*  $\text{Sm}^{3+} \ 4F_{5/2}$  to  $6H_{9/2}$  transition monitored.

TABLE III  
TIME-RESOLVED SPECTROSCOPY RESULTS FOR  $\text{CaWO}_4:\text{Eu}^{3+}$  AT 296K

Time After Pulse ( $\mu\text{s}$ )	Integrated Host Fluores- cence Intensity, $I_S$ (arb. units)	Integrated Impurity $5D_1$ Intensity, $I_A^1$ (arb. units)	Integrated Impurity $5D_1$ Intensity, $I_A^0$ (arb. units)	$\frac{I_A^1}{I_S}$	$\frac{I_A^0}{I_S}$
0.1	5031	78	21	0.016	0.0042
0.3	3124	41	26	0.013	0.0083
0.5	5896	78	58	0.013	0.0098
0.8	2425	50	82	0.021	0.034
1.0	1784	70	117	0.039	0.066



TABLE IV  
TIME-RESOLVED SPECTROSCOPY RESULTS FOR  $\text{CaWO}_4:\text{Eu}^{3+}$  AT 14K

Time After Pulse ( $\mu\text{s}$ )	Integrated Host Fluores- cence Intensity, $I_S$ (arb. units)	Integrated Impurity $5D_1$ Intensity, $I_A^1$ (arb. units)	Integrated Impurity $5D_0$ Intensity $I_A^0$ (arb. units)	$\frac{I_A^1}{I_S}$	$\frac{I_A^0}{I_S}$
0.1	2649	74	30	0.028	0.011
0.3	1577	80	39	0.051	0.025
0.5	2081	140	50	0.067	0.024
0.7	828	79	40	0.095	0.048
0.9	1315	176	74	0.13	0.056

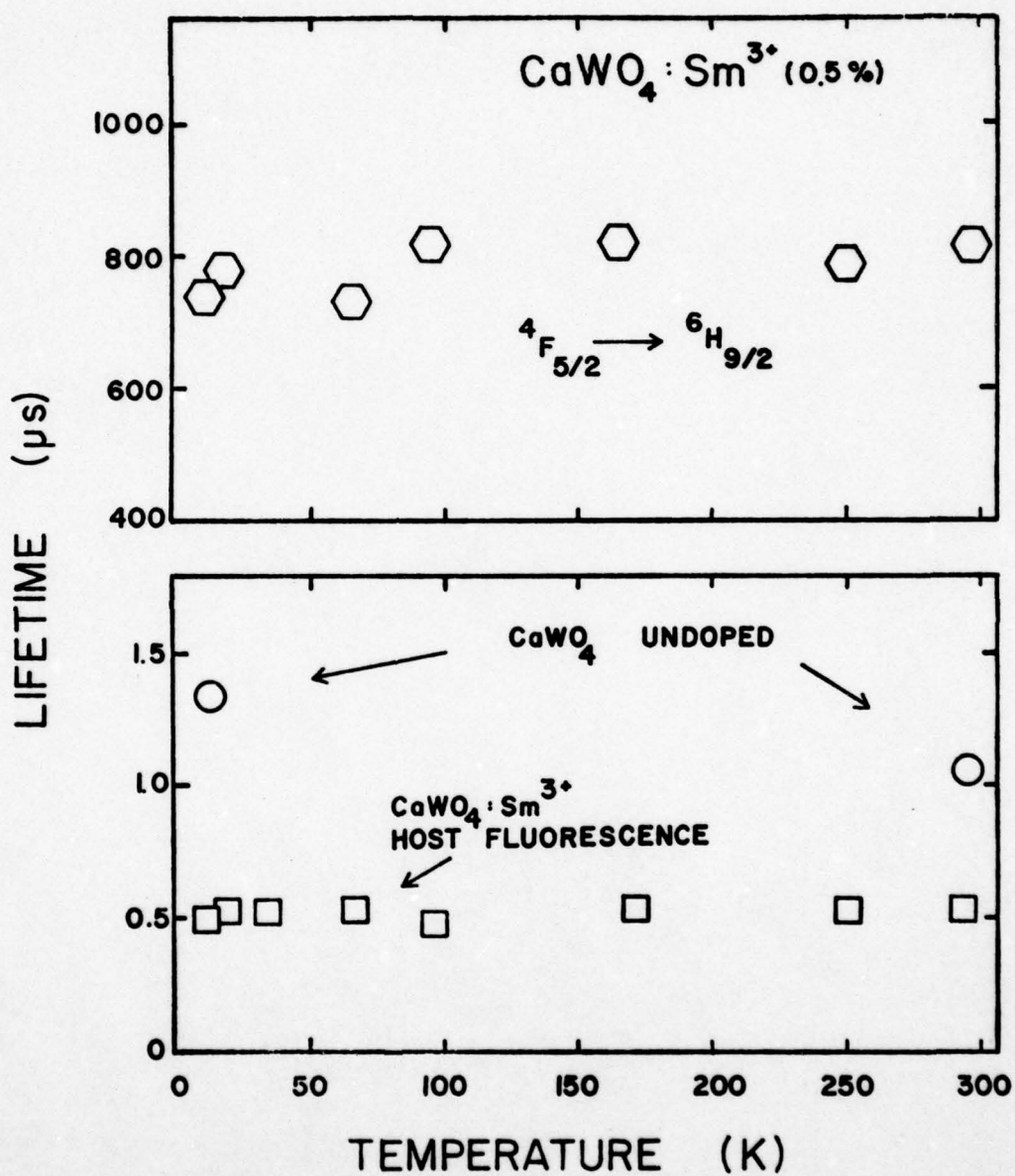


Figure 6. Temperature Dependence of the Fluorescence Lifetimes of the Undoped  $\text{CaWO}_4$  and  $\text{CaWO}_4:\text{Sm}^{3+}$  Host Fluorescence (Below) and the  $\text{CaWO}_4:\text{Sm}^{3+}$   $4F_{5/2}$  to  $6H_{9/2}$  Transition (Above)

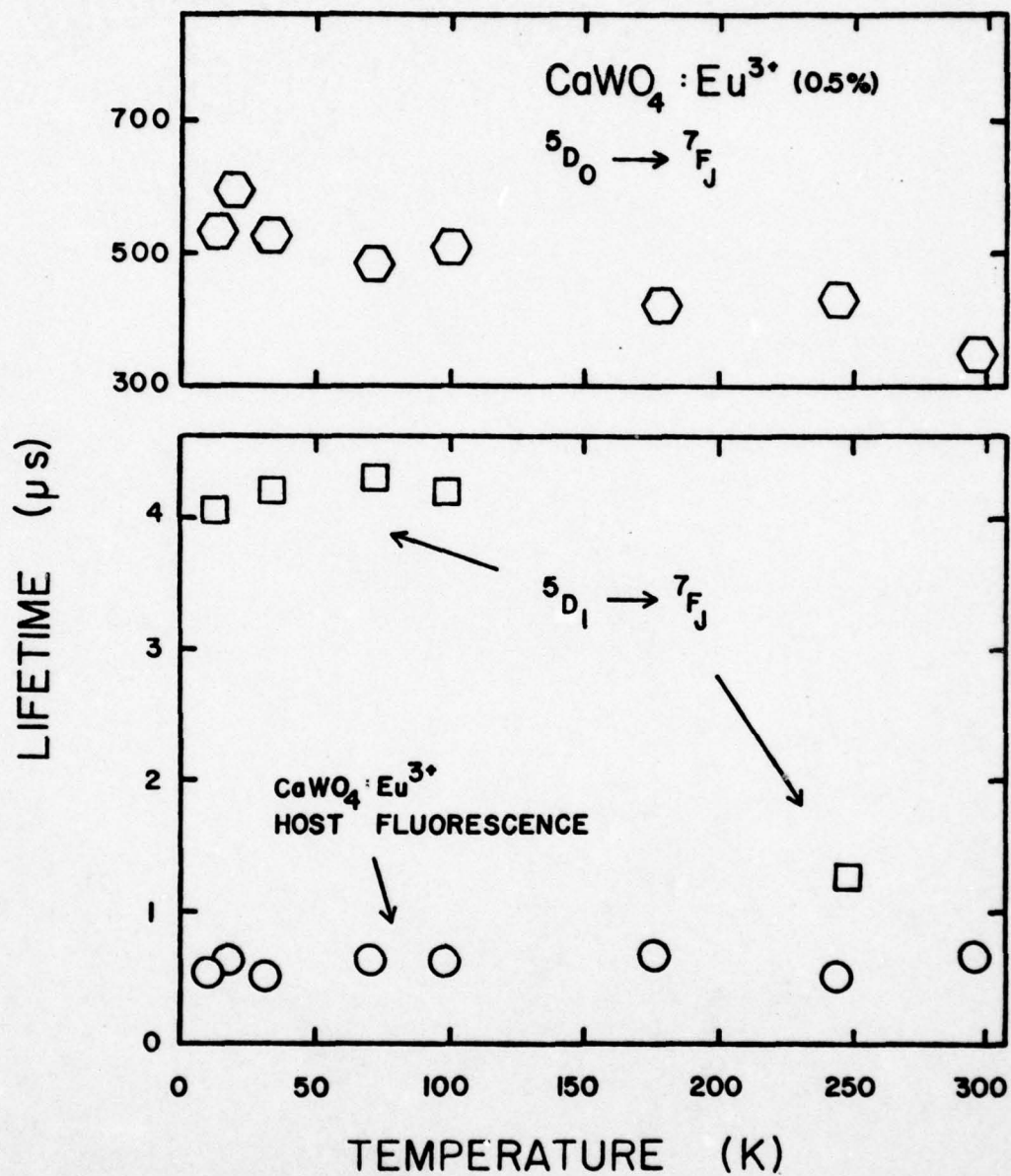


Figure 7. Temperature Dependence of the Fluorescence Lifetimes of the Host Fluorescence and  $5D_1$  to  $7F_J$  Transition in  $CaWO_4:Eu^{3+}$  (Below) and the  $5D_0$  to  $7F_J$  Transition (Above)



TABLE V  
FLUORESCENCE LIFETIMES ( $\mu$ s) AT VARIOUS TEMPERATURES FOR OBSERVED  
TRANSITIONS IN  $\text{CaWO}_4$ ,  $\text{CaWO}_4:\text{Sm}^{3+}$ ,  $\text{CaWO}_4:\text{Eu}^{3+}$

Sample	Temperature (K)*							
	14K	20K	33K	68K	97K	171K	251K	296K
<u>CaWO<sub>4</sub></u>								
Host	1.34	--	--	--	--	--	--	1.04
<u>CaWO<sub>4</sub>:Sm<sup>3+</sup></u>								
Host	0.50	0.53	0.53	0.53	0.47	0.53	0.52	0.52
4F <sub>5/2</sub> to 6H <sub>9/2</sub>	715	780	--	727	820	819	784	808
<u>CaWO<sub>4</sub>:Eu<sup>3+</sup></u>								
Host	0.58	0.68	0.55	0.64	0.63	0.69	0.52	0.66
5D <sub>0</sub> to 7F <sub>J</sub>	535	600	530	487	515	425	439	338
5D <sub>1</sub> to 7F <sub>J</sub>	4.05	--	4.2	4.3**	4.2	--	1.3	--

\* Temperatures above 68K are  $\pm$  5K

\*\* Average value

#### D. Discussion

The fluorescence spectra of samarium-doped and undoped calcium tungstate excited at  $3371 \text{ \AA}$  are essentially the same as observed for higher energy excitation into the major absorption bands [7,8]. However, the fluorescence lifetimes for the tungstate emission of both these samples are significantly shorter for the red edge excitation than for band excitation and they do not exhibit a sharp increase at low temperature as with band excitation. The increase in lifetime at low temperatures was previously interpreted as being due to the self-trapping of tungstate excitons which inhibits their migration to quenching centers. The lack of temperature dependence of the data reported here indicates that this process is not taking place for the nitrogen laser excitation. This is substantiated by the TRS results discussed below.

Fig. 8 shows the model proposed for explaining the TRS data obtained on  $\text{CaWO}_4:\text{Sm}^{3+}$ .  $n_x$  represents the concentration of excited tungstate molecular ions;  $W$  is the excitation pulse and  $\beta_x$  is the tungstate fluorescence decay rate;  $n_A$  represents the concentration of excited activator ions;  $\beta_A$  represents their fluorescence decay rate; and  $\omega$  is the energy transfer rate from tungstate to activator ions. The rate equations for the excited state populations are

$$dn_x/dt = W - (\beta_x + \omega)n_x, \quad (1)$$

$$dn_A/dt = \omega n_x - \beta_A n_A \quad (2)$$

Assuming a delta function excitation and a time independent energy transfer rate, these equations can be solved to give the time dependence of the ratios of the fluorescence intensities

$$I_A/I_s \propto n_A/n_x = \omega[(\beta_x + \omega) - \beta_A]^{-1}[\exp\{(\beta_x + \omega - \beta_A)t\} - 1]. \quad (3)$$

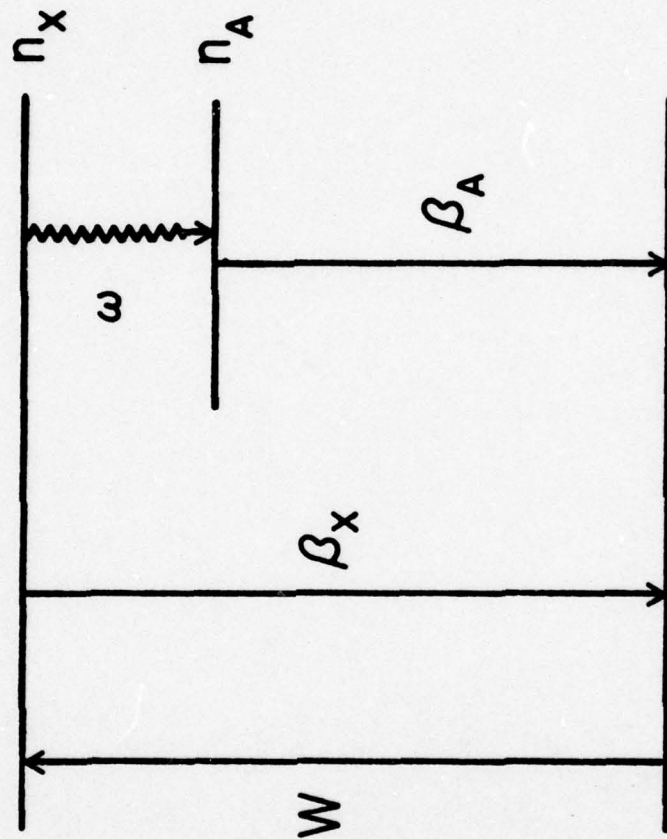


Figure 8. Proposed Model for Interpreting the Results of Time-Resolved Spectroscopy and Lifetime Measurements of  $\text{CaWO}_4:\text{Sm}^{3+}$



The solid lines in Fig. 4 represent the best fit to the data obtained from Eq. (3) by treating  $\omega$  as an adjustable parameter.

Fig. 9 shows the model used to interpret the TRS data on the  $\text{Eu}^{3+}$  doped sample. The same designations used in the previous model hold here with the exception of the two activator levels designated  $n_A^1$  and  $n_A^0$  with corresponding fluorescence decay rates  $\beta_A^1$  and  $\beta_A^0$ . The thermal processes between these two levels are designated  $\gamma_1$  and  $\gamma_2$ . The rate equations for this model are

$$dn_x/dt = W - (\beta_x + \omega)n_x, \quad (4)$$

$$dn_A^1/dt = \gamma_2 n_A^0 - (\gamma_1 + \beta_A^1)n_A^1 + \omega n_x, \quad (5)$$

$$dn_A^0/dt = \gamma_1 n_A^1 - (\gamma_2 + \beta_A^0)n_A^0. \quad (6)$$

Their solution can again be found assuming delta function excitation and a constant energy transfer rate,

$$I_A^0/I_s \propto n_A^0/n_x = \gamma_1 \omega \left[ \frac{1}{(\beta_x + \omega + P_1)(\beta_x + \omega + P_2)} + \frac{e^{(\beta_x + \omega + P_1)t}}{(\beta_x + \omega + P_1)(P_1 - P_2)} - \frac{e^{(\beta_x + \omega + P_2)t}}{(\beta_x + \omega + P_2)(P_1 - P_2)} \right] \quad (7)$$

$$I_A^1/I_s \propto n_A^1/n_x = \omega \left[ \frac{-\beta_x - \omega + \gamma_2 \beta_A^0}{(\beta_x + \omega + P_1)(\beta_x + \omega + P_2)} + \frac{(P_1 + \gamma_2 + \beta_A^0)e^{(\beta_x + \omega + P_1)t}}{(\beta_x + \omega + P_1)(P_1 - P_2)} - \frac{(P_2 + \gamma_2 + \beta_A^0)e^{(\beta_x + \omega + P_2)t}}{(\beta_x + \omega + P_2)(P_1 - P_2)} \right] \quad (8)$$

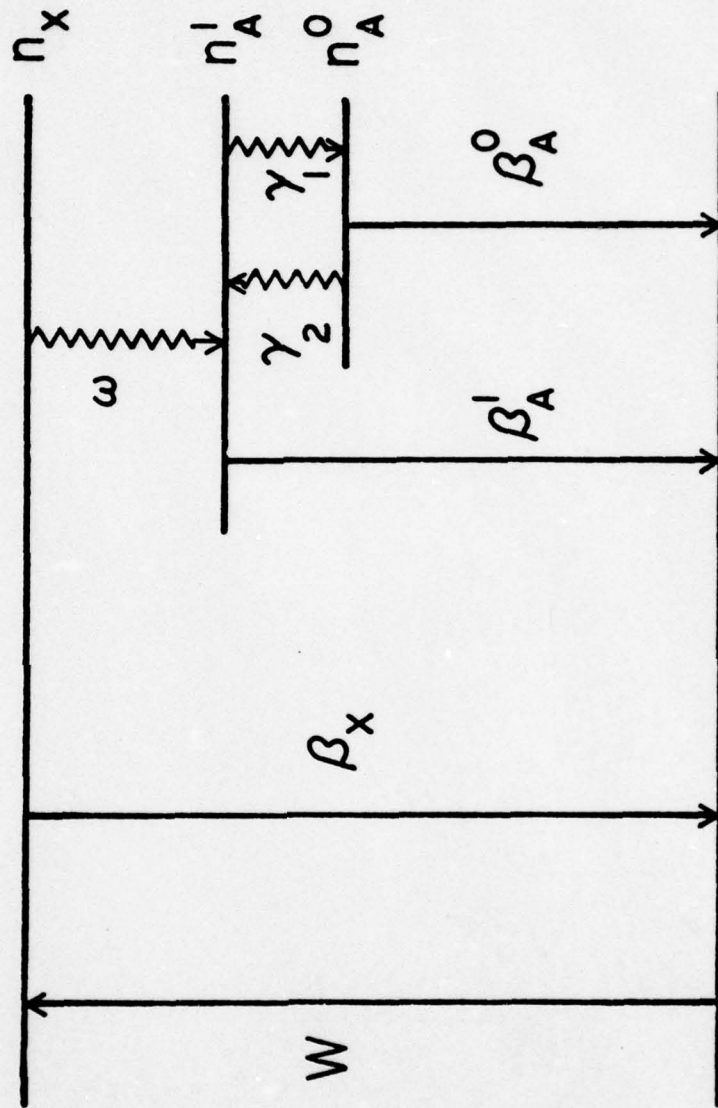


Figure 9. Proposed Model for Interpreting the Results of Time-Resolved Spectroscopy and Lifetime Measurements of  $\text{CaWO}_4:\text{Eu}^{3+}$

where

$$P_1, P_2 = - \frac{1}{2} [(\gamma_2 + \beta_A^0) + (\gamma_1 + \beta_A^1)] \pm \frac{1}{2} [(\gamma_2 + \beta_A^0) - (\gamma_1 + \beta_A^1)]^2 + 4\gamma_1\gamma_2 \}^{1/2} .$$

The solid lines in Fig. 7 represent the best fit to the data obtained by treating  $\omega$  and  $\gamma_1$  as adjustable parameters and  $\gamma_2 = \gamma_1 \exp(-\Delta E_{10}/kT)$ .

Table VI summarizes the parameters obtained from fitting the TRS data. The value of  $\gamma_1$  is consistent with the thermal relaxation rate for  $\text{Eu}^{3+}$  measured by other methods [9]. The energy transfer rates are consistent with those predicted from the quenching of the host fluorescence lifetime and are significantly greater than those obtained from excitation into the major absorption bands [8]. The fact that the data are consistent with a time independent energy transfer rate implies that each excited tungstate ion is surrounded by a similar activator environment. This, coupled with the higher transfer rate, suggests that energy is being transferred to activators which are nearest neighbors to excited tungstate ions. Thus excitation into the low energy tail of the absorption band appears to selectively excite tungstate ions next to activator impurities.

Both the lifetime quenching and TRS results indicate that the energy transfer rate is independent of temperature. The differences in the room temperature and low temperature TRS results shown in Figs. 4 and 5 are due to differences in constant factors now shown explicitly in Eqs. (3), (7), and (8). For example the multiplicative proportionality constants for the cases of  $\text{Sm}^{3+}$  and the  $^5\text{D}_1$  europium emission decrease by a factor of about five on going from low temperature to room temperature. No change in this factor is needed in fitting the  $^5\text{D}_0$  europium data. This factor includes the ratio of quantum efficiencies of the activator and perturbed host states and the variation with temperature most probably indicates a change in



TABLE VI  
ENERGY TRANSFER AND RELAXATION PARAMETERS

Parameter	$\text{CaWO}_4:\text{Sm}^{3+}$	$\text{CaWO}_4:\text{Eu}^{3+}$
$\omega(\text{TRS})$	$1.1 \times 10^6/\text{sec}$	$7.5 \times 10^5/\text{sec}$
$R_0(\text{EDD})$		
experimental	$3.8 \text{ \AA}$	$3.6 \text{ \AA}$
predicted	$4.0 \text{ \AA}$	$16.2 \text{ \AA}$
$R_0'(\text{exch})$		
experimental	$3.8 \text{ \AA}$	$3.6 \text{ \AA}$
Spectral Overlap	$3.35 \times 10^{-2} \text{ l/mole-cm}$	$1.35 \times 10^2 \text{ l/mole-cm}$
$\gamma_1$	--	$1.1 \times 10^5/\text{sec}$

this ration. In addition, in order to fit the  $\text{Eu}^{3+}$  data it was necessary to include an additive constant which has the same value for both the  $^5\text{D}_0$  and  $^5\text{D}_1$  data and decreases by a factor of three in going from low temperature to room temperature. This can be attributed to the increased importance of back transfer from activator to host or to direct pumping of the activator.

The two most likely mechanisms for the energy transfer are electric dipole-dipole (EDD) and exchange interaction. The rate of energy transfer for the former mechanism is given by

$$\omega(\text{EDD}) = (\tau_s^0)^{-1} (R_0/R)^6, \quad (9)$$

where  $R$  is the distance over which energy is transferred and  $R_0$  is the critical interaction distance. Using this expression, the data obtained here implies a value for  $R_0$  of  $3.9 \text{ \AA}$   $\text{Sm}^{3+}$  activators for EDD interaction and  $3.6 \text{ \AA}$  for  $\text{Eu}^{3+}$ . The critical energy transfer distance can be predicted theoretically from the spectral overlap integral. For  $\text{Sm}^{3+}$  it was found to be about  $4 \text{ \AA}$  which is close to the observed value. For  $\text{Eu}^{3+}$  the predicted value of  $R_0$  is  $16.2 \text{ \AA}$ , which is much greater than the observed value.

The simplest expression for the energy transfer rate for exchange interaction is

$$\omega(\text{ex}) = (\tau_s^0)^{-1} \exp[(2R'_0/L)(1 - R/R_0)], \quad (10)$$

where  $L$  is an effective Bohr radius and  $R_0$  is the critical interaction distance given by

$$R'_0 = \frac{1}{2} L \ln[(2\pi\tau_s^0/h)K^2\Omega], \quad (11)$$

where  $\Omega$  is the spectral overlap integral and  $K$  is a parameter which depends on the wave function overlap. Using the experimentally observed values for the energy transfer rate in Eq. (10) yields values for  $R'_0$  of  $3.8 \text{ \AA}$  for  $\text{Sm}^{3+}$  and  $\text{Eu}^{3+}$  activators

respectively. Here  $L$  is taken to be  $0.9 \text{ \AA}$  which is half the W-O separation. It is not possible to obtain an accurate estimate for  $R'_0$  since the wave function overlap is not known. However, these values of  $R'_0$  are physically reasonable.

More complicated theories of exchange require the use of explicit expressions for the atomic wave functions. They predict that the interaction strength falls off less rapidly than exponentially and is extremely anisotropic. The high W-O activator angle for this case is favorable for superexchange.

The fact that the theoretically predicted value of  $R_0$  for the europium-doped sample is much greater than the observed value may be due to the fact that  $\text{Eu}^{3+}$  ions are tending to form clusters instead of being uniformly distributed. Thus an excited tungstate ion might transfer its energy to one activator in a neighboring cluster while the rest of the activators in the cluster would not take part in any transfer process. It is difficult to unambiguously ascertain the mechanism for energy transfer in this case with the available data. However from the similarity of samarium and europium as activators, EDD and exchange compete about equally in the energy transfer process to both ions.

The TRS results reported here for red-edge excitation into the  $\text{CaWO}_4$  host absorption bands indicate that this type of excitation selectively excites tungstate molecular ions located next to activator impurity ions, and that energy transfer occurs very efficiently to the nearest-neighbor activators. Transfer to  $\text{Sm}^{3+}$  and  $\text{Eu}^{3+}$  activators may take place by either EDD or exchange interaction. It appears that the europium ions in our sample may be grouped in clusters instead of distributed randomly. This last point will be investigated by dye laser spectroscopy and the results reported at a later date.

These results substantiate the model for energy transfer in  $\text{CaWO}_4:\text{Sm}^{3+}$  proposed previously which postulated the existence of activator-induced host traps



surrounding each samarium impurity ion [8]. These were suggested to be tungstate molecular ions whose energy levels were perturbed due to the presence of the activator impurity. The perturbed levels acted as traps for migrating host excitons. In this case we directly excite into the traps and thus no migration of energy occurs in the host. Comparison of these results with those obtained previously for higher energy excitation indicate that the type of absorption center excited and the type of host-sensitized energy transfer taking place in rare earth activated calcium tungstate depends critically on the wavelength of excitation.

#### REFERENCES

- 1 F. A. Kröger, Some Aspects of the Luminescence of Solids (Elsevier, New York, , 1948).
- 2 Th. P. J. Botden, Phillips Res. Repts. 6 (1951) 425.
- 3 C. C. Valam, Phys 19 (1949) 609.
- 4 M. I. Tombak, A. M. Gurvich, Sov. J. Applied Spect. 4 (1966) 564.
- 5 Č. Barta, J. Dolejší, and A. Bohum, Kristall und Technik 5 (1970) 433.
- 6 A. M. Gurvich, V. B. Gutan, B. N. Meleshkin, V. V. Mikhailim, A. A. Mikhalev and M. I. Tombak, J. Luminescence 15 (1977) 187.
- 7 M. J. Treadaway and R. C. Powell, J. Chem. Phys. 61 (1974) 4003.
- 8 M. J. Treadaway and R. C. Powell, Phys. Rev. B11 (1975) 862.
- 9 E. D. Reed and H. W. Moos, Phys. B8 (1973) 988.

#### IV.2 Laser Time-Resolved Spectroscopy: Investigations

of Energy Transfer in  $\text{Eu}^{3+}$  and  $\text{Er}^{3+}$  Doped  $\text{YVO}_4$

##### A. Introduction

Yttrium vanadate crystals doped with trivalent rare earth ions are representative of an important class of laser and phosphor materials in which the excitation energy is absorbed mainly in the host material and then transferred to the activator ions. The most critical physical process involved in the practical application of these materials is the host-sensitized energy transfer. However, this process has

not been characterized in detail for most of these materials and in general is not well understood. This paper describes the results of an investigation of energy transfer in the systems  $\text{YVO}_4:\text{Eu}^{3+}$  and  $\text{YVO}_4:\text{Er}^{3+}$ .

We recently reported an investigation of the optical properties of europium doped yttrium vanadate in which energy transfer was characterized through the concentration and temperature dependences of the fluorescence intensities and lifetimes [1]. A simple model was proposed to explain the results which assumed that at very low temperatures energy transfer takes place as a single step process from self-trapped excitons to activator ions, whereas at high temperatures the excitons become thermally activated and migrate through the lattice to activators. The simple model used in interpreting the data could not explain all of the results and it was suggested that activator-induced host traps were present and played an important role in the total transfer process. In this present work we describe the use of laser time-resolved spectroscopy (TRS) techniques to characterize host-sensitized energy transfer. Work was done on both europium and erbium doped samples for the purpose of verifying and further developing the model proposed previously, especially in terms of characterizing the trapping process at an activator site. It is found that the time dependent data obtained by this method are more sensitive to the model used for interpretation than are the concentration and temperature quenching data. The results are found to be consistent with the general concepts of single step transfer at low temperatures and thermally activated exciton migration at high temperatures. However, to fit the TRS data it is necessary to include both activator-induced host traps and some radiationless transitions in the models. The parameters for exciton migration are found to be essentially independent of the type of activator ion whereas the trapping characteristics are different for  $\text{Eu}^{3+}$  and  $\text{Er}^{3+}$ .



The samples of yttrium vanadate were obtained from Raytheon, Inc. These include an undoped sample, one containing about  $1.27 \times 10^{19} \text{ cm}^{-3}$  europium, and one with about  $1.27 \times 10^{20} \text{ cm}^{-3}$  erbium. The experimental apparatus used to obtain the absorption, fluorescence and excitation spectra was described previously [1]. The fluorescence lifetimes and time-resolved spectra were obtained by exciting the samples with an Avco-Everett 20 kW pulsed nitrogen laser which produces a pulse having a duration of about 5 ns and a half-width of about  $4 \text{ \AA}$  at  $3371 \text{ \AA}$ . The signal was processed by a PAR 162/164 boxcar averager triggered by the laser pulse. This was either set to observe the fluorescence spectra at a specific time after the laser pulse or used to scan the fluorescence at a specific wavelength as a function of time after the laser pulse. The time resolution was of the order of 80 ns.

#### B. Results and Interpretation of Undoped $\text{YVO}_4$ Data

The details of the optical spectra of pure yttrium vanadate were reported previously [1]. The structure in the excitation spectrum was attributed to transitions between levels of the tetrahedral  $\text{VO}^{3-}$  molecular ion in a crystal field site of  $D_{2d}$  symmetry. The absorption is accompanied by a ligand-metal charge transfer. Fluorescence takes place from the lowest level of the excited state manifold after radiationless relaxation from higher excited states and lattice relaxation in the lowest level. This results in a significant Stokes shift.

Fig. 1 shows the temperature dependence of the fluorescence decay time under laser excitation. The value of 15  $\mu\text{s}$  measured at room temperature is similar to that found from broad band excitation as is the general increase in decay time as temperature is lowered. However, the value of 495  $\mu\text{s}$  measured at 12 K is significantly greater than the value found from broadband excitation. Also, under laser excitation a rise time is observed in the pulsed fluorescence profiles which has a distinct temperature dependence as shown in Fig. 1. This was not observed with broadband excitation.



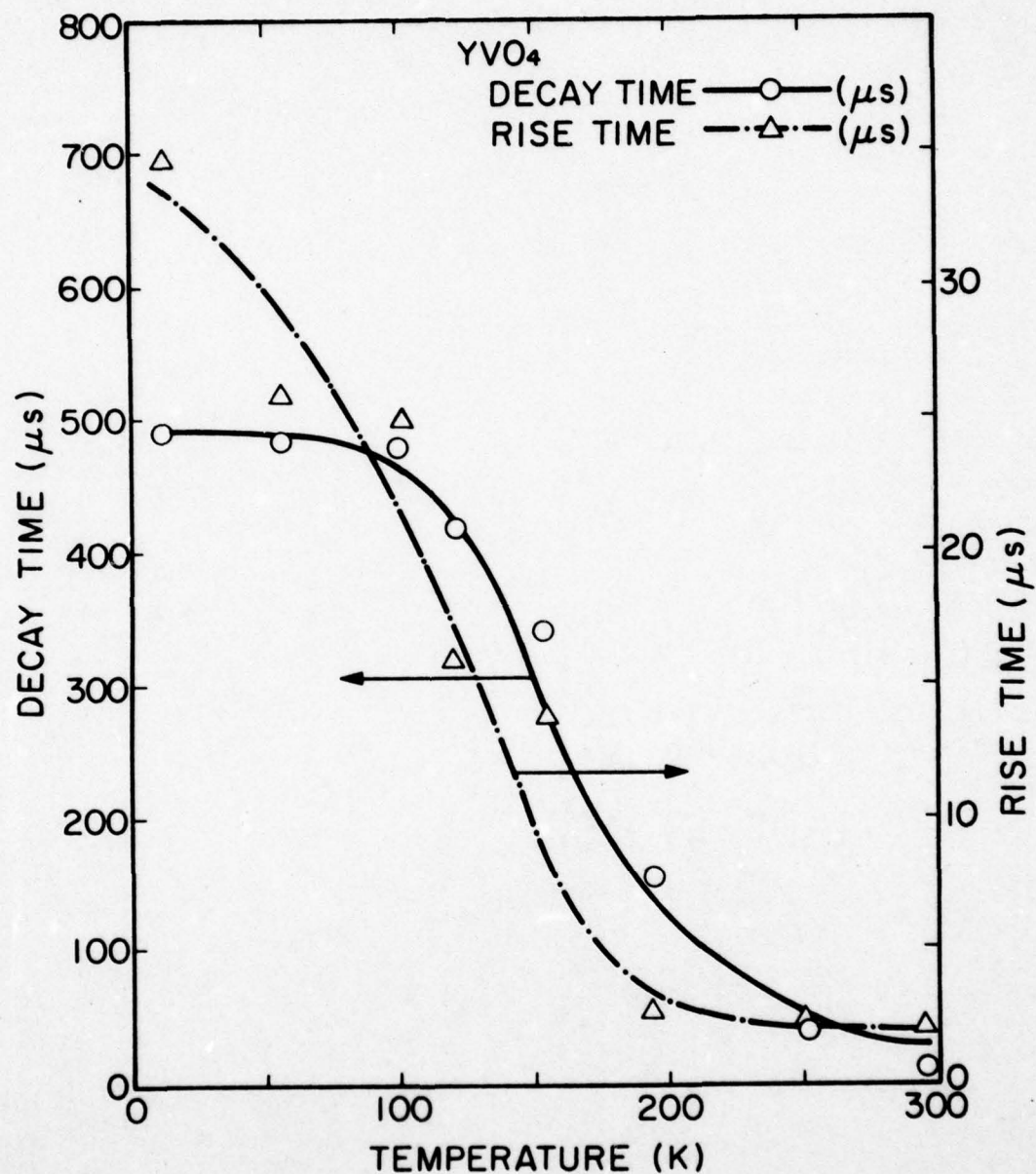


Figure 1. Temperature Dependences of the Fluorescence Decay Times and Rise Times of Undoped YVO<sub>4</sub> Crystals with 3371Å Laser Excitation; the Solid Line is from Eq. (2-1)

The laser-excited lifetime results can be explained by assuming that fluorescence occurs from the relaxed excited state with the relaxation rate from the terminal state of the absorption transition designated as  $\omega$  and the intrinsic fluorescence decay time of the level indicated by  $\tau_T$ . If the temperature dependence of the observed decay time  $\tau_H^0$  is due to thermally excited energy migration to radiationless quenching sites, this can be expressed theoretically as

$$(\tau_H^0)^{-1} = \tau_T^{-1} + k \exp(-\Delta E/k_B T), \quad (1)$$

where  $\Delta E$  is the activation energy for migration and  $k$  is the energy migration rate. In the same model the fluorescence rise time is given by

$$\tau_m = [\omega - (\tau_H^0)^{-1}]^{-1} \ln(\omega \tau_H^0). \quad (2)$$

The solid line in Fig. 1 represents the best fit to the lifetime data using Eq. (1). The activation energy for migration obtained from this fitting is  $625.5 \text{ cm}^{-1}$ , the migration rate is  $5.0 \times 10^5 \text{ s}^{-1}$ , and the intrinsic decay time of the fluorescence state is  $490 \text{ } \mu\text{s}$ . The temperature dependence of the fluorescence rise time can be correctly predicted by Eq. (2) and the value of  $\omega$  at low temperatures is found to be  $1.2 \times 10^5 \text{ s}^{-1}$ . These parameters are summarized in Table I.

Near room temperature the observed decay time decreases somewhat faster than predicted by this simple model. This can be attributed to the onset of other radiation-less decay processes which have been reported previously in this region [1]. The model used to interpret the laser-excited data is somewhat simpler than the model used in ref. [1] for broadband excitation. The quantitative differences in the life-time data for the two types of excitation may be due to the selective nature of the laser absorption. Broadband sources will excite several of the vanadate excited states whereas the nitrogen laser causes absorption transitions

TABLE I  
MODEL FITTING PARAMETERS

PARAMETER	SAMPLE		
	Undoped	Eu <sup>3+</sup> (1.27x10 <sup>19</sup> cm <sup>-3</sup> )	Er <sup>3+</sup> (1.27x10 <sup>20</sup> cm <sup>-3</sup> )
R <sub>0</sub> <sup>dd</sup> (13K)(Å)		4	2
k(sec <sup>-1</sup> )	5.0x10 <sup>5</sup>	1.0x10 <sup>4</sup>	2.2x10 <sup>5</sup> ; 2.0x10 <sup>5</sup> *
ω(sec <sup>-1</sup> )	1.2x10 <sup>5</sup>		
W <sub>SA</sub> (sec <sup>-1</sup> )		2.0x10 <sup>4</sup>	2.0x10 <sup>7</sup>
W <sub>10</sub> (sec <sup>-1</sup> )		1.1x10 <sup>5</sup>	
W <sub>X</sub> (sec <sup>-1</sup> )			3.0x10 <sup>7</sup>

\* The larger value is k; the smaller value is k'.



directly to the lowest excited crystal field state of the molecular ion. If the broad fluorescence band is composed of the superposition of emission transitions of the same energies from several excited states with different Stokes shifts, then the broadband excitation would be expected to lead to a shorter lifetime and no observed rise time since the transitions from some of the higher excited states are allowed in the  $\text{VO}_4^{3-}$  molecular ion whereas the transition from the lowest level selectively excited by the nitrogen laser is forbidden in the molecular ion and becomes allowed only through the effects of the crystal field.

### C. Results and Interpretation of $\text{YVO}_4:\text{Eu}^{3+}$ Data

The laser-excited fluorescence spectra of europium doped yttrium vanadate is similar to that observed with broadband excitation except that a high temperatures emission lines from the  $^5\text{D}_1$  metastable state of  $\text{Eu}^{3+}$  can be observed. The fluorescence lifetimes are shown as a function of temperature in Fig. 2. The rise times of the three transitions have similar temperature dependences to the decay times. These are listed in Table II. The host vanadate fluorescence rise time decreases from 26  $\mu\text{s}$  at 16 K to less than 1  $\mu\text{s}$  at room temperature. In the same temperature range, the europium  $^5\text{D}_0$  fluorescence rise time decreases around 100  $\mu\text{s}$  to 36  $\mu\text{s}$  with a distinct peak of about 300  $\mu\text{s}$  near 115 K. Similarly the  $^5\text{D}_1$  fluorescence rise time decreases as temperature is raised from about 12 to 6  $\mu\text{s}$  with a peak of about 14  $\mu\text{s}$  near 150 K. The complicated temperature dependences of the  $^5\text{D}_0$  and  $^5\text{D}_1$  lifetimes can be attributed to the effects of energy transfer from the host. The quenching of the host lifetime in the doped sample due to energy transfer is consistent with broadband excitation results.

The TRS results obtained at very low temperature and at room temperature are shown in Fig. 3, where the integrated fluorescence intensity of the europium emission divided by that of the host emission is plotted as a function of time after the laser pulse. At room temperature separate plots are made for transition originating on the  $^5\text{D}_0$  and the  $^5\text{D}_1$  levels of  $\text{Eu}^{3+}$ . At low temperatures only the

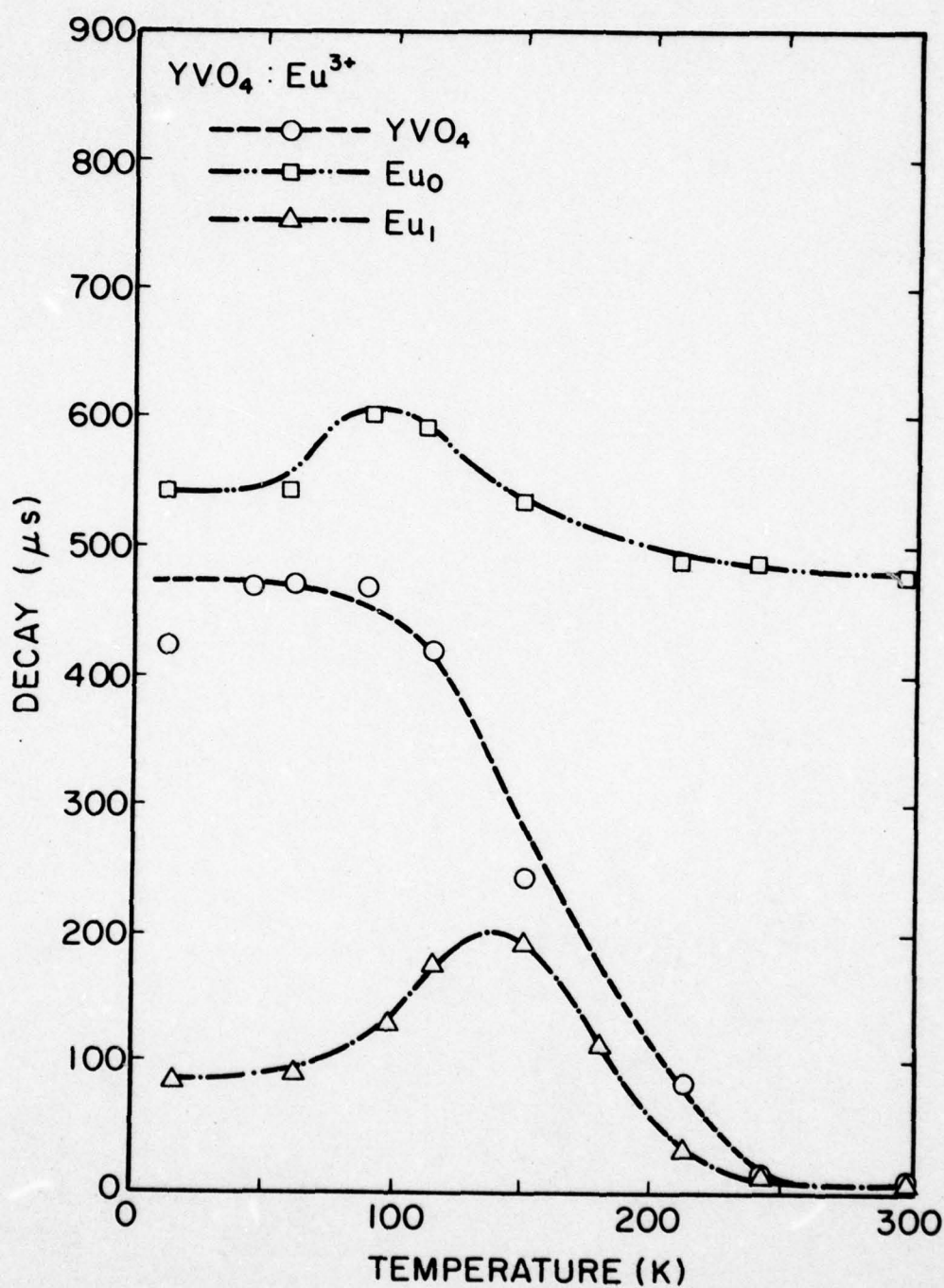


Figure 2. Temperature Dependences of the Fluorescence Decay Times in YVO<sub>4</sub>:Eu<sup>3+</sup>; Eu<sub>0</sub> and Eu<sub>1</sub> Indicate Emission from the <sup>5</sup>D<sub>0</sub> and <sup>5</sup>D<sub>1</sub> States, Respectively

TABLE II  
 FLUORESCENCE LIFETIMES AND RISETIME FOR  $\text{YVO}_4:\text{Eu}^{3+}$

Temperature (K)	Host		$5D_1$		$5D_0$	
	Risetime	Lifetime	Risetime	Lifetime	Risetime	Lifetime
16	26	462	12	87	85	546
61	22	470	13	93	90	548
98	35	486	12.5	130	100	605
115	6	423	6.4	179	300	596
150	4.5	243	14	193	275	539.2
210	1.9	86	14.5	34	90	491
240	1.7	13.8	9	17.5	57	490
300	--	4.3	6.2	8.5	36	478

Lifetimes and risetimes are given in ( $\mu\text{s}$ )



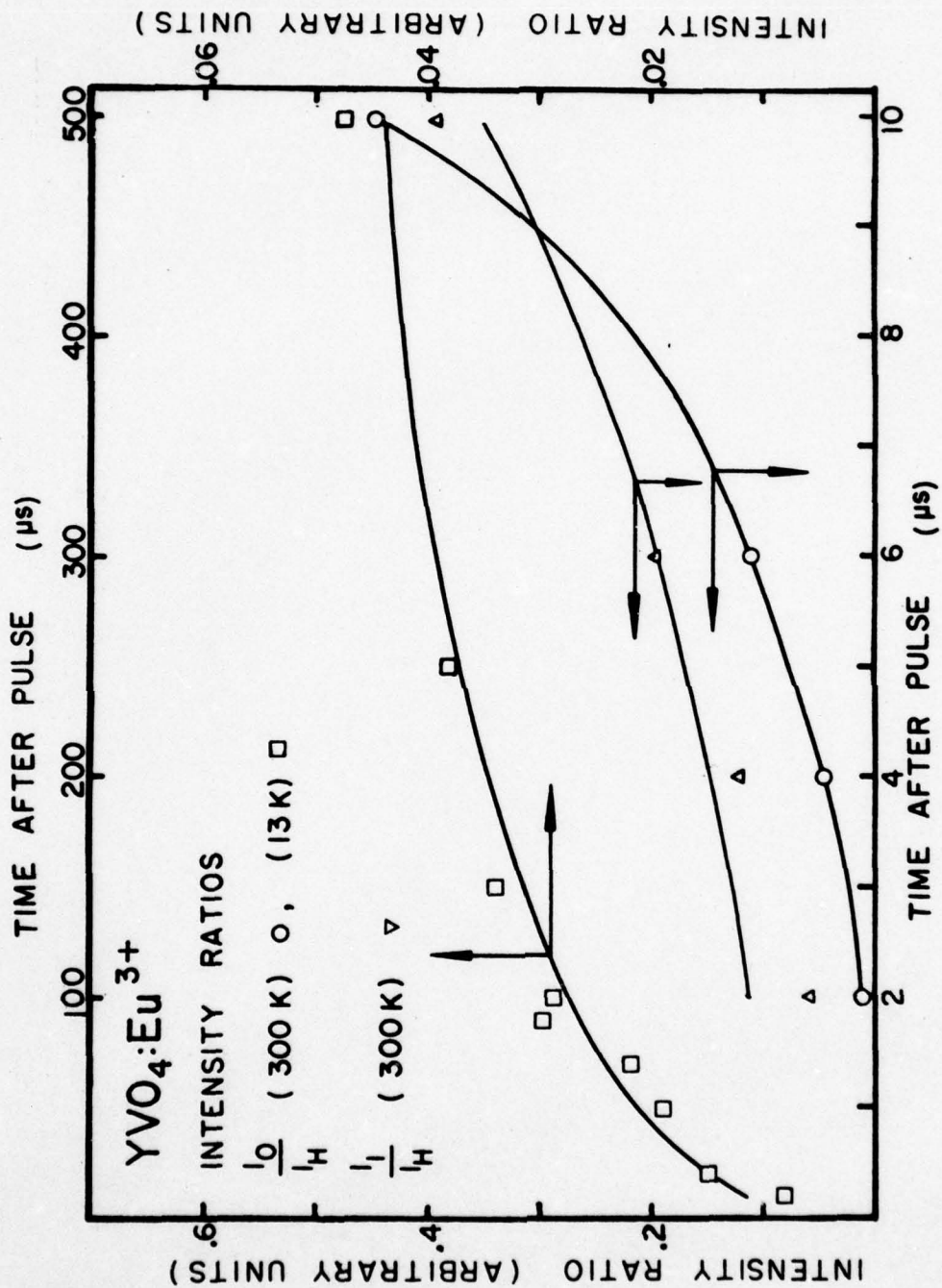


Figure 3. Laser TRS Results for YVO<sub>4</sub>:Eu<sup>3+</sup> Crystals with  $1.27 \times 10^{19} \text{ cm}^{-3} \text{ Eu}^{3+}$ ; See Text for Explanation of Theoretical Lines

former can be observed with any degree of accuracy. The data are listed in Table III. These results can be explained by a model in which the excited states of the host vanadate molecular ions are treated as localized excitons which are self-trapped due to lattice relaxation at low temperature and undergo thermally activated hopping migration at high temperature. The activator impurity ions distort the surrounding vanadate ions creating activator-induced host traps which can trap the excitons. The trapped excitons then transfer their energy to the nearby activators. The energy levels and transition rates are shown schematically in Fig. 4.  $W$  is the rate of creation of host excitons,  $n_H$  is the concentration of excitons and  $\beta_H$  is their fluorescence decay rate.  $k$  represents the rate of exciton migration and trapping at activator-induced host traps.  $n_{XA}$  is the concentration of excited traps and  $W_{SA}$  is the energy transfer rate from trap to nearest neighbor activator. It is assumed that transfer occurs preferentially to the  $^5D_1$  state which has a concentration  $n_1$  and can decay to the ground state with a rate  $\beta_1$  or to the  $^5D_0$  state with a rate  $W_{10}$ . The latter state has a population of  $n_0$  and a fluorescence decay rate  $\beta_0$ . The rate equations for the excited state populations are

$$dn_H/dt = W - \beta_H n_H - kn_H, \quad (3)$$

$$dn_{XA}/dt = kn_H - W_{SA} n_{XA}, \quad (4)$$

$$dn_1/dt = W_{XA} n_{XA} - (W_{10} + \beta_1) n_1, \quad (5)$$

$$dn_0/dt = W_{10} n_1 - \beta_0 n_0. \quad (6)$$

These can be solved assuming a delta function excitation pulse to obtain the required fluorescence intensity ratios,

TABLE III  
FLUORESCENCE INTENSITY RATIOS AT DIFFERENT TIMES  
AFTER THE LASER PULSE

Time After Pulse*	$I_0/I_H$	$I_1/I_H$	$(I_0+I_1)/I_H$	$I_1/I_0$
16K				
6	0.000	-	-	-
10	0.000	-	-	-
20	0.015	-	-	-
50	0.019	-	-	-
70	0.022	-	-	-
90	0.030	-	-	-
100	0.029	-	-	-
150	0.034	-	-	-
250	0.038	-	-	-
500	0.047	-	-	-
1000	0.044	-	-	-
17K				
2	0.000	0.000	0.000	0.000
6	0.004	0.010	0.014	2.500
10	0.011	0.022	0.033	2.000
25	0.060	0.039	0.099	0.650
50	0.323	0.080	0.404	0.250
300K				
2	0.011	0.055	0.067	5.000
4	0.044	0.122	0.166	2.772
6	0.113	0.187	0.301	1.654
10	0.444	0.398	0.842	0.896

\* Time after the pulse is given in microseconds.

$I_0$  is the intensity of  $^5D_0$  and  $I_1$  is the intensity of  $^5D_1$ .



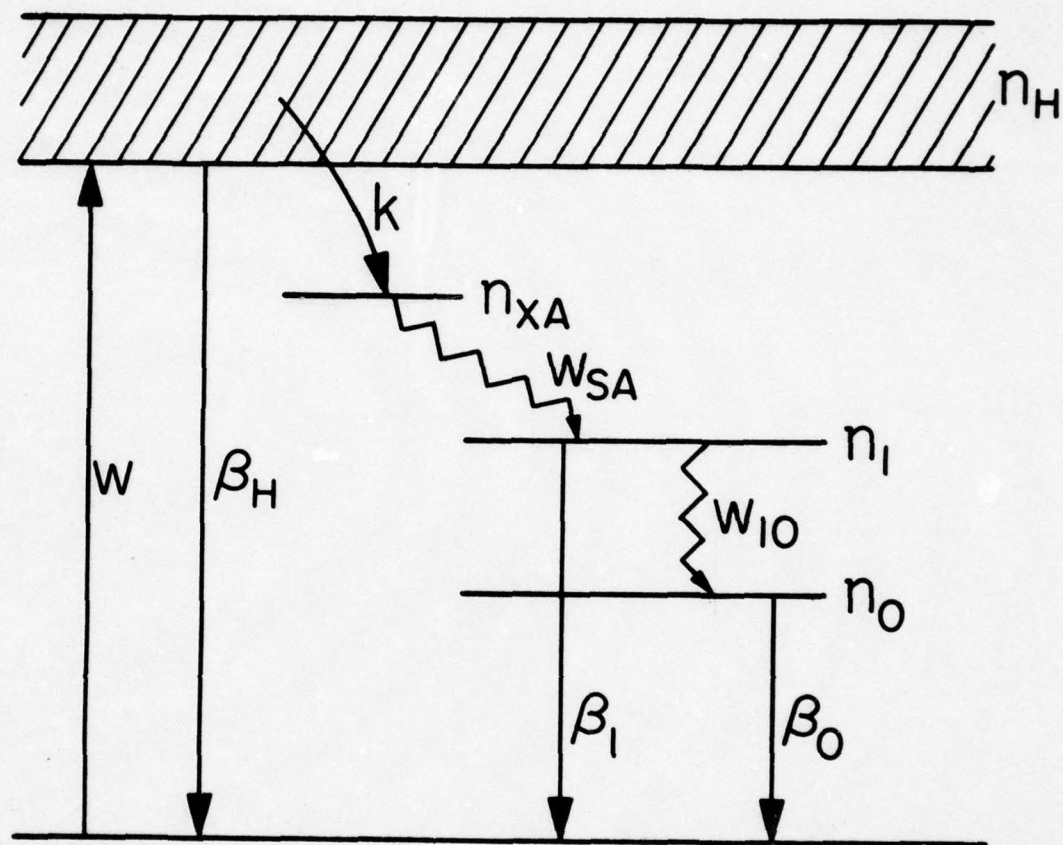


Figure 4. Model for Host-Sensitized Energy Transfer in  $YVO_4:Eu^{3+}$

$$\frac{I_1}{I_H} = \left[ \frac{\beta_1' k}{\beta_H'} \frac{W_{SA}}{W_{SA} - \tau_H^{-1}} \right] \left\{ \frac{1}{\tau_1^{-1} - \tau_H^{-1}} + \frac{1}{W_{SA} - \tau_1^{-1}} e^{-(W_{SA} - \tau_H^{-1})t} + \frac{W_{SA} - \tau_H^{-1}}{(\tau_1^{-1} - W_{SA})(\tau_1^{-1} - \tau_H^{-1})} e^{-(\tau_1^{-1} - \tau_H^{-1})t} \right\}, \quad (7)$$

$$\frac{I_0}{I_H} = \left[ \frac{\beta_0' k}{\beta_H'} \frac{W_{10} W_{SA}}{W_{SA} - \tau_H^{-1}} \right] \left\{ \frac{1 - e^{-(\tau_0^{-1} - \tau_H^{-1})t}}{(\tau_1^{-1} - \tau_H^{-1})(\tau_0^{-1} - \tau_H^{-1})} + \frac{e^{-(W_{SA} - \tau_H^{-1})t} - e^{-(\tau_0^{-1} - \tau_H^{-1})t}}{(W_{SA} - \tau_1^{-1})(\tau_0^{-1} - W_{SA})} + \frac{e^{-(\tau_1^{-1} - \tau_H^{-1})t} - e^{-(\tau_0^{-1} - \tau_H^{-1})t}}{(\tau_1^{-1} - W_{SA})(\tau_1^{-1} - \tau_H^{-1})(\tau_0^{-1} - \tau_1^{-1})} \right\} \quad (8)$$

where the prime indicates radiative decay rates and the lifetimes which can be measured have been used in place of the appropriate combinations of decay rates. The solid lines in Fig. 3 represent the best fit to the room temperature data using Eqs. (7) and (8) with  $W_{SA}$  and the factors in square brackets treated as adjustable parameters. If the constant lifetimes which are approached at low temperatures are taken as good approximations to the radiative decay times,  $k$  and  $W_{10}$  can also be determined. These parameters are summarized in Table I.

At low temperatures the model can be simplified greatly since no exciton migration is present and a-1 fluorescence occurs from the  $^5D_0$  level. Thus, the host excited states are self-trapped excitons which can fluoresce or transfer their energy in a single step process to the nearest activator which can effectively be treated as having only one excited state. If the transfer occurs through electric dipole-dipole interaction, the equation derived to describe the TRS data is

$$\frac{I_0(t)}{I_H(t)} = \frac{\beta'_0}{\beta'_H} \left\{ \frac{\omega(t)[\beta_H + \omega(t)]}{[\beta_H + \omega(t) - \beta_A]^2} \right\} \{e^{-[\beta_A - \beta_H - \omega(t)]t} - 1\}$$

with

$$\omega(t) = \frac{4}{3}\pi^{3/2} R_0^3 C_A (\tau_H^0 t)^{-1/2}, \quad (10)$$

where  $R_0$  is the critical interaction distance,  $C_A$  is the concentration of  $\text{Eu}^{3+}$ , and  $\tau_H^0$  is the host fluorescence decay time in the undoped sample. The solid line in Fig. 3 represents the best fit to the low temperature data using Eq. (9) and treating  $R_0$  as an adjustable parameter. The quantitative results are listed in Table I.

The predictions of the model assumed here give an excellent fit to the data involving the  $^5D_0$  europium emission at both high and low temperatures. The fit to the  $^5D_1$  TRS data is not as good. This may be due either to the poorer accuracy of these data or to the fact that the physical situation is more complicated than that considered in the model. The high temperature exciton transfer rate and trap to activator transfer rate and the low temperature value of  $R_0$  reported in Table I are all consistent with the values found from intensity and lifetime quenching investigations [1]. The radiationless relaxation rate between the excited states of  $\text{Eu}^{3+}$  is consistent with that reported from other investigations [2]. Also the complicated temperature dependence of the  $^5D_1$  fluorescence decay time can be explained by this model which describes the emission as the sum of three exponentials, one having the decay time of the host which dominates at high temperatures, and one having the intrinsic decay time of the  $^5D_1$  level which dominates at low temperatures.

#### D. Results and Interpretation of $\text{YVO}_4:\text{Er}^{3+}$ Data

The absorption spectrum of erbium doped yttrium vanadate is shown in Fig. 5 and the fluorescence spectra are shown in Fig. 6. The sharp line spectra are



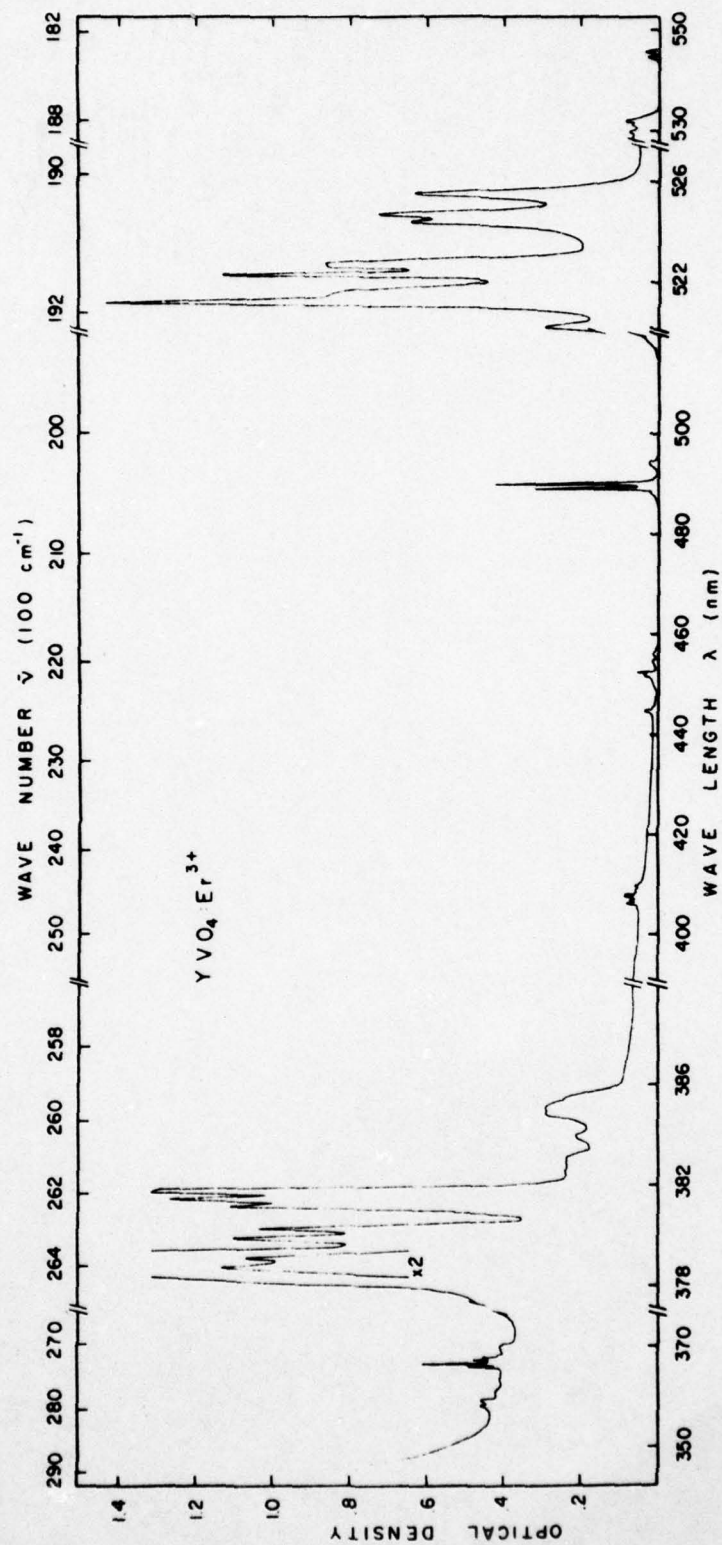


Figure 5. Room Temperature Absorption Spectrum of  $\text{YVO}_4:\text{Er}^{3+}$  Crystal with  $1.27 \times 10^{20} \text{ cm}^{-3}$   $\text{Er}^{3+}$ ; Sample Thickness is 0.9 mm

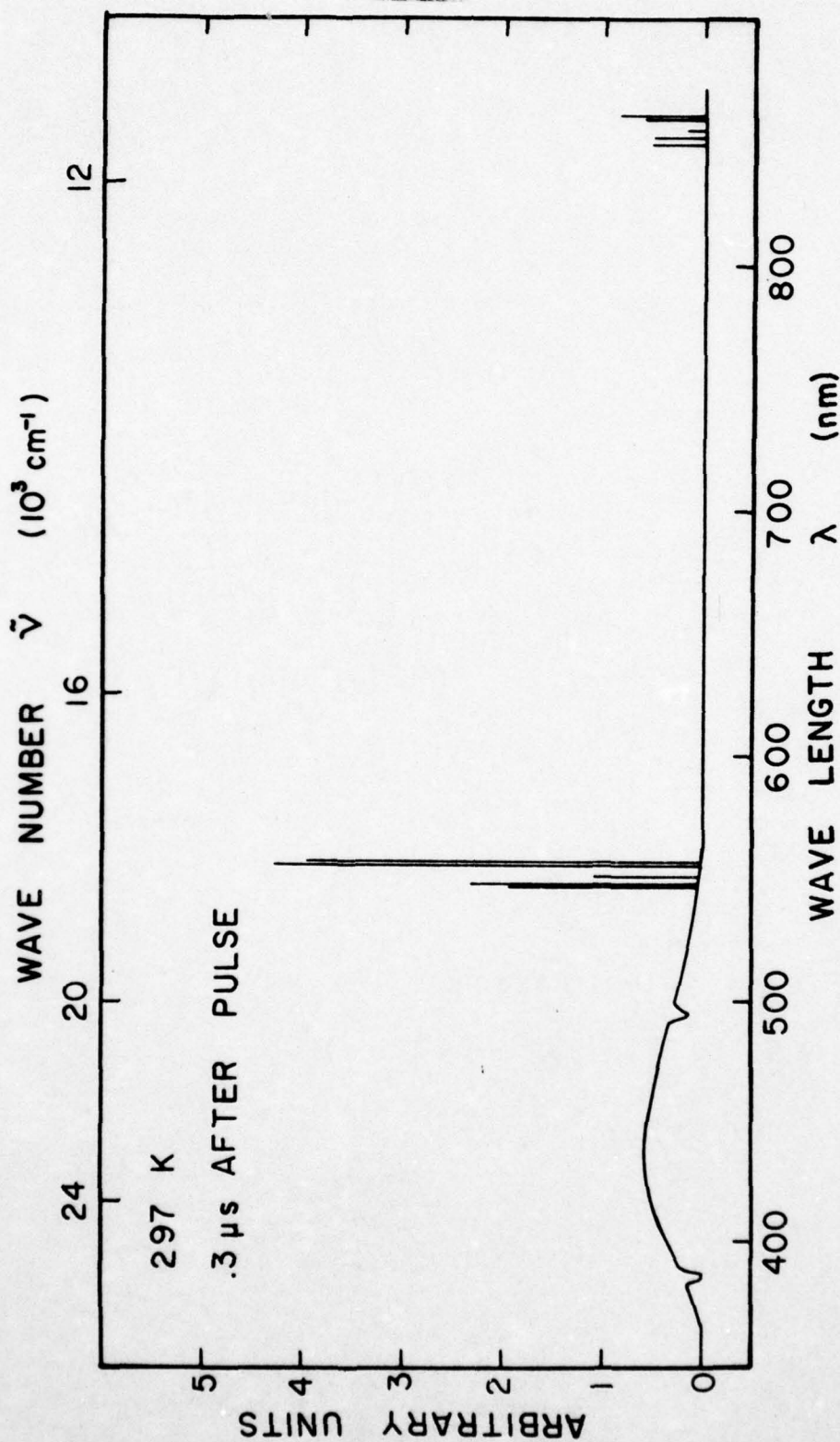


Figure 6a. Fluorescence Spectrum of  $\text{YVO}_4:\text{Er}^{3+}$  with  $1.27 \times 10^{20} \text{ cm}^{-3} \text{ Er}^{3+}$   
Taken at Room Temperature

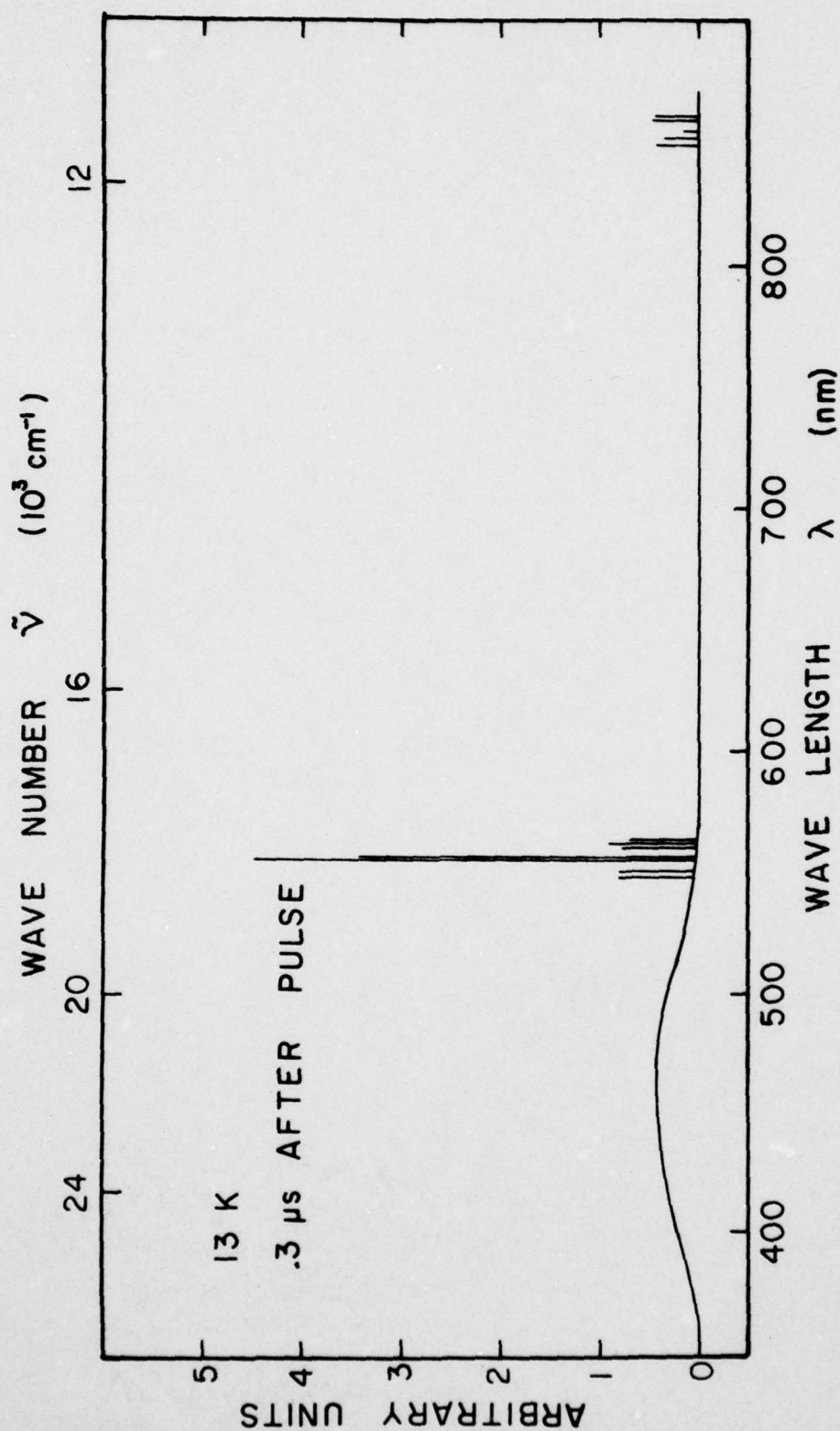


Figure 6b. Fluorescence Spectrum of  $\text{YVO}_4:\text{Er}^{3+}$  with  $1.27 \times 10^{20} \text{ cm}^{-3}$   
Taken at 13 K



similar to those observed for  $\text{Er}^{3+}$  in other hosts [3]. Again fluorescence from two metastable states can be observed at room temperature while only transitions originating from the lowest excited state remain. It is well known that trivalent erbium also has numerous efficient emission lines in the near infrared region of the spectrum not investigated here [3].

Fig. 7 shows the fluorescence lifetimes obtained at different temperatures. These are listed in Table IV. The observed fluorescence rise times in this case are all less than 1  $\mu\text{s}$ , and difficult to measure with any degree of accuracy. The erbium lifetimes decrease slightly due to radiationless transitions as temperature is raised. The temperature dependent of the vanadate fluorescence lifetime is similar to that seen in the europium doped sample. Fig. 8 shows the temperature dependences of the integrated fluorescence intensity and lifetime ratios which are directly related to the rate of energy transfer. These are listed in Table V. They both decrease slightly as temperature is raised from 13 K to about 65 K which can be attributed to the thermal activation of self-trapped excitons which decreases the amount of single step energy transfer. Above about 150 K both curves exhibit a sharp exponential increase with temperature as the excitons become mobile enough to migrate to activators. The solid lines represent the best fit to the data which is obtained with an activation energy of about  $1000\text{ cm}^{-1}$ . This is qualitatively consistent with the results obtained on the europium doped sample. The difference in magnitudes for the intensity and lifetime data can be attributed to the differences in quantum efficiencies of the  $\text{Er}^{3+}$  and host emissions.

Results of TRS investigations are shown in Fig. 9 and listed in Table VI for both room temperature and 13 K. The model used to interpret these data is shown in Fig. 10. The rate parameters and excited state populations are similar to those in Fig. 4. In this model back transfer from traps to the host band is included as is direct transfer from the host to both the metastable states of the

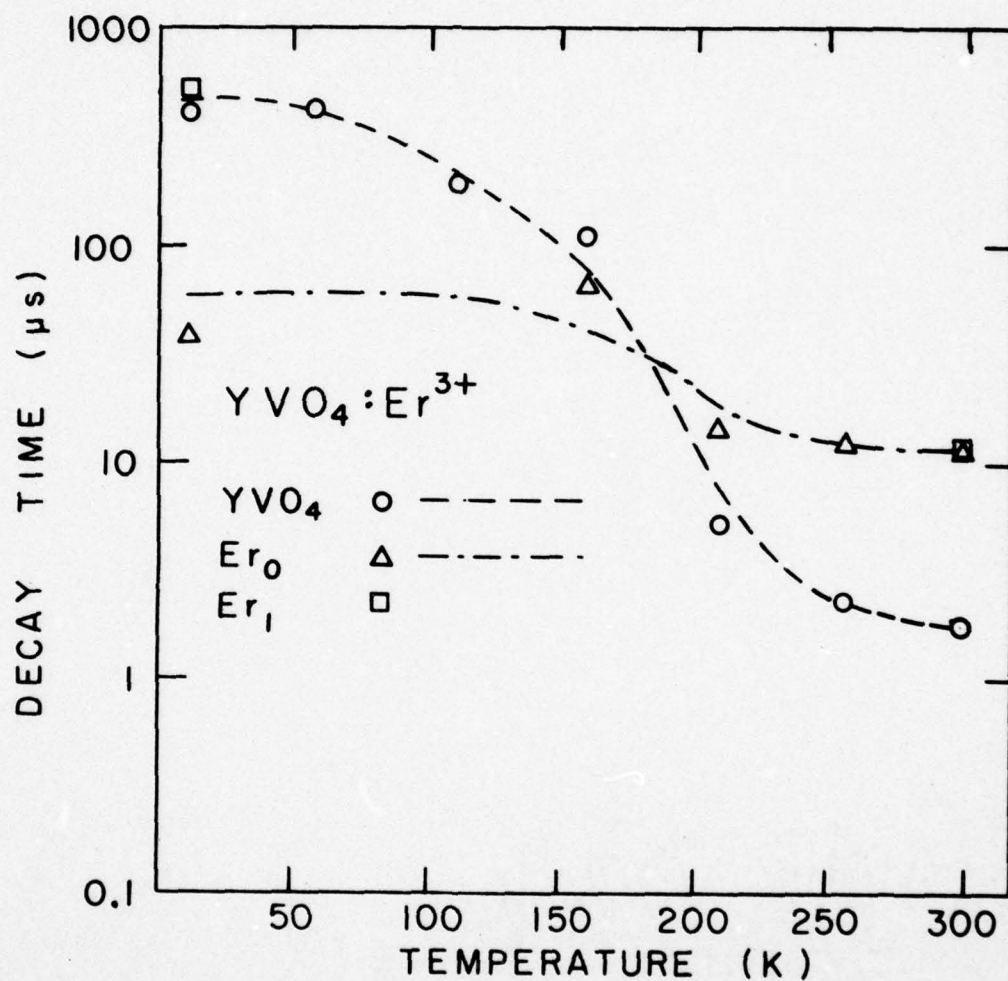


Figure 7. Temperature Dependences of the Fluorescence Decay Times in YVO<sub>4</sub>:Er<sup>3+</sup>; Er<sub>0</sub> and Er<sub>1</sub> Indicate Emission from the <sup>4</sup>S<sub>3/2</sub> and <sup>2</sup>H<sub>11/2</sub> States, Respectively

TABLE IV  
LIFETIMES AND RISETIMES OF THE SYSTEM  $\text{YVO}_4:\text{Er}^{3+}$  AT DIFFERENT TEMPERATURES

Temperature (K)	Host		$5D_1$		$5D_0$	
	Risetime	Lifetime	Risetime	Lifetime	Risetime	Lifetime
12	.16	414	.150	521	3	38
58	.60	434	--	--	--	--
113	.75	191	--	--	--	--
161	.90	112	--	--	6.5	67
210	.94	5	--	--	4.5	14
256	.43	2.3	--	--	2.4	12.8
300	.25	.53	.5	11.2	.85	11.4

Lifetimes and risetimes are given in ( $\mu\text{s}$ )



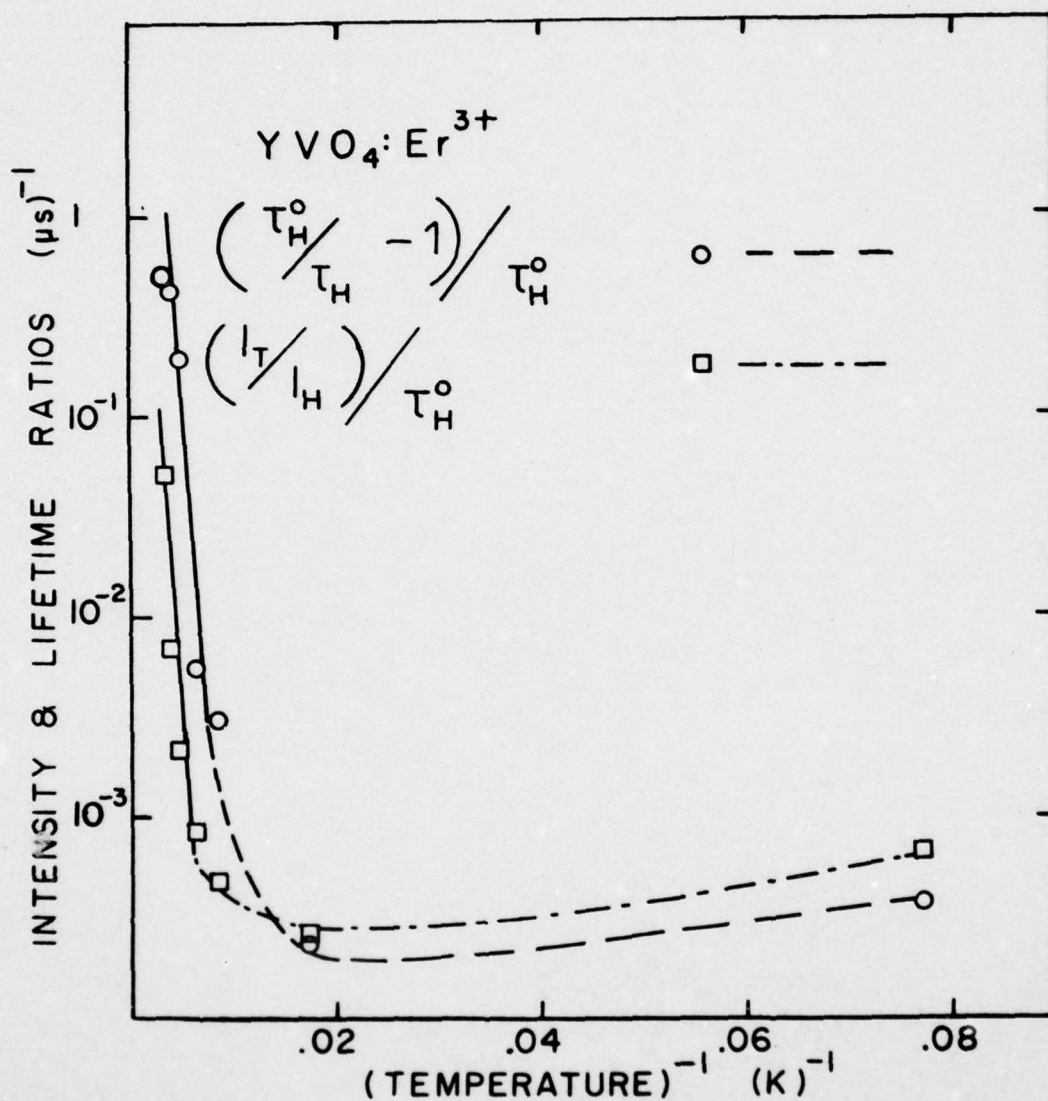


Figure 8. Temperature Dependences of the Fluorescence Intensity and Lifetime Ratios in  $\text{YVO}_4:\text{Er}^{3+}$ ;  $I_T$  Represents the Sum of All the  $\text{Er}^{3+}$  Transitions; the Intensities are Measured at  $0.7 \mu\text{s}$  After the Laser Pulse; the Solid Lines are Given by  $\text{Exp} [1,000 \text{ cm}^{-1}/(k_B T)]$

TABLE V  
FLUORESCENCE INTENSITIES AND LIFETIME RATIOS OF  $\text{YVO}_4:\text{Er}^{3+}$   
AT DIFFERENT TEMPERATURES

Temperature (K)	$(I_T/I_H)/\tau_H^0$ *	$(\tau_H^0/\tau_H - 1)/\tau_H^0$ **
13	$6.71 \times 10^{-14}$	$3.75 \times 10^{-4}$
58	$2.42 \times 10^{-4}$	$2.34 \times 10^{-4}$
113	$4.89 \times 10^{-4}$	$3.01 \times 10^{-3}$
161	$8.4 \times 10^{-4}$	$5.60 \times 10^{-3}$
210	$2.07 \times 10^{-3}$	$1.9 \times 10^{-1}$
256	$6.87 \times 10^{-3}$	$4.1 \times 10^{-1}$
300	$5.03 \times 10^{-2}$	1.8

\*  $I_T$  is the total intensity of the  $^5D_1$  and  $^5D_0$

\*\*  $\tau_H^0$  is the lifetime of the  $\text{YVO}_4$  when undoped and

$\tau_H$  is the lifetime of the  $\text{YVO}_4$  when doped

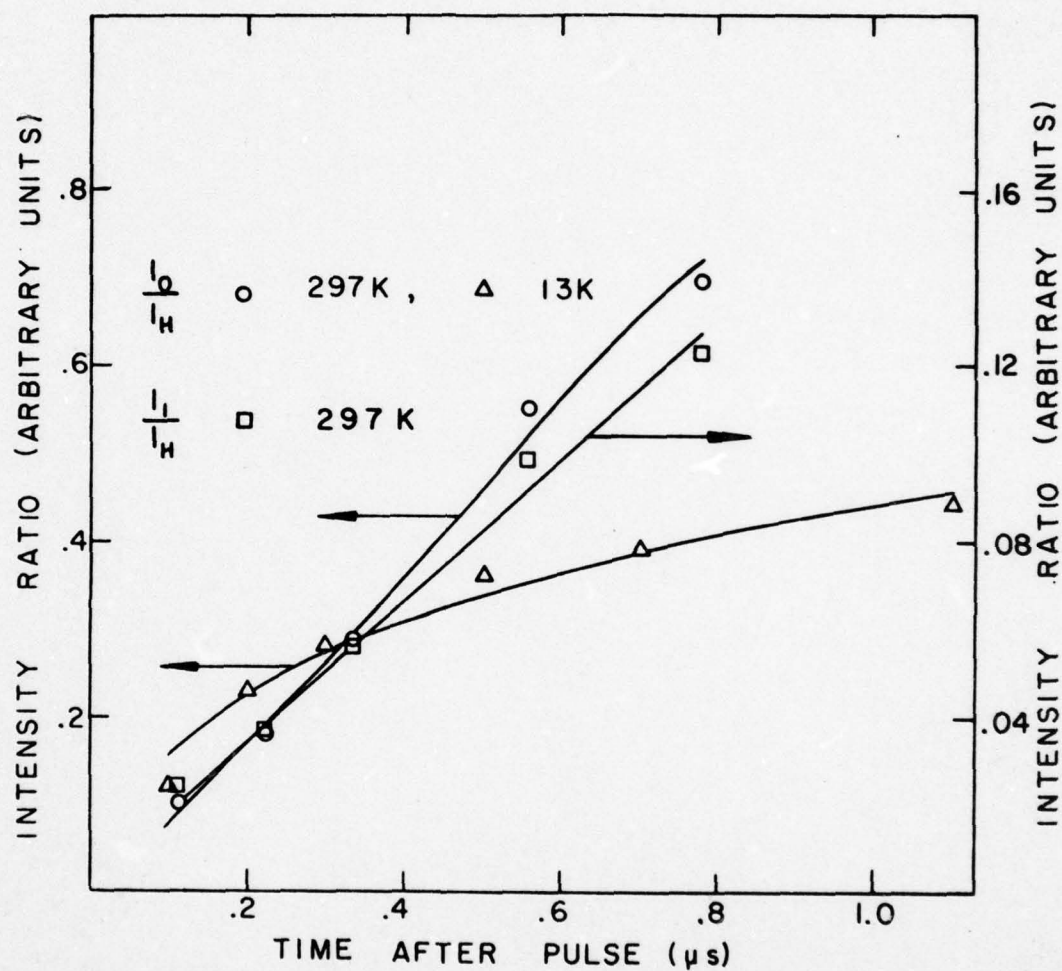


Figure 9. Laser TRS Results from YVO<sub>4</sub>:Er<sup>3+</sup> Crystals with  $1.27 \times 10^{20} \text{ cm}^{-3} \text{ Er}^{3+}$



TABLE VI  
 FLUORESCENCE INTENSITY RATIOS AT DIFFERENT TIMES  
 AFTER THE LASER PULSE AT ROOM TEMPERATURE  
 IN  $\text{YVO}_4:\text{Er}^{3+}$

Time A.P. ( $\mu\text{s}$ )	$I_0/I_H$	$I_1/I_H$
100	.103	.024
200	.177	.037
300	.288	.056
500	.556	.099
700	.698	.123
1100	--	--

AD-A066 086

OKLAHOMA STATE UNIV STILLWATER DEPT OF PHYSICS

F/G 20/5

MULTISTEP ENERGY MIGRATION AND RADIATIONLESS RELAXATION PROCESS--ETC(U)

DEC 78 R C POWELL

DAA629-76-G-0099

UNCLASSIFIED

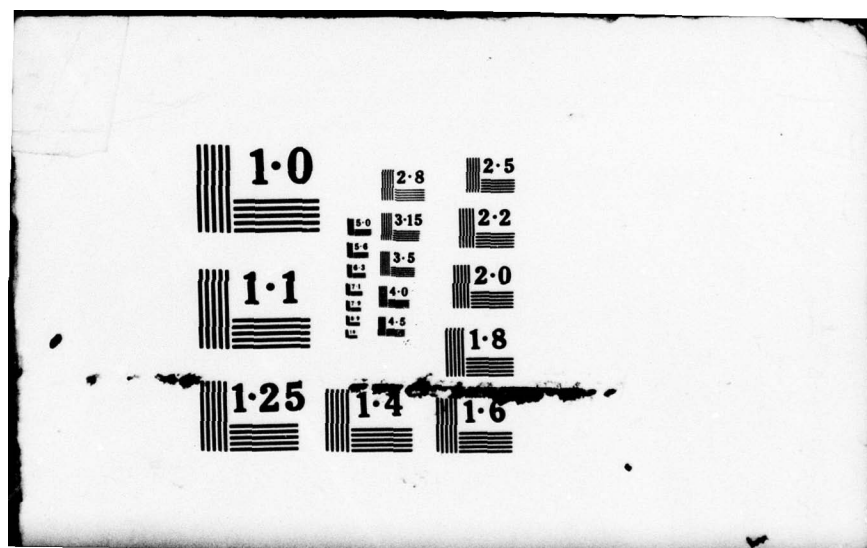
ARO-13318.8-P

NL

2 OF 4  
ADA  
066086

U.S. GOVERNMENT PRINTING OFFICE







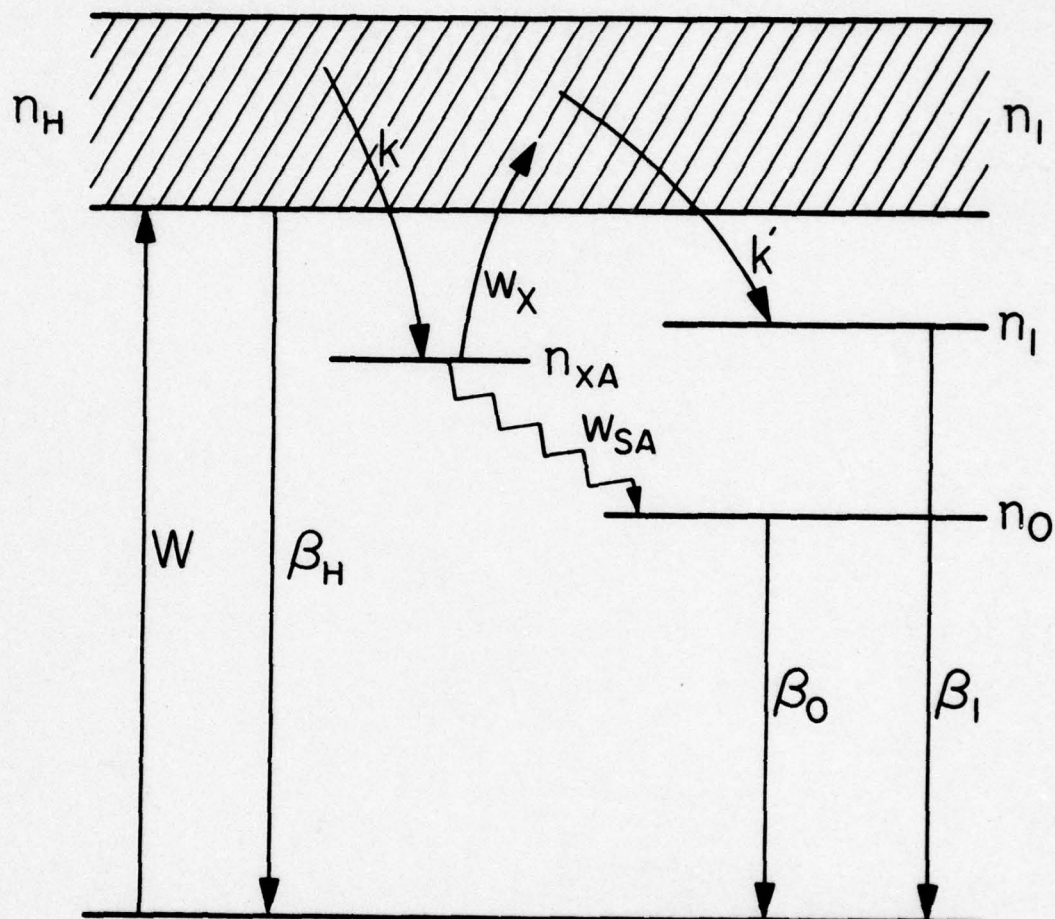


Figure 10. Model for Host-Sensitized Energy Transfer in  $\text{YVO}_4:\text{Er}^{3+}$

activators. It is unnecessary to include radiationless relaxation between the two excited metastable states of the activator in order to fit the data in the case.

The rate equations for the excited state populations are

$$dn_H/dt = W - \beta_H n_H - (k + k') n_H + W_X n_{XA}, \quad (11)$$

$$dn_{XA}/dt = k n_H - W_{SA} n_{XA} - W_X n_{XA}, \quad (12)$$

$$dn_1/dt = k' n_H - \beta_1 n_1, \quad (13)$$

$$dn_0/dt = W_{SA} n_{XA} - \beta_0 n_0. \quad (14)$$

These can be solved assuming a delta function excitation pulse to obtain the required fluorescence intensity ratios,

$$\frac{I_0}{I_H} = \left[ \frac{\beta_0' k}{\beta_H'} \frac{W_{SA}}{(W_{SA} + W_X)} \right] \left\{ \tau_0 (e^{-t/\tau_0} - 1) + \frac{1}{\tau_0^{-1} - W_{SA} - W_X} \right. \\ \left. \times (e^{-(W_{SA} + W_X)t} - e^{-t/\tau_0}) \right\}, \quad (15)$$

$$\frac{I_1}{I_H} = \left[ \frac{\beta_1' k'}{\beta_H} \right] \{ \tau_1 (1 - e^{-t/\tau_1}) \}, \quad (16)$$

where again the prime indicates radiative decay rates and the lifetimes which can be measured have been used in place of the appropriate combinations of decay rates. The solid lines in Fig. 9 represent the best fit to the room temperature data using Eqs. (15) and (16) with  $W_{SA}$ ,  $W_X$ , and the factors in square brackets treated as adjustable parameters. As before, the constant lifetimes approached at low temperatures are taken as good approximations to the radiative decay times in

order to determine  $k$  and  $k'$ . The parameters for this case are also summarized in Table I.

The model used to interpret the low temperature data is the same as that used in the previous section. The solid line in Fig. 9 represents the best fit to the low temperature data using Eq. (9) and treating  $R_0$  as an adjustable parameter. The result is given in Table I. The good fits to the data in Fig. 9 indicate the validity of the assumed model. Numerous other models were investigated, but none was found to be consistent with the observed results.

#### E. Discussion and Conclusions

The critical interaction distance between randomly distributed self-trapped excitons and activators at low temperatures, can be predicted theoretically for electric dipole-dipole interaction [1]. It is seen to be  $4 \text{ \AA}$  and  $2 \text{ \AA}$  for the europium and erbium activators, respectively. These are in close agreement with the values of  $R_0$  found experimentally. They indicate very weak energy transfer at these temperatures with the larger value for  $\text{Eu}^{3+}$  being due to a somewhat larger spectral overlap with the vanadate emission.

The data obtained on the quenching of the fluorescence intensity and lifetimes indicate an exponential increase in energy transfer with increasing temperature for all three samples investigated. The fact that the activation energies for the temperature dependences are different in each case indicates that the trapping process at activators has an exponential temperature dependence associated with it well as the thermal activation of exciton hopping. This is not surprising since emission and absorption of phonons may be involved for the conservation of energy.

In the analysis of TRS data the parameters characterizing exciton migration up to an activator trapping region and the final trap-to-activator transfer step are determined separately. In the simplest model for exciton diffusion where the



exciton is trapped on the first visit to any trapping site it happens to encounter, the energy transfer rate to the traps is given by [4]

$$k = 4\pi D R_A C_A, \quad (17)$$

where  $D$  is the diffusion coefficient,  $R_A$  is the trapping radius, and  $C_A$  is the concentration of activators. The trapping radius of an activator is determined by the differences in size and electronic structure between it and the host ion it replaces. In this case the activators substitute for  $Y^{3+}$  ions which have a radius of  $0.93 \text{ \AA}$ . The ionic radius of  $Eu^{3+}$  is  $1.03 \text{ \AA}$  and that of  $Er^{3+}$  is  $0.96 \text{ \AA}$ . This indicates a slightly larger size mismatch for the europium activators although the mismatch is not very large in either case. Because of this, a reasonable approximation to the trapping radius is the distance from the activator ions to the nearest neighbor vanadate molecular ion which is  $3.15 \text{ \AA}$ . Using this value in Eq. (17) predicts a diffusion coefficient of  $D = 2.0 \times 10^{-4} \text{ cm}^2 \text{ s}^{-1}$  for  $Eu^{3+}$  and  $4.4 \times 10^{-9} \text{ cm}^2 \text{ s}^{-1}$  for  $Er^{3+}$  activators. (In treating the  $Er^{3+}$  case  $k$  and  $k'$  have been added together which is justified by the fact that the diffusion contribution to these rate parameters is identical and they differ only in the number of activators which accept the energy in the higher metastable state as opposed to the lower level.)

If the exciton migration is approximated as a nearest neighbor hopping on a simple cubic lattice, the diffusion length and hopping time are given by

$$l = \sqrt{2D\tau_H^0}, \quad (18)$$

$$\tau_H = \alpha^2 / 6D, \quad (19)$$

where  $\alpha$  is the lattice spacing between  $VO_4^{3-}$  ions which is  $4.75 \text{ \AA}$  in  $YVO_4$  crystals. With the diffusion coefficient found above, these equations give values of  $l = 2.4 \times 10^{-7}$  and  $3.6 \times 10^{-7} \text{ cm}$  and  $\tau_H = 1.9 \times 10^{-7}$  and  $8.5 \times 10^{-8} \text{ s}$  for  $Eu^{3+}$  and  $Er^{3+}$  activators, respectively. The number of steps in the exciton's random walk can be

estimated from the expression

$$n = \tau_H^0 / t_H, \quad (20)$$

and is found to be 79 for  $\text{Eu}^{3+}$  and 176 for  $\text{Er}^{3+}$  activators.

These exciton migration parameters are summarized in Table VII. They should be expected to be independent of the type of activator ion which is essentially true for the  $\text{Eu}^{3+}$  and  $\text{Er}^{3+}$  doped samples considering the approximate nature of the simple diffusion model used to interpret the results.

Theoretical estimates for the single step rates for exciton hopping and trap-to-activator energy transfer can be obtained either from the expressions for electric dipole-dipole or exchange interactions. The predictions of electric dipole-dipole interaction are found to be inconsistent with the observed values. The transfer rate for exchange interaction is given by

$$W(\text{ex}) = (\tau_S^0)^{-1} \exp[\gamma(1 - R/R_0')]. \quad (21)$$

Here  $\gamma = 2R_0'/L$ , where  $L$  is an effective Bohr radius and  $R_0'$  is the critical interaction distance given by

$$R_0' = (L/2) \ln[(2\pi\tau_S^0/h)K^2\Omega], \quad (22)$$

where  $\Omega$  is the overlap integral of the absorption spectrum of the activator and the emission spectrum of the sensitizer, and  $K$  involves the wave function overlap which generally cannot be determined easily. Exchange interaction predicts the observed exciton hopping times for  $R_0'$  of the order of  $7 \text{ \AA}$  assuming a nearest neighbor vanadate separation of  $4.75 \text{ \AA}$  and a value of  $L$  equal to half the yttrium-oxygen spacing,  $\approx 1 \text{ \AA}$ . A similar analysis gives the observed values for  $W_{\text{SA}}$  for  $R_0'(\text{Eu}) = 2.5 \text{ \AA}$  and  $R_0'(\text{Er}) = 6.0 \text{ \AA}$  assuming a nearest neighbor vanadate-activator distance of  $3.15 \text{ \AA}$ . Since  $K$  is unknown for these cases it is not possible to derive values

TABLE VII  
EXCITON MIGRATION AND TRAPPING PARAMETERS

PARAMETER	Eu <sup>3+</sup> (1.27x10 <sup>19</sup> cm <sup>-3</sup> )	Er <sup>3+</sup> (1.27x10 <sup>20</sup> cm <sup>-3</sup> )
D (cm <sup>2</sup> sec <sup>-1</sup> )	2.0x10 <sup>-9</sup>	4.4x10 <sup>-9</sup>
λ (cm)	2.4x10 <sup>-7</sup>	3.6x10 <sup>-7</sup>
t <sub>H</sub> (sec)	1.9x10 <sup>-7</sup>	8.5x10 <sup>-8</sup>
n	79	176
t <sub>diff</sub> (sec)	1.0x10 <sup>-4</sup>	2.4x10 <sup>-6</sup>
t <sub>trap</sub> (sec)	5.0x10 <sup>-5</sup>	4.9x10 <sup>-8</sup>
C (Å)	5	9



of  $R_0'$  theoretically. However, the values obtained in this analysis appear to be physically reasonable.

Table VII also lists the reciprocal of the measured rate parameters for migration and trapping as the diffusion time  $t_{\text{diff}}$  and trapping time  $t_{\text{trap}}$ , respectively. For both samples the trapping time is found to be shorter than the diffusion time which is the case of "diffusion limited energy transfer". However, for a sample with europium activators of concentration equal to that of the erbium doped sample the diffusion time would be shorter than the trapping time giving the case of "trap limited energy transfer" as found previously [1].

An alternative way of interpreting the migration and trapping characteristics is through the generalized random walk theory developed by Soos and Powell [4]. This model has recently been used to explain energy transfer in cathodoluminescence of this type of phosphor material [5]. In this theory the energy transfer rate determined experimentally is given by

$$k = C_a V_m C(A) t_H^{-1}, \quad (23)$$

where  $V_m$  is the volume per molecule and  $C(A)$  is the capacity of the random walk. The latter quantity is defined as the rate at which new sites are sampled by the exciton per step in the limit of many steps. This can be calculated theoretically for simple cases and has been found empirically from TRS measurements for several systems of doped aromatic hydrocarbon crystals [6]. It can be directly related to the size and shape of the trapping region surrounding the activators and to the anisotropy of the random walk. The data discussed above yield values of 9 and 5 for the capacities of the erbium and europium doped samples, respectively. For a simple cubic lattice these values would correspond to trapping regions extending out to approximately third nearest neighbors around each activator [4].

In summary, host-sensitized energy transfer in yttrium vanadate crystals doped with trivalent rare earth impurity ions at low temperatures is consistent with a single step electric dipole-dipole interaction process from self-trapped excitons, whereas at high temperatures the transfer is dominated by thermally activated exciton hopping with activator-induced host traps playing an important part in the trapping process. In the latter case both the hopping steps and the trapping steps appear to be due to exchange interaction. This is consistent with the fact that the charge distribution of the  $^1A_1$  metastable state of the vanadate molecule lies outside the molecule, thus providing for the possibility of strong wave function overlap with neighboring vanadate molecules and impurity ions [7]. Since exchange interaction falls off rapidly with distance, it is not surprising that at low temperatures, where the excitons are immobile, longer range electric dipole-dipole interaction processes become important.

The transition models and rate equations used in interpreting the  $YVO_4:Eu^{3+}$  and  $YVO_4:Er^{3+}$  data are fairly complex. However, it should be reiterated that many simpler models were investigated and found to be unacceptable for fitting the data. The complexity due to the activator-induced host traps should be expected since similar defect sites are necessary for explaining the data obtained on undoped  $YVO_4$ . In this case the perturbing defects are structural imperfections or chemical impurities other than activator ions.

A final important point to note is that pulsed laser TRS measurements produce data which are consistent with conventional lifetime and intensity quenching studies but are more sensitive to the choice of models used in interpretation of the results. This leads directly to more primary experimental parameters, thus alleviating the necessity for many of the assumptions that generally must be made in obtaining migration and trapping characteristics from primary experimental parameters. This is especially important in cases where many different interaction and relaxation processes are present such as the systems investigated here.



## REFERENCES

- [1] C. Hsu and R. C. Powell, J. Lumin. 10 (1975) 273.
- [2] E. D. Reed and H. W. Moos, Phys. Rev. B8 (1973) 980.
- [3] B. DiBartolo, Boston College Report for the U. S. Air Force, unpublished.
- [4] Z. G. Soos and R. C. Powell, Phys. Rev. B6 (1972) 4035.
- [5] L. Ozawa and H. N. Hersch, Phys. Rev. Lett. 36 (1976) 683.
- [6] R. C. Powell and Z. G. Soos, J. Lumin. 11 (1975) 1.
- [7] D. S. Boudreaux and T. S. LaFrance, J. Phys. Chem. Solids 35 (1974) 897.

### IV.3 Laser Time-Resolved Spectroscopy Studies of Host-

#### Sensitized Energy Transfer in $\text{Bi}_4\text{Ge}_3\text{O}_{12}:\text{Er}^{3+}$ Crystals

##### A. Introduction

$\text{Bi}_4\text{Ge}_3\text{O}_{12}$  crystals have been reported as a good host material for  $\text{Nd}^{3+}$  lasers and the spectra of other rare earth ions have been studied in this material [1]-[3]. One of the attractive aspects of rare earth-bismuth germanate laser systems is the possibility of enhanced pumping of the active ions through host absorption and energy transfer. However, the spectroscopic properties of bismuth germanate crystals are still not well understood and energy transfer in doped crystals has not been characterized. We report here the results of an investigation of the spectroscopic properties of undoped and  $\text{Er}^{3+}$  doped  $\text{Bi}_4\text{Ge}_3\text{O}_{12}$  crystals. Pulsed laser time-resolved spectroscopy techniques were used to characterize the host-sensitized energy transfer. The results are interpreted in terms of a model in which the host luminescence center is treated as a trapped exciton at low temperatures and a mobile exciton undergoing thermally activated migration at high temperatures.

##### B. Experimental

The samples studied were good single crystals of  $\text{Bi}_4\text{Ge}_3\text{O}_{12}$ , on undoped and the other doped with 1%  $\text{Er}^{3+}$ . These were mounted in a cryogenic refrigerator to control the temperature and excited by an NRG pulsed nitrogen laser. The excitation



pulse was about 10 nsec in duration and less than 4 Å wide centered at 3371 Å. The fluorescence was analyzed by a one-meter spectrometer, detected by an RCA C31034 photomultiplier tube, and processed by a boxcar averager triggered by the laser pulse. The time resolution was of the order of 75 nsec.

The nitrogen laser excitation is on the edge of the host absorption band as can be seen in Fig. 1. The fluorescence from undoped  $\text{Bi}_4\text{Ge}_3\text{O}_{12}$  appears as a broad band as shown in Fig. 2. Below about 30 K the band peaks near 6200 Å whereas at higher temperatures the peak shifts to near 5200 Å. This spectral change is accompanied by a significant increase in fluorescence lifetime as shown in Fig. 3. Between room temperature and 100 K the decay time increases slightly from about 0.4 to 7.7 μsec and then sharply increases to about 46 μsec at 14 K. These results are consistent with those reported previously by others [4],[5].

The fluorescence spectra for the erbium doped bismuth germanate sample at low and high temperatures are shown in Figs. 4 and 5 for different times after the laser pulse. At short times, the peak of the host fluorescence band is at shorter wavelengths than in the undoped sample. At long times after the pulse, the peak of the band shifts to longer wavelengths. The sharp  $\text{Er}^{3+}$  fluorescence lines increase in intensity as a function of time after the laser pulse as the host fluorescence intensity decreases. This effect is more pronounced at room temperature than at low temperatures. The most intense lines in the spectrum are due to the  $^4\text{S}_{3/2}$  to  $^4\text{I}_{15/2}$  transition of the  $\text{Er}^{3+}$  ion. The sharp dips in the host fluorescence band are due to absorption of the host emission by the erbium ions. Figs. 6 and 7 show the ratios of the integrated fluorescence intensities of the activation ions and the host as a function of time after the laser pulse for three different temperatures. This time dependence is much stronger at higher temperatures.

The fluorescence lifetime of the bismuth germanate emission in the doped sample exhibits a similar temperature dependence to that in the undoped sample

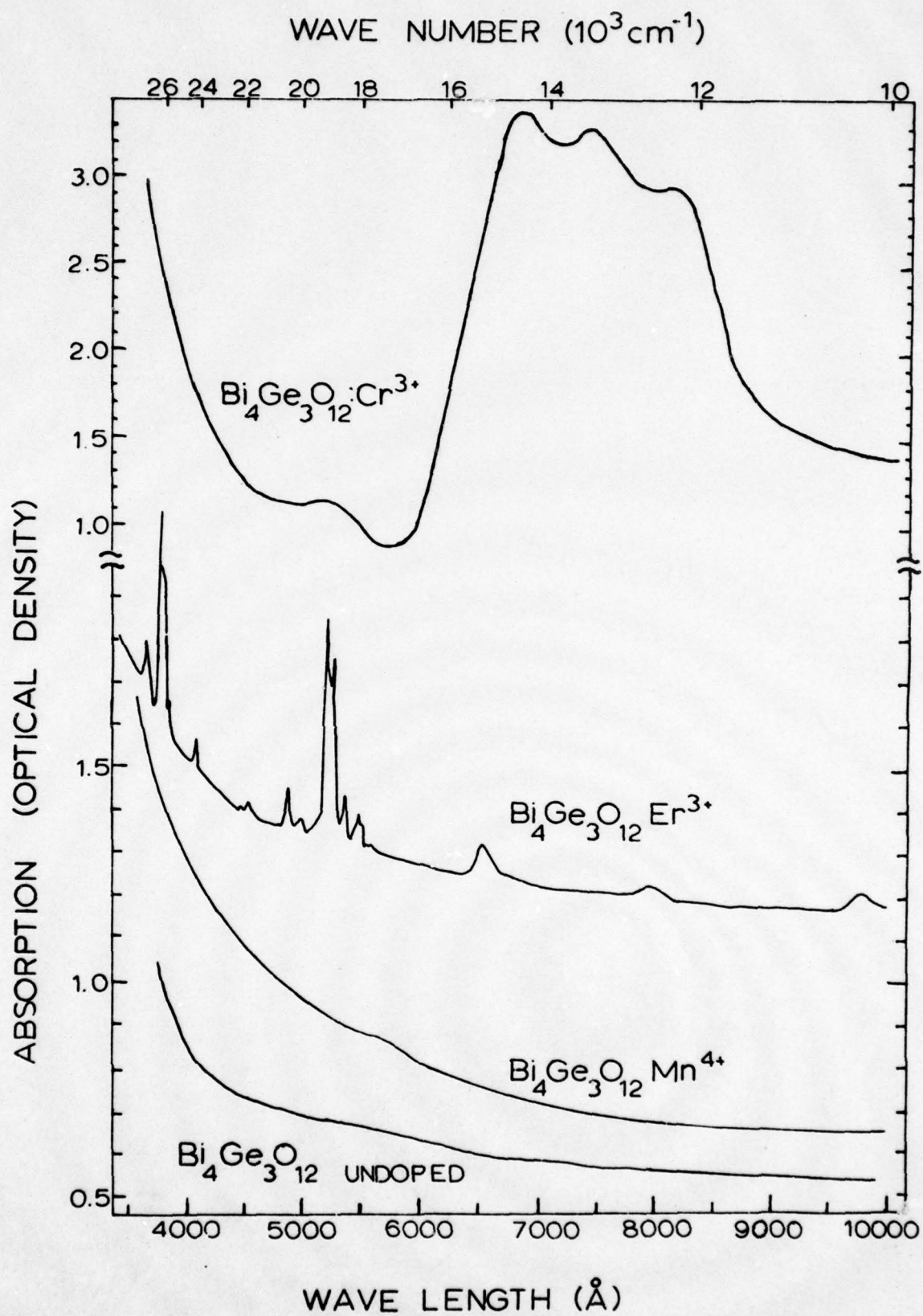


Figure 1. Absorption spectra of  $\text{Bi}_4\text{Ge}_3\text{O}_{12}$  Crystals at Room Temperature

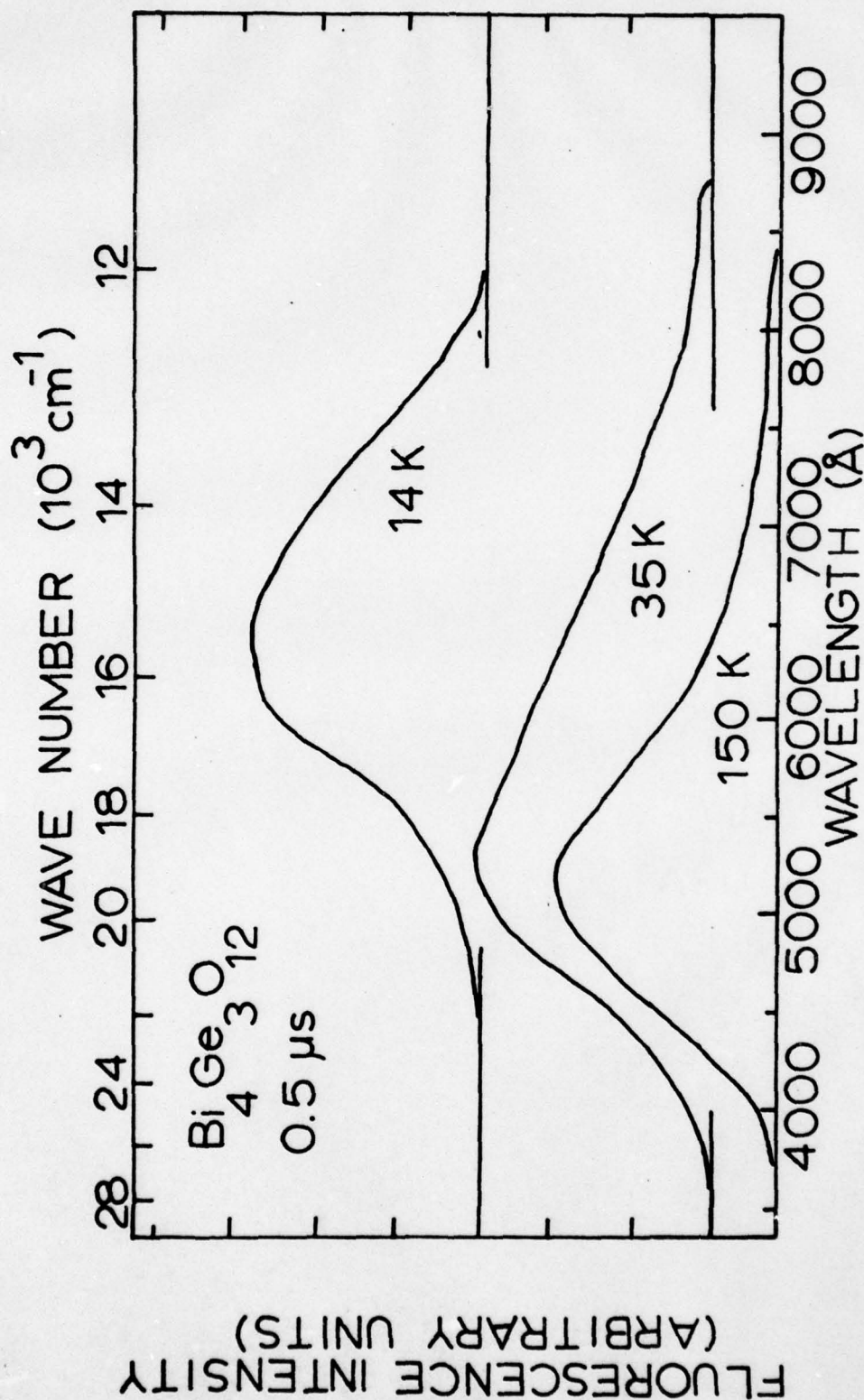


Fig 2. Fluorescence spectrum of  $\text{Bi}_4\text{Ge}_3\text{O}_{12}$  0.5  $\mu\text{s}$  After the Laser Pulse at Three Different Temperatures



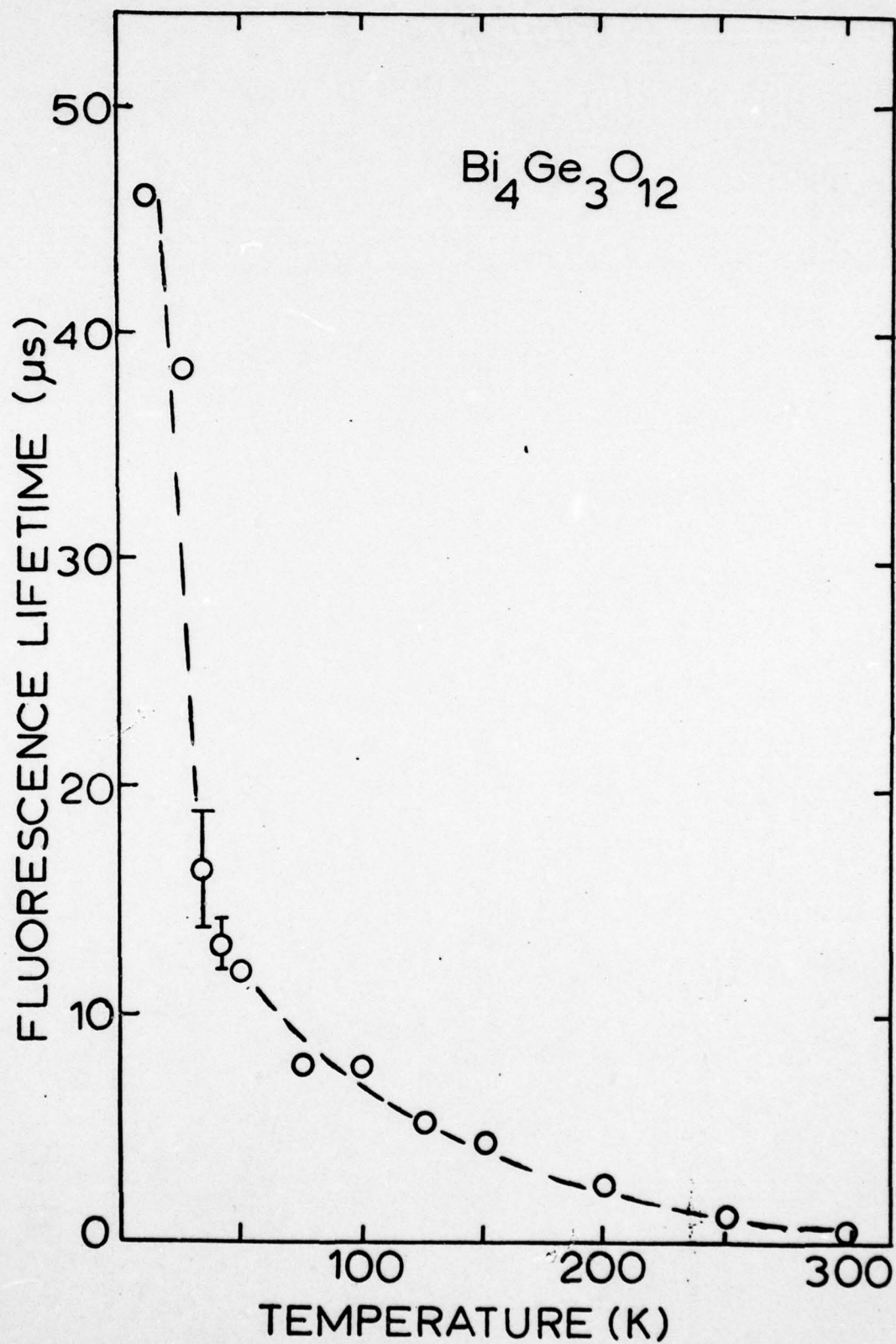


Figure 3. Temperature Dependence of the Fluorescence Lifetime of Bi<sub>4</sub>Ge<sub>3</sub>O<sub>12</sub> with Nitrogen Laser Excitation. Typical Error Bars are Shown for Two Points

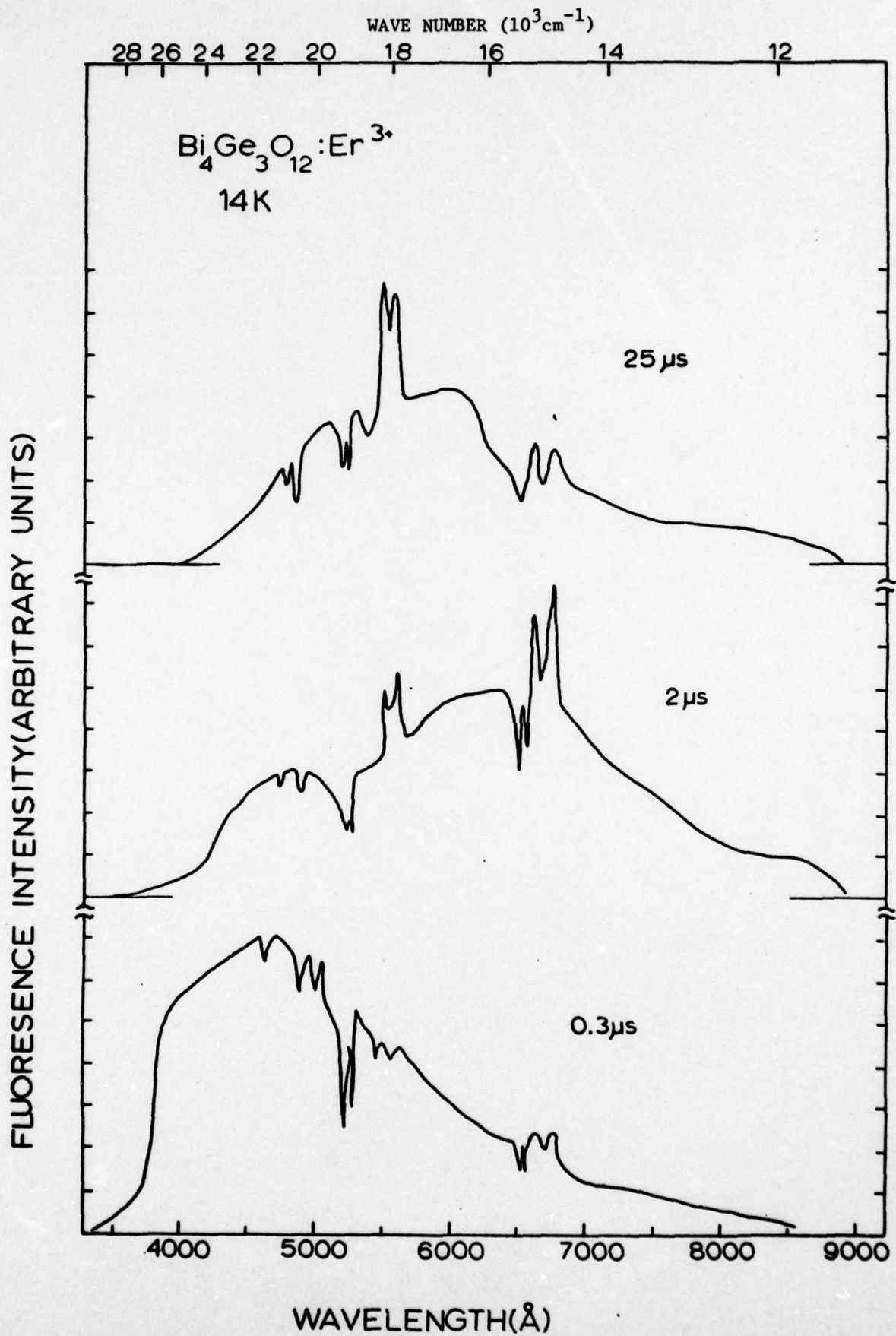


Figure 4. Fluorescence Spectrum of Bismuth Germanate Doped with 1%  $\text{Er}^{3+}$  at 14 K for Three Different Times After the Laser Excitation Pulse

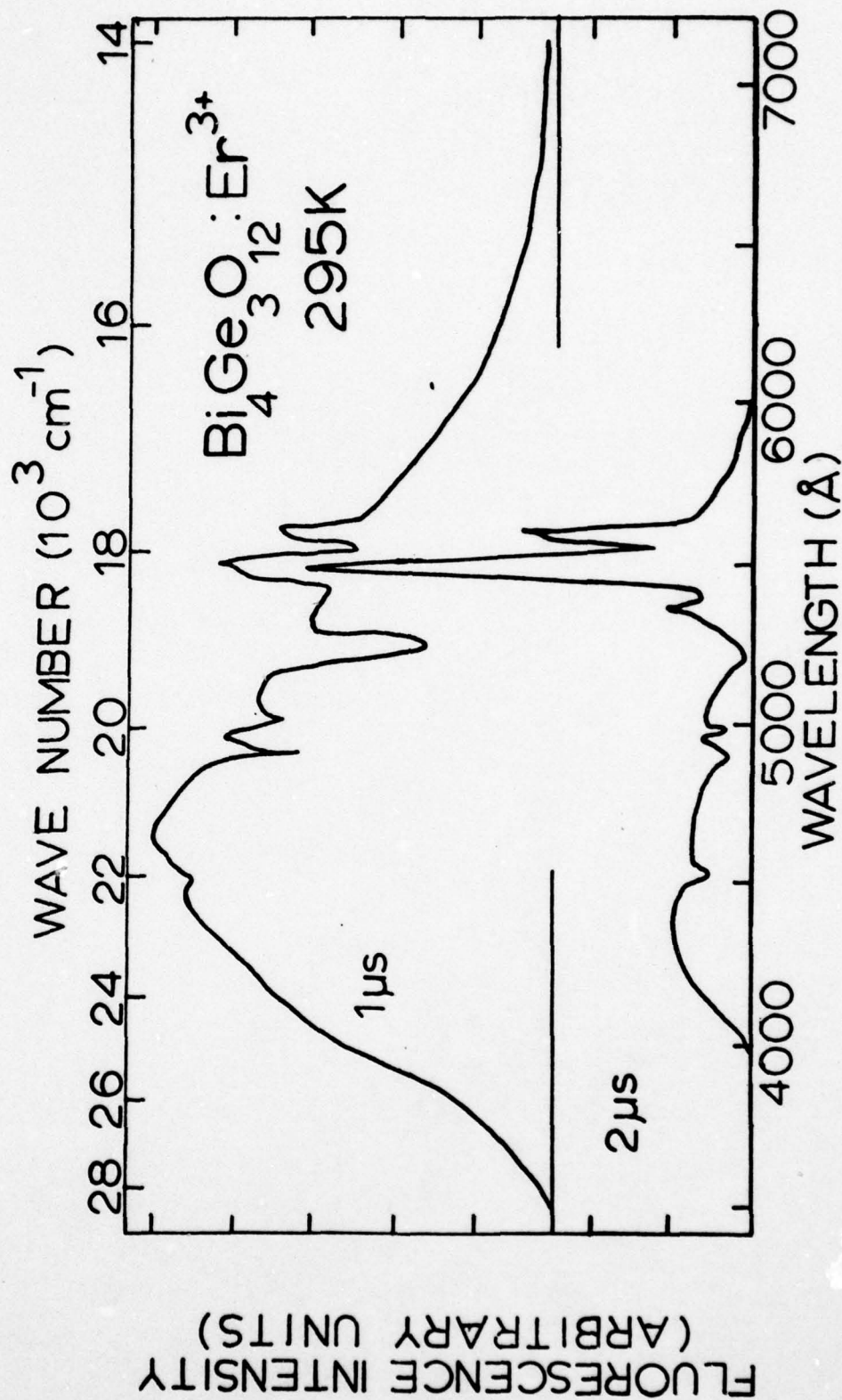


Figure 5. Fluorescence Spectrum of Bismuth Germanate Doped with 1%  $\text{Er}^{3+}$  at Room Temperature for Two Different Times After the Laser Excitation Pulse



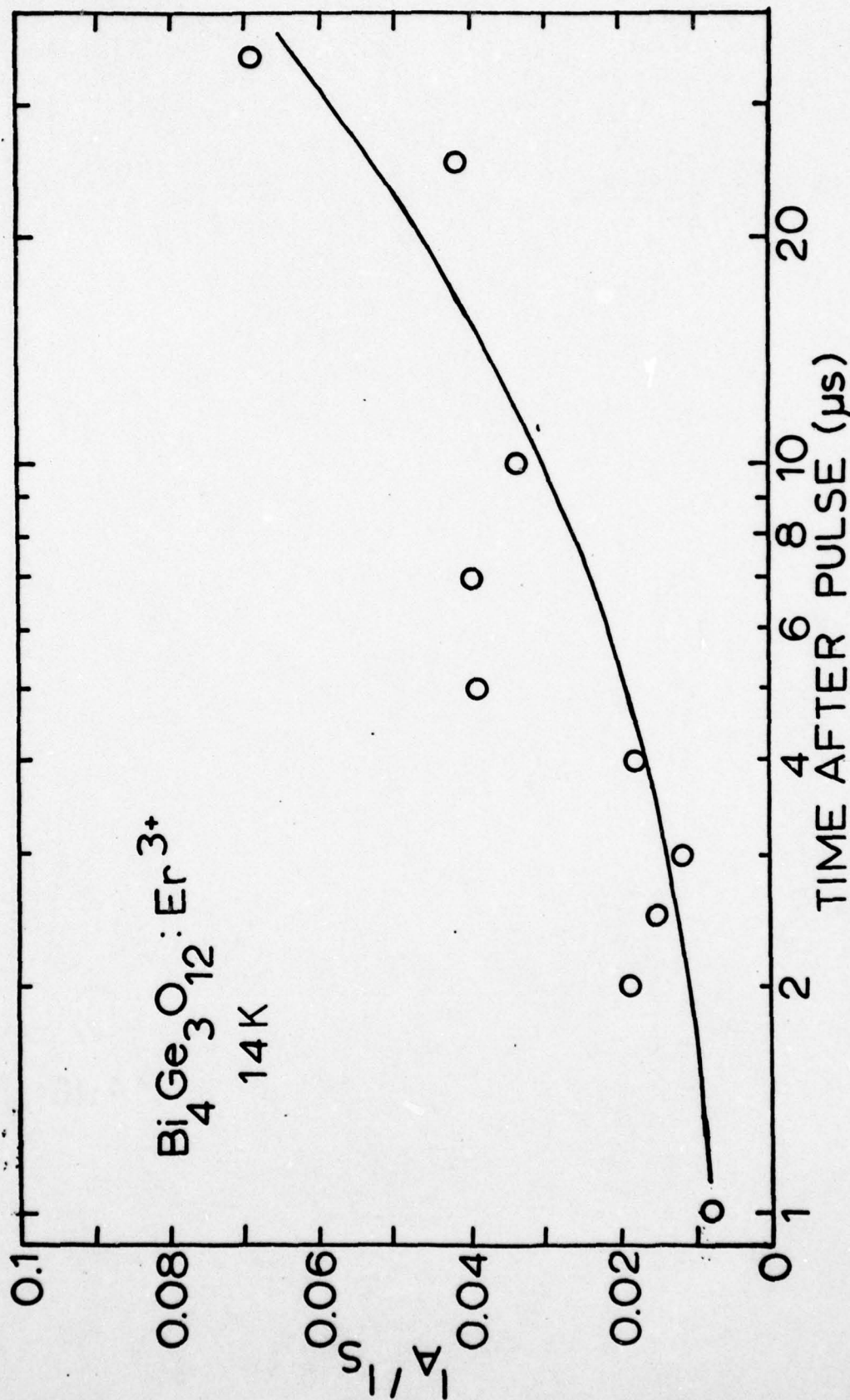


Figure 6. Ratio of Er<sup>3+</sup> and Host Integrated Fluorescence Intensities as a Function of Time After the Laser Pulse at 14 K. See Text for Explanation of Theoretical Lines

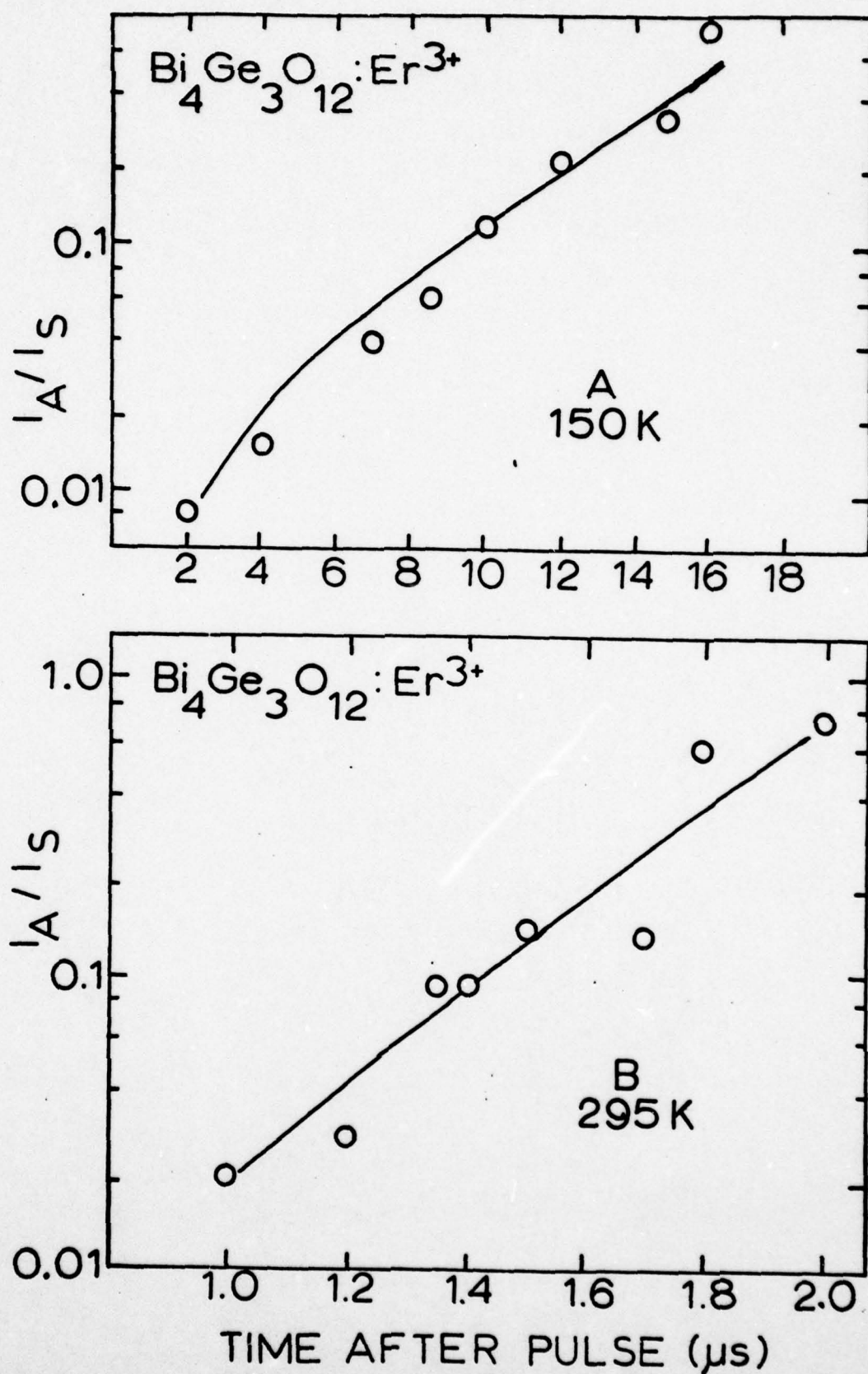


Figure 7. Ratio of  $\text{Er}^{3+}$  and Host Integrated Fluorescence Intensities as a Function of Time After the Laser Pulse for Two Temperatures. See Text for Explanation of Theoretical Lines

except that it is quenched to shorter values as shown in Fig. 8. It ranges from about 0.25  $\mu\text{sec}$  at room temperature to about 12.8  $\mu\text{sec}$  at 14 K. The  $\text{Er}^{3+}$  lifetime is about 22  $\mu\text{sec}$  from room temperature to near 150 K. Between 150 and about 75 K it exhibits a double exponential decay with the shorter decay time being of the order of 12  $\mu\text{sec}$  and the longer close to 20  $\mu\text{sec}$ . At lower temperatures the  $\text{Er}^{3+}$  lifetime again becomes single exponential and increases to about 32  $\mu\text{sec}$  at 14 K. Fig. 9 shows the temperature dependence of the ratios of the fluorescence intensities of the activator ions and the host emission at 5  $\mu\text{sec}$  after the laser pulse. This ratio decreases between room temperature and about 75 K and then shows an increase as temperature is lowered further. The differences in the inverses of the host fluorescence decay times of the doped and undoped samples is also shown in Fig. 9 and exhibits a similar temperature dependence.

### C. Interpretation

The results presented in the previous section indicate that energy transfer is occurring from the bismuth germanate host to the  $\text{Er}^{3+}$  activator ions. It appears that the transfer characteristics are distinctly different at high and low temperatures with the transition occurring between 50 and 125 K. This can be correlated with temperature dependent changes in the host emission spectrum and fluorescence decay time.

The basic mechanism for energy transfer can be best determined by analyzing the time dependent data shown in Figs. 6 and 7. Assuming a simple two level system for both the host and activator transitions, the rate equations describing the time dependences of the excited state populations are

$$\frac{dn_s}{dt} = W - \beta_s n_s - \omega_{sa} n_s \quad (1)$$

$$\frac{dn_a}{dt} = \beta_{sa} n_s - \beta_a n_a \quad (2)$$

Here  $n_s$  and  $n_a$  are the concentrations of excited host sensitizer states and excited



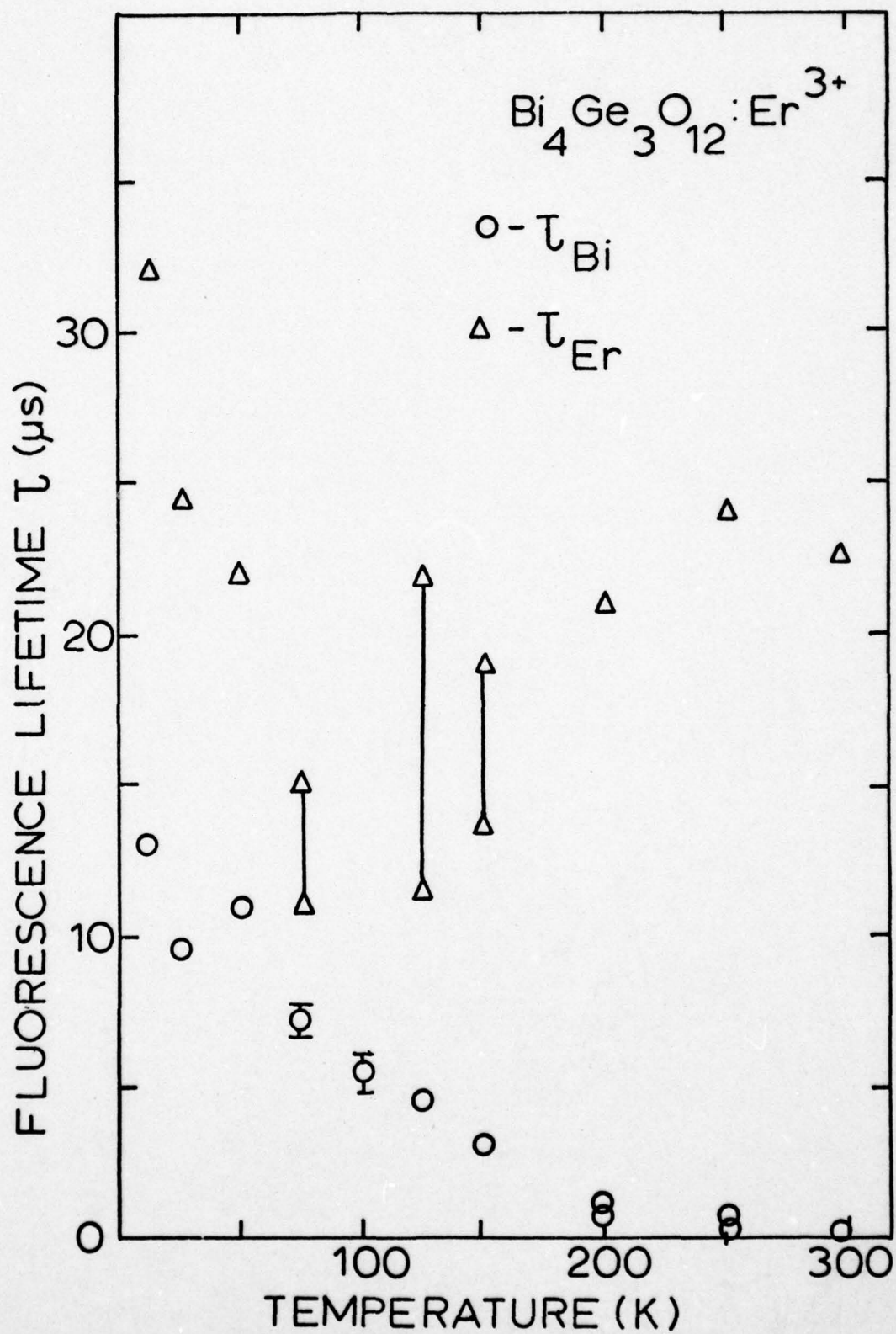


Figure 8. Temperature Dependences of the Fluorescence Lifetimes

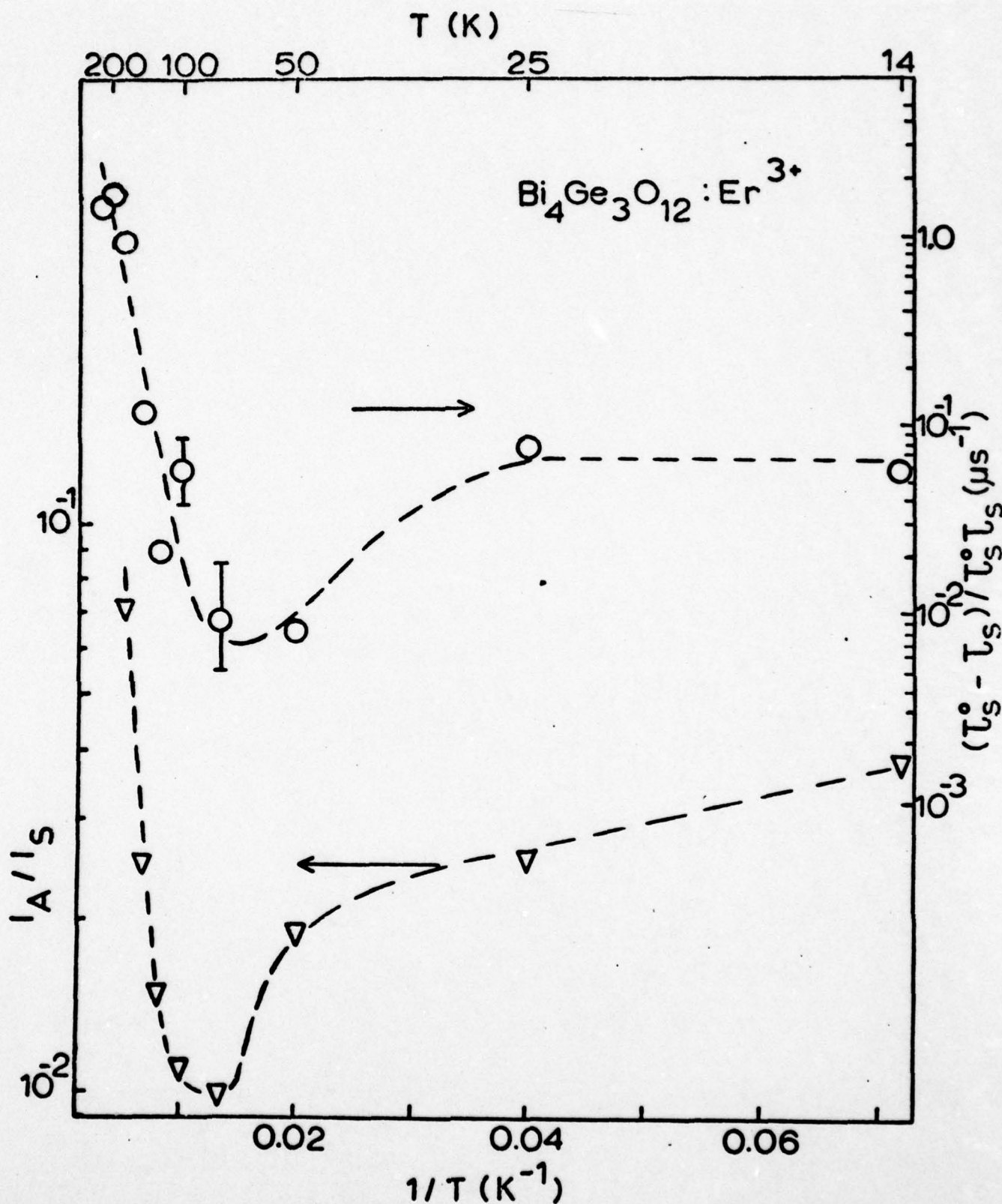


Figure 9. Temperature Dependence of the Ratio of  $\text{Er}^{3+}$  and Host Integrated Fluorescence Intensities 5  $\mu\text{sec}$  After the Pulse ( $\nabla$ ). Temperature Dependence of the Difference in the Inverses of the Fluorescence Lifetimes of the Doped and Undoped Samples (O).

activators,  $\tau_s$  and  $\tau_a$  are the fluorescence decay rates of the sensitizer and activator sites, respectively, and  $W$  is the pumping rate of the sensitizers. For this case any direct pumping of the activator ions can be neglected and  $W$  can be treated as a delta function.  $\omega_{sa}$  is the energy transfer rate. Because of the large difference in energy between the activator emission and the host absorption, no back transfer from activator to host is present. Equations (1) and (2) can be solved and the results fit to the data shown in Figs. 6 and 7 treating  $\omega_{sa}$  as an adjustable parameter.

First, consider the high temperature data shown in Fig. 7. Attempts were made to fit the data assuming a variety of different time dependences for the energy transfer rate. At both room temperature and 150 K it was found that a good fit to the data could only be obtained if the transfer rate was taken to be independent of time. The solutions to Eqs. (1) and (2) in this case give

$$I_a/I_s \propto n_a/n_s = \omega_{sa} (\beta_s + \omega_{sa} - \beta_a)^{-1} \{ \exp[(\beta_s + \omega_{sa} - \beta_a)t] - 1 \}. \quad (3)$$

The best fits to the data obtained with this equation are shown as solid lines in the figure and the values of  $\omega_{sa}$  are listed in Table I.

At low temperature it was not possible to fit the data with the same model. Instead, it was found that the best fit to the data was obtained with an energy transfer rate which varied as  $t^{-1/2}$ . If this is written explicitly as  $\omega_{sa} = 1/2 \gamma t^{-1/2}$  in Eqs. (1) and (2), their solution is then

$$I_a/I_s \propto n_a/n_s = \gamma \int_0^{t^{1/2}} \exp[-(\beta_s - \beta_a)x^2 - \gamma x] dx \exp[(\beta_s - \beta_a)t + \gamma t^{1/2}]. \quad (4)$$

This can be integrated numerically with the use of a computer and the resulting best fit to the data is shown as a solid line in Fig. 5. The value of  $\gamma$  used to obtain this fit is listed in Table I.



TABLE I  
MODEL FITTING PARAMETERS

Primary Parameters	Secondary Parameters	Theoretical Estimate
$\gamma = 0.2 \text{ } \mu\text{sec}^{-1/2}$	$R_o = 10 \text{ } \text{\AA}$	$R_o = 10 \text{ } \text{\AA}$
$\omega_{sa}(295\text{K}) = 1.0 \text{ } \mu\text{sec}^{-1}$	$D(295\text{K}) = 1.7 \times 10^{-8} \text{ cm}^2/\text{sec}$	
$\omega_{sa}(150\text{K}) = 0.058 \text{ } \mu\text{sec}^{-1}$	$D_o = 9.5 \times 10^{-8} \text{ cm}^2/\text{sec}$	
$\Delta E = 352 \text{ cm}^{-1}$	$l(295\text{K}) = 20 \text{ } \text{\AA}$	
	$t_H(295\text{K}) = 1.5 \times 10^{-8} \text{ sec}$	
	$N(295\text{K}) = 27$	

At high temperatures where the energy transfer rate is time independent the lifetime ratios plotted in Fig. 9 should equal the energy transfer rate. Also, the intensity ratios at long time after the laser pulse shown in this figure are proportional to the transfer rate with the proportionality constant being the ratio of the activator and host radiative decay rates. At room temperature the values of  $\omega_{sa}$  determined from these measurements are consistent with that determined from fitting the time-resolved data. The temperature dependences shown in Fig. 9 between room temperature and 125 K can be fit with an expression of the form  $\omega_{sa}(T) = \omega_{sa} \exp(-\Delta E/kT)$  with  $\Delta E = 352 \text{ cm}^{-1}$ . Such a direct comparison cannot be made at low temperatures since the transfer rate is time dependent.

#### D. Discussion and Conclusions

The time independent energy transfer rate found to be consistent with the data at high temperatures is indicative of a multistep energy migration process. The  $t^{-1/2}$  dependence found for the transfer rate at low temperatures is indicative of a single step dipole-dipole interaction mechanism among randomly distributed sensitizer-activator pairs. This can be attributed to having a trapped host exciton at low temperatures and thermally activated exciton migration at high temperatures. The exponential temperature dependence observed at high temperatures and the nearly constant temperature dependence at low temperature are also consistent with this model. The  $\text{Er}^{3+}$  absorption lines appearing in the host emission band as shown in Fig. 4 shows that some radiative energy transfer is taking place. However, corrections were made for this in analyzing the data and it is a small effect compared to the radiationless transfer processes.

If a single step dipole-dipole interaction mechanism is assumed at low temperatures, the observed energy transfer rate can be expressed as [6]

$$\gamma = \frac{4}{3} \pi^3 R_o^3 C_a (\tau_s^o)^{-1/2} \quad (5)$$

where  $R_0$  is the critical interaction distance and  $C_a$  is the concentration of activators. Using the measured energy transfer rate at 14 K gives a value of about  $10^8$  Å for  $R_0$ . A theoretical prediction for the critical transfer rate can be obtained from spectral considerations using the expression [6]

$$R_0 = [5.86 \times 10^{-25} \phi_s^0 \Omega / (n \bar{\nu}_{sa})^4].$$

Here  $\phi_s^0$  is the quantum efficiency of the sensitizer,  $n$  is the refractive index of the host,  $\Omega$  is the overlap integral of the sensitizer emission spectrum and the activator absorption spectrum,  $\bar{\nu}_{sa}$  is the average wave number in the region of spectral overlap, and the numerical factor includes terms for unit conversion and for averaging over the randomly oriented dipoles. Taking the bismuth germanate quantum efficiency to be unity results in a predicted value of about  $10^8$  Å for  $R_0$  which is consistent with the observed value. These values for the critical interaction distance are equal to about two and a half times the nearest Bi-Bi spacing. However, both the theoretical and experimentally measured values for  $R_0$  are upper limit estimates and the actual value may be somewhat smaller.

At high temperature the rate for energy transfer by exciton diffusion can be expressed as [ ]

$$\omega_{sa} = 4\pi D R C_a \quad (7)$$

where  $D$  is the diffusion coefficient,  $R$  is the trapping radius, and  $C_a$  is the concentration of activator traps. If  $R$  is taken to be a nearest neighbor Bi-Bi spacing of  $3.88^8$  Å, the diffusion coefficient at room temperature is found to be about  $1.7 \times 10^{-8} \text{ cm}^2 \text{ sec}^{-1}$ . For thermally activated hopping motion the diffusion coefficient can be expressed as

$$D = D_0 e^{-\Delta\epsilon/kT}. \quad (8)$$

Using the observed thermal activation energy, the value of  $D_0$  is found to be  $9.5 \times 10^{-8} \text{ cm}^2 \text{ sec}^{-1}$ . Rough estimates for the exciton diffusion length, hopping time,



and number of steps in the random walk can be found from the following expressions:

$$l = \sqrt{D\tau_s^0} , \quad (9)$$

$$t_H = d^2/(6D) , \quad (10)$$

$$N = \tau_s^0/t_H . \quad (11)$$

The hopping distance,  $d$ , can be approximated as the nearest neighbor Bi-Bi distance.

At room temperature this leads to the values listed in Table I.

The thermal variation of the fluorescence lifetime in the undoped sample above 75K is also consistent with an exciton migration model. In this case the trapping occurs at some unknown type of defect site and the quenching of the lifetime is expressed as

$$1/\tau_s^0 = 1/\tau_s' + \omega_{st}^0 e^{-\Delta\epsilon/kT} . \quad (12)$$

In this case the lifetime data can be fit with a thermal activation energy of the order of  $350 \text{ cm}^{-1}$  and an intrinsic decay time of about 8  $\mu\text{sec}$  which is consistent with the results for the doped sample. The quenching rate is similar in both samples indicating the concentration of defect quenching sites in the undoped sample is of the same order of magnitude as the concentration of  $\text{Er}^{3+}$  in the doped sample.

The sharp increase in lifetime below 50 K must be explained by a much smaller thermal activation energy. Since our measurements do not go to low enough temperatures to observe the maximum decay time, it is not possible to fit these data. However, the previous work of Moncorgé, et al. [5] indicate that the thermal activation energy in this region is about  $23 \text{ cm}^{-1}$ . Because of the spectral changes that occur in this region, this activation energy appears to be associated with excitation into a different electronic state. The decrease in energy transfer around 50 K indicates that the higher energy electronic level is not as effective in transferring energy as is the lower energy state except at very high temperatures where

strong thermal activation is present. The double exponential decays observed for the  $\text{Er}^{3+}$  emission in 75-150 K range also indicate the transition from a region of weak energy transfer to one of efficient energy transfer.

In summary, the results reported here indicate that at low temperatures the excited electronic state of the bismuth germanate crystal is immobile and transfers its energy to randomly distributed activator ions by a single step process. At somewhat higher temperatures thermal activation into a higher energy electronic state occurs which is less efficient in transferring its energy to  $\text{Er}^{3+}$  activators through a single step process but in which thermally activated exciton migration can occur. Other results show that radiationless quenching occurs above room temperature [4]. This model is similar to those used to explain host-sensitized energy transfer in rare earth doped  $\text{YVO}_4$  and  $\text{CaWO}_4$  crystals and the value of the exciton diffusion coefficient is similar to those found on these other systems [8],[9]. Since the nature of the luminescent center in  $\text{Bi}_4\text{Ge}_3\text{O}_{12}$  is not completely established [10],[11], it is not possible to describe in any more detail the mechanism for exciton hopping. Mongorgé, et al. [5] from their study of undoped bismuth germanate also concluded that exciton migration takes place in this system but they attributed the lifetime quenching at very low temperatures to the exciton migration which is not consistent with the results reported here on a doped sample. Finally, it should be noted that the magnitude of the transfer rate at room temperature for the erbium doped bismuth germanate crystal is of the same order of magnitude as the room temperature transfer rates found by Risefeld, et al. [12],[13] for energy transfer from bismuth to  $\text{Nd}^{3+}$ ,  $\text{Eu}^{3+}$  and  $\text{Sm}^{3+}$  at 1% concentration in germanate glass. However, in the latter case  $\text{Bi}^{3+}$  was present in concentrations of only 1% and thus, it is not clear whether or not efficient migration of energy among the bismuth luminescent centers is taking place.

## REFERENCES

- [1] L. F. Johnson and A. A. Ballman, J. Appl. Phys. 40 (1969) 297.
- [2] S. K. Dickinson, R. M. Hilton, and H. G. Lipson, Mater. Res. Bull. 7 (1972) 181.
- [3] A. A. Kaminskii, D. Schultze, B. Hermoneit, S. E. Sarkisov, L. Li, J. Bohm, P. Reiche, R. Ehlert, A. A. Mayer, V. A. Lomonov, and V. A. Balashov, Phys. Stat. Sol. (A) 33 (1976) 737.
- [4] M. J. Weber and R. R. Monchamp, J. Appl. Phys. 44 (1973) 5495.
- [5] R. Moncorgé, B. Jacquier and G. Boulon, J. Luminescence 14 (1976) 337.
- [6] Th. Förster, Ann. Physik 2 (1948) 55; Z. Naturforsch. 4a (1949) 321; Discussions Faraday Soc. 27 (1959) 7.
- [7] R. C. Powell and Z. G. Soos, J. Luminescence 11 (1975) 1.
- [8] C. Hsu and R. C. Powell, J. Luminescence 10 (1975) 273; G. E. Venikouas and R. C. Powell, J. Luminescence 16 (1978) 29.
- [9] M. J. Treadaway and R. C. Powell, J. Chem. Phys. 61 (1974) 4003; M. J. Treadaway and R. C. Powell, Phys. Rev. B11 (1975) 862; R. G. Peterson and R. C. Powell, J. Luminescence 16 (1978) 285.
- [10] R. Moncorgé, B. Jacquier, G. Boulon, F. Gaume-Mahn and J. Janin, J. Luminescence 12/13 (1976) 467.
- [11] G. Blasse and A. Brill, J. Chem. Phys. 50 (1969) 2974.
- [12] R. Reisfeld, N. Lieblisch, L. Boehm, and B. Barnett, J. Luminescence 12/13 (1976) 749.
- [13] R. Reisfeld and Y. Kalisky, Chem. Phys. Lett. 50 (1977) 199.

### IV.4 Laser Time-Resolved Studies of Exciton Migration in Doped

#### Lithium Niobate

##### A. Introduction

Pulsed laser time-resolved spectroscopy techniques have recently been shown to be useful in elucidating the characteristics of host-sensitized energy transfer



in rare earth doped phosphors.<sup>1-3</sup> A model based on thermally activated migration and trapping of molecular excitons has been developed to explain the results. In this paper we report the results of further investigations of this type on the system  $\text{LiNbO}_3:\text{Eu}^{3+}, \text{Cr}^{3+}$ . The data are again found to be consistent with host exciton migration and trapping, but in this case no thermal activation is required. These results are especially interesting in light of the importance of lithium niobate in electro-optic and laser host applications.

The samples studied were good optical quality single crystals of  $\text{LiNbO}_3$  one of which was undoped and the other contained  $3.70 \times 10^{19} \text{ cm}^{-3} \text{ Eu}^{3+}$  and  $1.27 \times 10^{17} \text{ cm}^{-3} \text{ Cr}^{3+}$  ions. These were mounted on the cold finger of a cryogenic refrigerator which was able to control sample temperature between about 10 K and room temperature. The excitation was provided by a nitrogen laser which produced a pulse about 10 nsec in duration and less than 4 Å wide centered at 3771 Å. The fluorescence was analyzed by a one-meter monochromator, detected by an RCA C31034 photomultiplier tube, and averaged by a boxcar integrator triggered by the laser pulse. The time resolution was of the order of 10 nsec.

#### B. Experimental Results

Fig. 1 shows the absorption band edge of the  $\text{LiNbO}_3$  host crystal. The nitrogen laser excitation pumps the low energy side of this band. The host fluorescence appears as a broad band centered at about 5000 Å. In the doped sample, additional sets of sharp lines are observed in the visible region of the spectrum characteristic of  $\text{Eu}^{3+}$  absorption transitions. No absorption characteristic of  $\text{Cr}^{3+}$  could be observed due to the low concentration of chromium ions in the sample. The host fluorescence emission in the doped sample is similar to that observed in the undoped sample. In addition, the doped sample exhibits a broad, intense emission centered

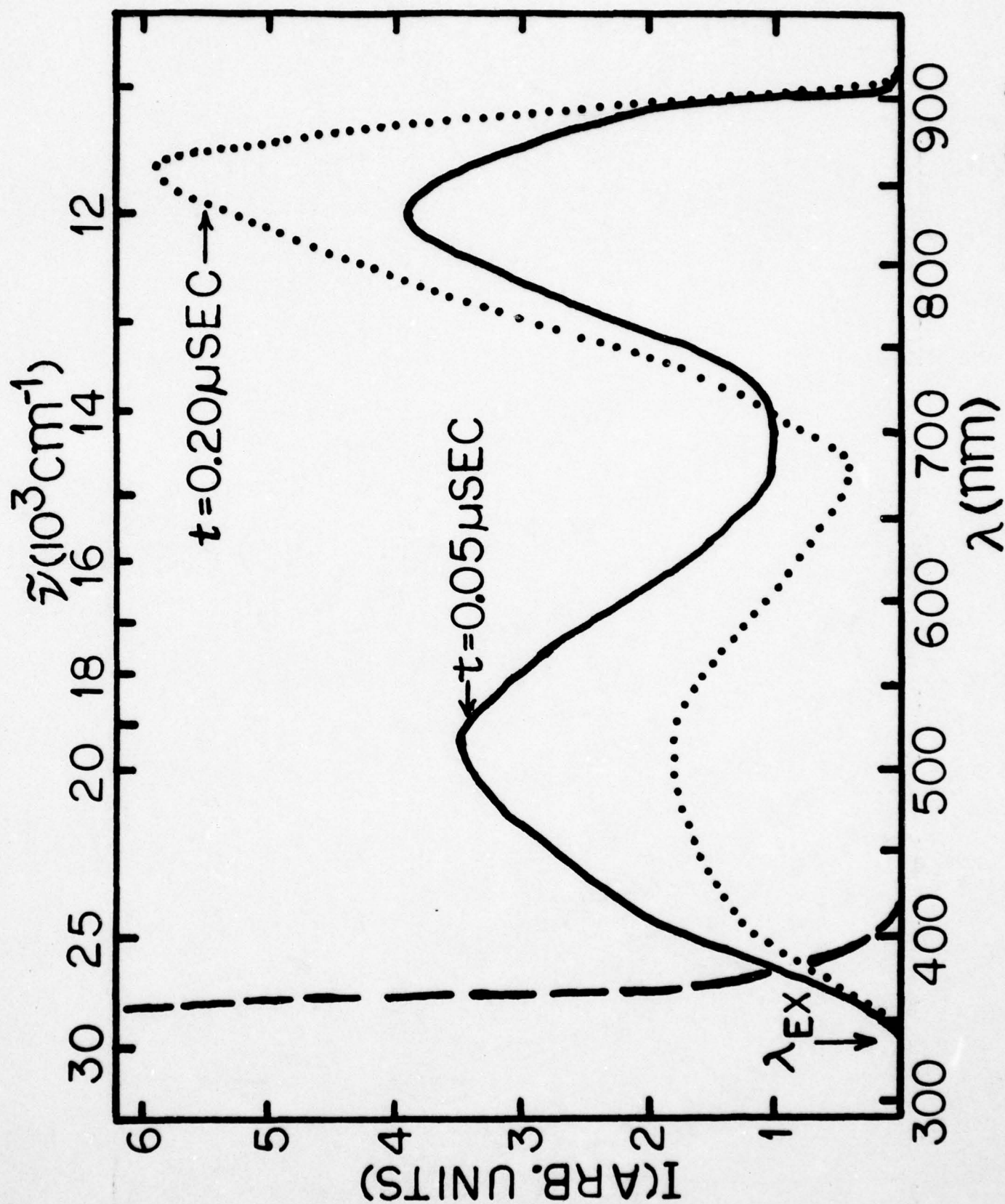


Figure 1. Room Temperature Absorption Spectrum (----) of  $\text{LiNbO}_3:\text{Eu}^{3+}, \text{Cr}^{3+}$  at Two Times After Pulsed Laser Excitation at  $3371 \text{ Å}$  (—, ....).

near 8650 Å. This type of emission has been reported previously<sup>4-7</sup> with the peak position varying from 8400 Å to 9200 Å and is attributed to the  $^4T_2 - ^4A_2$  transition of  $Cr^{3+}$ . The variation in observed peak position is probably due to the strong variation in experimental sensitivity in this spectral range. Both the phototube and monochromator sensitivities decrease above 8500 Å which accounts for the sharp decrease in the low energy side of the peak shown in the uncorrected spectra of Fig. 1. The spectra in Fig. 1 were taken at two different times after the laser pulse and it is obvious that as time increases the  $Cr^{3+}$  emission intensity increases with respect to that of the host. Similar results are obtained at low temperatures. Trivalent europium emission can be seen as very weak, sharp lines on the low energy side of the host emission band at low temperatures at intermediate times after the excitation pulse.

Fig. 2 shows the variation of the integrated fluorescence intensity ratio of the chromium band to the host band as a function of time after the laser pulse at both high and low temperatures. The distortion of the observed  $Cr^{3+}$  emission band due to the spectral response of the equipment is taken into account in these relative intensity measurements. At both temperatures the intensity ratios vary approximately exponentially with a characteristic constant of about  $6.7 \mu\text{sec}^{-1}$ .

The temperature dependence of the fluorescence lifetimes are shown in Fig. 3. The lifetime of the fluorescence in the undoped sample is independent of temperature. In the doped sample the host fluorescence lifetime is still independent of temperature but is less than the lifetime in the undoped sample. The chromium fluorescence lifetime decreases greatly between 14 K and room temperature. All of the fluorescence decays were observed to be purely exponential. The europium fluorescence was too weak to be resolved from the host fluorescence in order to make lifetime measurements.

### C. Interpretation of Results

The results presented above indicate that energy is being transferred from the host to the  $Cr^{3+}$  impurity ions. The most general model for describing the kinetics



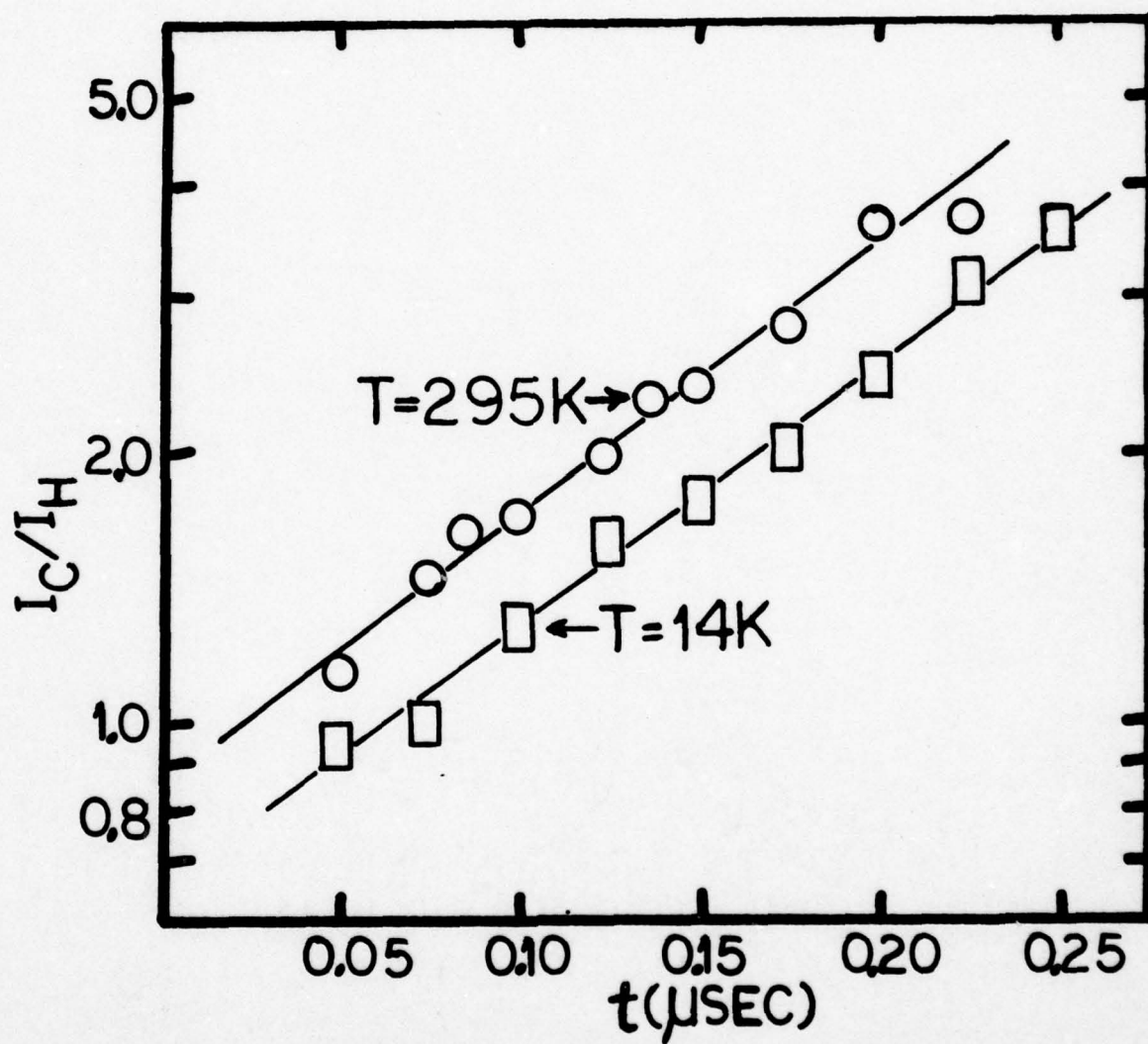


Figure 2. Ratios of the Integrated Fluorescence Intensities of the Chromium and Host Emissions as a Function of Time After the Laser Pulse at High and Low Temperatures for  $\text{LiNbO}_3:\text{Eu}^{3+}, \text{Cr}^{3+}$

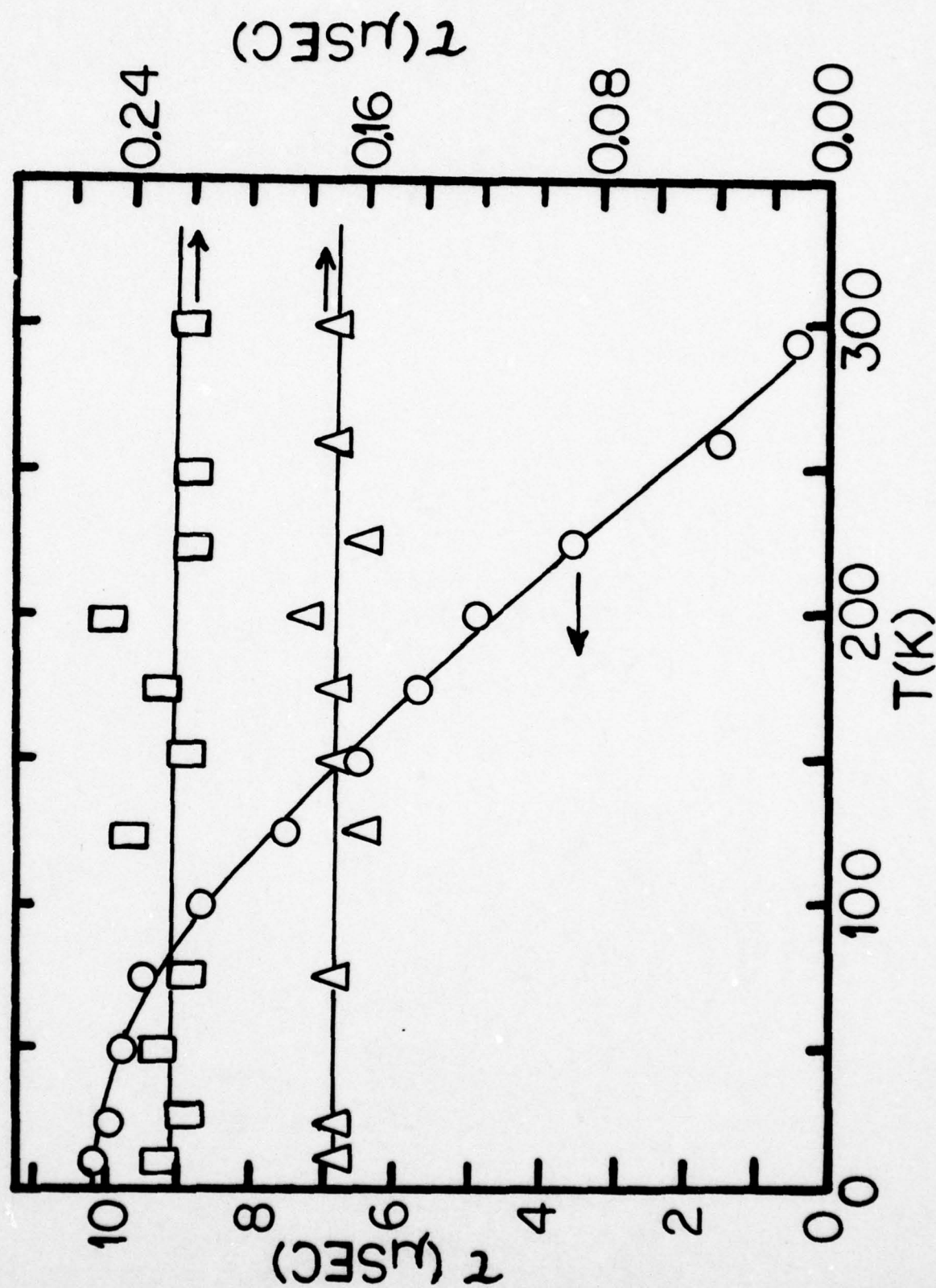


Figure 3. Temperature Dependences of the Fluorescence Lifetimes in  $\text{LiNbO}_3$  and  $\text{LiNbO}_3:\text{Eu}^{3+}$ ,  $\text{Cr}^{3+}$  Crystals.  $\square$ -Undoped Host;  $\Delta$ -Undoped Host;  $\circ$ - $\text{Cr}^{3+}$

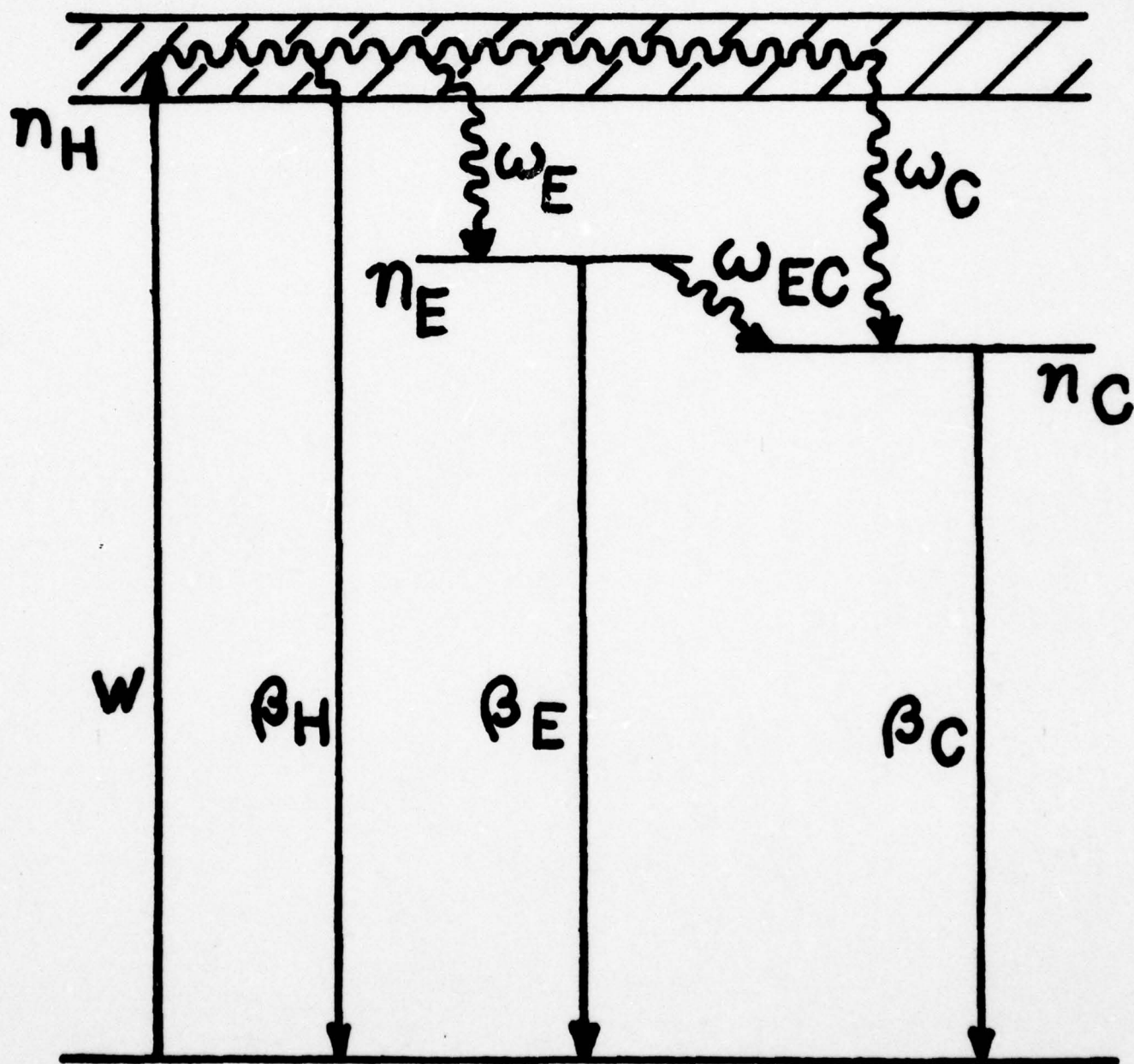


Figure 4. Model for Explaining Host-Sensitized Energy Transfer in  $\text{LiNbO}_3:\text{Eu}^{3+}, \text{Cr}^{3+}$ . See Text for Definition of Parameters



of energy transfer in this case is shown in Fig. 4. The rate equations for the populations of excited states of the host  $n_H$ , the europium ions  $n_E$ , and the chromium ions  $n_C$  are

$$\frac{dn_H}{dt} = W - \beta_H n_H - \omega_C n_H - \omega_E n_H \quad (1)$$

$$\frac{dn_E}{dt} = \omega_E n_H - \omega_{EC} n_E - \beta_E n_E \quad (2)$$

$$\frac{dn_C}{dt} = \omega_C n_H + \omega_{EC} n_E - \beta_C n_C \quad (3)$$

$W$  is the pumping rate of the host and  $\beta_H, \beta_E$  and  $\beta_C$  are the intrinsic decay rates of the host, europium, and chromium ions, respectively. The energy transfer rates from the host to the two types of impurity ions are  $\omega_E$  and  $\omega_C$  while the transfer rate from the europium to the chromium ion is  $\omega_{EC}$ . All back transfer processes have been neglected since there are large Stokes shifts involved in each step and no experimental evidence is observed for any back transfer.

Treating the laser pumping pulse as a delta function and assuming the transfer rates to be independent to time, Eqs. (1) - (3) can be solved to give

$$n_H(t) = n_H(0) e^{-\beta t} \quad (4)$$

$$n_E(t) = n_H(0) \left( \frac{\omega_E}{\beta' - \beta} \right) (e^{-\beta t} - e^{-\beta' t}) \quad (5)$$

$$n_C(t) = n_H(0) \left( \frac{\omega_{EC} \omega_E}{\beta' - \beta} \right) \left[ \left( \frac{\omega_C}{\omega_{EC} \omega_E} + \frac{1}{\beta' - \beta} \right) e^{-\beta t} - \left( \frac{\beta_C - \beta}{(\beta' - \beta)(\beta_C - \beta')} \right) e^{-\beta' t} \right. \\ \left. + \left( \frac{\beta_C - \beta}{(\beta' - \beta)(\beta_C - \beta')} - \frac{\omega_C}{\omega_{EC} \omega_E} - \frac{1}{\beta' - \beta} \right) e^{-\beta_C t} \right] \quad (6)$$

where  $\beta = \beta_H + \omega_E + \omega_C$  and  $\beta' = \beta_E + \omega_{EC}$ . The important ratio for explaining the experimental results is

$$\frac{I_c(t)}{I_H(t)} = \left( \frac{\beta_c^{\text{rad}}}{\beta_H^{\text{rad}}} \right) \left( \frac{\omega_{EC} \omega_E}{\beta_c - \beta} \right) \left[ \left( \frac{\omega_c}{\omega_{EC} \omega_E} + \frac{1}{\beta' - \beta} \right) - \left( \frac{\beta_c - \beta}{(\beta' - \beta)(\beta_c - \beta')} \right) e^{-(\beta' - \beta)t} \right. \\ \left. + \left( \frac{\beta_c - \beta}{(\beta' - \beta)(\beta_c - \beta')} - \frac{\omega_c}{\omega_{EC} \omega_E} - \frac{1}{\beta' - \beta} \right) e^{-(\beta_c - \beta)t} \right] \quad (7)$$

where  $\beta^{\text{rad}}$  indicates the radiative transition rate. From lifetime measurements it is possible to estimate the rate parameters and thus simplify Eq. (7) to give

$$I_c(t)/I_H(t) = (\beta_c^{\text{rad}}/\beta_H^{\text{rad}}) \left[ \omega_E/(\beta_H + \omega_E) \right] \exp \left[ (\beta - \beta_c)t \right]. \quad (8)$$

Equation (8) predicts an exponential time dependence for the ratios of the integrated fluorescence intensities of the  $\text{Cr}^{3+}$  ions and the host which is consistent with the results shown in Fig. 2. The characteristic constant needed for the exponential fit of the data is  $6.7 \mu\text{sec}^{-1}$  at both high and low temperatures. Equation (8) predicts that this constant should be the difference in the decay times of the host in the doped sample and the  $\text{Cr}^{3+}$  ions. This is measured to be about  $5.8 \mu\text{sec}^{-1}$  at low temperature and  $5.2 \mu\text{sec}^{-1}$  at high temperature. These values are very close to the measured value, especially considering the simplicity of the model used.

The quenching of the host fluorescence decay time in the doped sample can be attributed to transfer of energy to the dominant type of impurity ions  $\text{Eu}^{3+}$ . This is measured to be  $1.3 \mu\text{sec}^{-1}$  at all temperatures. If the mechanism of energy transfer is the diffusion and trapping of host excitons, the transfer rate can be expressed as

$$\omega_E = 4\pi D R C_E \quad (9)$$

where  $D$  is the diffusion coefficient,  $C_E$  is the concentration of  $\text{Eu}^{3+}$  ions, and  $R$  is the trapping radius. Assuming a nearest neighbor trapping radius and

using the measured transfer rate in Eq. (9) gives a value of  $D = 9.6 \times 10^{-8} \text{ cm}^2 \text{ sec}^{-1}$ . The diffusion length is given by  $l = \sqrt{6D\tau_H^0}$  where  $\tau_H^0$  is the fluorescence decay time of the host in the undoped sample. For this case the value of  $l$  is found to be about  $36\text{\AA}$ . The time for each step in the exciton's random walk can be approximated by  $t_H = a^2/(6D)$  where  $a$  is the hopping distance. Assuming the latter to be approximately the closest distance between Nb ions gives a hopping time of about  $2.8 \times 10^{-9} \text{ sec}$ . The number of steps in the random walk is  $n = \tau_H^0/t_H = 79$ .

There is no way to directly measure the rate of the europium to chromium energy transfer step in this model. However, it must be greater than the host decay rate in the doped sample in order for the simplified expression in Eq. (8) to be valid. Since this gives a good fit to the data, a lower bound of  $\omega_{EC} \geq 6 \mu\text{sec}^{-1}$  can be established for this rate constant. A theoretical estimate can be obtained for this transfer rate from the expression<sup>8</sup>

$$\omega_{EC} = (4/3)\pi^{3/2} R_0^3 C_c (\tau_E^0)^{-1/2} \quad (10)$$

where  $R_0$  is the critical transfer distance. This has been determined by Weber to be about  $22\text{\AA}$  for transfer between  $\text{Eu}^{3+}$  and  $\text{Cr}^{3+}$  ions in a glass host.<sup>9</sup> It is not expected to be significantly greater than this in other hosts. If this value is used in Eq. (10) along with a  $\text{Eu}^{3+}$  lifetime of about  $500 \mu\text{sec}$  characteristic of  $5_{D_0}$  emission, a value of  $\omega_{EC}$  is found which is far too small to satisfy the lower bound requirement established earlier for relevant times. This may indicate that transfer is taking place from a higher excited  $\text{Eu}^{3+}$  level before relaxation to the  $5_{D_0}$  state.

#### D. DISCUSSION AND CONCLUSIONS

The time-resolved spectroscopy results obtained on host-sensitized energy transfer in  $\text{LiNbO}_3:\text{Eu}^{3+}$ ,  $\text{Cr}^{3+}$  were shown above to be consistent with the



predictions of a model based on host exciton diffusion with the activator ions acting as exciton traps and including an efficient transfer of energy from the  $\text{Eu}^{3+}$  to the  $\text{Cr}^{3+}$  activator ions. The fact that the host fluorescence decay was observed to be purely exponential is indicative of a multistep migration process and justifies the assumption of a time independent rate parameter for the host energy transfer in the time regime of interest. The fact that the energy transfer rate is found to be independent of temperature implies that no thermal activation is necessary for migration to occur. The strong temperature dependence observed for the fluorescence decay time of the  $\text{Cr}^{3+}$  emission together with the lack of temperature dependence of the host fluorescence decay time and the known characteristics of  $\text{Eu}^{3+}$  in other hosts indicate that the measured decay time at  $8600\text{\AA}$  is the intrinsic decay time of  $\text{Cr}^{3+}$  emission in this host even though it is pumped through energy transfer instead of being directly excited. In order for the predictions of this model to fit the results, the transfer rate between the  $\text{Eu}^{3+}$  and  $\text{Cr}^{3+}$  ions must be very large compared to the other rates in the model. It is also taken to be independent of time in order to simplify the solutions of the rate equations, but this is not a necessary assumption since it does not appear in the final expression used to fit the results. In fact, this transfer rate will almost certainly exhibit the time dependence indicated in Eq. (10) which is characteristic of a single-step, dipole-dipole energy transfer process between randomly distributed sensitizers and activators. Quantitative estimates of this rate parameter indicate that energy transfer may be taking place from a higher excited  $\text{Eu}^{3+}$  level before relaxation to the lowest metastable state. Studies involving directly pumping the  $\text{Eu}^{3+}$  ions will be carried out in the future in an attempt to clarify this interesting point.

The model used to interpret these data is similar to the utilized previously<sup>1-3</sup> in explaining host-sensitized energy transfer in other rare earth doped crystals

such as  $\text{CaWO}_4$ ,  $\text{YVO}_4$ , and  $\text{Bi}_4\text{Ge}_3\text{O}_{12}$ . The value of the exciton diffusion coefficient found here is similar to that found for the bismuth germanate host but somewhat larger than the values for the tungstate and vanadate hosts. In the three crystals investigated previously, it was found that a thermal activation energy was required for exciton migration to occur. This was attributed to a self-trapping of the excitons in  $\text{CaWO}_4$  and  $\text{YVO}_4$  and excitation from an immobile to a mobile electronic state in  $\text{Bi}_4\text{Ge}_3\text{O}_{12}$ . The fact that no activation is required for exciton mobility in  $\text{LiNbO}_3$  indicates that the interaction causing the exciton to migrate is stronger than the electron-lattice relaxation rate in the excited state. The excitons in the tungstate and vanadate hosts are excited electronic states localized on the  $\text{WO}_4^{2-}$  and  $\text{VO}_4^{3-}$  molecular ions. In  $\text{Bi}_4\text{Ge}_3\text{O}_{12}$  the exact nature of the exciton is not well understood, but it appears to be associated with excited electronic states of the  $\text{Bi}^+$  ions. In  $\text{LiNbO}_3$ , the exciton can be identified as an excited electronic state of the  $\text{NbO}_6$  octahedron. It has been found that the optical absorption and emission characteristics of  $\text{NbO}_6$  octahedra are similar in different host crystals and the transition giving rise to the observed spectra involve a charge transfer of an electron from a molecular orbital consisting mainly of a 2p oxygen orbital to a  $t_{2g}$  molecular orbital localized mainly on the  $\text{Nb}^{5+}$  ion<sup>10</sup>. There is a considerable Stokes shift between the absorption and emission bands indicating significant lattice relaxation in the electronic excited state. This would generally lead to the requirement of thermal activation for energy transfer to occur to a neighboring  $\text{NbO}_6$  complex. However, the extended nature of the excited  $t_{2g}$  molecular orbital can lead to significant overlap with the wave functions of electrons in neighboring complexes, which facilitates energy transfer through resonant exchange interaction.

Figure 5 shows a schematic representation of the  $\text{LiNbO}_3$  structure in terms of an ordered array of oxygen octahedra with central ions alternating between Nb, Li, and vacancies.<sup>11</sup> This is a simplified picture of the real lattice since the actual oxygen octahedra are distorted and the central ions offset such that it is very difficult to draw a three dimensional picture of the true structure. However, this indicates the possible path for  $\text{NbO}_6$  exciton diffusion. The nearest Nb-Nb separation is  $3.765\text{\AA}$ . The trivalent rare earth and transition metal impurity ions can enter the lattice substitutionally for either the  $\text{Li}^+$  or  $\text{Nb}^{3+}$  ions. The mechanism of required charge compensation is not known. The closest Nb-Li separation in the lattice is about  $3.01\text{\AA}$ .

The rate of energy transfer by exchange interaction between two ions separated by a distance  $R$  can be approximated by the simple expression.<sup>12</sup>

$$\omega(\text{ex}) = (\tau_H^0)^{-1} \exp[(2 R'_0/L)(1-R/R'_0)] \quad (11)$$

where  $R'_0$  is a critical transfer distance which depends on the wave function overlap and  $L$  is an effective Bohr radius. For nearest neighbor transfer between  $\text{NbO}_6$  octahedra the exciton hopping time obtained in the last section can be predicted if  $R'_0 = 6\text{\AA}$  and  $L$  is taken to be half the Nb-oxygen spacing. It is not possible to theoretically determine a value for  $R'_0$  without a knowledge of the wavefunctions and their overlap. Also, superexchange through intermediate oxygen ions may complicate the picture. However, the magnitude of  $R'_0$  obtained by fitting the simple expression in Eq. (11) to the experimental results appears to be a physically reasonable value. The trapping step at an activator site may also take place by an exchange mechanism with a similar transfer rate and critical transfer distance.

The spectra of  $\text{Cr}^{3+}$  impurity ions in  $\text{LiNbO}_3$  has been studied extensively and explained by Glass using crystal field considerations.<sup>4-7</sup> His results



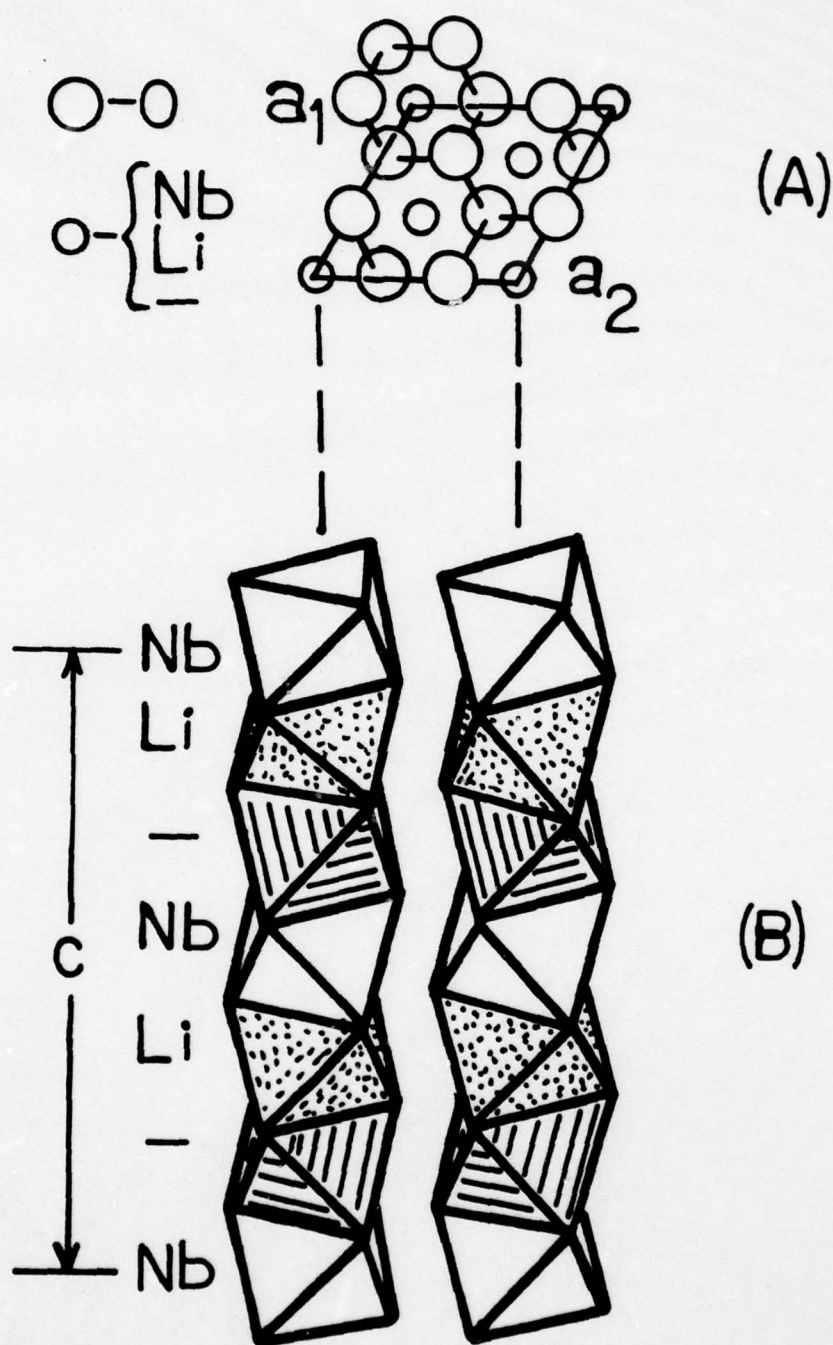


Fig. 5. Schematic representation of the  $\text{LiNbO}_3$  lattice in terms of the oxygen octahedra. (A) View down the  $c$ -axis. (B) View perpendicular to the  $c$ -axis. Note that in the actual structure the octahedra are distorted as discussed in reference 11.

indicate that the  $\text{Cr}^{3+}$  ions most probably substitute for the  $\text{Nb}^{5+}$  ions non-local charge compensation. Although there is a charge transfer transition below  $\sim 3500\text{\AA}$ , the extremely small concentration of  $\text{Cr}^{3+}$  in our sample results in negligible direct pumping effects. Glass calculated a radiative decay time for the  ${}^4\text{T}_2$  level of  $\sim 11\mu\text{sec}$  which is close to the measured fluorescence decay time at low temperatures. He measured a quantum efficiency for the  ${}^4\text{T}_2$  level of about unity at 4.2K and 0.05 at room temperature which is consistent with our measurements of the temperature dependence of the fluorescence decay time if we define quantum efficiency as  $\eta(T) = \tau(4.2\text{K})^{-1}/\tau(T)^{-1}$ .

The spectra of several trivalent rare earth ions have also been studied in  $\text{LiNbO}_3$  crystals.<sup>13,14</sup> The major interest in these investigations has been the study of laser action in an electro-optic host so that optical modulation and second harmonic generation can be obtained in the laser material itself instead of requiring an additional optical component. Another possible advantage of  $\text{LiNbO}_3$  as a laser host which is indicated by the present work is increased pumping of the active ions through host absorption and energy transfer. A possible problem with rare earth doped lithium niobate as a laser material is the efficient quenching of the rare earth fluorescence by only a very small concentration of  $\text{Cr}^{3+}$  impurities. In standard, commercial  $\text{LiNbO}_3$  small amounts of impurities such as chromium, iron, manganese, etc. are almost always found. Another problem of  $\text{LiNbO}_3$  as a laser host is the formation of localized irregularities in the refractive index due to optical pumping. These act as scattering centers and can inhibit stimulated emission and other nonlinear optical effects.<sup>15</sup>

The optical damage centers mentioned above form the basis for utilizing  $\text{LiNbO}_3$  as a material for three dimensional holographic information storage.<sup>16,17</sup> Although much work has been done in characterizing the photorefractive effects in this material, they are still not completely understood.<sup>7,18-23</sup> It is

clear that the most sensitive effects involve the creation of free electrons by optical excitation of one type of trapping site, photoconduction of the electrons in an applied electric field, and trapping at a second type of trapping site. The traps can be chemical impurities such as iron or structural imperfections such as vacancies. Without an applied field, the charge displacement is extremely small. The maximum peak in the photoconductivity spectrum occurs at  $\sim 4000\text{\AA}$  and it decreases sharply at higher energies. It is suggested that this peak is due to host absorption from the valence band to a conduction band consisting of mainly Nb orbitals. Higher energy excitation involves the charge transfer transition mentioned previously and does not result in photoconductivity. However, exciting further into the ultraviolet ( $\sim 2650\text{\AA}$ ) by two-photon processes again results in the generation of free electrons and optical damage centers.<sup>7,23</sup> The presence of  $\text{Cr}^{3+}$  impurities does not appear to enhance the optical damage properties directly as  $\text{Fe}^{2+}$  impurities do, but  $\text{Cr}^{3+}$  ions have been useful in enhancing the refractive index changes produced by two-photon absorption by providing a real intermediate state.

The fact that no change in valence state of the  $\text{Eu}^{3+}$  ions is observed between absorption and emission indicates that the host-sensitized transfer we report here is not associated with free carrier migration. Since exciton diffusion involves the migration of a coupled electron-hole pair without an effective charge, it will not directly effect the photorefractive effect of interest in information storage applications. High densities of excitons could cause the formation of free electrons and holes through exciton-exciton interaction ionization. It is not clear that this would have any advantage over the excitation techniques now employed, but there may be some advantage gained from pumping into the charge transfer band which is much stronger than the absorption regions now being pumped.



The local polarization due to charge displacement in the optically excited states of impurity ions in  $\text{LiNbO}_3$  can also be used for holographic recording applications.<sup>21</sup> This has been shown for the  $^4T_2$  state of  $\text{Cr}^{3+}$  to have much lower recording sensitivity than the mechanisms involving the generation of free charge carriers, but it may be useful in applications requiring low power such as modulation in integrated optics systems. In this case, the enhanced pumping of the  $\text{Cr}^{3+}$  ions through host-sensitized energy transfer as shown in this work could be extremely useful.

In conclusion, we find that host exciton migration and trapping at impurity ions occurs in  $\text{LiNbO}_3$  after pumping into the charge transfer band in the near ultraviolet region of the spectrum. This may effect the use of this material in some laser host and holographic storage applications. The efficient transfer of energy between different types of impurity ions is also observed, but the properties of this process are not completely understood and will be studied further.

#### REFERENCES

- [1] M. J. Treadaway and R. C. Powell, J. Chem. Phys. 61, 4003 (1974); Phys. Rev. B11, 862 (1975); R. G. Peterson and R. C. Powell, J. Lumin. 16, 285 (1978).
- [2] C. Hsu and R. C. Powell, J. Lumin. 10, 273 (1975); G. E. Venikouas and R. C. Powell, J. Lumin. 16, 29 (1978).
- [3] D. P. Neikirk and R. C. Powell, J. Lumin., to be published.
- [4] A. M. Glass, J. Chem. Phys. 50, 1501 (1969); J. Appl. Phys. 44, 508 (1973).
- [5] A. Hordvik and H. Schlossberg, Appl. Phys. Lett. 20, 197 (1972); J. Appl. Phys. 44, 509 (1973).

- [6] G. Burns, D. F. O'Kane and R. S. Title, Phys. Lett. 23, 56 (1966).
- [7] D. von der Linde, A. M. Glass, and K. F. Rodgers, J. Appl. Phys. 47, 217 (1976).
- [8] M. Inokuti and F. Hirayama, J. Chem. Phys. 43, 1978 (1965).
- [9] M. J. Weber, Phys. Rev. B4, 2932 (1971).
- [10] G. Blasse and A. Bril, Z. Physik. Chem. 57, 187 (1968).
- [11] S. C. Abrahams, J. M. Reddy, and J. L. Bernstein, J. Phys. Chem. Solids 27, 997 (1966).
- [12] D. L. Dexter, J. Chem. Phys. 21, 836 (1953).
- [13] L. F. Johnson and A. A. Ballman, J. Appl. Phys. 40, 297 (1969).
- [14] A. A. Kaminskii, Soviet Physics - Crystallography 17, 194 (1972);  
V. T. Gabrielyan, A. A. Kaminskii, and L. Li, Phys. Stat. Sol (a) 3, K37 (1970); K. G. Belabaev, A. A. Kaminskii, and S. E. Sarkisov. Phys. Stat. Sol. (a) 28, K17 (1975).
- [15] A. Ashkin, G. D. Boyd, J. M. Dziedzic, R. G. Smith, A. A. Ballman, J. J. Levinstien, and K. Nassau, Appl. Phys. Lett. 9, 72 (1966).
- [16] F. S. Chen, J. T. LaMacchia, and D. B. Frase, Appl. Phys. Lett. 13, 233 (1968).
- [17] H. Kurz, Philips Tech. Rev. 37, 109 (1977) and references therein.
- [18] F. S. Chen, J. Appl. Phys. 40, 3389 (1969).
- [19] J. J. Amodei, RCA Rev. 32, 185 (1971).
- [20] W. D. Johnston, J. Appl. Phys. 41, 3279 (1970).
- [21] A. M. Glass, D. von der Linde, D. H. Auston, and T. J. Negran, J. Elect. Mat. 4, 915 (1975); A. M. Glass and D. von der Linde and A. M. Glass, Appl. Phys. 8, 85 (1975).
- [22] Y. Ohmori, Y. Tasojima, and Y. Inuishi, Japanese J. Appl. Phys. 14, 1291 (1975).

[23] D. von der Linde, O. F. Schirmer, and H. Kurz, Appl. Phys. 15, 153 (1978).

## V. SITE-SELECTION SPECTROSCOPY RESULTS

### V.I Laser Site-Selection Spectroscopy Investigation of $\text{Eu}^{3+}$ Ions in $\text{YVO}_4$ Crystals

#### A. INTRODUCTION

Narrow-line tunable dye lasers have recently been used as excitation sources for studying energy transfer between ions in solids.<sup>1-7</sup> The high-resolution capabilities have allowed the effects of inhomogeneous broadening to be proved and the fast pulses make it possible to monitor the dynamics of the interaction processes. The new and more-detailed information available from these studies has stimulated interest in developing new theoretical models and methods of interpreting energy-transfer data.<sup>8,9</sup> This paper describes the results of an investigation of energy transfer between trivalent europium ions in yttrium orthovanadate crystals using laser time-resolved-spectroscopy (TRS) techniques.

There has been great interest in  $\text{YVO}_4$  as a material for a variety of optical applications such as a phosphor, a laser host, and an infrared polarizer, because of its mechanical and optical properties. For example,  $\text{YVO}_4$  doped with trivalent Nd has been found to be an excellent laser with a threshold factor of 2 lower than for  $\text{YAlG:Nd}$  (Refs. 10 and 11) and  $\text{YVO}_4:\text{Eu}^{3+}$  is an excellent red phosphor.<sup>12</sup> Thus, it is of practical importance to understand the spectral properties and interactions of trivalent rare-earth ions in this host.

Previous studies of  $\text{YVO}_4:\text{Eu}^{3+}$  have identified the energy levels and transitions of europium<sup>13,14</sup> and characterized the properties of energy transfer from the host to the activator ions.<sup>14,15</sup> In the work reported here, the  $\text{Eu}^{3+}$  ions are directly excited with a pulsed-laser source whose bandwidth is much less than the width of the absorption transition, and the fluorescence emission under these conditions can be resolved into a series of lines originating from



ions in different crystal-field sites. Thus, by tuning the laser wavelength, ions in specific crystal-field sites can be electively excited and energy transfer to ions in other types of sites can be monitored.

#### B. EXPERIMENTAL

A single crystal of yttrium orthovanadate doped with 1.0-at.%Eu<sup>3+</sup> was obtained from Raytheon, Inc. The boule was grown along the crystallographic c axis and a sample of about 5-mm thickness was cut parallel to this direction.

The sample was mounted on the cold finger of a cryogenic refrigerator capable of continuously varying the temperature between about 7 and 300 K. Absorption measurements were made on a Cary 14 spectrophotometer. Fluorescence spectra and decay-time measurements were obtained using a Systems Science and Software tunable dye laser pumped by a NRG pulsed nitrogen laser. The peak power output of the nitrogen laser is about 350 kW and the output of the dye laser with 7-diethylamino-4-methylcoumarin dye is a pulse of about 10 nsec in duration and  $0.46 \text{ cm}^{-1}$  in halfwidth. The sample fluorescence is focused onto the entrance slit of a 1-m Czerny-Turner monochromator capable of resolution in first order of  $0.04\text{\AA}$ . The signal is detected by a cooled RCA C31034 photomultiplier tube, averaged by a boxcar integrator triggered by the nitrogen laser, and displayed on a strip-chart recorder. The time resolution is about 0.5  $\mu\text{sec}$ .

The dye laser was tuned to pump into one of the strong absorption lines of the  ${}^7\text{F}_0 - {}^5\text{D}_2$  transitions located at  $4668.2\text{\AA}$  as shown in Fig. 1. Since the halfwidth of about  $5.5 \text{ cm}^{-1}$  of this line is an order of magnitude greater than the width of the laser, it is possible selectively to excite into different regions of the absorption line. The linewidth has contributions from both homogeneous broadening due to radiationless relaxation to the lower-lying  ${}^5\text{D}_J$

levels and from inhomogeneous broadening due to the presence of ions in slightly different crystal-field sites. The latter effect allows for selective excitation of ions in specific sites by appropriately tuning the laser wavelength.

The fluorescence transition from the  $^5D_0$  metastable state to the lowest Stark component of the  $^7F_1$  level was monitored as the laser was tuned across the absorption line. The emission appeared as a series of several closely spaced sharp lines centered at about 5943 Å. Three of these lines were significantly more intense than the others and their relative intensities vary as the excitation wavelength is changes as shown in Fig. 1. These three lines have halfwidths of about  $1.4\text{ cm}^{-1}$ . The middle- and high-energy lines are separated by  $3.03\text{ cm}^{-1}$  and the middle- and low-energy lines by  $4.75\text{ cm}^{-1}$ .

The fluorescence decay were observed to vary slightly from pure exponentials by an amount which varied with the wavelength of excitation. For conditions giving rise to nearly exponential decays at 14 K the decay times were 472  $\mu\text{sec}$  for the high-energy line, 527  $\mu\text{sec}$  for the middle line, and 503  $\mu\text{sec}$  for the low-energy line. At 122 K, the lifetimes of these fluorescence lines were found to be 440, 501, and 461  $\mu\text{sec}$ , respectively. These measurements are accurate to about  $\pm 10\text{ }\mu\text{sec}$ .

To study energy transfer between trivalent europium ions in different crystal-field sites, the fluorescence spectra of the three emission lines were obtained for different times after the laser pulse. These TRS results were then analyzed by finding the integrated fluorescence intensities at each time. Figure 2 shows the ratios of the intensities of the high- and low-energy emission lines to that of the middle line as a function of time after the laser pulse for high-energy excitation (4667.8 Å) at 11 K. There data are listed in Table I. The accuracy of these data points is equal to or better than 0.02 of the arbitrary units in Fig. 2. The accuracy is greater at shorter times where

the signal-to-noise ratio is better. Similar TRS results are shown in Fig. 3 for low-energy excitation (4669.0Å) at 11 K. In this case, the ratios of the intensities of each line to the total intensity of the three lines are plotted versus time. For other settings of the excitation wavelength, a variety of different time dependences can be obtained for the fluorescence-intensity ratios. Similar measurements were made at numerous temperatures up to 138 K and only a very small increase in intensity ratios with temperature was observed as shown in Fig. 4.

### C. INTERPRETATION

The TRS data shown in Figs. 2 and 3 can be interpreted in terms of the model shown in Fig. 5. The excited-state populations are designated  $n_L$ ,  $n_M$ , and  $n_H$  for low-, middle-, and high-energy levels, respectively. The direct pumping rates of these levels are  $W_L$ ,  $W_M$ , and  $W_H$ , while their intrinsic decay rates are  $B_L$ ,  $B_M$ , and  $B_H$ .  $P_{HL}(t)$ ,  $P_{MH}(t)$ ,  $P_{ML}(t)$ , etc., are the probabilities per unit time for energy transfer between ions in sites giving rise to the low-, high-, and middle-energy lines. The pumping rates for ions in a given type of site depend explicitly on the ground-state concentration of these ions and the energy-transfer probability depend on the ground-state concentration of activator ions. The assumption is made that the ground-state populations of ions in specific sites are equal to the total concentration of these ions. This is a valid assumption at the low-excitation levels used here. The rate equations for the excited state populations are

$$\frac{dn_M}{dt} = W_M - B_M n_M - (P_{MH} + P_{ML}) n_M + P_{HM} n_H + P_{LM} n_L \quad (1)$$

$$\frac{dn_H}{dt} = W_H - B_H n_H - (P_{HM} + P_{HL}) n_H + P_{MH} n_M + P_{LH} n_L \quad (2)$$



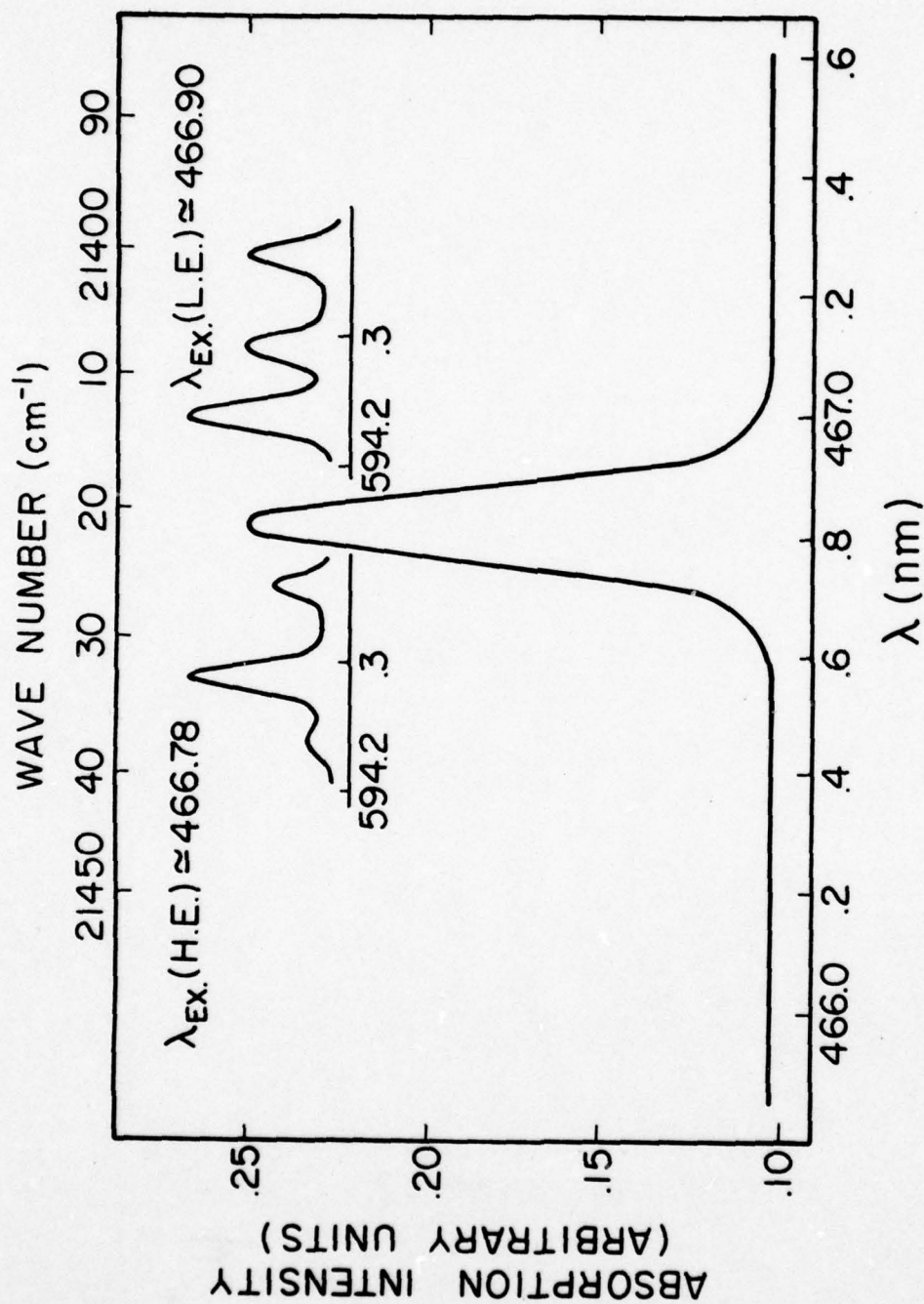


Figure 1. Absorption Line of the  $7F_5-5D_3$  Transition of  $YVO_4:Eu^{3+}$ ; Pumping at the High (H.E.) and Low (L.E.) Energy Side of This Line Produced Fluorescence Depicted on the Upper Two Scaled Down Diagrams

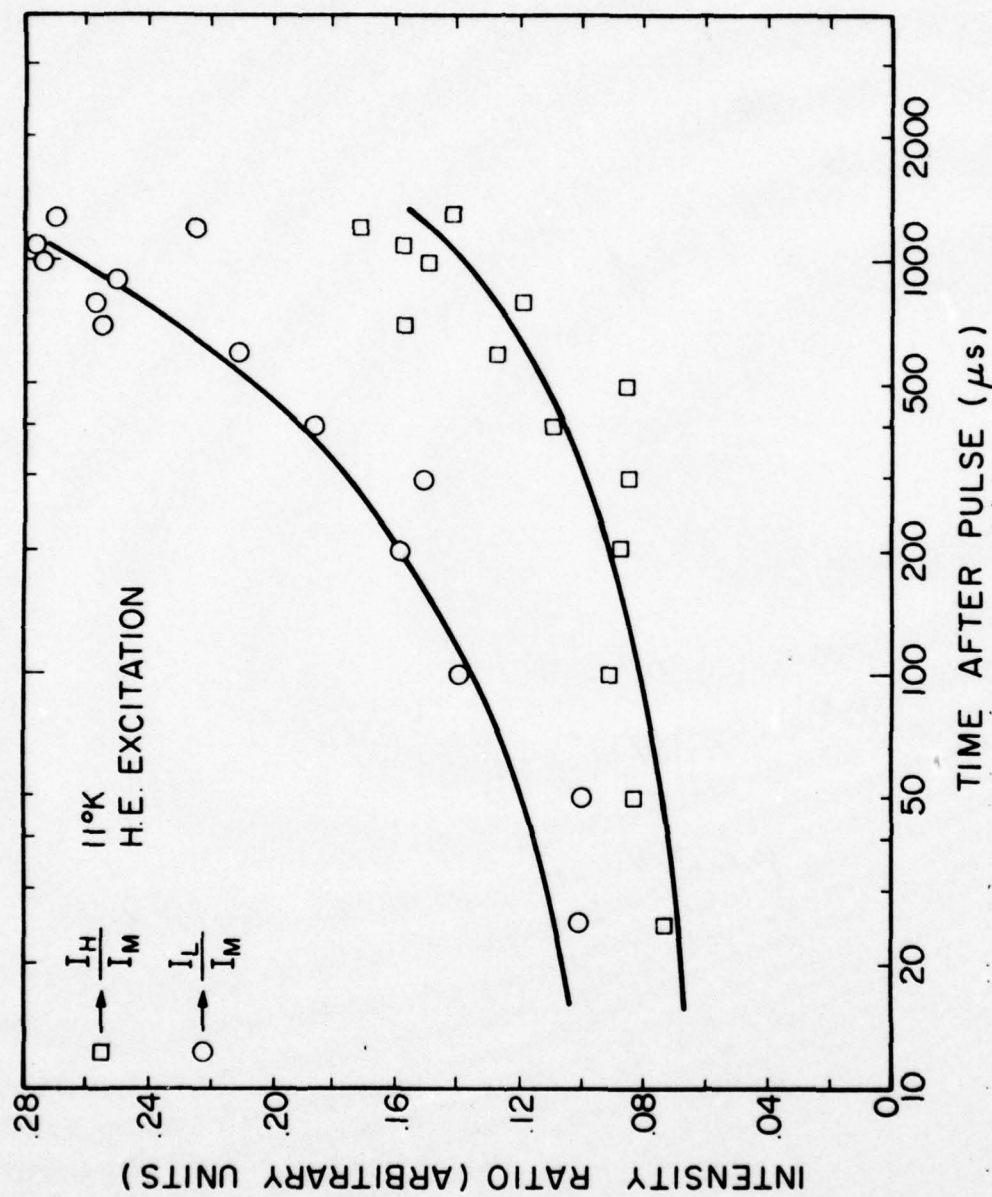


Figure 2. Ratios of the Intensities of the High ( $I_H$ ) and Low ( $I_L$ ) Energy Emission Lines to That of the Middle Line for a Function of Time After the Laser Pulse for 4667.8 Å Excitation at 110°K

TABLE I  
FLUORESCENCE INTENSITY RATIOS FOR HIGH ENERGY EXCITATION  
MEASURED AT DIFFERENT TIMES AFTER PULSE (FIGURE 19)

$\mu\text{s}$ After Pulse	$I_H/I_M$	$I_L/I_M$
25	.074	.103
50	.084	.100
100	.092	.140
200	.088	.160
300	.085	.152
400	.110	.187
500	--	--
600	.128	.212
700	.159	.256
800	.120	.258
900	.153	.251
1000	.150	.275
1100	.158	.277
1200	.172	.225
1300	.142	.270



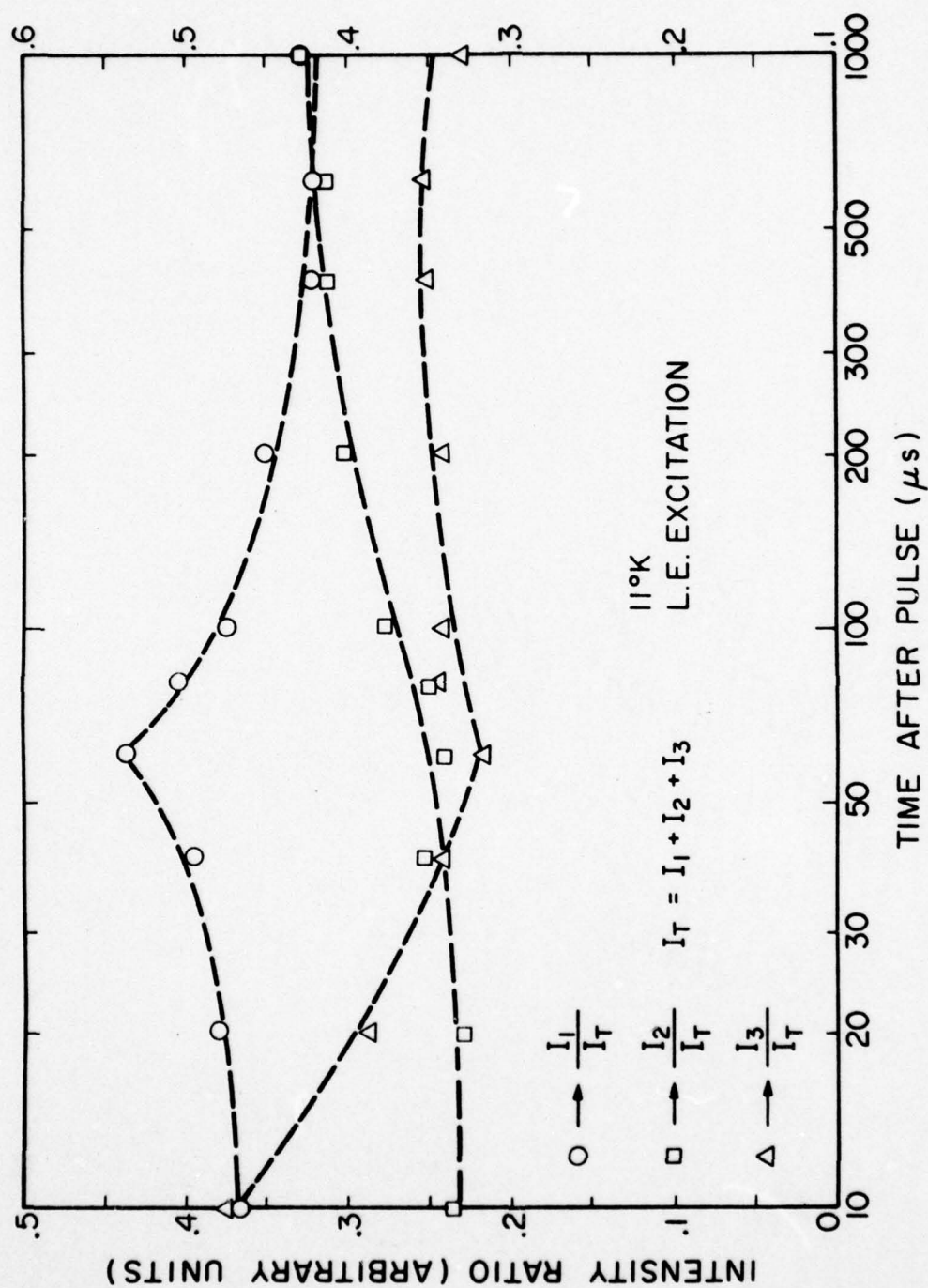


Figure 3. Ratios of the Intensities of High ( $I_H$ ), Middle ( $I_M$ ) and Low ( $I_L$ ) Energy Emission Lines, to the Sum of the Three Intensities as a Function of Time After the Laser Pulse for 4669.0Å Excitation at  $11^\circ\text{K}$

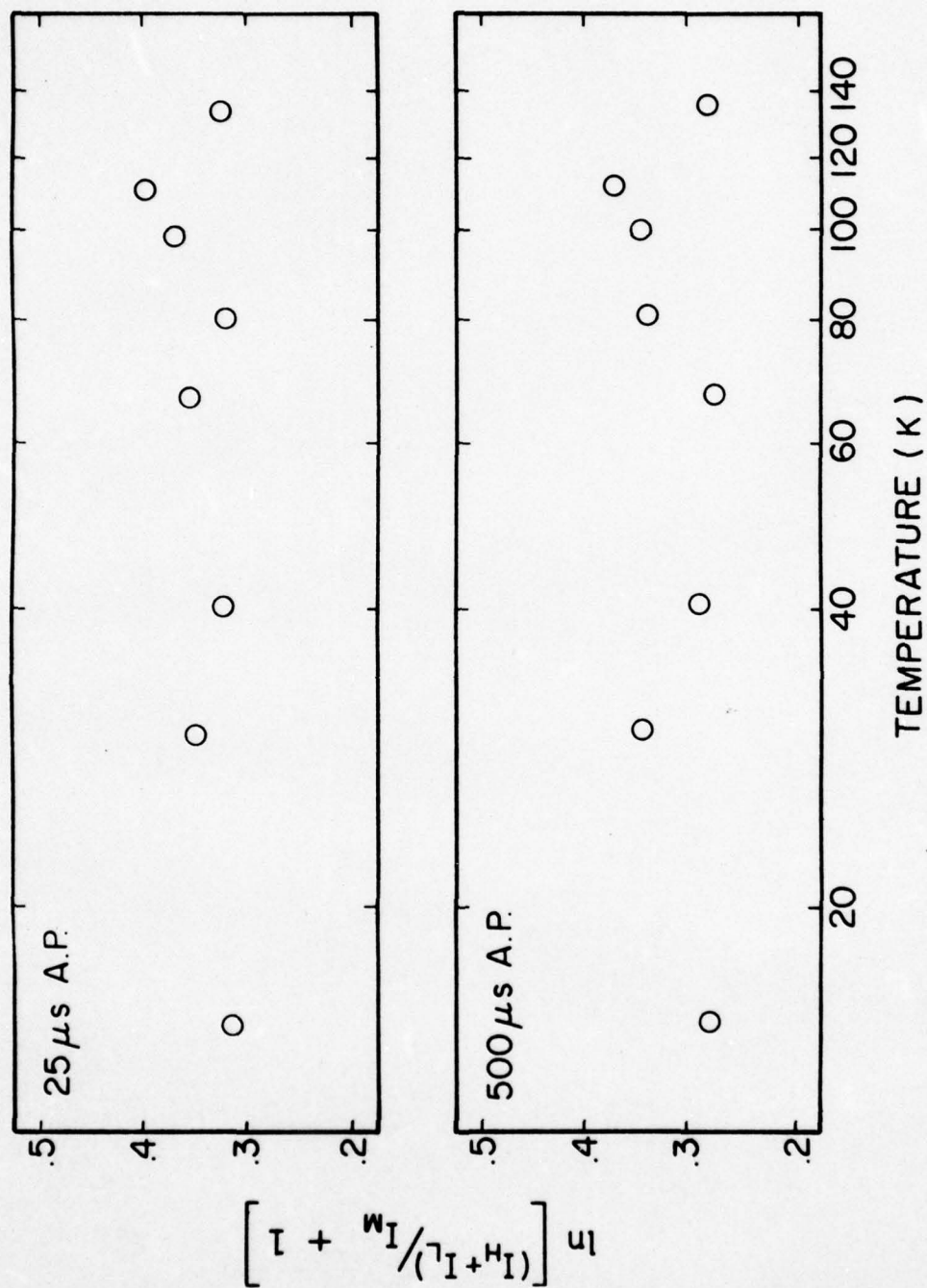


Figure 4. Temperature Dependence of the Intensity Ratios Taken at 25 and 500  $\mu$ s After the Laser Pulse

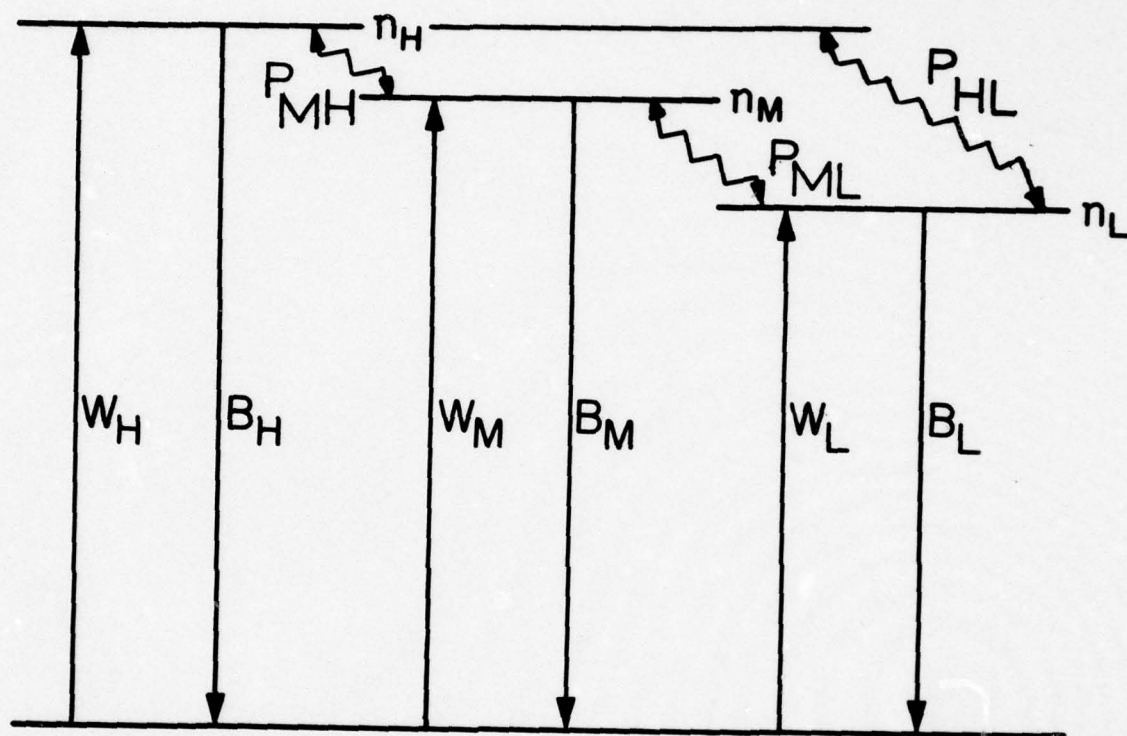


Figure 5. Model Used for Interpreting the Site Selection Spectroscopy Results for  $\text{YVO}_4:\text{Eu}^{3+}$



$$\frac{dn_L}{dt} = W_L - B_L n_L - (P_{LM} + P_{LH}) n_L + P_{ML} n_M + P_{HL} n_H. \quad (3)$$

The time dependences of the populations obtained from solving these equations are proportional to the observed fluorescence intensities. To obtain a tractable solution we assume a  $\delta$ -function excitation and neglect the small differences in fluorescence lifetimes and radiative-decay rates for ions in the three different sites. Numerous attempts were made to fit the TRS data shown in Fig. 2 for high-energy excitation. The only good fit which was found was based on selective excitation of the ions giving rise to the middle-energy line and electric dipole-dipole energy transfer to ions in the higher- and lower-energy sites with negligible back transfer. The resulting equation are

$$\begin{aligned} \frac{I_H}{I_M} &= \frac{I_H(0)}{I_M(0)} + \frac{P_{MH}}{P_{MH} + P_{ML}} \\ &\times \exp[(P_{MH} + P_{ML})t] - \frac{P_{ML}}{P_{MH} + P_{ML}}, \end{aligned} \quad (4)$$

$$\begin{aligned} \frac{I_L}{I_M} &= \frac{I_L(0)}{I_M(0)} + \frac{P_{ML}}{P_{MH} + P_{ML}} \\ &\times \exp[(P_{MH} + P_{ML})t] - \frac{P_{ML}}{P_{MH} + P_{ML}}, \end{aligned} \quad (5)$$

$$\frac{I_H + I_L}{I_M} = \frac{I_H(0) + I_L(0)}{I_M(0) + 1} \exp[(P_{MH} + P_{ML})t] - 1. \quad (6)$$

These expressions give the fits to the data shown as solid lines in Fig. 2 obtained by treating  $P_{MH}$  and  $P_{ML}$  as adjustable parameters. The procedure for

obtaining these fits was first to plot the ratio  $(I_H + I_L)/I_M$  on a semilog scale versus time to different powers in order to determine the time dependence of the energy transfer. The energy-transfer rate for a single-step process between randomly distributed sensitizers and activators is given by <sup>16</sup>

$$P_{SA} = \Gamma(1-3/q) \frac{4}{3} \pi R_0^3 C_A (t/\tau)^{3/q} t^{-1}, \quad (7)$$

where  $q=6$ ,  $8$ , or  $10$  for electric dipole-dipole, dipole-quadrupole, and quadrupole-quadrupole interactions, respectively;  $R_0$  is the critical interaction distance; and  $C_A$  is the activator concentration. In this case, the results are consistent with a  $t^{1/2}$  time dependence with  $P_{MH} + P_{ML} = 6.35 \times 10^{-3} \mu\text{sec}^{-1/2}$ . These results were used in Eqs. (4) and (5) to fit the  $I_H/I_M$  and  $I_L/I_M$  curves of Fig. 2. This gives  $P_{MH} = 4.49 \times 10^{-3} \mu\text{sec}^{-1/2}$  and  $P_{ML} = 1.86 \times 10^{-3} \mu\text{sec}^{-1/2}$ .

The values for the critical energy-transfer distances can be found by substituting the measured values of the energy-transfer rates into Eq. (7). To do this, it is necessary to know the value of the activator-ion concentration, which means in this case knowing the number of  $\text{Eu}^{3+}$  ions in each different kind of site. Although this is difficult to determine accurately, a reasonably good estimate can be obtained by comparing the relative intensities of the three lines normalized to the total emission for all excitation wavelengths across the absorption line at short times after the laser pulse. Then, the maximum intensity of each line, adjusted to account for differences in total-excitation energy, is taken to be an indication of the concentration of europium ions in the type of site giving rise to the line. The results indicate that 0.28 of the  $\text{Eu}^{3+}$  ions are in the type of sites giving the high-energy emission line; 0.57 of the ions are in the sites having the middle-energy emission line; and 0.15 of the ions are in the low-energy sites. Using these numbers in Eq. (7) gives values of  $R_0(\text{MH}) = 8.8$  and  $R_0(\text{ML}) = 8.2 \text{ \AA}$ . The accuracy of these estimates depends on the

amount of variation in oscillator strengths in the different types of sites and the fluorescence lifetime measurements indicate that this is probably less than 10%.

A theoretical estimate for  $R_0$  can be obtained from the expression<sup>17,18</sup>

$$R_0 = (3e^4 f_S f_A \Omega \tau_S^0 / 8\pi^2 m^2 c^3 n^4 \bar{\nu}_{SA})^{1/6}, \quad (8)$$

where  $f_S$  and  $f_A$  are the oscillator strengths of the sensitizer and activator transitions,  $\Omega$  is the overlap integral of the absorption spectrum of the activator and the emission spectrum of the sensitizer,  $n$  is the index of refraction, and  $\bar{\nu}_{SA}$  is the average wave number in the region of spectral overlap. To determine  $R_0$  accurately from this expression, it would be necessary to observe transitions from the  $^5D_0$  level to the ground state in both absorption and emission. Since these are forbidden transitions and thus very weak, it is difficult to observe them accurately with the required resolution to separate the lines from ions in different sites. However, if it is assumed that the line positions and shapes are determined primarily by the  $^5D_0$  level, the fluorescence spectra such as those shown in Fig. 1 can be used to determine spectral overlap. This can be done using the expression for the convolution integral of two overlapping Lorentzian line-shape function

$$\begin{aligned} \Omega &= g_S(\bar{\nu}) g_A(\bar{\nu}) d\bar{\nu} \\ &= \frac{1}{\pi} \frac{\Delta\bar{\nu}_S + \Delta\bar{\nu}_A}{(\Delta\bar{\nu}_S + \Delta\bar{\nu}_A)^2 + (\bar{\nu}_S^0 - \bar{\nu}_A^0)^2}, \end{aligned} \quad (9)$$

where  $\bar{\nu}^0$  is the peak position and  $\Delta\bar{\nu}$  is the Lorentzian contribution to the line width. Analyzing the Voigt profile of the observed line shape indicates that Lorentzian linewidths are  $\sim 1.09 \text{ cm}^{-1}$  which gives  $\Omega(\text{MH}) = 0.056 \text{ cm}$  and  $\Omega(\text{ML}) = 0.26 \text{ cm}$ .



The  ${}^5D_0 \rightarrow {}^7F_0$  transition is a forbidden transition whose oscillator strength will be less than  $10^{-6}$ .<sup>19</sup> In this case, Eq. (8) predicts values of  $R_0$  equal to or less than those obtained from fitting the TRS results. Since Eq. (7) is derived assuming a random distribution of activators, any aggregating of the  $\text{Eu}^{3+}$  ions would cause the experimentally determined values of  $R_0$  to be smaller. Although the estimates for the oscillator strengths and overlap integral are very crude, all parameters in Eq. (8) are taken to the  $\frac{1}{6}$ th power and thus the resulting estimates for  $R_0$  should be reasonable. Since the estimates for these parameters are probably high, the predicted values of  $R_0$  are at least good upper limits.

The TRS results for low-energy excitation shown in Fig. 3 are more difficult to interpret quantitatively. It appears that the low-energy site is preferentially excited and both energy transfer and back transfer occur among all three types of sites. Equations (1)-(3) can be solved to describe this situation but the resulting expressions have too many adjustable parameters to allow for a unique fit to the data to be obtained.

#### D. DISCUSSION

The results described above indicate that there are three major types of crystal field sites for  $\text{Eu}^{3+}$  ions to occupy in  $\text{YVO}_4$  crystals and that the values of the critical-interaction distances for ions in these different types of sites are of the order of  $8\text{\AA}$ . This is much smaller than the average separation of uniformly distributed europium ions of  $25\text{\AA}$  in a sample containing 1.0-at.%  $\text{Eu}^{3+}$ , which indicates that the europium ions in different sites may tend to form clusters. Spectroscopic evidence for defect clustering has been observed in other systems<sup>20,21</sup> and it has been found previously that energy transfer is more efficient between ions within a cluster than to more distant ions.<sup>21,22</sup>

The  $\text{Eu}^{3+}$  ions substitute for the  $\text{Y}^{3+}$  ions in yttrium orthovanadate and are in a site of  $D_{2d}$  symmetry with ten vanadate sites and four other yttrium sites within  $5\text{\AA}$  away. There are two equivalent types of sites related by a  $90^\circ$  rotation about the c axis. The ionic radius of  $\text{Eu}^{3+}$  is  $1.03\text{\AA}$  which is somewhat larger than the  $0.93\text{\AA}$  radius of  $\text{Y}^{3+}$ . From previous studies of host-sensitized energy transfer in this material is known that  $\text{Eu}^{3+}$  impurity ions create local distortions in the neighboring  $\text{VO}_4^{3-}$  complexes.<sup>14,15</sup> These local distortions may be different in the two types of yttrium sites making them non-equivalent. Also having nearby europium ions due to clustering can give rise to different nonequivalent sites. In addition, one of the major problems of yttrium orthovanadate crystals is the presence of imperfections introduced during crystal growth. If a chemical or structural imperfection is located near to the  $\text{Eu}^{3+}$  ion different types of sites could result. Thus, there are several possible origins for the different types of crystal-field sites for  $\text{Eu}^{3+}$ . There has been some previous evidence for different types of sites  $\text{Nd}^{3+}$  in  $\text{YVO}_4$  at higher concentrations, which is not observed at lower concentrations.<sup>23</sup> This may again indicate clustering is important. However, in the  $\text{Nd}^{3+}$  case, the energy difference between sites is several hundred wave numbers as compared to the very small splitting of only a few wave numbers observed here for  $\text{Eu}^{3+}$ .

Recently, there has been a significant amount of interest in characterizing the dependence of energy transfer rates on the differences in transition energies of the sensitizer and activator ions and on temperatures,<sup>4,5,7-9</sup> This interest is derived from the fact that the use of high-resolution laser excitation allows the study of energy transfer between ions whose energy mismatch is so small that the density of single phonons available to conserve energy is negligible, and thus the usual treatments of phonon-assisted energy transfer do not apply. Because of this, Holstein and co-workers<sup>8,9</sup> have developed theories of

two-phonon-assisted energy transfer, which show that the different types of possible two-phonon processes give rise to a variety of dependences on temperature and energy mismatch. For the results obtained on  $\text{Eu}^{3+}$  ions with high-energy excitation, the energy-transfer rates to the high- and low-energy lines from the middle line are approximately proportional to  $1/\Delta E^2$  where  $\Delta E$  is the energy difference between the middle line and either the high- or low-energy lines. The temperature dependence of the transfer rates for this case is very weak, approximately proportional to the homogeneous line broadening. These results are consistent with standard resonant energy-transfer theory where the temperature and energy mismatch dependences are contained in the spectral overlap factor as given by Eq. (9). If the linewidths  $\Delta\omega$  are small compared to the line splittings  $\Delta E$ , this predicts  $P_{SA} \propto \Delta\omega/\Delta E^2$ . Although this is only marginally true in this case, this simple theory appears to give the most satisfactory description of the observed results. Orbach<sup>24</sup> has pointed out that the spectral-overlap approach is valid for this situation if in addition the energy mismatch and the linewidths are much less than  $kT$ . All of these criteria are met in the case discussed here. Also, if the transfer occurs between europium ions only  $8\text{\AA}$  apart as concluded above, the long-wavelength phonon approximation will be valid and such things as phonon-interference factors can be neglected.

In summary, high-resolution laser time-resolved site-selection spectroscopy has been shown to give useful information on the characteristics of energy transfer between europium ions in yttrium orthovanadate crystals. The  $\text{Eu}^{3+}$  ions are shown to occupy several different types of crystal-field sites and are probably in clusters. The energy-transfer mechanism is electric dipole-dipole interaction and the transfer takes place over distances of the order of  $8\text{\AA}$ . The characteristics of the energy transfer can be successfully explained using a resonant interaction theory and the properties of spectral overlap.



The characteristics of the fluorescence emission and energy transfer are critically dependent on the exact wavelength of excitation and, in some cases, the results are too complicated to interpret through a simple rate-equation approach.

#### REFERENCES

- [1] N. Motegi and S. Shionoya, J. Lumin, 8, 1 (1973).
  - [2] D. R. Tallant and J. C. Wright, J. Chem. Phys. 63, 2074 (1975).
  - [3] M. D. Kurz and J. C. Wright, J. Lumin. 15, 169 (1977).
  - [4] C. Hsu and R. C. Powell, Phys. Rev. Lett. 35, 734 (1975); J. Phys. C 9, 2467 (1976).
  - [5] R. Flach, D. S. Hamilton, P. S. Selzer, and W. M. Yen, Phys. Rev. Lett. 35, 1034 (1975); Phys Rev. B 15, 1248 (1977).
  - [6] J. Koo, L. R. Walker, and S. Geschwind, Phys. Rev. Lett. 35, 1669 (1975).
  - [7] P. M. Selzer, D. S. Hamilton, and W. M. Yen, Phys. Rev. Lett. 38, 858 (1977).
  - [8] T. Holstein, S. K. Lyo, and R. Orbach, Phys. Rev. Lett. 36, 891 (1976).
  - [9] T. Holstein, S. K. Lyo, and R. Orbach, Phys. Rev. B. (to be published).
- A preliminary account of this work was presented at the Colloque International du Centre National de la Recherche Scientifique, 1976 (unpublished).
- [10] J. R. O'Conner, Appl. Phys. Lett. 9, 407 (1966).
  - [11] P. P. Yaney and L. G. DeShazer, J. Opt. Soc. Am. 66, 1405 (1976).
  - [12] A. K. Levin and F. C. Palilla, Appl. Phys. Lett. 5, 118 (1964).
  - [13] C. Brecher, H. Samelson, A. Lempicki, R. Riley, and T. Peters, Phys. Rev. 155, 178 (1967).
  - [14] C. Hsu and R. C. Powell, J. Lumin. 10, 273 (1975).
  - [15] G. E. Venikouas and R. C. Powell, J. Lumin. 16, 29 (1978).
  - [16] K. B. Eisenthal and S. Siegel, J. Chem. Phys. 41, 652 (1964).

- [17] Th. Forster, Ann. Phys. (Leipz.) 2, 55 (1948).
- [18] D. L. Dexter, J. Chem. Phys. 21, 836 (1953).
- [19] L. A. Riseberg and M. J. Weber, in *Progress in Optics*, edited by E. Wolf (North-Holland, Amsterdam, 1975), Vol. 14.
- [20] J. B. Fern, J. C. Wright, and F. K. Foug, J. Chem. Phys. 59, 5591 (1973).
- [21] M. N. Sunberg, H. V. Louer, and F. K. Fong, J. Chem. Phys. 62, 1853 (1975).
- [22] D. R. Tallant, M. P. Miller, and J. C. Wright, J. Chem. Phys. 65, 510 (1976).
- [23] Kh. S. Bagdasarov, G. A. Bogomolova, A. A. Kaminskii, and V. I. Popov, Sov. Phys. Doki. 13, 516 (1968).
- [24] R. Orbach (private communication).

## V.2 Energy Transfer Among $\text{Nd}^{3+}$ Ions in $\text{Y}_3\text{Al}_5\text{O}_{12}$ and $\text{Y}_3\text{Ga}_5\text{O}_{12}$ Crystals

### A. Introduction

Although  $\text{Y}_3\text{Al}_5\text{O}_{12}:\text{Nd}^{3+}$  is one of the most important and most studied crystalline laser materials,<sup>1</sup> there are still some important physical properties of this system which are not well characterized and understood. Energy transfer between neodymium ions is one example of a physical process which has not been thoroughly investigated in this host. We report here the results of an investigation of energy transfer among  $\text{Nd}^{3+}$  ions in both  $\text{Y}_3\text{Al}_5\text{O}_{12}$  and  $\text{Y}_3\text{Ga}_5\text{O}_{12}$  crystals. The technique of laser-excited, time-resolved site-selection spectroscopy was employed. The time dependence and temperature dependence of the energy transfer was found to be consistent with two-phonon assisted migration and trapping processes.

The study of energy transfer between ions in solids has received renewed interest during the past few years because of the ability to use pulsed laser

excitation.<sup>2</sup> The fast pulse capabilities allow time-resolved spectroscopy techniques to be used to characterize the time evolution of the energy transfer whereas the high resolution capabilities allow the probing of the effects of the inhomogeneities in the system. Studies of the latter type can be divided into two categories. The first includes the ultra-high resolution investigations utilizing the fluorescence line narrowing of an inhomogeneously broadened transition.<sup>3</sup> The second involves systems whose inhomogeneities give rise to significantly different crystal field sites for the active ions thus allowing the transitions from ions in nonequivalent crystal field sites to be distinctly resolvable in the spectrum.<sup>4</sup> These new experimental techniques have resulted in the requirement for new theoretical models for interpreting the data which account for the effects of both spatial and spectral randomness on the characteristics of energy transfer.<sup>5,6</sup> So far, these investigations have been applied to only a very few cases and continued experimental and theoretical efforts are both still necessary.

The motivation for the work described here was to further our knowledge of the effects of different microscopic environments on the properties of  $\text{Nd}^{3+}$  ions and the transfer of energy between  $\text{Nd}^{3+}$  ions in garnet crystals. Obtaining this type of information on  $\text{Nd}^{3+}$  doped garnet materials is of special interest because of the relevance it has to the laser performance of these materials.<sup>1</sup> It was also hoped that our general understanding of the physics of energy transfer between ions in solids could be enhanced by this work and especially that the experimental information obtained by new laser spectroscopy techniques could be used to check the validity of some of the proposed theories of energy transfer. Again the  $\text{Nd}^{3+}$ -garnet system was thought to be a good choice for this type of fundamental study since so much previous work has been done in establishing the spectral properties of these materials such as transition



matrix elements and branching ratios. The results of this investigation indicate that the characteristics of energy transfer in YAlG-Nd crystals are quite different than previously thought.<sup>1</sup> A combination of proposed theories of migration kinetics and phonon assisted ion-ion interaction is shown to adequately explain the major portion of the results. However, as has generally been the case when the microscopic details of a complex system are probed, the results are quite complicated and some of them are not completely understood. We also point out where further theoretical development is necessary to provide a more exact description of the real physical situation being investigated.

#### B. Theoretical Background

The theoretical approach generally used in recent investigations of energy transfer between rare earth ions in solids<sup>7,8</sup> was developed by Yokota and Tanimoto<sup>9</sup> and includes terms for both the migration of energy among sensitizer ions as well as the direct transfer of energy from an excited sensitizer to an unexcited activator ion by electric dipole-dipole interaction. This was outlined in section III.1. In this treatment the rate equation for the concentration of excited sensitizers  $n_s$  is

$$\partial n_s / \partial t = -\beta_s N_s + DV^2 N_s - \sum_i W_{sa}(R_i) N_s \quad (1)$$

where  $\beta_s$  is the intrinsic decay rate of the sensitizer,  $D$  is the diffusion coefficient for the sensitizer excitation,  $R_i$  is the separation between a given sensitizer-activator pair, and  $W_{sa}(R_i)$  represents the strength of the energy transfer interaction which is discussed below. To obtain the expression for the time dependence of the concentration of excited sensitizers, Eq. (1) must be integrated over time and averages over the spatial distribution of activators. This is a difficult procedure and was achieved by Yokota and Tanimoto<sup>9</sup> by assuming a uniform distribution of activators, using an operator expansion for the

integrand, and dropping terms in  $(Dt^{2/3}W_{sa}^{-1/3}R_{sa}^{-2})$  for  $n > 3$ . Here  $R_{sa}$  is the average closest sensitizer-activator separation. Then by use of the Pade approximant technique the solution of Eq. (1) is simplified to

$$N_s(t) = N_s(0)\exp[-\beta_s t - \frac{4}{3}\pi^{3/2}C_a W_{sa}^{1/2}R_{sa}^3 t^{1/2} \left( \frac{1 + 10.87X + 15.50X^2}{1 + 8.743X} \right)^{3/4}] \quad (2)$$

where  $X = Dt^{2/3}W_{sa}^{-1/3}R_{sa}^{-2}$  and  $C_a$  is the concentration of activator ions. At short times after pulsed excitation the electric dipole-dipole interaction between sensitizers and activators dominates the energy transfer and Eq. (2) reduces to the standard time dependent expression for the energy transfer rate in the absence of diffusion.<sup>10-12</sup> At long times after the excitation pulse the diffusion limited situation is reached in which the time-independent energy transfer rate can be expressed as

$$W_s = 4\pi DC_a \rho \quad (3)$$

$$\rho = 0.676 W_{sa}^{1/4} R_{sa}^{3/2} D^{-1/4} \quad (4)$$

is the trapping radius. Both of these two limiting cases have been observed in studies of energy transfer between rare earth ions in solids.<sup>13,14</sup> For the results obtained in this work the fluorescence decays are found to be exponential and the data are consistent with a time-dependent energy transfer rate indicating that the diffusion limited situation is applicable.

It should be mentioned that there are several other approaches to the treatment of energy transfer involving both diffusion among sensitizers as well as direct interaction with activators. The treatment of Kurskii and Selivanenko<sup>15</sup> has been shown to be equivalent to that of Yokota and Tanimoto<sup>9</sup> when used to fit

the same experimental data. The results of Burshtein,<sup>16</sup> et al. reduce to the expressions of Yokota and Tanimoto in the limit of weak diffusion while in the limit of strong diffusion their expressions are equivalent to those of the theory developed by Soos and Powell<sup>17</sup> which is applicable to the physical situation of large trapping regions surrounding activators. Thus the Yokota-Tanimoto formalism outlined above appears to provide the best available description to the physical situation of interest in this work.

Now it is necessary to obtain the theoretical expression for the diffusion coefficient in Eq. (3) in terms of the sensitizer ion-ion interaction rate. This is a well known mathematical problem which is generally treated by setting up the problem in a random walk formalism and showing the equivalence between the random walk picture and diffusion in the limit of many steps in the random walk.<sup>18</sup> In this approach the diffusion coefficient is described in terms of the average random walk hopping time  $t_h$  by the expression  $D = R_{sa}^2 / (6t_h)$ . The hopping time is then expressed in terms of the physical interaction causing the hop to occur. Trlifaj<sup>19</sup> has applied this approach to the specific problem of excitons migrating via electric dipole-dipole interaction and finds the resulting expression for the diffusion coefficient to be

$$D = 3.4 C_s^{4/3} R_{ss}^6 W_{ss} \quad (5)$$

where  $C_s$  is the sensitizer concentration,  $R_{ss}$  is the sensitizer-sensitizer separation, and  $W_{ss}$  is the interaction strength between two sensitizers. It should be noted that this expression is exactly true only for the case of a random walk on a simple cubic lattice with each step having the same hopping time. For the physical situation of interest here the migration occurs on a lattice of randomly distributed sites resulting in the possibility of significantly different hopping times for different steps. In order to apply this



result to the case of interest it is necessary to use the average Nd ion separation for  $R_{ss}$  and the average interaction strength at this separation. Although it has been shown<sup>20</sup> that the formal random walk results remain unchanged when a small hopping time dispersion is introduced and accounted for by using the average value of  $t_h$ , it is not clear that a large dispersion in hopping times can be legitimately handled in the same simple way. We are currently investigating the effects of treating broad distributions of hopping times in this formalism using Monte Carlo numerical procedures.<sup>21</sup> However, at the present time this is the only method we have of treating the problem and thus we will follow the usual practice of utilizing Eq. (5) with average values for the parameters.

Finally, it is necessary to decide on the appropriate expression to use for the ion-ion interaction rates. This depends on the mechanism of the interaction (exchange, electric dipole-dipole etc.) and on whether the transfer is resonant or phonon assisted. These questions can not be answered until the experimental results are analyzed but it is possible to speculate about the various possibilities. First, the optical transitions of trivalent neodymium ions in solids are generally thought to occur by forced electric dipole transitions<sup>8</sup> and therefore the energy transfer between two  $Nd^{3+}$  ions is usually considered to take place through forced electric dipole-dipole interaction.<sup>22</sup> Second, it has been suggested that the small energy mismatch in the transitions of two similar ions must be made up by two-phonon processes instead of a one-phonon process since the density of states of very low energy phonons is quite small and a single long wavelength phonon may modulate the environments of two closely spaced impurity ions in the same way instead of providing the necessary modulation of one ion with respect to the other.<sup>5</sup> There are many different combinations of possible two-phonon processes resulting in a variety of different possible temperature

dependences for the energy transfer rate such as  $T^3$ ,  $T^7$  and  $\exp(-\delta/k_B T)$  where  $\delta$  is the energy between one of the states involved in the energy transfer transition and a real intermediate state reached by the phonons involved.

The procedure used in analyzing the data in this work was to first determine from the time dependence of the energy transfer rate the nature of the interaction mechanism and whether or not we are dealing with a diffusion limited case. Then from the temperature dependence the nature of the phonon assisting processes was determined. Finally the magnitude of the energy transfer rate determined from fitting the data compared to that predicted by the expression

$$W_s = 21.2 C_a C_s R_{Nd}^6 W_{ss}(T)^{3/4} W_{sa}(T)^{1/4} \quad (6)$$

derived above using known parameters for  $Nd^{3+}$  ions in garnet crystal hosts and the appropriate expression for the phonon assisted interaction rate. Here both  $R_{ss}$  and  $R_{sa}$  have been set equal to the average  $Nd^{3+}$  ion separation  $R_{Nd}$ . The details of this procedure are described further in Section V.

### C. Experimental

The samples investigated were good single crystals of  $Y_3Al_5O_{12}$  containing 0.85% ( $1.17 \times 10^{20} \text{ cm}^{-3}$ ) neodymium and  $Y_3Ga_5O_{12}$  containing 0.25% ( $3.23 \times 10^{19} \text{ cm}^{-3}$ ) neodymium. These were mounted in a cryogenic refrigerator capable of varying temperature between about 7 and 300 K. Broad band excitation was provided by a 150 W xenon lamp while a nitrogen laser pumped tunable dye laser was used for selective excitation. With rhodamine 6-G dye, the laser provided pulses less than 10 nsec in duration and less than  $0.4\text{\AA}$  in halfwidth. The peak power of the pulses was approximately 20 kW at a 30 Hz repetition rate. The sample fluorescence was analyzed by a 1-m spectrometer capable of a resolution in first order of  $0.16\text{\AA}$ . The signal was detected by a cooled RCA C31034

photomultiplier tube, averaged by a boxcar integrator triggered by the laser, and displayed on a strip-chart recorder. The time resolution used was about 0.1  $\mu$ sec.

Figure 1 shows the energy levels relevant to this investigation of  $\text{Nd}^{3+}$  in the two types of garnet host crystals. Our results are quite similar to those published previously.<sup>23-25</sup> With the experimental equipment described above, the ions are pumped in the various components of the  $^2\text{G}_{7/2}$  and  $^4\text{G}_{5/2}$  states and fluorescence occurs after radiationless relaxation to the  $^4\text{F}_{3/2}$  levels. We monitored the fluorescence transitions from this metastable state to the four lowest components of the  $^4\text{I}_{9/2}$  ground state manifold.

Figure 2 shows the absorption spectra in the region of pumping and fluorescence at room temperature while Fig. 3 shows the fluorescence spectra at room temperature under broad band excitation. The differences in relative peak intensities for similar lines show the differences in oscillator strength and branching ratios for the  $\text{Nd}^{3+}$  transitions in the two different hosts.

Figures 4 and 5 show the fluorescence spectra for the two samples at low temperatures under selective excitation at short times after the laser pulse. The structure in the spectra near each major line is indicative of the variation of transition energies for ions in nonequivalent crystal field sites. The variation of this structure with pumping wavelength indicates that ions in specific types of crystal field sites are being selectively excited. For each sample, comparison of the intensities of the same transitions in absorption and emission spectra show that the branching ratios and oscillator strengths are quite different for ions in different crystal field sites.

The fluorescence lifetimes were measured to be about 200  $\mu$ sec for the  $\text{Y}_3\text{Al}_5\text{O}_{12}$  host and 250  $\mu$ sec for the  $\text{Y}_3\text{Ga}_5\text{O}_{12}$  host. These are essentially



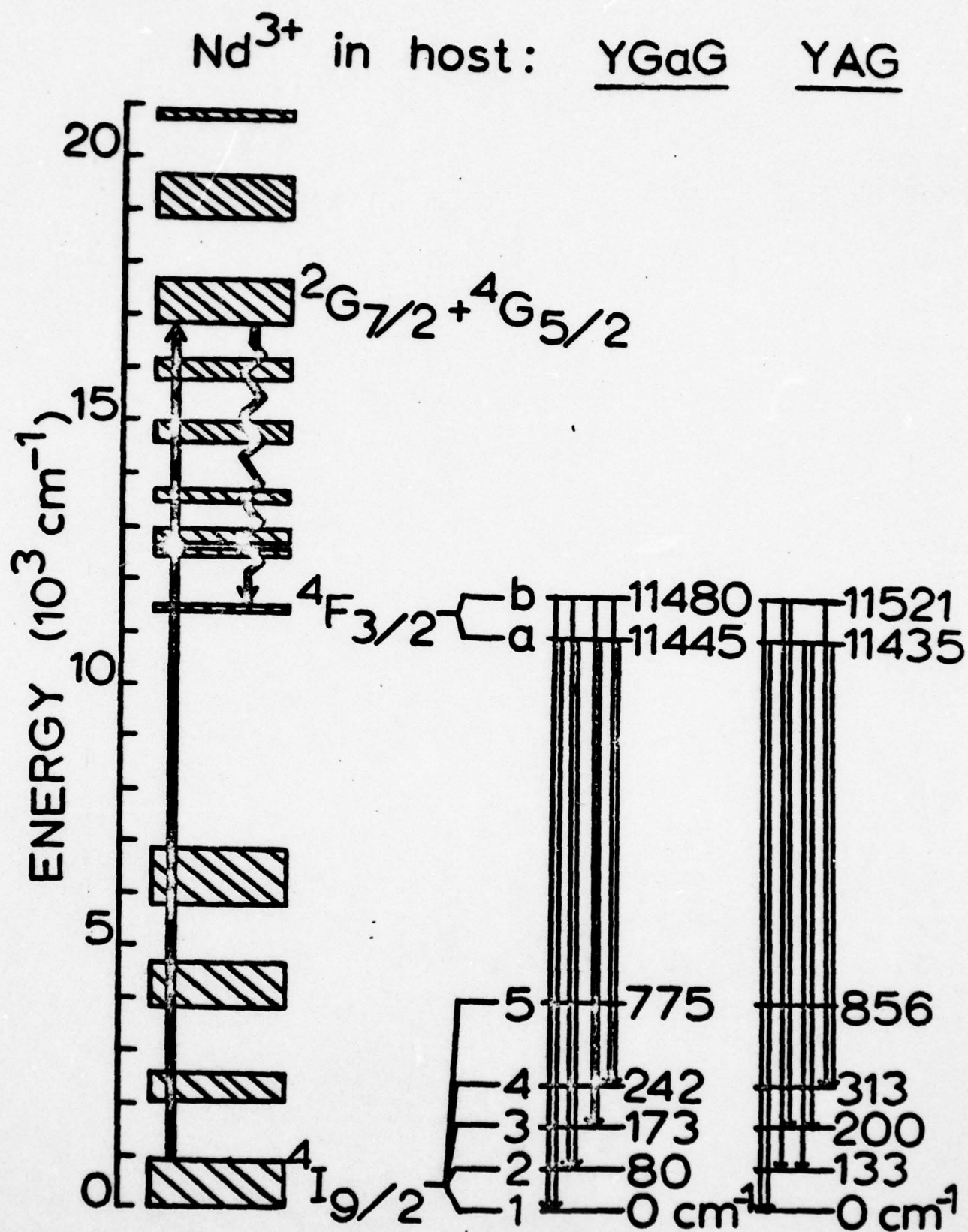


Fig. 1. Energy levels of Nd<sup>3+</sup> ions in Y<sub>3</sub>Ga<sub>5</sub>O<sub>12</sub> and Y<sub>3</sub>Al<sub>5</sub>O<sub>12</sub> crystals.

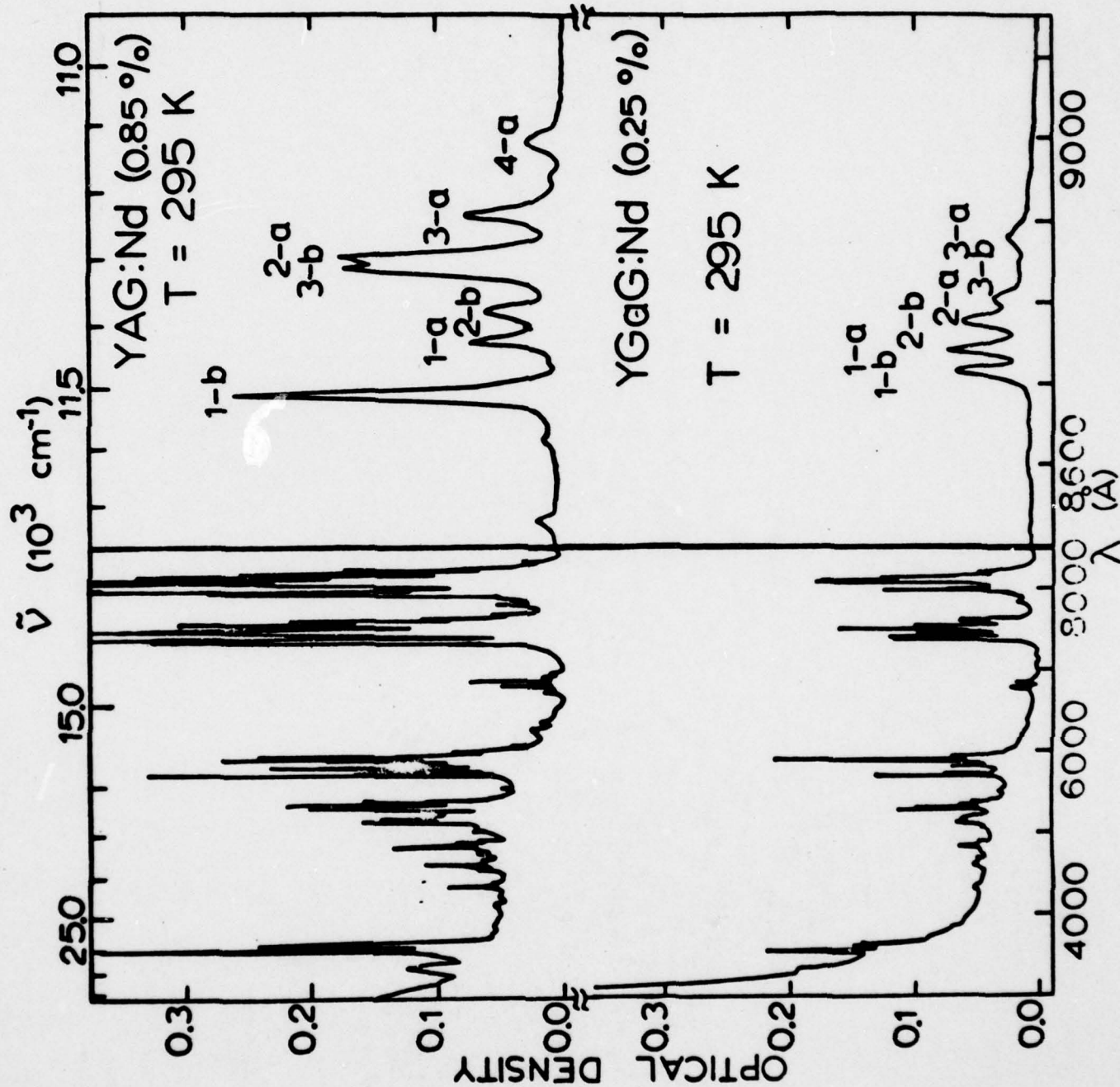


Fig. 2. Room temperature absorption spectra of  $\text{Y}_3\text{Ga}_5\text{O}_{12}:\text{Nd}^{3+}$  (3.0 mm thick) and  $\text{Y}_3\text{Al}_5\text{O}_{12}:\text{Nd}^{3+}$  (2.9 mm thick).

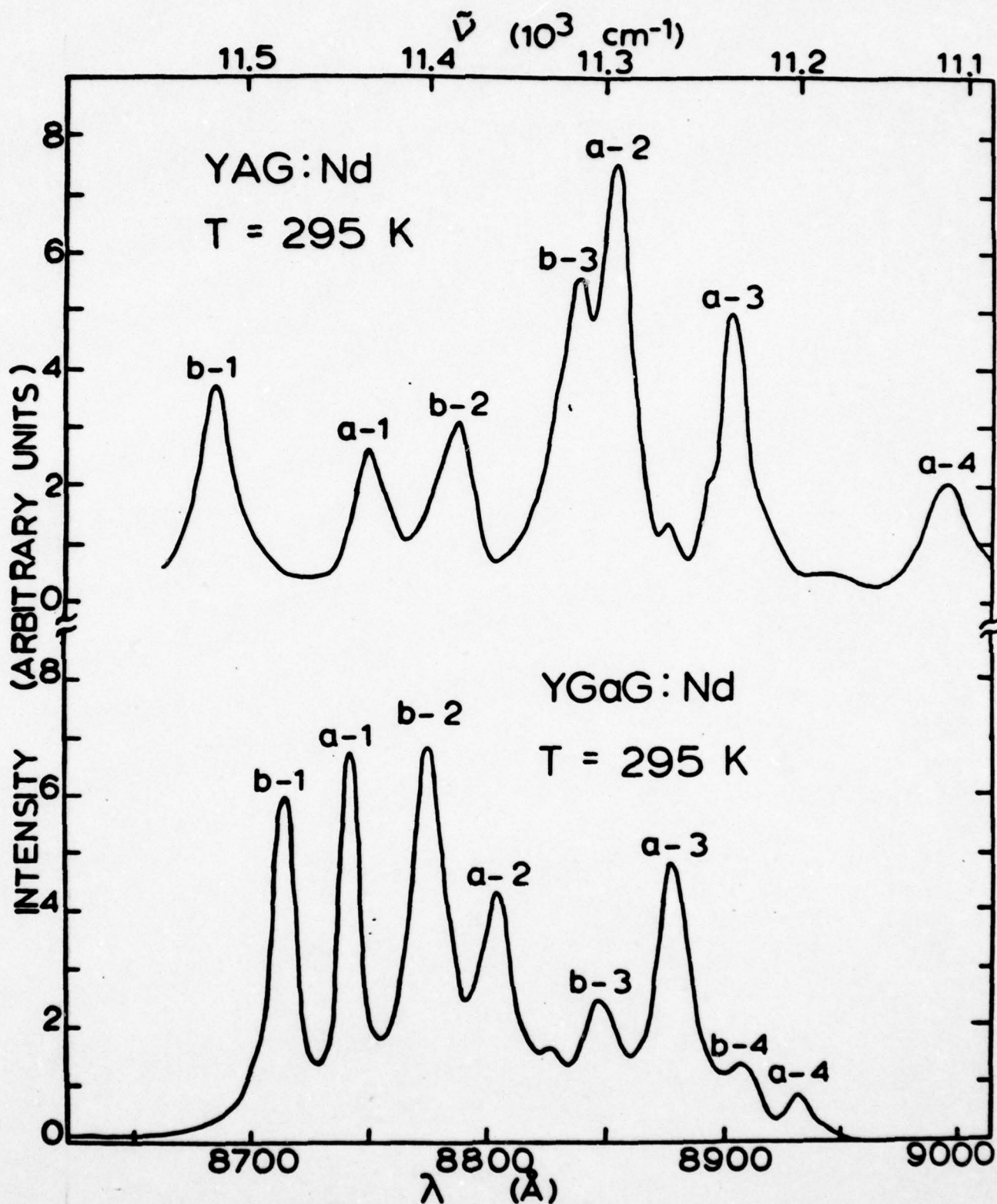


Fig. 3. Room temperature fluorescence spectra of the  ${}^4F_{3/2} - {}^4I_{9/2}$  transitions under broad band excitation. (See Fig. 1 for the transition designations of the lines.)



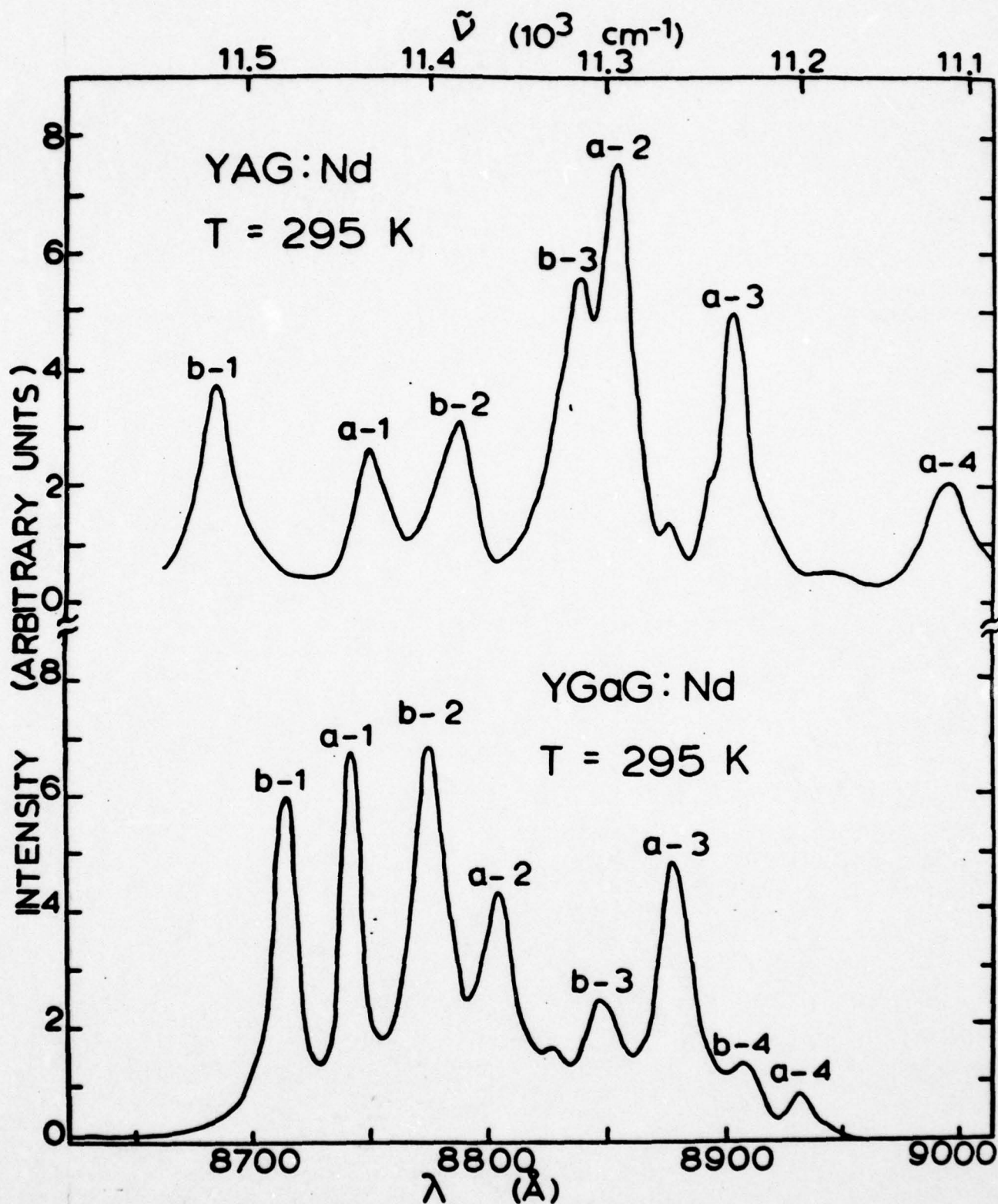


Fig. 3. Room temperature fluorescence spectra of the  $^4F_{3/2} - ^4I_{9/2}$  transitions under broad band excitation. (See Fig. 1 for the transition designations of the lines.)

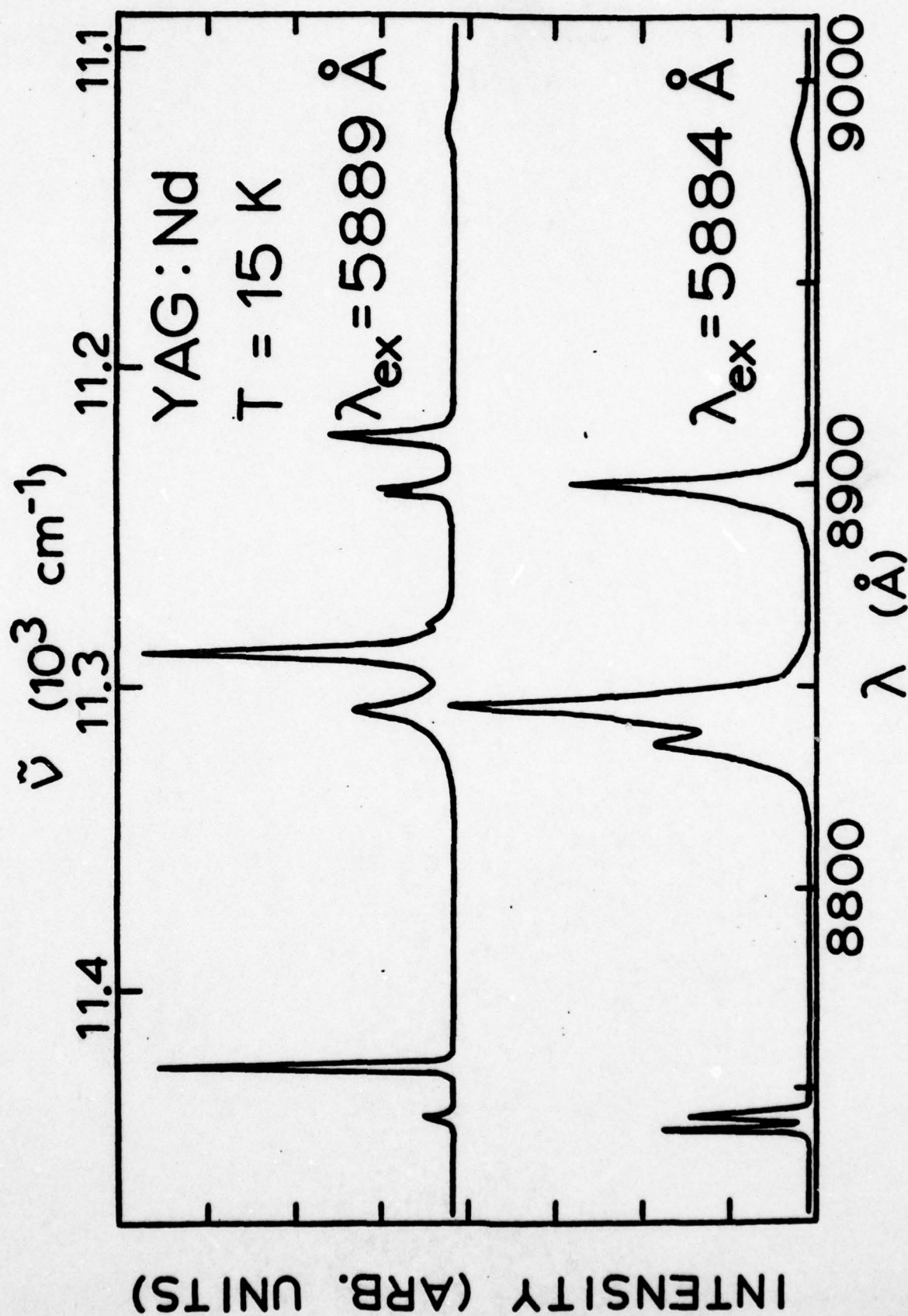


Fig. 4. Fluorescence spectra of  $\text{YAlO}_5\text{:Nd}^{3+}$  at low temperatures for two different narrow line laser excitation wavelengths.

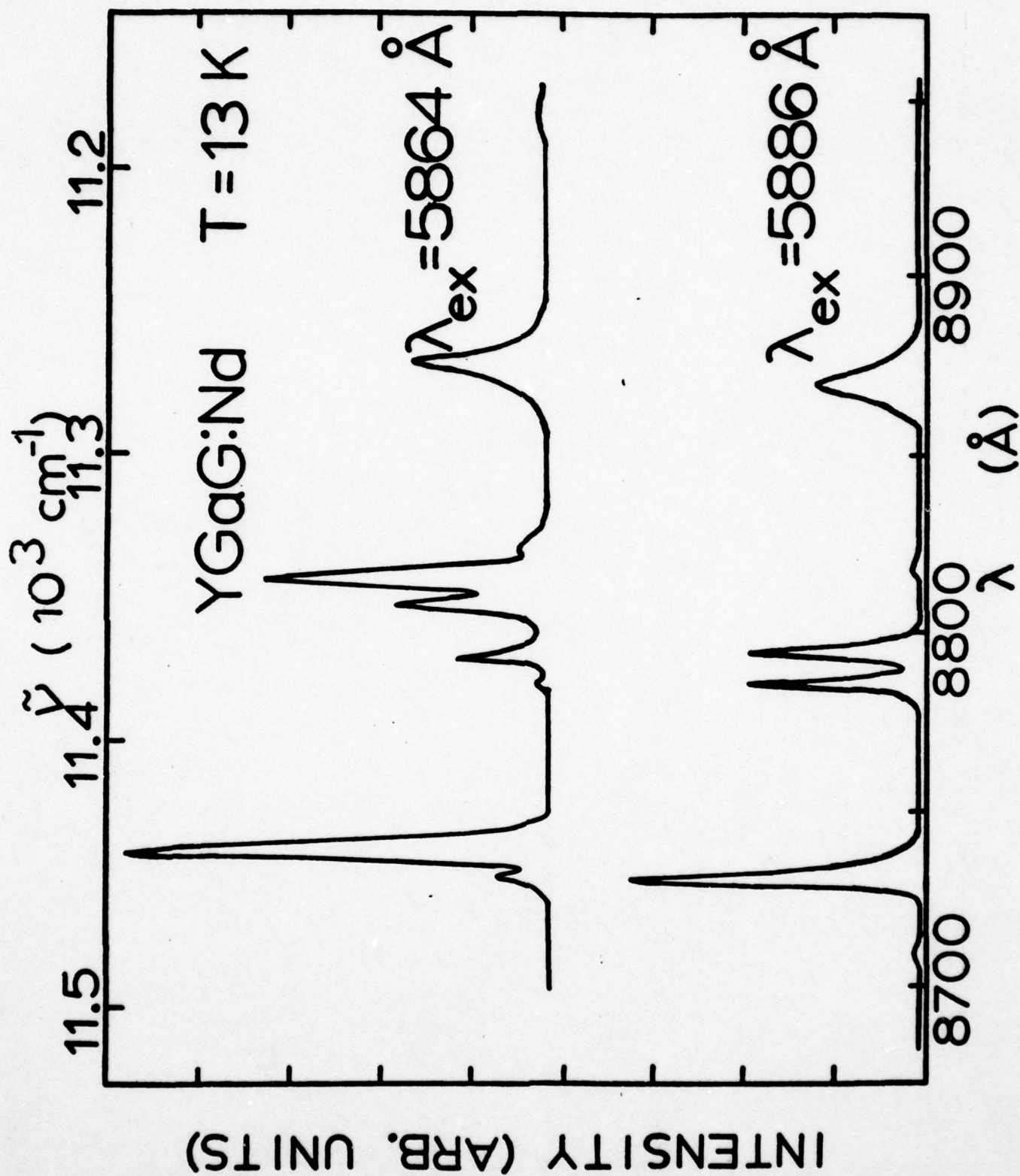


Fig. 5. Fluorescence spectra of  $\text{YGaO}_5:\text{Nd}^{3+}$  at low temperatures for two different narrow line laser excitation wavelengths.



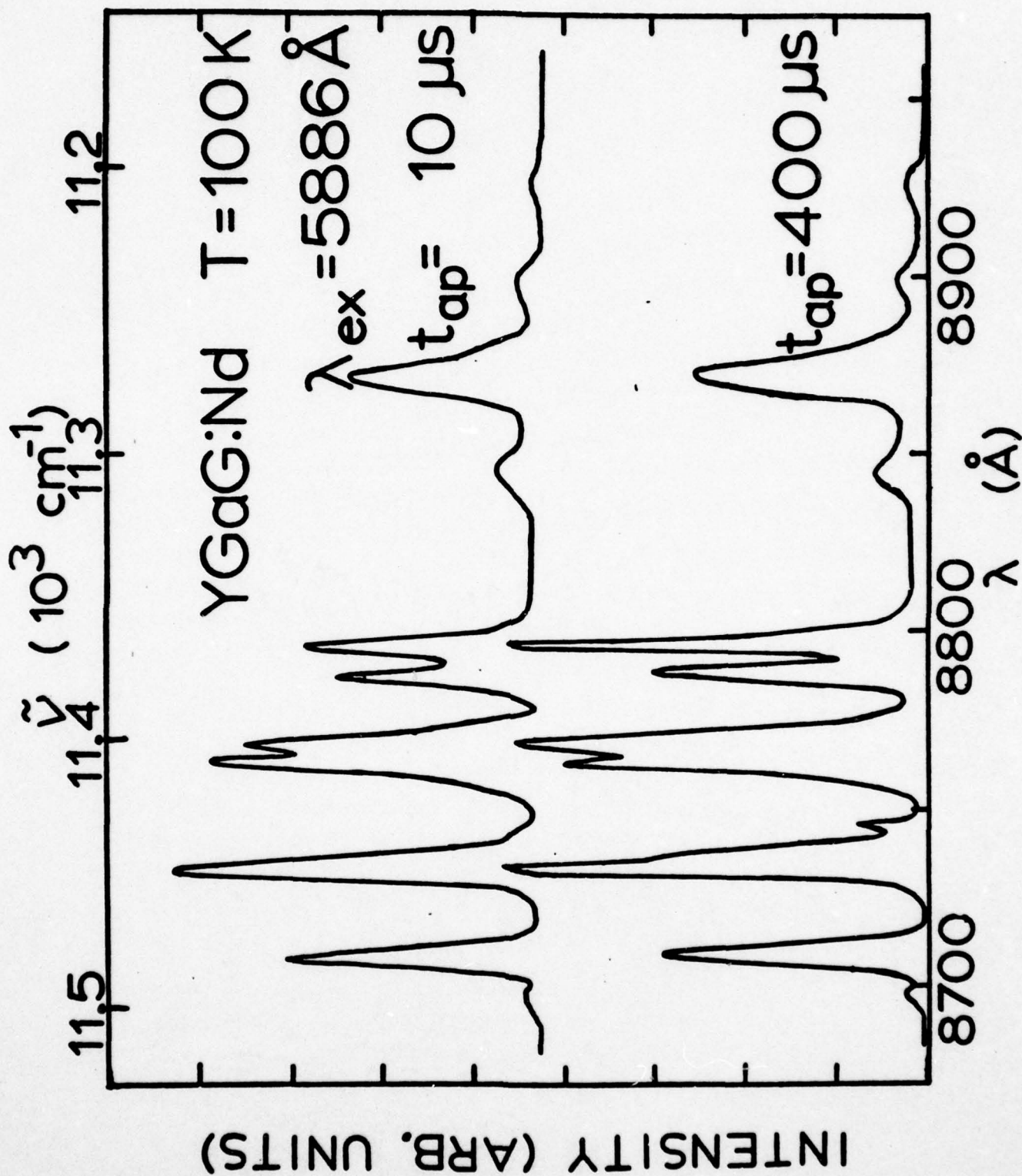


Fig. 6. Fluorescence spectra of  $\text{YGa}_5\text{O}_{12}:\text{Nd}^{3+}$  at 100 K for two different times after the laser pulse.

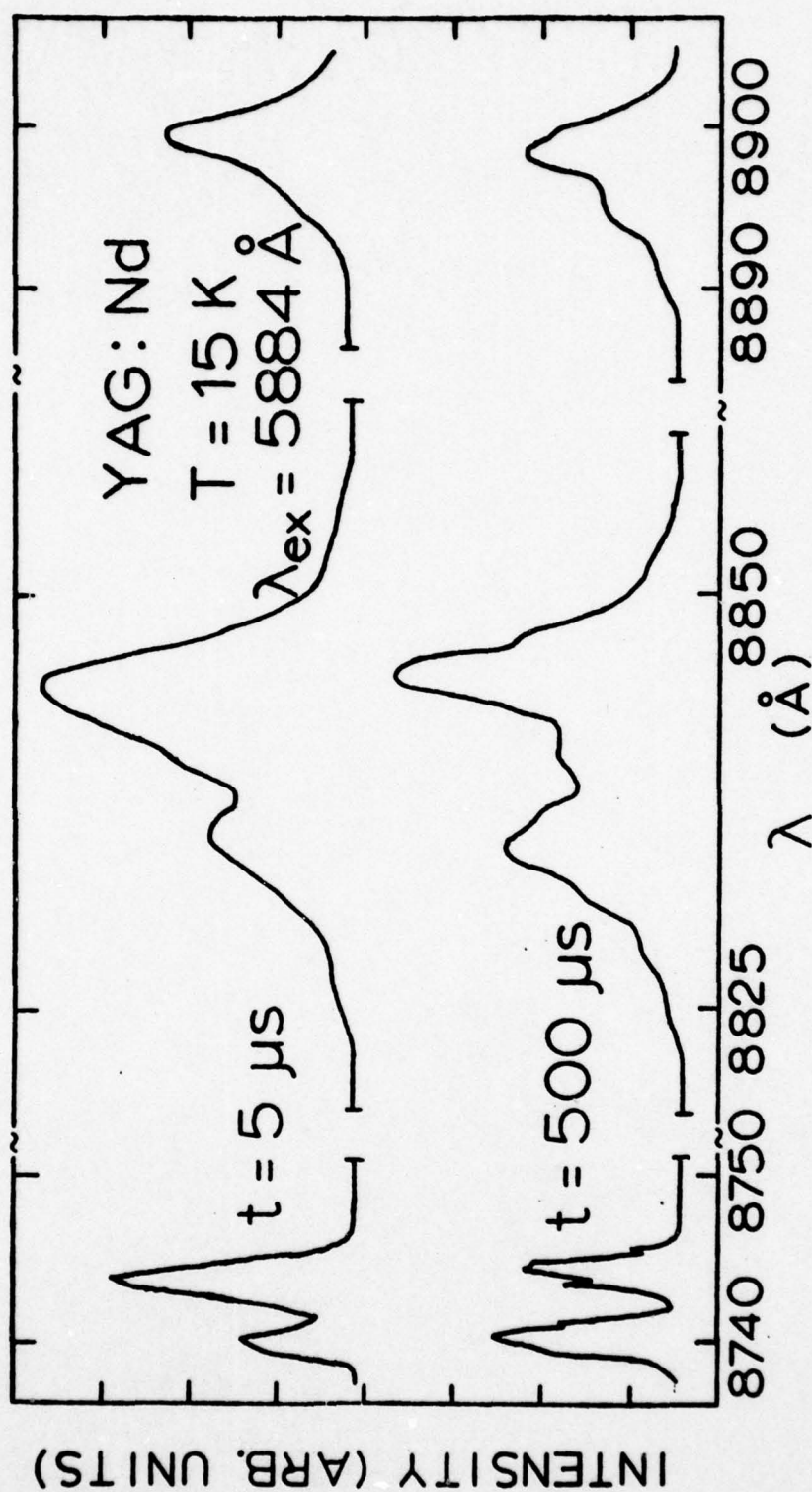


Fig. 7. Time Dependence of YAG:Nd Fluorescence at 15 K

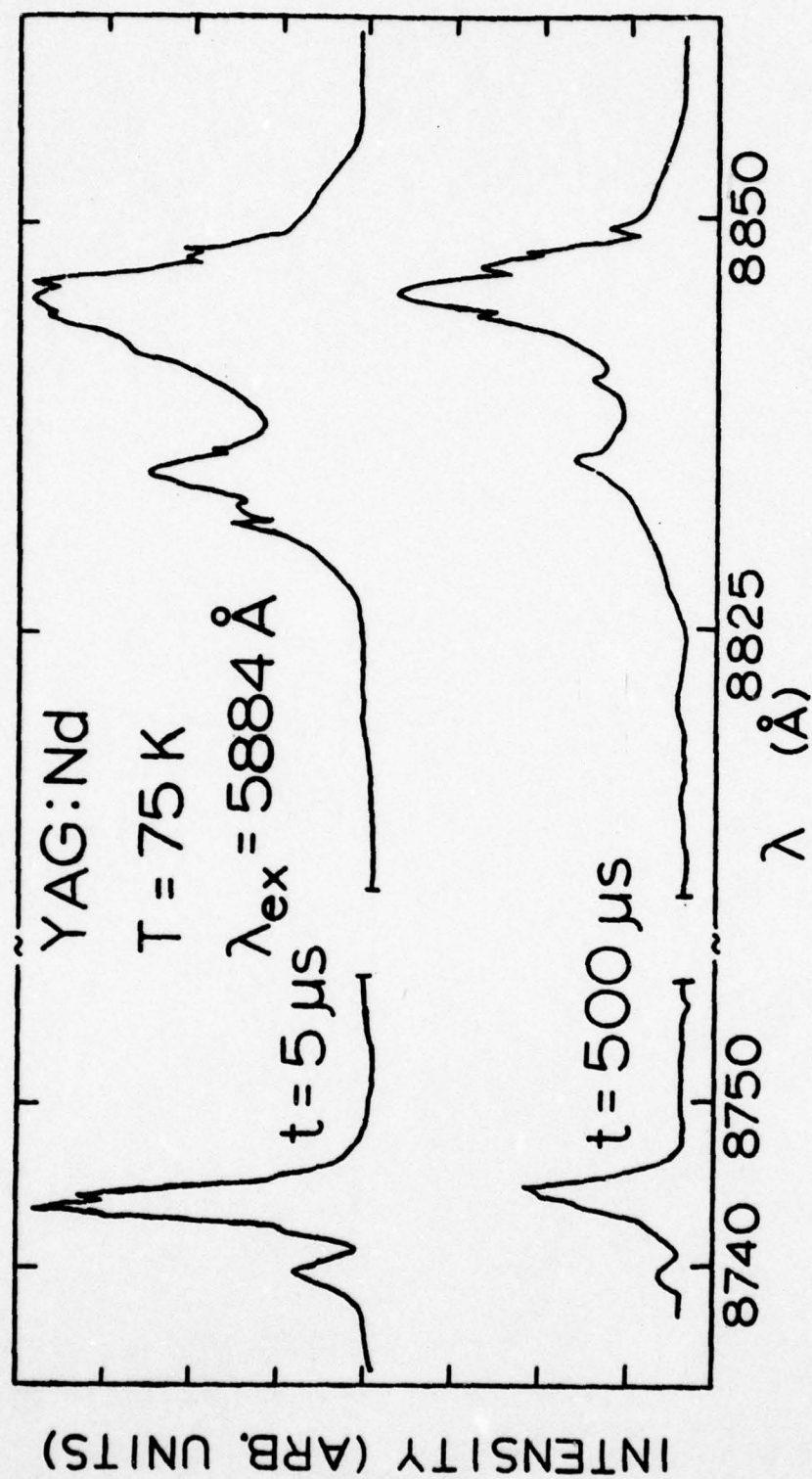


Fig. 8. Time Dependence of YAG:Nd Fluorescence at 75 K



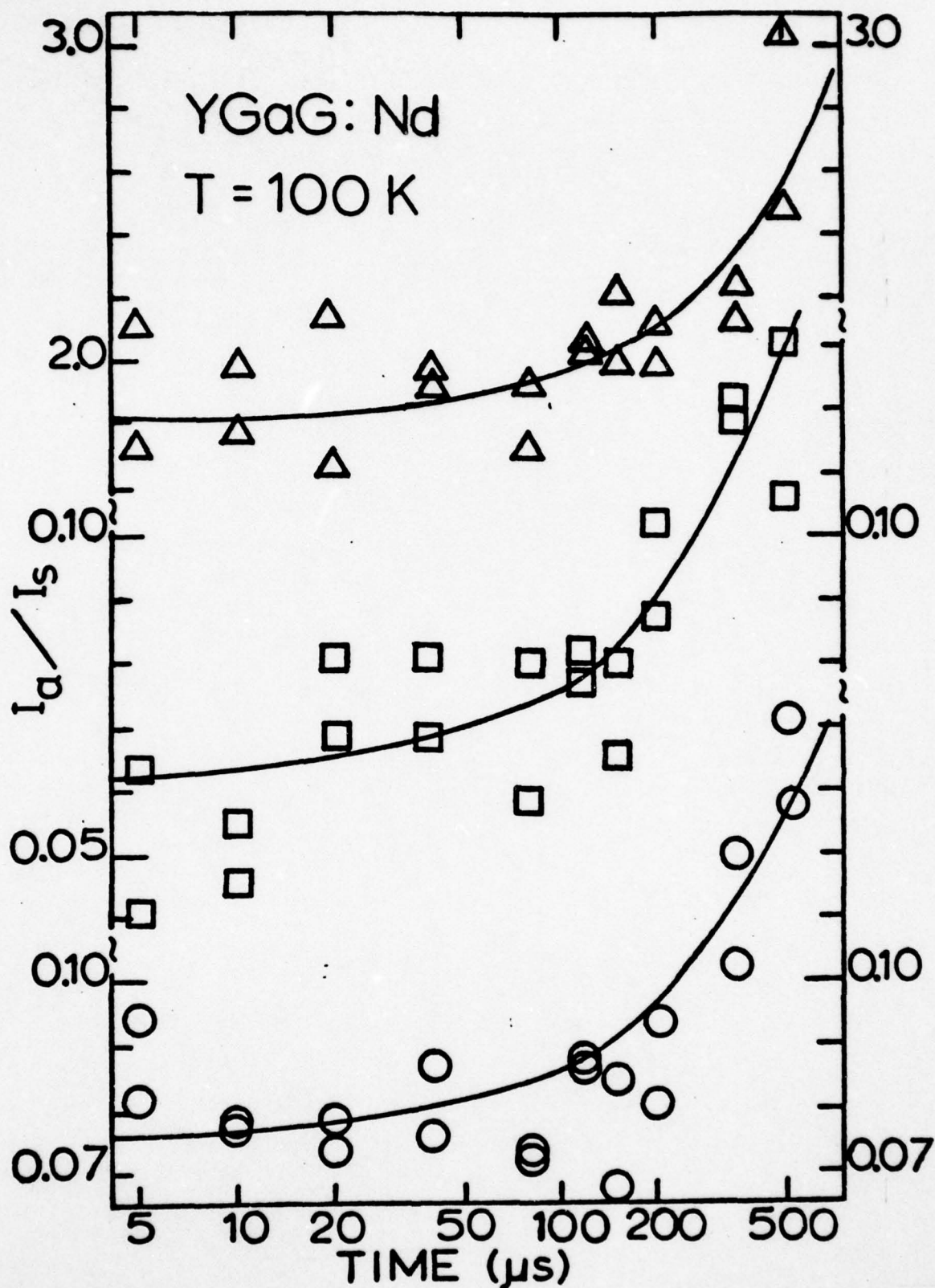


Fig. 9. Ratios of the integrated fluorescence intensities of transitions from  $Nd^{3+}$  ions in different crystal field sites in  $Y_3Ga_5O_{12}$  as a function of time after the laser pulse at 100 K.  $\Delta$ - $I_{8796} \text{ \AA} / I_{8788} \text{ \AA}$ ,  $\square$ - $I_{8744} \text{ \AA} / I_{8732} \text{ \AA}$ ,  $O$ - $I_{8697} \text{ \AA} / I_{8708} \text{ \AA}$ . (See text for explanation of theoretical lines.)

temperature independent for the range investigated. Also they were found to be the same within experimental error for ions in all of the major sites which could be electively excited in both host crystals.

The relative integrated fluorescence intensities of transitions from ions in different crystal field sites change as a function of time after the laser pulse. Since the fluorescence lifetimes are found to be essentially the same for ions in all major types of sites in the same host, this time dependence can be attributed to energy transfer among ions in different types of sites. Figures 6-8 show examples of the fluorescence spectra of  $\text{Nd}^{3+}$  at two different times after the laser pulse. Figure 9 shows the time dependences of the relative integrated fluorescence intensity ratios of three sets of lines in this spectrum. Similar results are observed from the yttrium-aluminum garnet host. The time dependences are much stronger at high temperatures than at low temperatures. However, above 200 K no site selection can be detected probably due to the phonon broadening of the terminal state of the pumping transitions. Below about 25 K the time dependence of the relative intensities ratios of ions in different types of sites is essentially negligible in the  $\text{Y}_3\text{Ga}_5\text{O}_{12}:\text{Nd}^{3+}$  sample. At these lowest temperatures in the  $\text{Y}_3\text{Al}_5\text{O}_{12}:\text{Nd}^{3+}$  sample the relative intensity ratios vary with time in the opposite direction as that observed at high temperatures. An example of this time dependence is shown in Fig. 10.

#### D. Analysis

The time-resolved site-selection results on energy transfer between ions in different types of crystal field sites described above can be analyzed, using a simple two site model with the rate parameters shown in Fig. 11. The rate equations for the populations of the excited states of the two sites can be written as

$$\frac{dn_s}{dt} = W_s - \beta n_s - \omega_s n_s + \omega_a n_a \quad (6)$$

$$\frac{dn_a}{dt} = W_a - \beta n_a + \omega_s n_s - \omega_a n_a \quad (7)$$

where  $W_s$  and  $W_a$  are the pumping rates,  $\beta$  is the intrinsic fluorescence decay rate,  $\omega_s$  and  $\omega_a$  are the energy transfer and back transfer rates between the sensitizer and activator sites and  $\Delta E$  is the energy mismatch between the excited levels of the ions in the two sites. In order to solve these equations a specific mechanism must be assumed for the energy transfer process to determine the time dependence of the transfer rate.

First let us consider the data obtained on the  $Y_3Ga_5O_{12}:Nd^{3+}$  sample. The energy transfer was characterized for an excitation wavelength of 5886 Å. At low temperature it was difficult to detect any time dependence of the relative fluorescence intensities, and it is concluded that very little energy transfer is taking place. At 100 K a distinct time dependence is observed as shown in Fig. 9. The three lines treated as sensitizer intensities all appear to be associated with transitions from Nd ions in the same crystal field subset and all the activator lines are from transitions from ions in a different subset. It was found that the best fits to these data could be obtained only by assuming a time independent energy transfer rate with no back transfer. Then treating the pumping rates as delta functions, Eqs. (6) and (7) can be solved for constant  $\omega_a$  and  $\omega_s$  to give

$$I_a/I_s = K \left[ \frac{(\omega_s/\omega_a)(1+n_{ao}/n_{so}) - (\omega_s/\omega_a - n_{ao}/n_{so})e^{-(\omega_s+\omega_a)t}}{(1+n_{ao}/n_{so}) + (\omega_s/\omega_a - n_{ao}/n_{so})e^{-(\omega_s+\omega_a)t}} \right] \quad (8)$$



where K represents the ratio of the oscillator strengths and branching ratios for the transitions of the ions in the different crystal field sites. The average value of the energy transfer rate needed to give the solid line fits to the data for the three sets of transitions is listed in Table 1. The best fits were found with  $\omega_a = 0 \text{ sec}^{-1}$ .

The data for the  $\text{Y}_3\text{Al}_5\text{O}_{12}:\text{Nd}^{3+}$  are more difficult to interpret since the transfer proceeds in one direction at 15 K and in the opposite direction at higher temperatures. The low temperature data in Fig. 10 can be fit by either Eq. (8) or a similar equation with the transfer rate replaced by  $\omega \rightarrow \omega t^{-1/2}$  to show an explicit time dependence. As the solid and dashed lines in that figure indicate, the  $t^{-1/2}$  time dependence for the transfer rate gives a somewhat better fit to the data than the constant rate but the latter can not be ruled out by this analysis. The fitting parameters are listed in Table 1.

The temperature dependence of the energy transfer rate can be determined from Eq. (8) and measurements at very short and long times after the laser pulse. The results for the  $\text{Y}_3\text{Ga}_5\text{O}_{12}:\text{Nd}^{3+}$  are shown in Fig. 12. Above about 30 K the transfer rate is found to increase exponentially with an activation energy of about  $83 \text{ cm}^{-1}$ . In analyzing these data the factor K accounting for differences in branching ratios is taken to be independent of temperature. A similar analysis was made of the  $\text{Y}_3\text{Al}_5\text{O}_{12}:\text{Nd}^{3+}$  data and an exponential temperature dependence was again found for the transfer rate as shown in Fig. 11. In this case the weak energy transfer observed at low temperatures was treated as a temperature independent back transfer process at high temperatures. The activation energy is about  $140 \text{ cm}^{-1}$ .

#### E. Interpretation

Since the observed energy transfer rate is found to be independent of time, energy migration among sensitizer ions may be treated in the diffusion

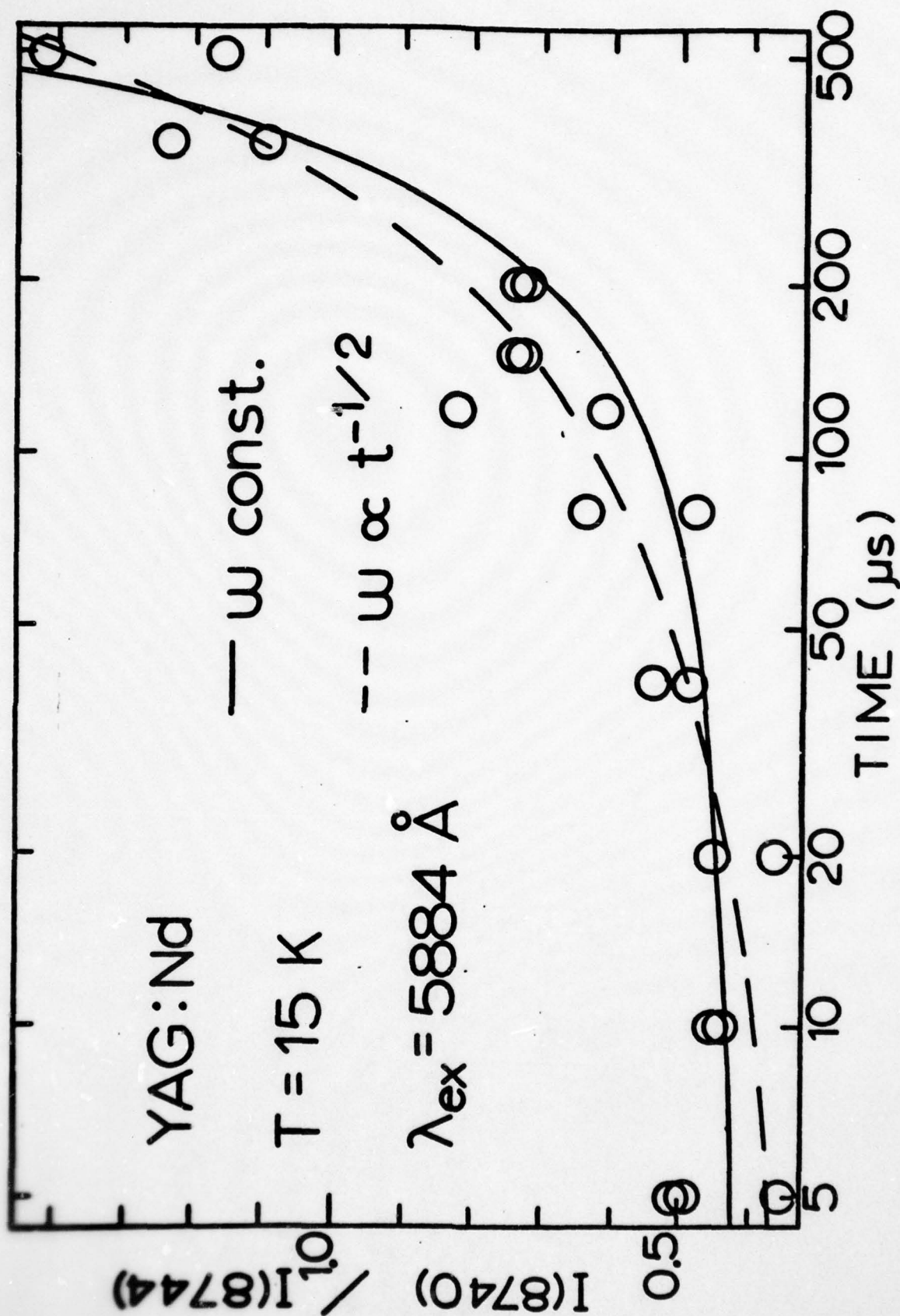


Fig. 10. Time dependence of the integrated fluorescence intensity ratios of lines from  $\text{Nd}^{3+}$  ions in different crystal field sites in  $\text{Y}_3\text{Al}_5\text{O}_{12}$  at 15 K. (See text for explanation of theoretical lines.)

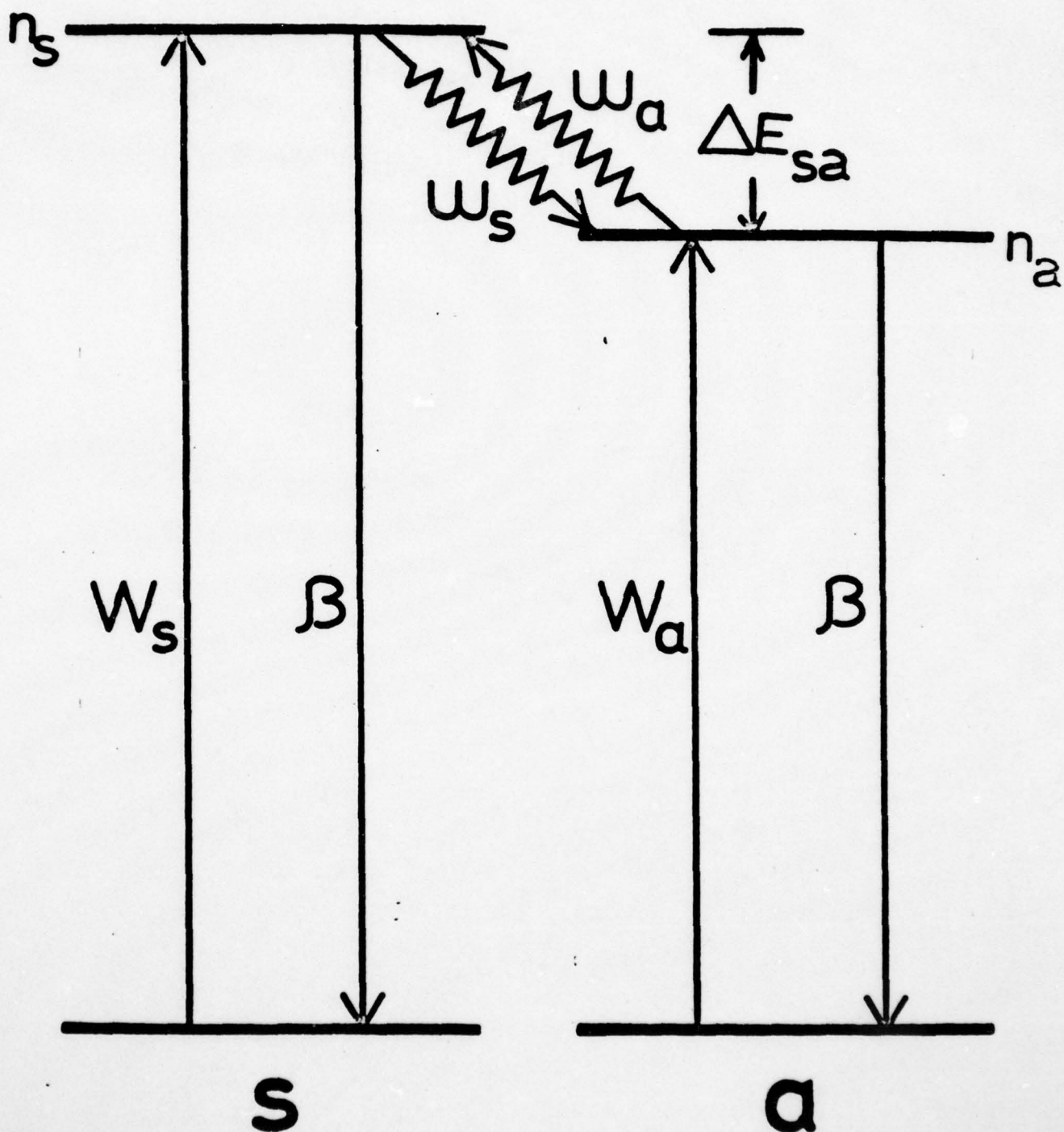


Fig. 11. Energy level and transition rate model used for explaining energy transfer between  $\text{Nd}^{3+}$  ions in different crystal field sites. (See text for explanation of symbols.)



TABLE 1: Energy Transfer Parameters

	$\text{Y}_3\text{Al}_5\text{O}_{12}:\text{Nd}^{3+}$ ( $1.18 \times 10^{20} \text{ cm}^{-3}$ )	$\text{Y}_3\text{Ga}_5\text{O}_{12}:\text{Nd}^{3+}$ ( $3.24 \times 10^{19} \text{ cm}^{-3}$ )
SPECTRAL PARAMETERS:		
$C_s (\text{cm}^{-3})$	$1.1 \times 10^{20}$	$2.7 \times 10^{19}$
$C_a (\text{cm}^{-3})$	$8.4 \times 10^{18}$	$5.4 \times 10^{18}$
$\Delta v_{ss}^{\text{inhomo}} (\text{cm}^{-1})$	$\sim 1.5$	$\sim 1.5$
$\Delta E_{sa} (\text{cm}^{-1})$	5.2	6.6
$\Delta E_{12} (\text{cm}^{-1})$	133	80
$\Gamma (\text{cm}^{-1})$	$\sim 7$	$\sim 5$
$\tau_s^0 (\text{sec}^{-1})$	$2.0 \times 10^{-4}$	$2.5 \times 10^{-4}$
ESTIMATED PARAMETERS:		
$J_{a1}^{2R6} (\text{cm}^4)$	$0.6 \times 10^{-50}$	$3.5 \times 10^{-50}$
$J_{a2}^{2R6} (\text{cm}^4)$	$12.0 \times 10^{-50}$	$3.9 \times 10^{-50}$
FITTING PARAMETERS:		
$\omega_s (\text{sec}^{-1})^*$	$3.9 \times 10^2$	$1.4 \times 10^2$
$\omega_a (\text{sec}^{-1})$	$2.5 \times 10^3$	0
$\delta (\text{cm}^{-1})$	140	83
$\Delta E_{ss} (\text{cm}^{-1})$	0.29	0.35
MODEL PARAMETERS:		
$D_o (\text{cm}^2 \text{sec}^{-1})$	$6.7 \times 10^{-10}$	$2.9 \times 10^{-10}$
$D (\text{cm}^2 \text{sec}^{-1})^{**}$	$3.5 \times 10^{-10}$	$2.0 \times 10^{-10}$
$l (\text{cm})^{**}$	$6.5 \times 10^{-7}$	$5.5 \times 10^{-7}$

\*  $T = 100 \text{ K}$ ; \*\*  $T = 295 \text{ K}$

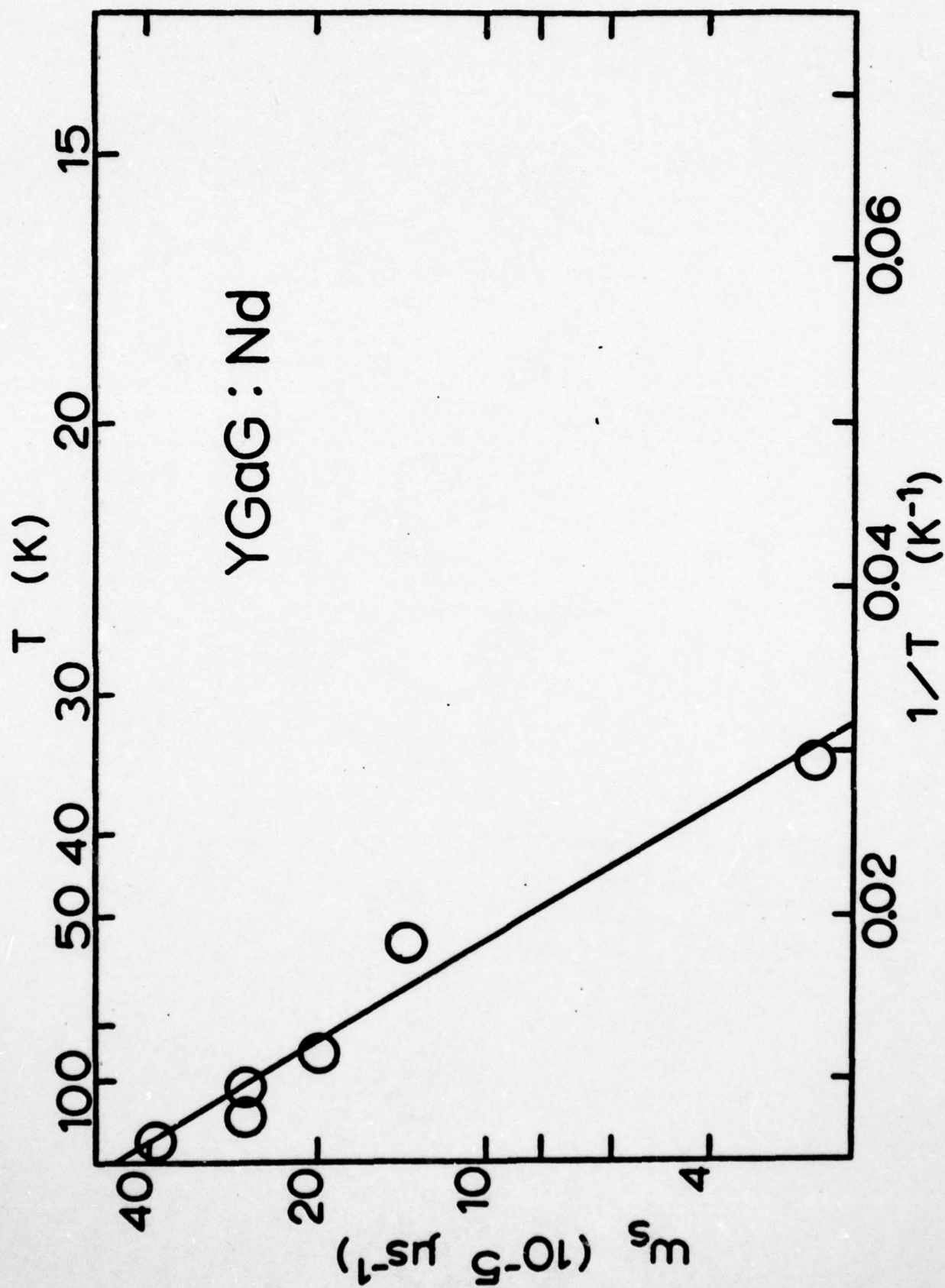


Fig. 12. Temperature dependence of the energy transfer rate between  $Nd^{3+}$  ions in nonequivalent crystal field sites in  $Y_3Ga_5O_{12}$ . (See text for explanation of theoretical line.)

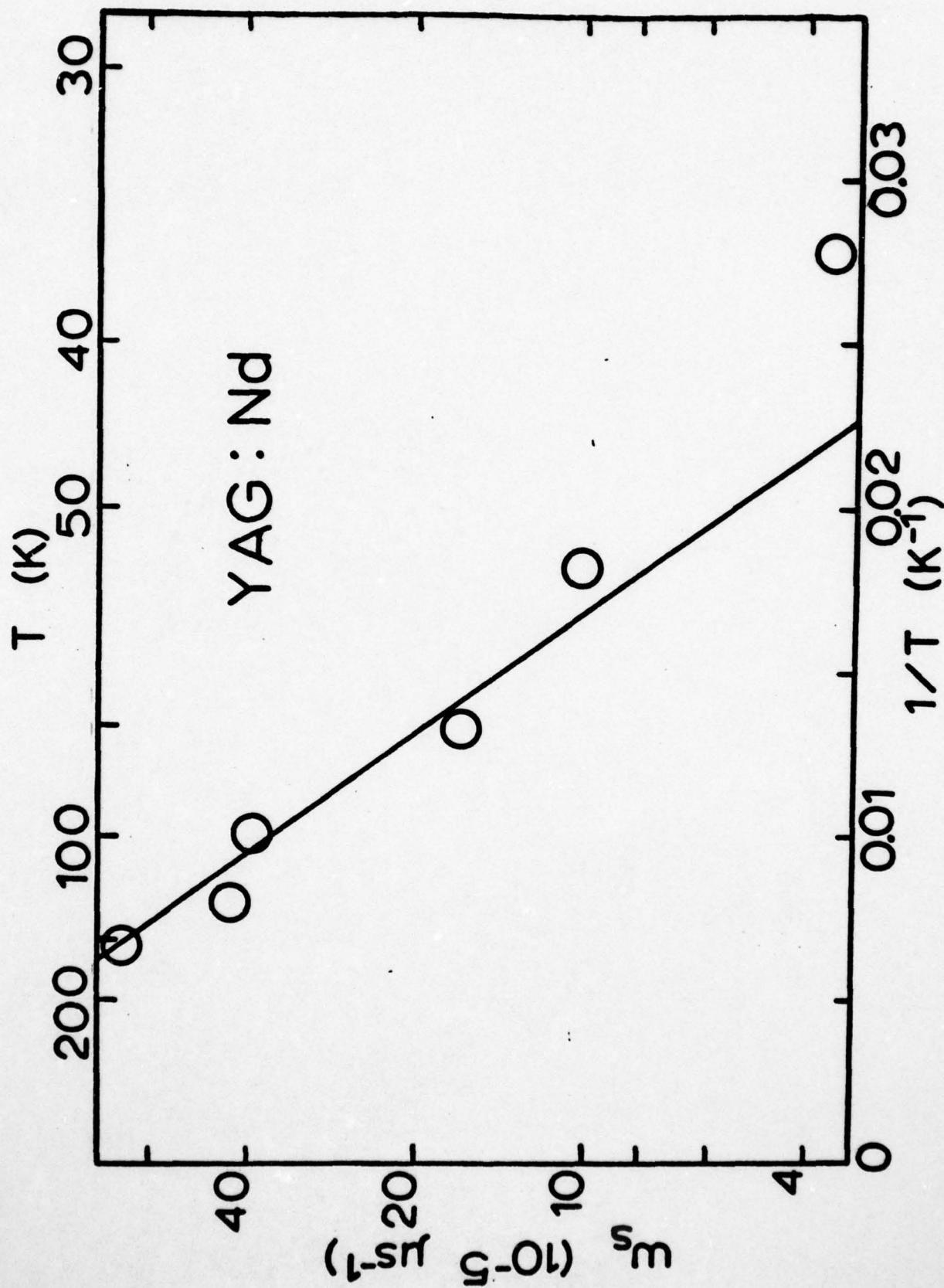


Fig. 13. Temperature dependence of the energy transfer rate between  $\text{Nd}^{3+}$  ions in nonequivalent crystal field sites in  $\text{Y}_3\text{Al}_5\text{O}_{12}$ . (See text for explanation of theoretical line.)



limited regime and the use of Eq. (6) is justified. The temperature dependence appears to be the key in understanding the energy transfer in this case. For an exciton hopping type of energy transfer phonons can effect the hopping rate in two different ways.<sup>26</sup> The first is enhanced diffusion when new transitions are thermally activated.<sup>13</sup> The activation energies for both samples are consistent with the splitting between the found state and the first excited states of the  $^4I_{9/2}$  manifold. This explanation might be reasonable for the  $Y_3Al_5O_{12}:Nd^{3+}$  sample for which the a-2 transition is much stronger than the a-1 transition. However, this is not true for the  $Y_3Ga_5O_{12}:Nd^{3+}$  sample and a consistent explanation for both samples should be expected. The second possible effect is a thermal activation required for either the hopping or trapping steps. The only way we were able to obtain the type of mechanism that appears to give a consistent fit to all of the data was by assuming that both the migration and trapping steps are themally activated by one of the two-phonon assisted energy transfer processes suggested by Holstein and coworkers<sup>5</sup> and discussed in Section III.2. The mechanism providing the good fits to the data is one in which the two phonons are in resonance with a nearby real electronic state. The transfer rate between ions i and j for this mechanism is

$$W_{ij} = [J_1^2 + J_2^2 \frac{2(\Delta E_{ij})^2}{(\Delta E_{ij})^2 + 8\Gamma^2}] (\frac{2\Gamma}{h(\Delta E_{ij})^2})^2 [1 + \exp(\Delta E_{ij}/kT)] \exp(-\delta/kT) \quad (9)$$

where  $J_1$  and  $J_2$  are the matrix elements for transfer involving the initial excited state and the ground state and for transfer involving the intermediate state reached by the phonons, respectively.  $\Delta E_{ij}$  is the energy mismatch between the transitions of the two ions involved in the transfer process,  $\delta$  is the energy of the resonant phonons, and  $\Gamma$  is the width of the intermediate state reached by the phonons. For the Nd-Nd energy transfer considered here the

exponential factor involving  $\delta$  dominates the temperature dependence and is consistent with the splitting of the lowest two components of the  $^4I_{9/2}$  ground state manifold.

If both sensitizer-sensitizer and sensitizer-activator interactions are described by the expression for two-phonon assisted energy transfer given in Eq. (9) the measured transfer rate is expressed as

$$\omega_s = 71.6 C_a C_s R_{Nd}^6 (\Gamma/h) (1 + e^{\Delta E_{sa}/kT})^{1/4} \left[ \frac{J_1^2}{\Delta E_{ss}^2} + \frac{J_2^2}{4\Gamma^2} \right]^{3/4}$$

$$X \left[ \frac{J_1^2}{\Delta E_{sa}^2} + \frac{2J_2^2}{\Delta E_{sa}^2 + 8\Gamma^2} \right]^{1/4} [e^{-\delta/kT}] \quad (10)$$

where it has been assumed that  $\Delta E_{ss}$  is small compared to  $\Gamma$  and  $kT$ .

The solid lines in Figs. 10 and 11 represent the best fits to the data given by Eq. (10) with the values for  $\delta$  being the differences between the ground and first excited state in each sample. To obtain these fits to the data it was necessary to estimate the concentrations of sensitizer and activator ions, the strengths of the matrix elements, the widths of the intermediate states reached by the phonons, the sensitizer-activator energy mismatches and an average values for the energy mismatch between sensitizer ions. Although variation of oscillator strength between ions in different sites complicates this high resolution absorption data at low temperature can be used to estimate the concentrations of ions in different sites from relative line strengths. For the types of sites investigated in  $Y_3Al_5O_{12}:Nd^{3+}$  the concentrations are  $C_s = 1.1 \times 10^{20}$  and  $C_a = 8.4 \times 10^{18} \text{ cm}^{-3}$  while for the  $Y_3Ga_5O_{12}:Nd^{3+}$  sample

they are  $C_s = 2.7 \times 10^{19}$  and  $C_a = 5.4 \times 10^{18} \text{ cm}^{-3}$ .

Kushida<sup>22</sup> has modified the general electric dipole-dipole energy transfer expression of Förster<sup>10</sup> and Dexter<sup>11</sup> to apply specifically to rare earth ions.

The squared matrix elements can be estimated from his expression

$$J_{fi}^2 = \frac{(2/3)(e^2/R^3)^2}{(2J_s + 1)(2J_a + 1)} \left[ \sum_k \Omega_{sk} | \langle J_a | U^{(k)} | J_s' \rangle |^2 \right] \left[ \sum_k \Omega_{ak} | \langle J_a | U^{(k)} | J_a' \rangle |^2 \right] \quad (11)$$

where f and i indicate the final and initial states of the system R is the separation between the two ions and the  $\Omega$  are the Judd-Ofelt parameters. The latter have been determined by Krupke<sup>27</sup> and for the  $^4F_{3/2} - ^4I_{9/2}$  transitions the expression for the squared matrix element becomes

$$J_{fi}^2 = (1.39 \times 10^{-23}) \frac{ch^2 \lambda^2}{(n^2 + 2)^4 \pi^7 R^6} (\text{erg}^2) \quad (12)$$

where n is the refractive index of the crystal at the wavelength of the fluorescence  $\lambda$ . A factor for the branching ratio must be included to determine the squared matrix elements for specific transitions between individual crystal field levels within the ground and excited multiplets. For the two transitions of interest in expression (10) the squared matrix elements have the values

$$\begin{aligned} J_{a1}^2 &= 0.6 \times 10^{-50} R_{Nd}^{-6} \text{ cm}^4; J_{a2}^2 = 12.0 \times 10^{-50} R_{Nd}^{-6} \text{ cm}^4; Y_3Al_5O_{12}:Nd^{3+} \\ J_{a1}^2 &= 3.5 \times 10^{-50} R_{Nd}^{-6} \text{ cm}^4; J_{a2}^2 = 3.9 \times 10^{-50} R_{Nd}^{-6} \text{ cm}^4; Y_3Ga_5O_{12}:Nd^{3+} \end{aligned} \quad (13)$$

The level width of the intermediate state can be taken from measured spectral data to be about  $7 \text{ cm}^{-1}$  for the aluminum garnet host and about  $5 \text{ cm}^{-1}$  for the gallium garnet. Also, the sensitizer-activator energy mismatches are measured to be about  $5.2 \text{ cm}^{-1}$  for the aluminum garnet sample and  $6.6 \text{ cm}^{-1}$  for the gallium garnet.



The various estimated values of the parameters given in the preceding three paragraphs can be substituted into Eq. (10). The remaining unknown parameter in the equation is the average transition energy mismatch between two sensitizer ions. An upper bound on  $\Delta E_{ss}$  is the inhomogeneous linewidth for the sensitizer transitions,  $\Delta E_{ss}^2$  inhom which is measured to be of the order of one and a half wave numbers. The best fits to the data using Eq. (10) are shown as solid lines in Figs. 10 and 11. They required values of  $\Delta E_{ss}$  of about one-third of a wave number which is somewhat less than the inhomogeneous linewidth as expected.

With the estimated parameters and those obtained from fitting the data, it is now possible to obtain a value for the diffusion coefficient from Eqs. (5) and (9) with the temperature dependence expressed explicitly as

$$D = D_0 e^{-\delta/kT}. \quad (14)$$

The values of  $D_0$  and  $D$  at room temperature are listed in Table 1. The diffusion length  $l$  can be estimated from the expression<sup>26</sup>

$$l = \sqrt{6D\tau_s^0} \quad (15)$$

Again the room temperature values of this parameter are listed in Table 1. Note that the extrapolation of these parameters to room temperature may not give exact values but it provides useful estimates for comparison to other data obtained at room temperature.

#### F. Discussion and Conclusions

To summarize, the time dependent and temperature dependent data obtained on energy transfer between  $Nd^{3+}$  ions in two different garnet host crystals can only be explained by a multistep energy migration process where both the

hopping between ions in similar types of sites and the transfer of energy to ions in nonequivalent crystal field sites take place by a two-phonon assisted mechanism involving resonant transitions between the ground and first excited states. For both hosts the sites which are selectively excited by the narrow band laser pulse are the dominant types of sites for  $\text{Nd}^{3+}$  ions in the lattice whereas there are significantly less  $\text{Nd}^{3+}$  ions in activator type sites. The nature of the different types of crystal field sites is not known but the dominant sensitizer sites may be  $\text{Nd}^{3+}$  ions in unperturbed  $\text{Y}^{3+}$  lattice sites whereas the less populous activator sites may be  $\text{Nd}^{3+}$  ions in sites near to lattice defects or impurities which alter the local crystal field environment. It is well known that substitutional impurities purposely introduced into the garnet lattice produce a variety of sites with different transition energies for  $\text{Nd}^{3+}$  ions.<sup>23,28</sup> It should be noted that time independent energy transfer rate could also indicate single-step transfer between sensitizer-activator pairs all at the same fixed distances. This type of distribution is not physically reasonable unless some clustering of  $\text{Nd}^{3+}$  ions occurs. Clustering, however, would lead to cross-relaxation quenching which is not observed.

The major complication in interpreting the results is the complex nature of the system. The excitation energy is migrating on a lattice of randomly distributed sites with a superimposed random distribution of transition energies. No exact method for treating this problem has been developed, and it may be that numerical techniques are the only possible solution.<sup>5,6</sup> The theoretical approach used here assumes that the inhomogeneities in the transition energies are more important in determining energy transfer characteristics than the inhomogeneities in the spatial distribution of ions. Thus, the expression describing exciton diffusion in Eqs. (3), (5) and (15) are all based on a uniform distribution of ions with the transition energy inhomogeneities

sensitizer concentrations, the diffusion coefficient for Nd excitons will be intrinsically larger in the  $\text{Y}_3\text{Al}_5\text{O}_{12}$  host compared to the  $\text{Y}_3\text{Ga}_5\text{O}_{12}$  host due to the increased values of the matrix elements in Eq. (9) which make  $W_{ss}$  larger in Eq. (5). Note that increased inhomogeneous broadening will decrease  $D_0$  by decreasing  $W_{ss}$  in Eq. (5). There are two previous estimates of the energy diffusion characteristics for the  $\text{Y}_3\text{Al}_5\text{O}_{12}:\text{Nd}^{3+}$  system. Danielmeyer, Blatte and Balmer<sup>31</sup> theoretically estimated a diffusion length of about  $500\text{\AA}$  from spectral considerations and Danielmeyer<sup>32</sup> determined the anomalously large value of  $D = 5 \times 10^{-7} \text{ cm}^2 \text{ sec}^{-1}$  for a sample containing only 0.4%  $\text{Nd}^{3+}$  from analyzing its single-mode laser operation. The time-resolved site-selection technique utilized in the experiments reported here is the most direct way of characterizing the energy migration reported thus far.

In conclusion, laser-excited time-resolved site-selection spectroscopy has been used to characterize the transfer of energy among  $\text{Nd}^{3+}$  ions in two types of garnet host crystals and the results interpreted in terms of an exciton diffusion and trapping model. Both the diffusion and trapping mechanisms are consistent with the predictions of one of the new theoretical models for two-phonon assisted transfer processes. The migration parameters obtained in this way are consistent with those obtained for other similar systems but it is obvious that there is an important need for an exact way to theoretically treat cases of energy migration on a random lattice.

#### REFERENCES

- [1] H. G. Danielmeyer in "Lasers, Vol. 4", ed. A. K. Levine and A. J. DeMaria (Dekker, New York, 1976) p. 1.
- [2] R. C. Powell in "Luminescence of Inorganic Solids", ed. B. DiBartolo (Plenum, New York, 1978).



- [3] N. Motegi and S. Shionoya, *J. Luminescence* 8, 1 (1973); R. Flach, D. S. Hamilton, P. S. Selzer, and W. M. Yen, *Phys. Rev. B* 15, 1248 (1977); P. M. Selzer, D. S. Hamilton and W. M. Yen, *Phys. Rev. Letters* 38, 858 (1977); D. S. Hamilton, P. M. Selzer, and W. M. Yen, *Phys. Rev. B* 16, 1858 (1977); P. M. Selzer, D. L. Huber, B. B. Barnett, and W. M. Yen, *Phys. Rev. B* 17, 4979 (1978); R. Flach, D. S. Hamilton, P. S. Selzer and W. M. Yen, *Phys. Rev. Lett.* 35, 1034 (1975).
- [4] C. Hsu and R. C. Powell, *Phys. Rev. Lett.* 35, 734 (1975); C. Hsu and R. C. Powell, *J. Phys. C* 9, 2467 (1976); G. E. Venikouas and R. C. Powell, *Phys. Rev. B* 17, 3456 (1978); L. D. Merkle and R. C. Powell, *J. Chem. Phys.* 67, 371 (1977); D. R. Tallant and J. C. Wright, *J. Chem. Phys.* 63, 2074 (1975); M. D. Kurz and J. C. Wright, *J. Luminescence* 15, 169 (1977).
- [5] T. Holstein, S. K. Lyo and R. Orbach, *Phys. Rev. Lett.* 36, 891 (1976); T. Holstein, S. K. Lyo and R. Orbach, *Phys. Rev. B* (to be published).  
A preliminary account of this work was presented at the Colloque International du Centre National de la Recherche Scientifique, 1976 (unpublished).
- [6] D. L. Huber, D. S. Hamilton and B. Barnett, *Phys. Rev. B* 16, 4642 (1977); W. Y. Ching, D. L. Huber, and B. Barnett, *Phys. Rev. B* 17, 5025 (1978).
- [7] R. K. Watts, in "Optical Properties of Ions in Solids", ed. B. DiBartolo (Plenum, New York, 1975).
- [8] L. A. Riseberg and M. J. Weber, *Progress in Optics* 14, 1 (1975).
- [9] M. Yokota and O. Tanimoto, *J. Phys. Soc. Japan* 22, 779 (1967).
- [10] T. Förster, *Ann. Physik* 2, 55 (1948); *Z. Naturforsch.* 49, 321 (1949).
- [11] D. L. Dexter, *J. Chem. Phys.* 21, 836 (1953).
- [12] K. B. Eisenthal and S. Siegel, *J. Chem. Phys.* 41, 652 (1964).

- [13] M. J. Weber, Phys. Rev. B 4, 2932 (1971).
- [14] W. B. Gangrud and H. W. Moos, J. Chem. Phys. 49, 2170 (1968).
- [15] Y. A. Kurskii and A. S. Selivanenko, Opt. i Spektroskopiya 8, 340 (1960).
- [16] A. J. Burshtein, Sov. Phys. JETP 35, 882 (1972).
- [17] Z. G. Soos and R. C. Powell, Phys. Rev. B 6, 4035 (1972).
- [18] S. Chandrasekhan, Rev. Mod. Phys. 15, 1 (1943).
- [19] M. Trlifaj, Czech. J. Phys. 5, 463 (1955); 6 533 (1956); 8, 510 (1958).
- [20] E. W. Montroll and G. H. Weiss, J. Math. Phys. 6, 167 (1965).
- [21] D. D. Smith, R. C. Powell, and A. H. Zewail, unpublihsed.
- [22] T. Kushida, J. Phys. Soc. Japan 34, 1318 (1973); *ibid*, 1327; *ibid*, 1334.
- [23] R. K. Watts and W. C. Holton, J. Appl. Phys. 45, 873 (1974).
- [24] J. A. Koningstein, J. Chem. Phys. 44, 3957 (1966).
- [25] A. A. Kaminskii, G. A. Bogomolova, D. N. Vylegzhanin, Kh. S. Bagdasarov, A. M. Kevorkov, and M. M. Gritsenko, Phys. Stat. Sol. (a) 38, 409 (1976).
- [26] R. C. Powell and Z. G. Soos, J. Luminescence 11, 1 (1975).
- [27] W. F. Krupke, IEEE J. Quant. Elec QE-7, 153 (1971).
- [28] L. A. Riseberg and W. C. Holton, J. Appl. Phys. 43, 1876 (1972); L. A. Riseberg, R. M. Brown, and W. C. Holton, Appl. Phys. Lett. 23, 127 (1973); L. A. Riseberg and W. C. Holton, Optics Comm. 9, 298 (1973).
- [29] T. Kushida, Phys. Rev. 185, 500 (1969).
- [30] M. V. Artamonova, Ch. M. Briskina, A. I. Burshtein, L. D. Zusman and A. G. Skleznev. Sovet Phys. JETP 35, 457 (1972).
- [31] H. G. Danielmeyer, M. Blatte, and P. Balmer, Appl. Phys. 1, 269 (1973).
- [32] H. G. Danielmeyer, J. Appl. Phys. 42, 3125 (1971).

### V.3 Time-Resolved Site-Selection Spectroscopy of $\text{Nd}^{3+}$ Ions in Mixed Garnet Crystals

#### A. Introduction

Neodymium doped yttrium aluminum garnet has been established as one of the most important available laser systems. It has been shown that the laser properties can be altered to meet specific requirements by forming different compositions of mixed host crystals of, for example, aluminum and gallium garnets.<sup>1,2</sup> This makes it important to characterize the optical properties of mixed crystal systems and thus far only a limited amount of work has been done in characterizing the properties of  $\text{Y}_3(\text{Al}_{1-x}\text{Ga}_x)_5\text{O}_{12}:\text{Nd}^{3+}$ . In this paper we describe some of the effects of forming mixed crystals on the energy levels and dynamics of  $\text{Nd}^{3+}$  in garnet hosts. Specific emphasis is placed on studying the effects of disorder on energy transfer between the Nd ions.

Most of the previous work on this system has centered around characterizing the properties of the  $^4\text{F}_{3/2} - ^4\text{I}_{11/2}$  transitions in the region of laser action.<sup>1,2</sup> In the present work we investigated the transitions to the  $^4\text{I}_{9/2}$  ground state manifold. The shift in the position of the various crystal field levels is shown to be linear with Ga concentration. The addition of Ga also causes inhomogeneous broadening of the spectral lines and an analysis of the line shape shows the Ga ions to be generally uniformly distributed. Narrow line laser excitation shows that  $\text{Nd}^{3+}$  ions with specific Ga environments can be selectively pumped and the emission line position varies linearly with pumping wavelength.

Distinct structure appears in the spectral lines of Nd transitions in mixed crystals indicating that some sites have significantly different transitions energies from others. Tunable, pulsed dye laser excitation was used to selectively pump ions in one type of site and the time evolution of the spectrum



AD-A066 086

OKLAHOMA STATE UNIV STILLWATER DEPT OF PHYSICS

F/G 20/5

MULTISTEP ENERGY MIGRATION AND RADIATIONLESS RELAXATION PROCESS--ETC(U)

DEC 78 R C POWELL

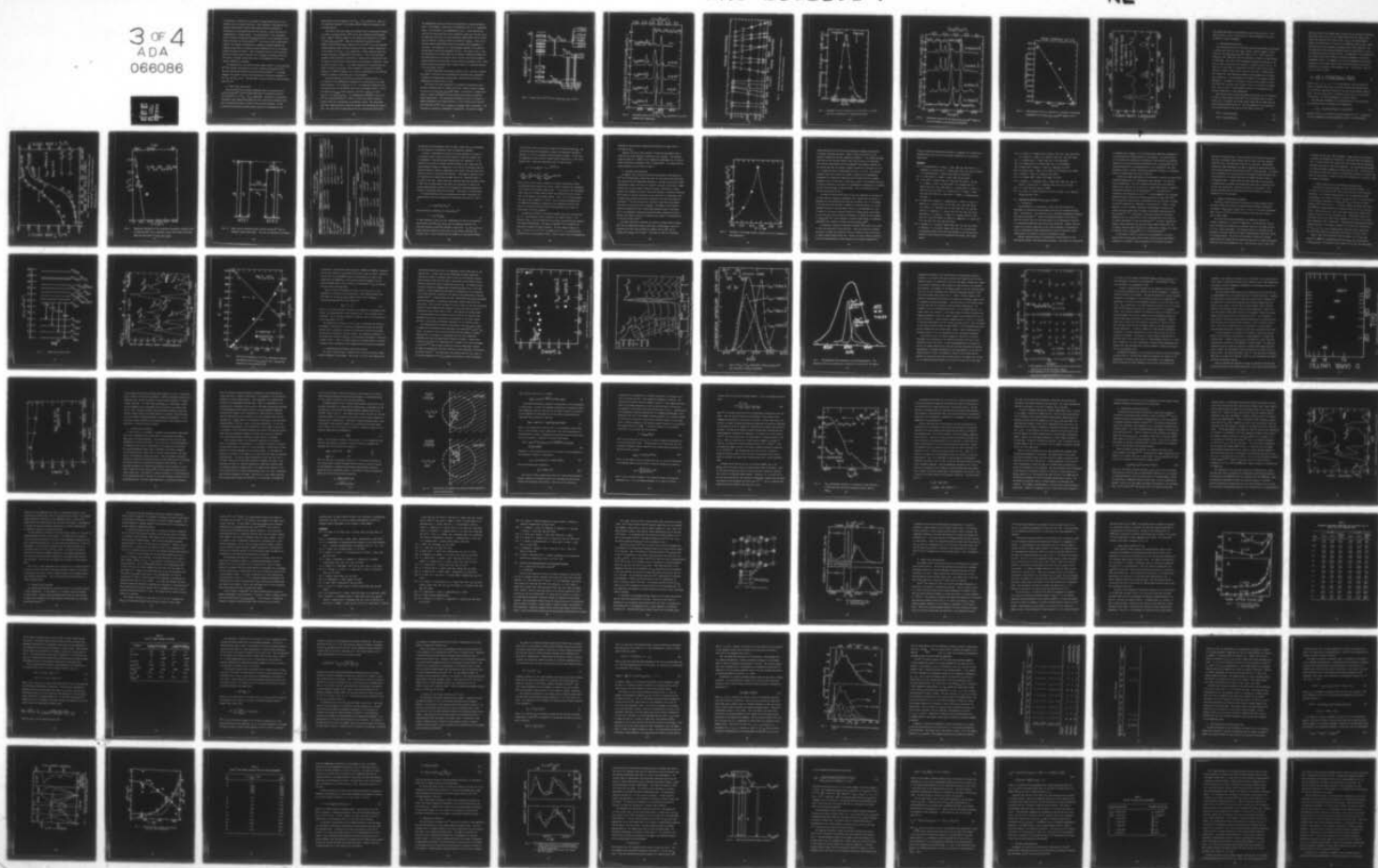
DAAG29-76-G-0099

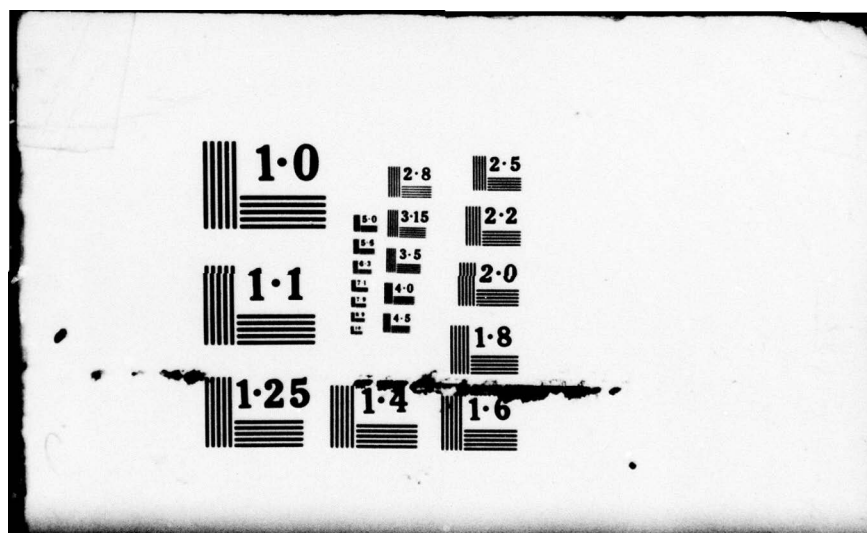
UNCLASSIFIED

ARO-13318.8-P

NL

3 OF 4  
ADA  
066086





was monitored to characterize the transfer of energy between Nd ions in two different types of crystal field sites. This technique of time-resolved site-selection spectroscopy<sup>3</sup> and the similar higher resolution technique of fluorescence line narrowing<sup>4</sup> have been used recently to probe the effects of inhomogeneities on energy transfer. The greater detail of the experimental results available through these techniques has lead to the requirement for new theoretical models for energy transfer.<sup>5,6</sup> For the case of Nd in mixed garnet crystals, the transfer is explained by a thermally activated migration and trapping process where the thermal activation mechanism is one of the recently proposed two-phonon processes.<sup>5</sup> This is consistent with the results reported earlier for energy transfer among Nd ions in  $Y_3Al_5O_{12}$  and  $Y_3Ga_5O_{12}$  hosts<sup>7</sup> and the effects of forming a mixed crystal host on the magnitude of the energy transfer parameters is discussed.

The samples used in this study were good single crystals of  $Y_3(Al_{1-x}Ga_x)_5O_{12}:Nd^{3+}$  with varying concentrations of Ga each containing approximately 1% Nd. The laser spectroscopy apparatus has been described elsewhere.<sup>8</sup> It provides pumping in the region of the spectrum consisting of the various components of the  $^2G_{7/2}$  and  $^4G_{5/2}$  levels. The band width is about 0.4Å and the time resolution about 0.1 μsec.

#### B. Mixed Crystal Spectroscopy

Watts and Holton<sup>2</sup> have reported preliminary work on the spectra of the  $Y_3(Al_{1-x}Ga_x)_5O_{12}:Nd^{3+}$  system including differences in branching ratios and cross sections for the  $^4F_{3/2} - ^4I_{11/2}$  transitions. Variations in fluorescence wavelengths versus pumping wavelengths were also reported and transitions from ions in nonequivalent types of crystal field sites were resolved. We have continued characterizing the spectroscopic properties of neodymium in this



mixed garnet host with emphasis on the  ${}^4F_{3/2} - {}^4I_{9/2}$  transitions. These are the transitions important to the energy transfer properties discussed in the following section.

The crystal field splittings of the energy levels in mixed garnet crystals are found to be between those of  $\text{Nd}^{3+}$  ions in pure aluminum or gallium garnet hosts. Figure 1 shows an example of the energy levels observed for a crystal of  $\text{Y}_3(\text{Al}_{0.5}\text{Ga}_{0.5})_5\text{O}_{12}:\text{Nd}^{3+}$ . These are consistent with previous results. Figure 2 shows the fluorescence spectra at 14 K for  $\text{Nd}^{3+}$  ions in pure aluminum and gallium garnet hosts and mixed crystals with three different compositions in the region of the  ${}^4F_{3/2} - {}^4I_{9/2}$  transitions. Several important points can be made concerning the comparison of these spectra. First, each individual transition shifts uniformly in position as a function of Ga concentration, but the amount of shift and the direction differs with different transitions. These are shown in detail in Fig. 3. The linear variations are consistent with the linear variation in the garnet lattice parameter<sup>7,2</sup> going from 12.005 Å in  $\text{Y}_3\text{Al}_5\text{O}_{12}$  to 12.265 Å for  $\text{Y}_3\text{Ga}_5\text{O}_{12}$ , but a detailed understanding of the different shifts for different transitions has not been developed.

The second important observations concerning the spectra in Fig. 2 is the increase in the inhomogeneous broadening of the transitions as the composition parameter  $x$  is increased up to 0.5. The transition linewidths in the pure garnet hosts are much smaller than in any of the mixed crystals. For the a-2 transition  $\Delta\tilde{\nu}_{\text{inhomo}}$  varies from about  $6.39 \text{ cm}^{-1}$  in  $\text{Y}_3\text{Al}_5\text{O}_{12}$  to about  $28.9 \text{ cm}^{-1}$  in  $\text{Y}_3(\text{Al}_{0.5}\text{Ga}_{0.5})_5\text{O}_{12}$ . The inhomogeneous broadening is due to the  $\text{Nd}^{3+}$  ions being distributed in a variety of sites with slightly different crystal fields due to differences in microscopic strains. The inequivalent sites have slightly different transition energies thus broadening the spectral line. The linear shift in peak position with Ga concentration implies that

the inhomogeneous spectral profile can be explained by a simple statistical model. As an example, consider the  $a_2$  transition in the  $x = 0.5$  composition sample. This is shown at low temperatures in Fig. 4. About each Nd ions there are ten close sites that can be occupied by either Ga or Al ions. As Ga is substituted for one Al ion the Nd transition energy shifts 1/10 of the way from its position in  $Y_3Al_5O_{12}$  toward its position in  $Y_3Ga_5O_{12}$ . There are 11 different equally spaced line positions for possible Ga/Al arrangements in this model. The probability of a given arrangement depends on the number of distinct ways in which this arrangement can occur. The points in Fig. 4 show the predictions of this model which fit the observed lineshape extremely well. The slight deviation in the wings is due to the fact that we have assumed no intrinsic width to the transitions of ions in specific individual sites. These results confirm the conclusion that in general there is a random distribution of Ga ions around a Nd site.

The third observation concerning the spectra in Fig. 2 is that a significant amount of structure can be resolved in the spectral lines, especially in samples with high gallium concentrations. These are due to Nd ions in significantly different types of sites.

With narrow line laser excitation it is possible to selectively excite Nd ions in specific types of crystal field sites. Figure 5 shows an example of this for the  $Y_3(Al_{0.5}Ga_{0.5})_5O_{12}:Nd^{3+}$  sample. As the laser is scanned from shorter to longer wavelengths the peak positions and relative intensities change significantly. The fluorescence lifetimes also vary as a function of pumping wavelength in the range from 200  $\mu s$  to 250  $\mu s$  which are the fluorescence lifetimes of  $Nd^{3+}$  ions in  $Y_3Al_5O_{12}$  and  $Y_3Ga_5O_{12}$  hosts, respectively. The lifetimes are essentially independent of temperature. The spectral changes



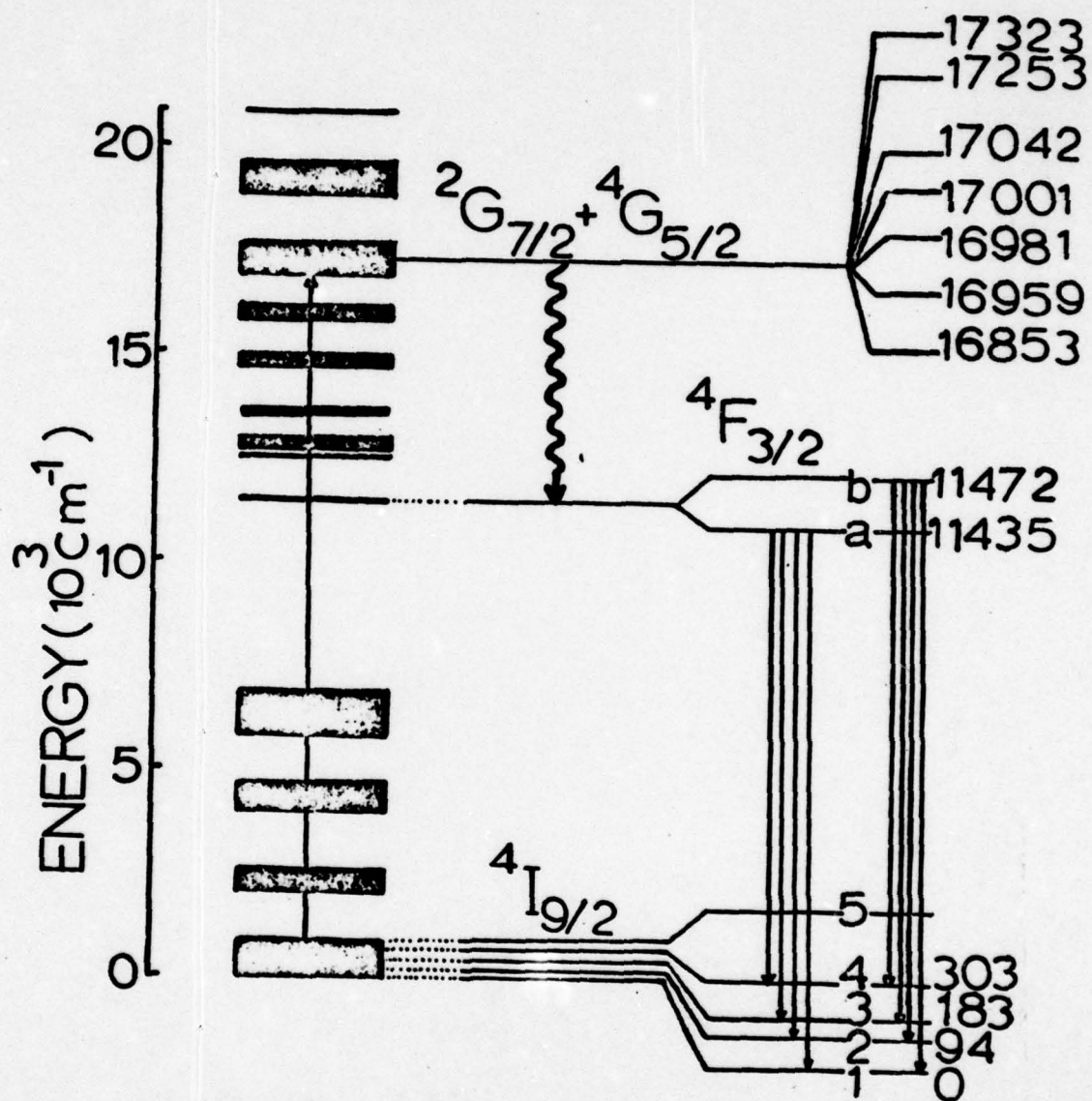


Fig. 1. Energy levels of  $\text{Nd}^{3+}$  ions in  $\text{Y}_3(\text{Al}_{0.5}\text{Ga}_{0.5})_5\text{O}_{12}$  crystals.



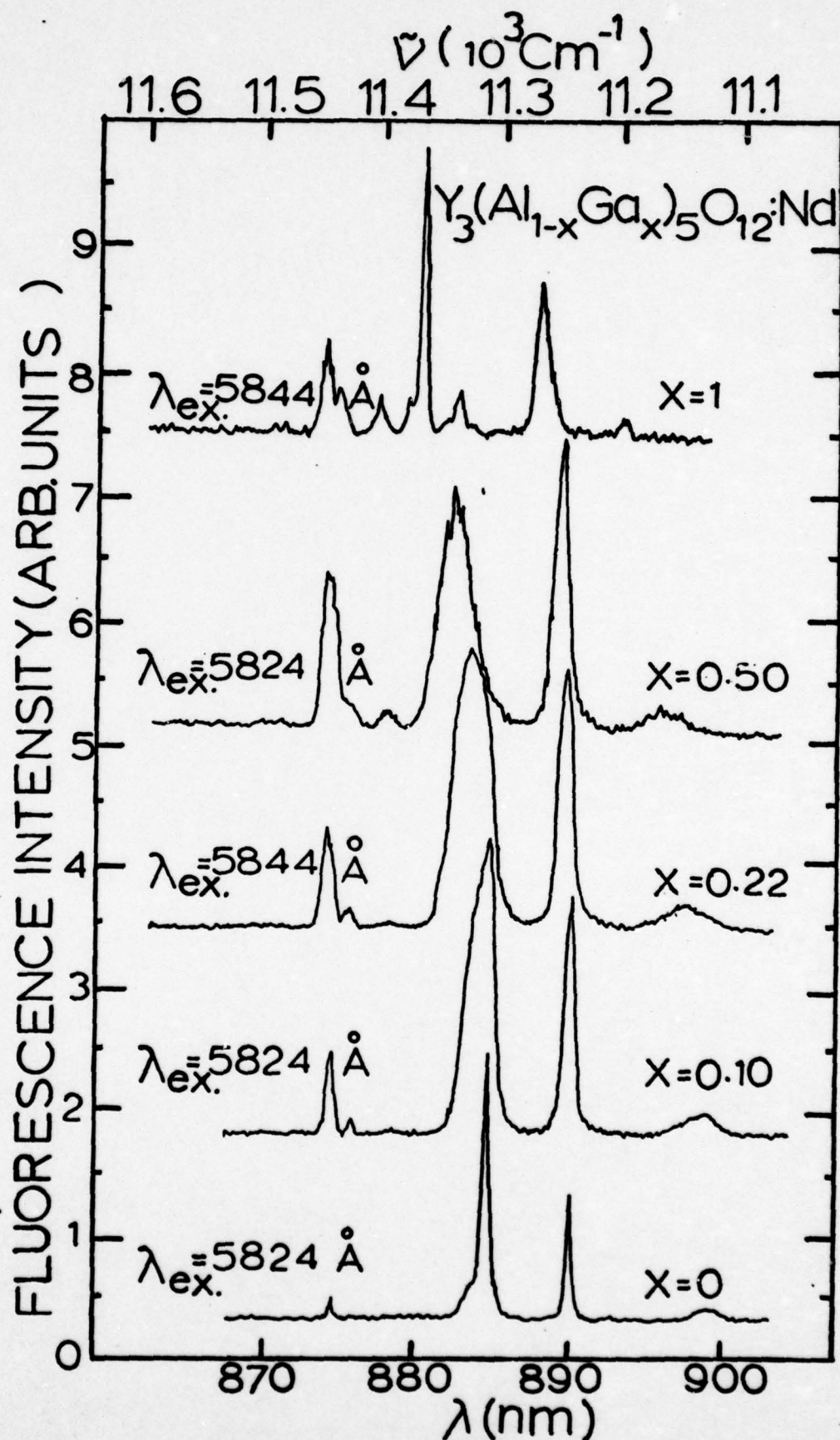


Fig. 2. Fluorescence spectra of the  ${}^4\text{F}_{3/2} - {}^4\text{I}_{9/2}$  transitions at 14 K for different host compositions.

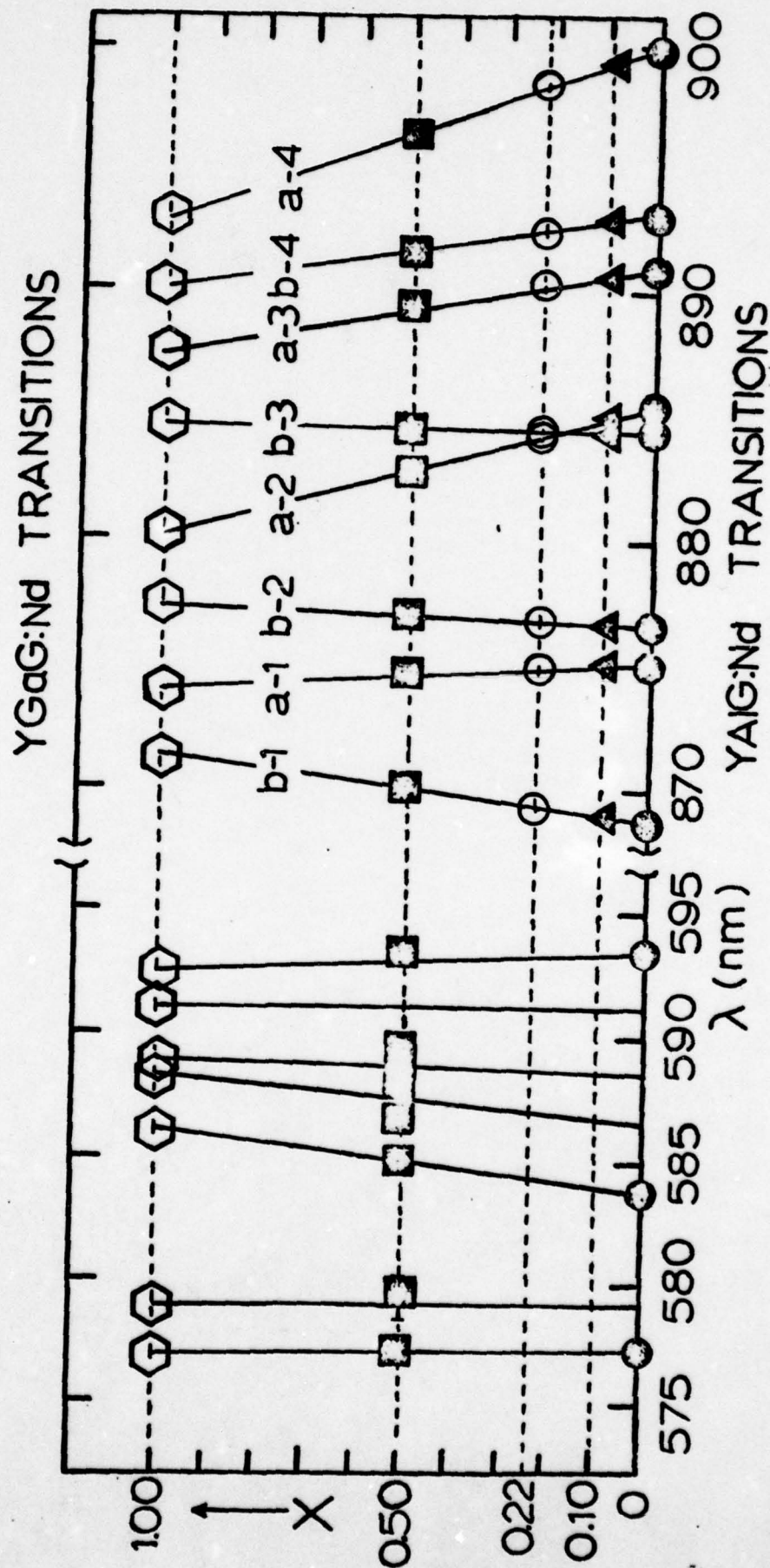


Fig. 3. Fluorescence peak positions as a function of host composition.

See Fig. 1 for transitions designations.

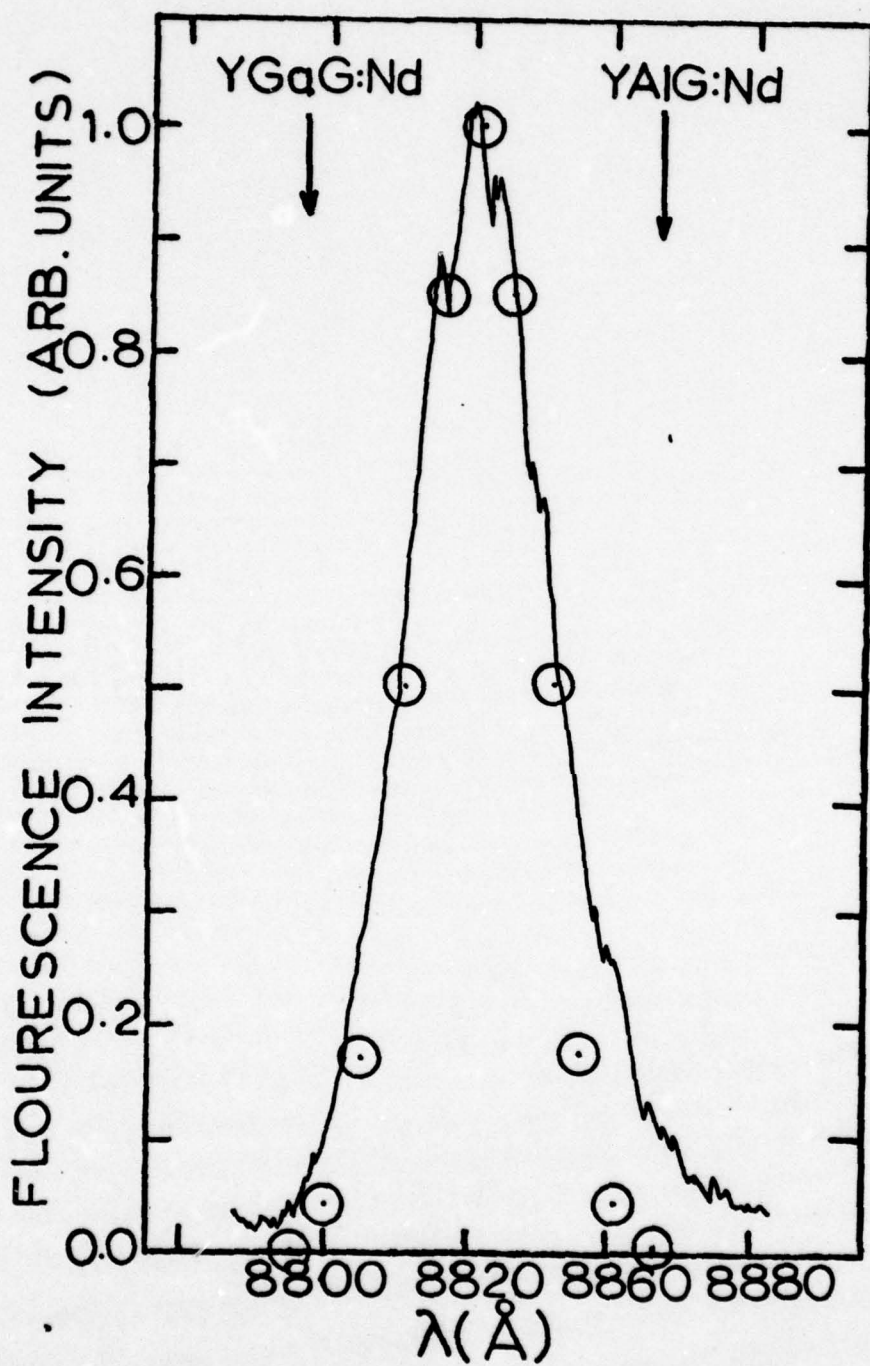


Fig. 4. Lineshape of the a-2 transition at 14 K for the  $x = 0.5$  host.

(See text for explanation of theoretical points.)



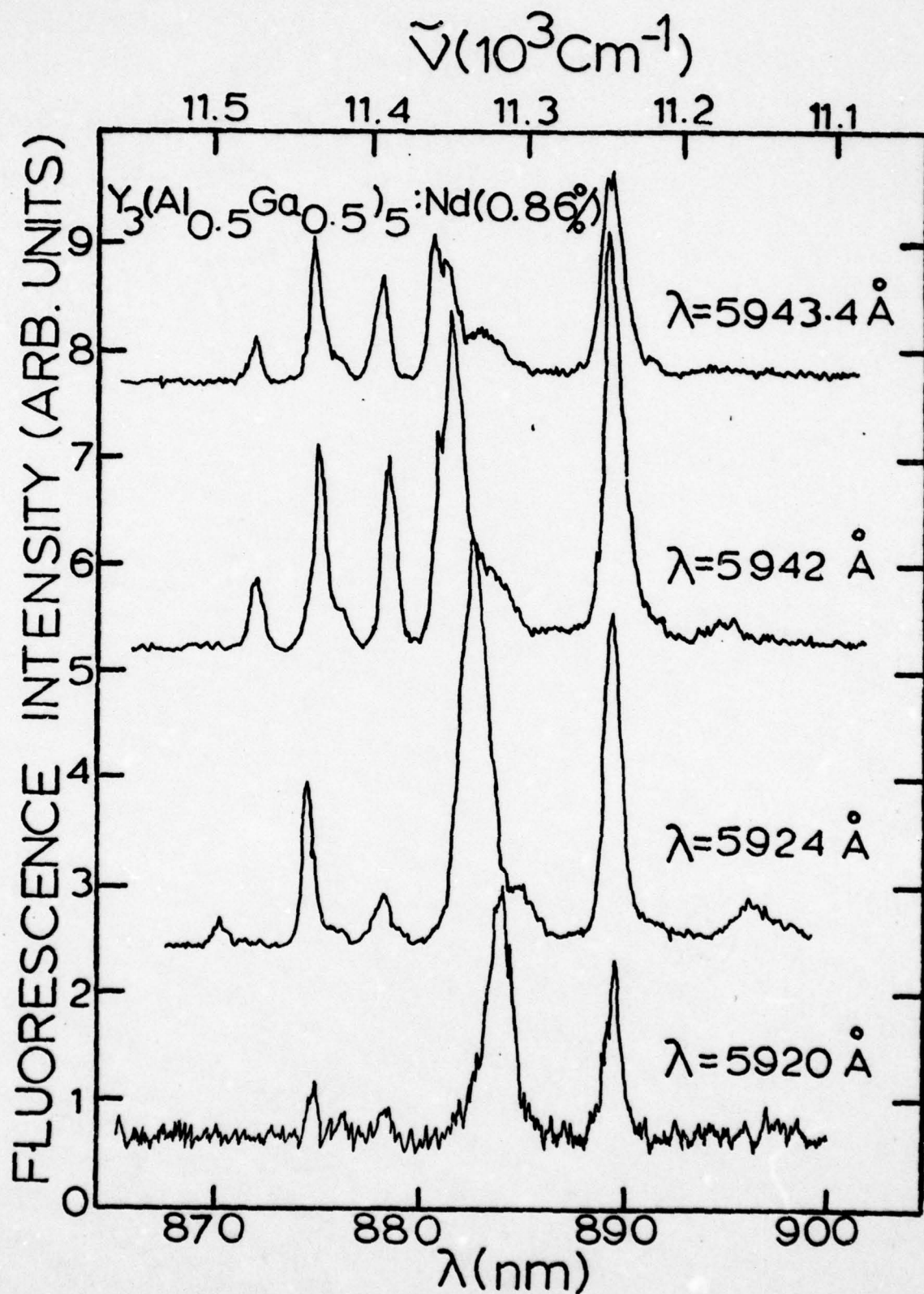


Fig. 5. Fluorescence spectra for the  $\text{Y}_3(\text{Al}_{0.5}\text{Ga}_{0.5})_5\text{O}_{12}:\text{Nd}^{3+}$  sample at 14 K for different laser excitation wavelengths.

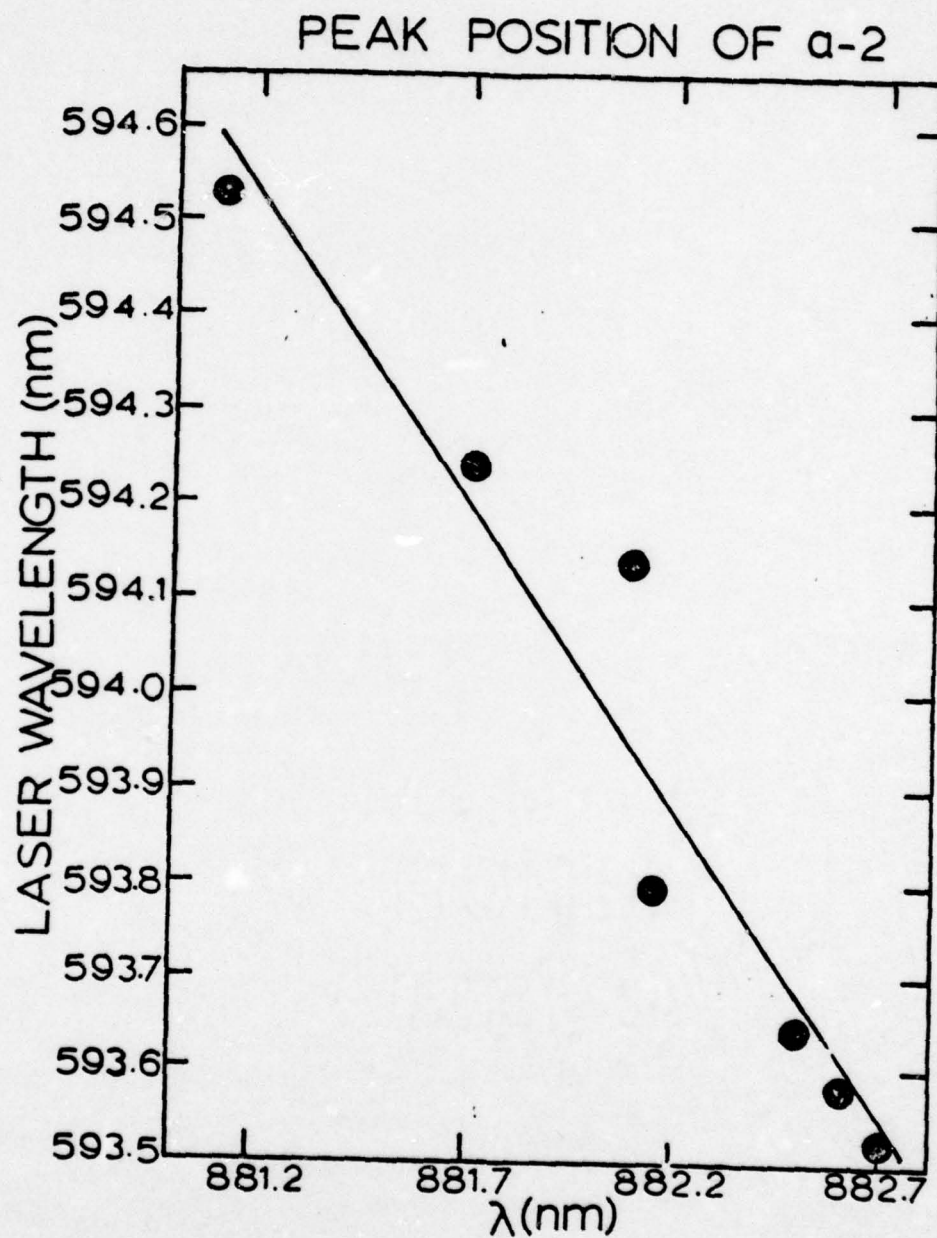


Fig. 6. Peak position of the a-2 transition as a function of excitation wavelength for the  $Y_3(Al_{0.5}Ga_{0.5})_5O_{12}:Nd^{3+}$  sample at 14 K.

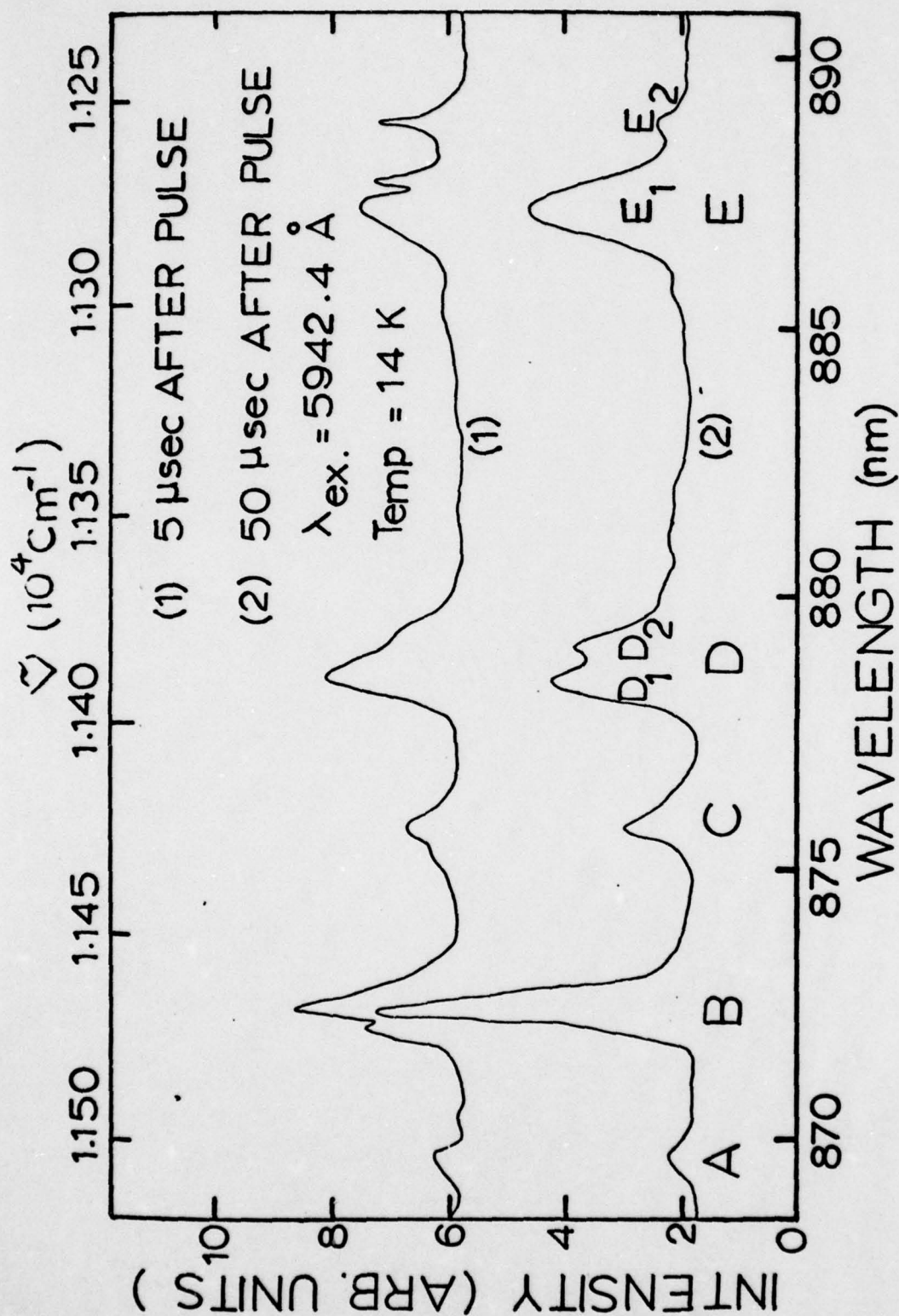


Fig. 7. Fluorescence spectra at two times after the laser pulse for the  $\text{Y}_3(\text{Al}_{0.5}\text{Ga}_{0.5})\text{O}_{12}:\text{Nd}^{3+}$  sample at 14 K.



with pumping wavelength are approximately linear as shown in Fig. 6. This shows the shift in the a-2 line position to lower wavelengths as the laser is shifted to higher wavelengths.

### C. Time-Resolved Spectroscopy

The fluorescence spectra for different excitation wavelengths were monitored at various times after the laser pulse. Figure 7 shows an example of these results for the  $Y_3(Al_{0.5}Ga_{0.5})_5O_{12}:Nd^{3+}$  sample at 14 K. Some of the lines observed at short times after the pulse decrease as a function of time relative to other lines. The ratios of the integrated fluorescence intensities of two sets of lines in these spectra are shown as a function of time in Fig. 8. For both sets of lines there is a significant increase in these ratios at short times and a tendency toward constant values at long times. Similar results were observed for other pumping wavelengths and other samples with different host compositions. The time dependence is observed to be stronger at higher temperatures. An example of the asymptotic values of the intensity ratios at long times after the laser pulse is shown in Fig. 9 as a function of temperature. They are found to be approximately constant at low temperatures and increase exponentially at high temperatures.

These time-resolved site-selection spectroscopy results can be interpreted in terms of energy transfer between  $Nd^{3+}$  ions in different types of crystal fields sites. An analysis can be made using a simple two site model with the various parameters shown in Fig. 10. The rate equations for the populations of the excited states of the ions in the two types of sites are

$$\frac{dn_s}{dt} = W_s - \beta_{ss} n_s - \omega_{ss} n_s + \omega_{as} n_a \quad (1)$$

$$\frac{dn_a}{dt} = W_a - \beta_{aa} n_a + \omega_{sa} n_s - \omega_{aa} n_a \quad (2)$$

where  $W_s$  and  $W_a$  are the pumping rates,  $\beta_s$  and  $\beta_a$  are the intrinsic fluorescence decay rates, and  $\omega_s$  and  $\omega_a$  are the energy transfer and back transfer rates between the sensitizer and activator sites.  $\Delta E_{sa}$  is the energy mismatch between the excited levels of the ions in the different types of sites. These equations can be solved treating the pumping rates as delta functions. The time dependence of the resulting population ratios is proportional to that of the observed fluorescence intensity ratios. The magnitudes of the transfer and back transfer rates can be treated as adjustable parameters in fitting the experimental results. We attempted to fit the data assuming various possible expressions for the energy transfer rates and found that good fits could be obtained only by assuming a time independent rate. The solutions to Eqs. (1) and (2) in this case give

$$\frac{I_a}{I_s} = K \frac{n_s(0)}{n_a(0)} \frac{\omega_s}{\omega_a} \frac{\{[n_a(0)/n_s(0)](\beta/\omega_s) + 1 - \exp(-\beta t)\}}{1 + \{[n_s(0)/n_a(0)](\beta/\omega_a) - 1\}\exp(-\beta t)} \quad (3)$$

where  $\beta = \beta_s + \omega_s - \beta_a - \omega_a$ .  $K$  is a proportionality factor including the ratios of radiative decay times, oscillator strengths and branching ratios for the specific transitions involved for the ions in the different types of sites. The solid lines in Fig. 8 represent the best fits to the data using this equation. The fitting parameters are listed in Table 1.

The temperature dependence of the intensity ratios at long times after the excitation pulse in this model can be expressed as

$$I_a/I_s \approx K[n_s(0)/n_a(0)](\omega_s/\omega_a) = \omega_0 \exp(-\Delta E/kT). \quad (4)$$

The data in Fig. 9 is fit with an activation energy of  $95 \text{ cm}^{-1}$ . A comparison of the low temperature and high temperature values of the time-resolved

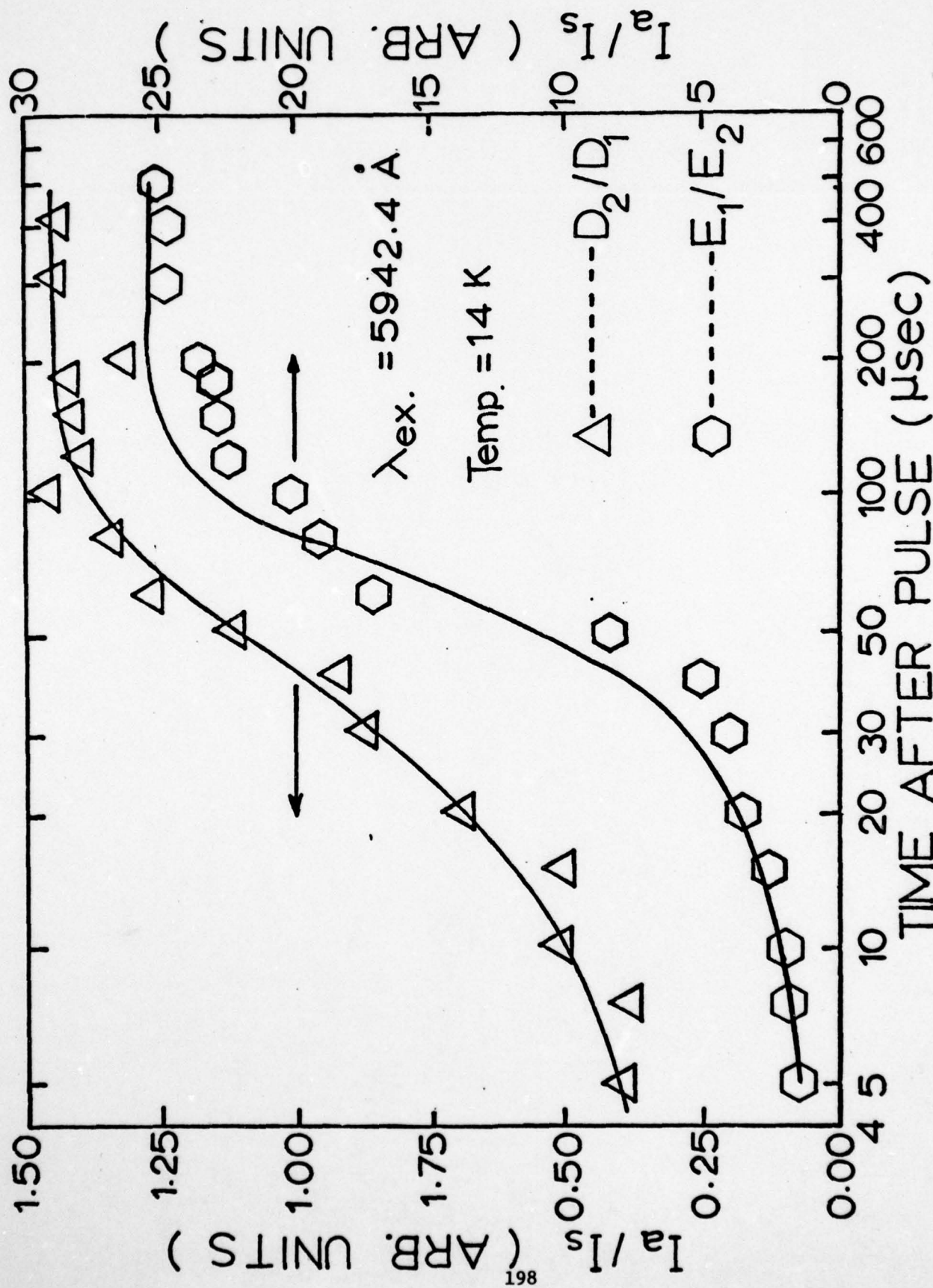


Fig. 8. Time dependence of the integrated fluorescence intensity ratios

of lines from  $\text{Nd}^{3+}$  ions in different crystal field sites in

$\text{Y}_3(\text{Al}_{0.5}\text{Ga}_{0.5})\text{O}_{12}$  at 14 K.



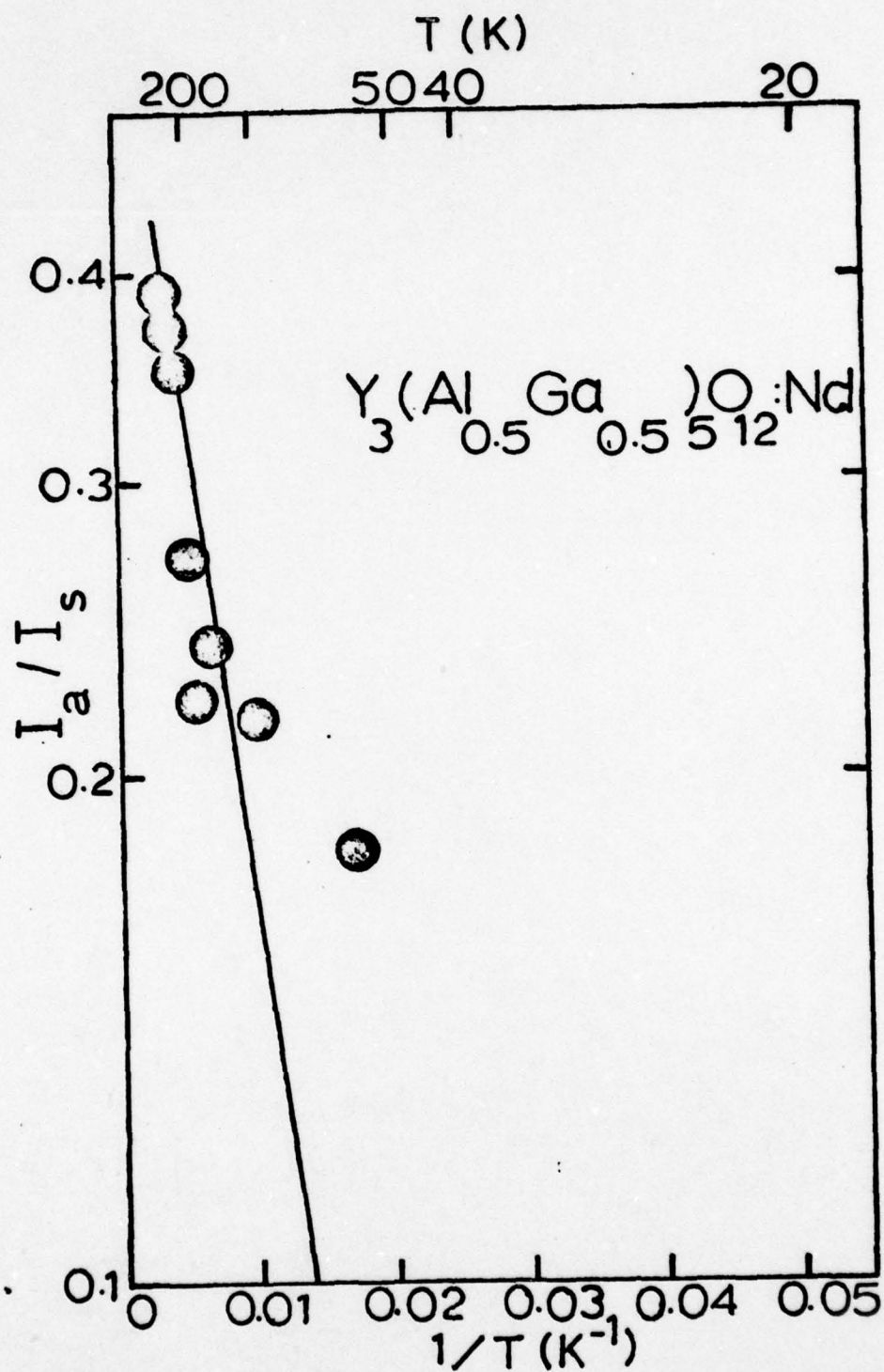


Fig. 9. Temperature dependence of the integrated fluorescence intensity ratios of lines from Nd<sup>3+</sup> ions in different crystal field sites at 250  $\mu$ sec after the laser pulse in Y<sub>3</sub>(Al<sub>0.5</sub>Ga<sub>0.5</sub>)<sub>5</sub>O<sub>12</sub>.

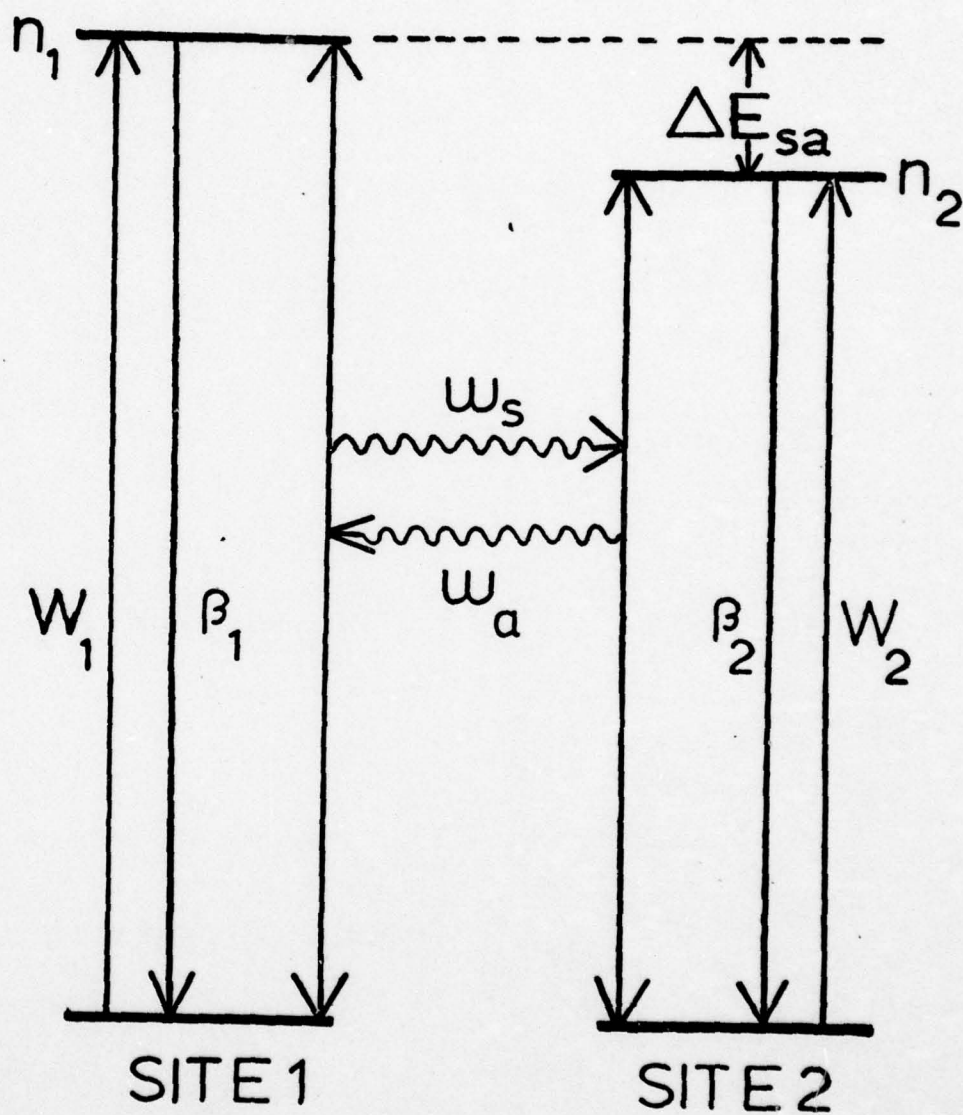


Fig. 10. Model used for explaining energy transfer between  $\text{Nd}^{3+}$  ions in different crystal field sites. (See text for explanation of symbols.)

TABLE 1: Energy Transfer Parameters

A:  $Y_3(Al_{0.5}Ga_{0.5})O_{12}:Nd^{3+}$  Sample

SPECTRAL PARAMETERS	ESTIMATED PARAMETERS	FITTING PARAMETERS	MODEL PARAMETERS
$C_s = 5.95 \times 10^{19} \text{ cm}^{-3}$	$J_{al}^2 R_{Nd}^6 = 0.7 \times 10^{-50} \text{ cm}^4$	$\omega_s (14 \text{ K}) = 2 \times 10^4 \text{ sec}^{-1}$	$D_o = 2.6 \times 10^{-9} \text{ cm}^2 \text{ sec}^{-1}$
$C_a = 5.95 \times 10^{19} \text{ cm}^{-3}$	$J_{a2}^2 R_{Nd}^6 = 0.7 \times 10^{-50} \text{ cm}^4$	$\omega_s (133 \text{ K}) = 5 \times 10^4 \text{ sec}^{-1}$	$D = 6.2 \times 10^{-9} \text{ cm}^2 \text{ sec}^{-1}$
$\Delta v_{ss}^{\text{inhomo}} = 8.27 \text{ cm}^{-1}$		$\omega_a (14 \text{ K}) = 1.4 \times 10^4 \text{ sec}^{-1}$	$l = 3 \times 10^{-6} \text{ cm}^*$
$\Delta E_{sa} = 8.53 \text{ cm}^{-1}$		$\omega_a (133 \text{ K}) = 1 \times 10^4 \text{ sec}^{-1}$	
$\Delta E_{12} = 94 \text{ cm}^{-1}$		$\delta = 95 \text{ cm}^{-1}$	
$\Gamma = 4 \text{ cm}^{-1}$		$\Delta E_{ss} = 4.8 \times 10^{-2} \text{ cm}^{-1}$	
$\tau_s^0 = 2.14 \times 10^{-4} \text{ sec}^{-1}$			

\*Extrapolated value at room temperature.

201

B: Other Host Compositions

PARAMETERS	COMPOSITION.		
	$x = 0.00^{**}$	0.22	0.39
			1.00**
$C_s (\text{cm}^{-3})$	$1.1 \times 10^{20}$	$3.08 \times 10^{19}$	$3.08 \times 10^{19}$
$C_a (\text{cm}^{-3})$	$8.4 \times 10^{18}$	$8.3 \times 10^{19}$	$5.12 \times 10^{19}$
$\Delta v_{ss}^{\text{inhomo}} (\text{cm}^{-1})$	$\sim 1.5$	5.4	6.8
$\omega_s (\text{sec}^{-1})^*$	$3.9 \times 10^2$	$3.85 \times 10^3$	$5 \times 10^3$
$\omega_a (\text{sec}^{-1})^*$	$2.5 \times 10^3$	$3.5 \times 10^3$	$2.7 \times 10^3$
			0

\*Values at  $T = 100 \text{ K}$ 

\*\*Values from Ref. 7.



spectroscopy fitting parameters listed in Table 1 shows that  $\omega_s$  is responsible for the increase in the intensity ratios as temperature increases.

In order to understand the results of the above analysis of the data, it is necessary to have a theory of energy transfer in which the transfer rate is independent of time and increases exponentially with temperature. It is important to note that the thermal activation energy is much larger than the energy mismatch between the transitions of the ions in the different types of sites and instead is similar in magnitude to the crystal field splitting of the lowest two levels of the ground state manifold. This might be expected if the a-2 transition were significantly stronger than the a-1 transition which is not true in this case. These results are consistent with those obtained recently on  $\text{Nd}^{3+}$  ions in unmixed garnet hosts which were interpreted in terms of an exciton migration model in which both the hopping and trapping mechanisms are assisted by two-phonon interaction processes.<sup>7</sup> This theory is outlined below.

For exciton diffusion with a weak sensitizer-activator interaction the energy transfer rate can be expressed as<sup>9</sup> discussed in Sections III.1 and V.2 is

$$\omega_s = 8.5 C_a D^{3/4} W_{sa}^{1/4} R_{sa}^{3/2} \quad (5)$$

and the diffusion coefficient can be expressed as<sup>10</sup>

$$D = 3.4 C_s^{4/3} R_{ss}^6 W_{ss} \quad (6)$$

In these equations  $C_a$  and  $C_s$  are the concentrations of ions in the sensitizer and activator sites while  $W_{ss}$  and  $W_{sa}$  are the sensitizer-sensitizer and sensitizer-activator interaction strengths, respectively.  $R_{ss}$  and  $R_{sa}$  are the nearest distances between two sensitizer ions and between sensitizer and activator ions. If all of the Nd ions are assumed to be distributed randomly

in the crystal, these can both be set equal to an average distance  $R_{Nd}$ . The interaction rates can be expressed in terms of the expressions derived by Holstein, et al.<sup>5</sup> for two-phonon assisted transfer processes. In this case the appropriate process involves resonant phonon transitions to a real intermediate state. Using this expression in Eqs. (5) and (6) gives

$$\omega_s = 71.6 C_a C_s R_{Nd}^6 (\Gamma / ) (1 + e^{\Delta E_{sa}/kT})^{1/4}$$

$$\left[ \frac{J_1^2}{\Delta E_{ss}^2} + \frac{J_2^2}{4\Gamma^2} \right]^{3/4} \left[ \frac{J_1^2}{\Delta E_{sa}^2} + \frac{2J_2^2}{\Delta E_{sa} + 8\Gamma^2} \right]^{1/4} e^{-\delta/kT}. \quad (7)$$

Here  $J_1$  and  $J_2$  are the matrix elements for transfer involving the initial excited state and the ground state and for transfer involving the intermediate state reached by the phonons, respectively.  $\Gamma$  is the width of the intermediate state,  $\Delta E_{sa}$  is the energy mismatch between the transitions of the two ions, and  $\delta$  is the energy of the resonant phonons. In Eq. (7) it has been assumed that  $\Delta E_{ss}$  is small compared to  $\Gamma$  and  $kT$ . For the system investigated here the temperature dependence is dominated by the exponential involving  $\delta/kT$  where  $\delta$  is consistent with the crystal field splitting of the lowest two Stark levels of the  $^4I_{9/2}$  manifold.

A quantitative estimate of the energy transfer rate can be obtained from Eq. (7). The parameters used for doing this are listed in Table 1. The values for  $\Delta E_{sa}$ ,  $\Gamma$  and the sensitizer and activator concentrations are obtained from spectral observations. The results of Kushida<sup>11</sup> and of Krupke<sup>12</sup> have been used to estimate the matrix elements. The only unknown parameter is  $\Delta E_{ss}$ . A value of  $4.8 \times 10^{-2} \text{ cm}^{-1}$  is needed for Eq. (7) to be quantitatively consistent with the experimental results. This is smaller than the inhomogeneous

linewidth of the sensitizer transition which should be an upper limit on the value of  $\Delta E_{ss}$ .

Using Eq. (6) and the above method of fitting the experimental data, a value for the exciton diffusion coefficient can be obtained. The diffusion length is given by  $l = \sqrt{6Dt_s^0}$  and the temperature independent part of the diffusion coefficient is determined from  $D = D_0 \exp(-\Delta E/kT)$ . The values found for these parameters are also listed in Table 1.

#### D. Discussion and Conclusions

In summary, laser excited site-selection spectroscopy investigations of  $Nd^{3+}$  ions in mixed garnet crystal hosts show that the crystal field splittings vary linearly with the composition parameter  $x$ . The mixed crystal host creates nonequivalent crystal field sites for the  $Nd^{3+}$  ions some of which have a random distribution of closely spaced transition energies contributing to inhomogeneous line broadening and some of which have distinctly resolvable transitions. The variation of spectral properties of rare earth ions in nonequivalent sites in glasses have recently been studied extensively with laser site-selection techniques.<sup>13</sup> The site-selection for the mixed crystal hosts investigated here varies linearly with laser wavelength. The degree of site-selection observed by pumping into such a high energy absorption band is surprising due to the homogeneous broadening arising from phonon relaxation processes. However, the terminal levels of the absorption are known to be hypersensitive to the local crystal field.<sup>14</sup>

The model used here to interpret the results on energy transfer between  $Nd^{3+}$  ions in nonequivalent crystal field sites in mixed garnet crystals is consistent with that used previously for similar work on  $Nd^{3+}$  ions in  $Y_3Al_5O_{12}$  and  $Y_3Ga_5O_{12}$  host crystals.<sup>7</sup> This model is based on a multistep



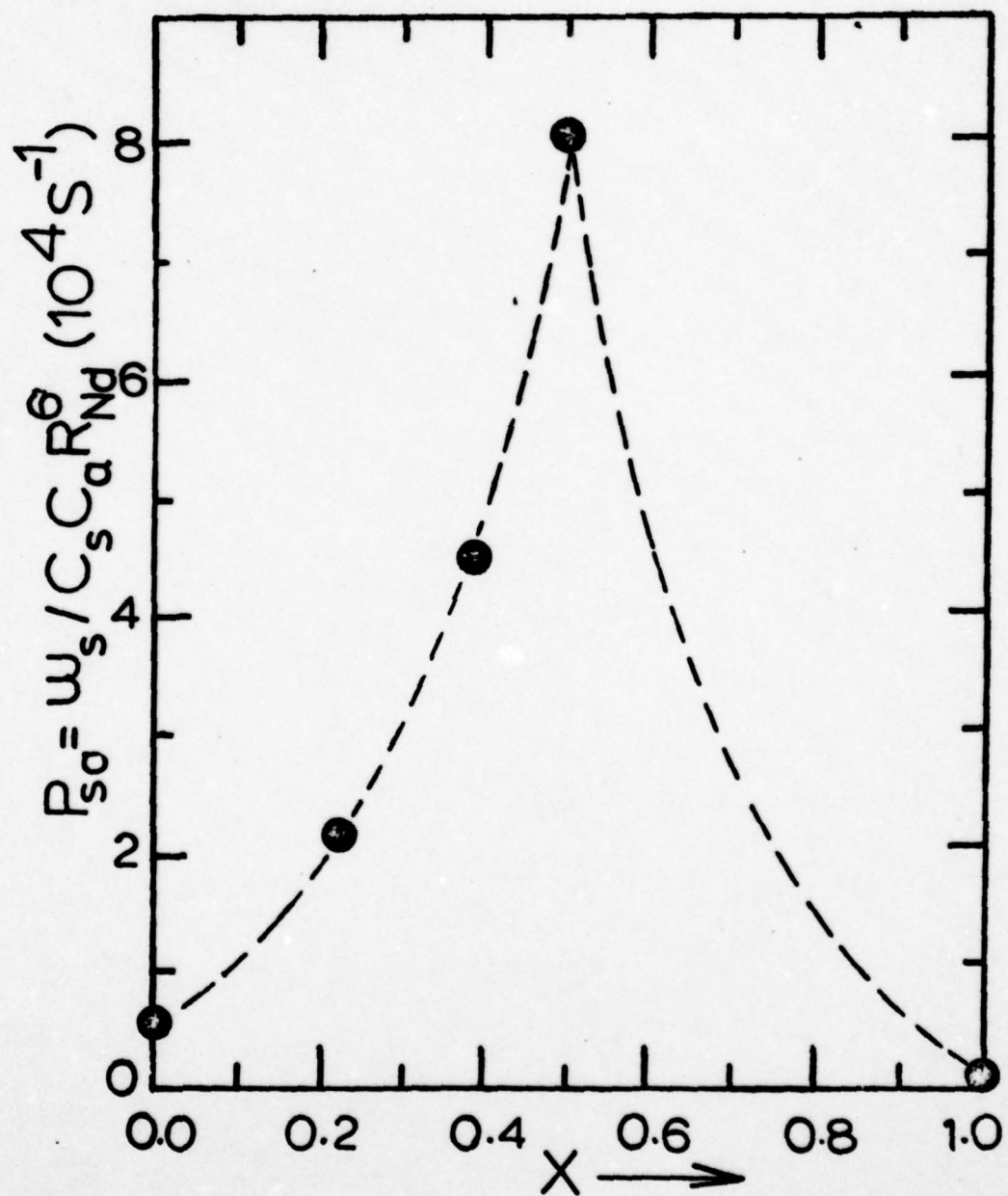


Fig. 11. Variation of the energy transfer strength at 14 K as a function of host composition.

energy migration with both the exciton hopping and trapping steps assisted by resonant two-phonon processes. Figure 11 shows the variation of the transfer strength with the host composition parameter  $x$ . The transfer strengths shown here are the observed transfer rates with the factors for sensitizer and activator concentrations and the average  $\text{Nd}^{3+}$  ion separation divided out. The results show that the transfer strength increases as  $x$  increases up to the  $x = 0.5$  sample but then is smaller again for the  $x = 1.0$  host. The two main parameters which could effect the transfer strength are the inhomogeneous broadening of the sensitizer transition and the transition matrix elements. Comparison of Eq. (7) with Fig. 11 shows that  $\omega_s$  goes in the opposite direction as would be predicted by the effects of inhomogeneous broadening but is consistent with the observed changes in matrix elements. This is consistent with the spectral observations in Fig. 2.

One aspect of these results which is still not understood is the nature of the small amount of temperature independent back transfer which was found in analyzing the time-resolved spectroscopy data obtained on the  $x = 0.50$  sample. In fitting the results obtained on samples with different values of  $x$  it was sometimes necessary to include finite values of  $\omega_a$  and sometimes not. This is similar to the results reported previously on unmixed garnet hosts<sup>7</sup> where it was found that no back transfer was necessary in fitting the data obtained on  $\text{Y}_3\text{Ga}_5\text{O}_{12}:\text{Nd}^{3+}$  but it was necessary to include a small amount of temperature independent back transfer in fitting the data on  $\text{Y}_3\text{Al}_5\text{O}_{12}:\text{Nd}^{3+}$ .

In conclusion, varying the composition of mixed crystal hosts can be used to alter the properties of laser materials. Laser site-selection techniques are useful in probing the properties of ions in different types of sites and for energy transfer between these ions. However, the basic diffusion equations used in the interpretation of these results are all based on migration on a

lattice of uniformly distributed sites and it is important for a theory to be developed which treats exactly the problem of migration on a lattice with random sites.

#### REFERENCES

- [1] L. A. Riseberg and W. C. Holton, J. Appl. Phys. 43, 1876 (1972); L. A. Riseberg, R. M. Brown, and W. C. Holton, Appl. Phys. Lett. 23, 127 (1973); L. A. Riseberg and W. C. Holton, Optics Comm. 9, 298 (1973).
- [2] R. K. Watts and W. C. Holton, J. Appl. Phys. 45, 873 (1974).
- [3] C. Hsu and R. C. Powell, Phys. Rev. Lett. 35, 734 (1975); C. Hsu and R. C. Powell, J. Phys. C 9, 2467 (1976); G. E. Venikouas and R. C. Powell, Phys. Rev. B 17, 3456 (1978); L. D. Merkle and R. C. Powell, J. Chem. Phys. 67, 371 (1977); D. R. Tallant and J. C. Wright, J. Chem. Phys. 63, 2074 (1975); M. D. Kurz and J. C. Wright, J. Luminescence 15, 169 (1977).
- [4] N. Motegi and S. Shionoya, J. Luminescence 8, 1 (1973); R. Flach, D. S. Hamilton, P. S. Selzer, and W. M. Yen, Phys. Rev. B 15, 1248 (1977); P. M. Selzer, D. S. Hamilton and W. M. Yen, Phys. Rev. Lett. 38, 858 (1977); D. S. Hamilton, P. M. Selzer, and W. M. Yen, Phys. Rev. B 16, 1858 (1977); P. M. Selzer, D. L. Huber, B. B. Barrett, and W. M. Yen, Phys. Rev. B 17, 4979 (1978); R. Flach, D. S. Hamilton, P. S. Selzer and W. M. Yen, Phys. Rev. Lett. 35, 1034 (1975).
- [5] T. Holstein, S. K. Lyo and R. Orbach, Phys. Rev. Lett. 36, 891 (1976); T. Holstein, S. K. Lyo and R. Orbach, Phys. Rev. B (to be published).  
A preliminary account of this work was presented at the Colloque International du Centre National de la Recherche Scientifique, 1976 (unpublished).



- [6] D. L. Huber, D. S. Hamilton and B. Barnett, Phys. Rev. B 16, 4642 (1977);  
W. Y. Ching, D. L. Huber, and B. Barnett, Phys. Rev. B 17, 5025 (1978).
- [7] L. D. Merkle and R. C. Powell, Phys. Rev. (to be published).
- [8] J. M. Flaherty and R. C. Powell, Phys. Rev. (to be published).
- [9] M. Yokota and O. Tanimoto, J. Phys. Soc. Japan 22, 779 (1967).
- [10] M. Trlifaj, Czech. J. Phys. 5, 463 (1955); 6, 533 (1956); 8, 510 (1958).
- [11] T. Kushida, J. Phys. Soc. Japan 34, 1381 (1973).
- [12] W. F. Krupke, IEEE J. Quant. Elec. QE-7, 153 (1971).
- [13] C. Brecher, L. A. Riseberg, and M. J. Weber, Appl. Phys. Lett. 30, 475  
(1977); C. Brecher and L. A. Riseberg, Phys. Rev. B 13, 81 (1976).
- [14] B. R. Judd, Phys. Rev. 127, 750 (1962).
- [15] R. K. Watts, in "Optical Properties of Ions in Solids", ed. B. DiBartolo  
(Plenum, New York, 1975).

## VI. CONCENTRATION QUENCHING IN $\text{Nd}_{x-1-x}\text{Y}_x\text{P}_5\text{O}_{14}$ CRYSTALS

### A. Introduction

The development of the technology of fiber optics has resulted in a requirement for miniature optically pumped lasers with low threshold and high gain.<sup>1</sup> Stoichiometric laser materials such as neodymium pentaphosphate ( $\text{NdP}_5\text{O}_{14}$ ) meet these requirements.<sup>2-4</sup> Despite the significant amount of work that has been done recently there are still some aspects of the luminescence properties of concentrated Nd materials which are not well understood. Complete characterization of the optical properties of this class of materials is important not only for technological design considerations but also for obtaining a basic understanding of the physical interaction mechanisms involved.

The most important property of stoichiometric laser materials is that they exhibit unusually weak concentration quenching. This allows the concentration

of neodymium ions in  $\text{NdP}_{514}\text{O}_{14}$  to be very high without significant degradation of the fluorescence and lasing properties of the material. The characteristics of the concentration quenching in stoichiometric laser materials are different from those in other well characterized materials such as  $\text{Y}_3\text{Al}_5\text{O}_{12}:\text{Nd}^{3+}$  and the physical mechanism for the quenching process is not understood at this time. Developing a model to explain concentration quenching in  $\text{NdP}_{514}\text{O}_{14}$  is an important problem in understanding this class of materials.

To date three basic mechanisms have been proposed to explain the concentration quenching characteristics of stoichiometric laser materials. All have been proven unsatisfactory. The first mechanism postulated was cross-relaxation between pairs of Nd ions in the bulk of the crystal which predicted a quadratic concentration dependence for the quenching rate<sup>5-8</sup>. This prediction is inconsistent with experimental results.<sup>1-9</sup> A second suggestion for a quenching mechanism involved crystal field overlap mixing effects between  $\text{Nd}^{3+}$  ions<sup>10</sup> but this has been proved wrong by the observation that the oscillator strengths of the  $\text{Nd}^{3+}$  transitions are independent of concentration.<sup>11</sup> Finally, energy migration to ions in randomly distributed sites throughout the bulk of the crystal acting as "sinks" where the energy is dissipated radiationlessly has been proposed.<sup>6,7,9,12</sup> Unfortunately, this model requires the unrealistic assumption that the concentration of ions in quenching sites is the same for all samples independent of total Nd concentration.<sup>9</sup> We recently reported preliminary results indicating that spectral energy transfer between  $\text{Nd}^{3+}$  ions in slightly different types of sites is not taking place in  $\text{NdP}_{514}\text{O}_{14}$  as it does in materials such as  $\text{Y}_3\text{Al}_5\text{O}_{12}:\text{Nd}^{3+}$  even at low concentrations.<sup>13</sup>

In this paper we report the results of an investigation of the mixed crystal system of  $\text{Nd}_x\text{Y}_{1-x}\text{P}_{514}\text{O}_{14}$  where we have utilized some new spectroscopic techniques in an attempt to better understand the concentration quenching

mechanism in these materials. Laser time-resolved site-selection spectroscopy was used to investigate energy transfer and the results show that migration among  $\text{Nd}^{3+}$  ions in non-equivalent sites does not take place. Photoacoustic spectroscopy (PAS) measurements were made to characterize radiationless relaxation processes among the excited states of  $\text{Nd}^{3+}$  in these materials. The results are not consistent with those expected for PAS signals originating mainly from those phonons due to relaxation processes from higher absorption levels to the metastable level. A model based on surface quenching of the excitation is proposed which can explain the observed PAS results and is consistent with all the other spectroscopic observations obtained on this material. The possible mechanisms for the quenching process and the effects of radiative reabsorption are also discussed.

#### B. Samples and Experimental Equipment

The  $\text{NdP}_{5-x}\text{Y}_x\text{O}_{14}$  crystal was grown from solution at Philips Laboratory while the mixed crystals were grown at the Army Electronics Command Laboratories. Six samples of  $\text{Nd}_{1-x}\text{Y}_x\text{P}_5\text{O}_{14}$  ranging from  $x = 1.00$  to  $x = 0.10$  were investigated. These consisted of small crystallites varying in size from about 2.0mm on a side to about 0.50mm.

For optical spectroscopy measurements the samples were mounted in a cryogenic refrigerator to control the temperature. For photoacoustic spectroscopy the samples were mounted in an acoustical cavity and the signal detected by a 1-in. electret microphone. The excitation source for obtaining PAS and fluorescence excitation spectra was a 1000-W tungsten/halogen lamp passed through a 1/4-m monochromator. For measuring fluorescence lifetime and obtaining time-resolved spectroscopy data the excitation source was a nitrogen laser-pumped tunable dye laser with rhodamine 6-G dye. This provided a pulse of about 10ns



in duration and less than  $0.5\text{\AA}$  in halfwidth. Sample emission was analyzed by a one-meter monochromator and detected by a cooled RAC C31034 photomultiplier tube. To obtain steady state spectral data the incident light was chopped and the signal processed by a PAR lock-in amplifier. For processing pulsed signals a PAR boxcar averager triggered by the laser pulse was used. The time gate of the boxcar was either set to observe the fluorescence spectrum at a specific time after the laser pulse or scanned to obtain the fluorescence as a function of time at a specific wavelength.

### C. General Spectroscopy and Concentration Quenching Results

The absorption spectrum of  $\text{NdP}_{50}\text{O}_{14}$  has been presented elsewhere.<sup>1</sup> It is similar to the spectrum of  $\text{Nd}^{3+}$  ions in other hosts with lower doping concentrations. The strongest absorption band occurs at approximately  $8000\text{\AA}$  corresponding to the transition from the  $^4\text{I}_{9/2}$  ground state to a band consisting of the unresolved components of the  $^2\text{H}_{9/2}$  and  $^4\text{F}_{5/2}$  levels (see the energy diagram of  $\text{Nd}^{3+}$  shown in Fig. 1). The second strongest absorption band occurs near  $5800\text{\AA}$  and is associated with the unresolved levels of the  $^2\text{G}_{7/2}$  and  $^4\text{G}_{5/2}$  levels. After absorption into any of the higher energy levels, radiationless relaxation occurs to the  $^4\text{F}_{3/2}$  metastable state. Fluorescence emission then takes place from the two crystal field components of this level to the various Stark components of the  $^4\text{I}_J$  multiplets. Branching ratios determined previously<sup>7</sup> indicate that most of the energy is emitted in the transitions terminating on the  $^4\text{I}_{11/2}$  and  $^4\text{I}_{9/2}$  levels centered around  $1.06\mu\text{m}$  and  $0.89\mu\text{m}$ , respectively. The fluorescence spectrum is discussed in more detail in the next section.

Figure 2 shows the fluorescence excitation spectra of the  $^4\text{F}_{3/2}$  level monitored at  $8880\text{\AA}$  at room temperature for both  $\text{NdP}_{50}\text{O}_{14}$  and a mixed crystal of  $\text{Nd}_{0.5}\text{Y}_{0.5}\text{P}_{50}\text{O}_{14}$ . The spectra are quite similar for the pure and mixed samples.

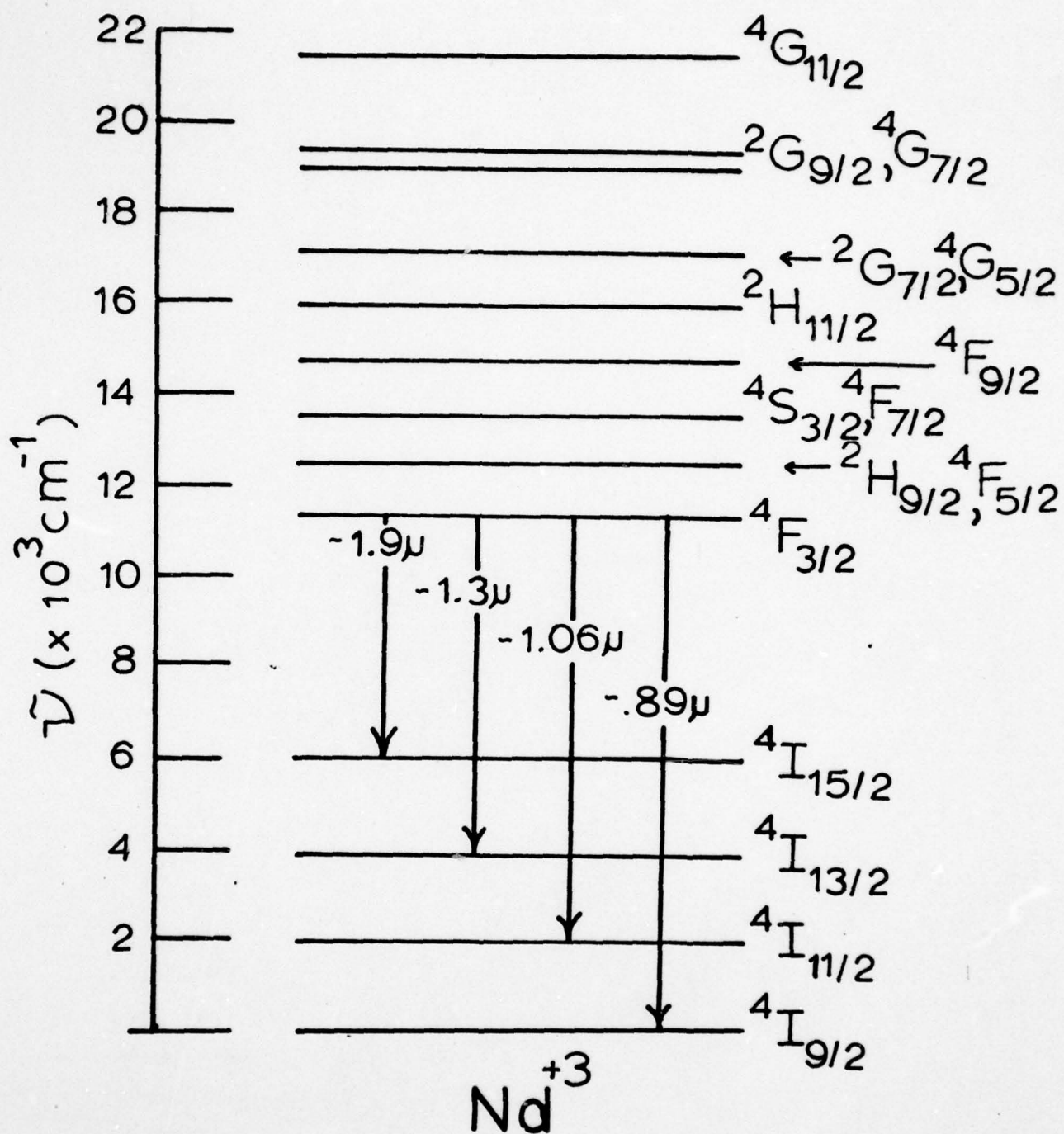


Fig. 1. Energy level scheme of  $\text{Nd}^{3+}$ .

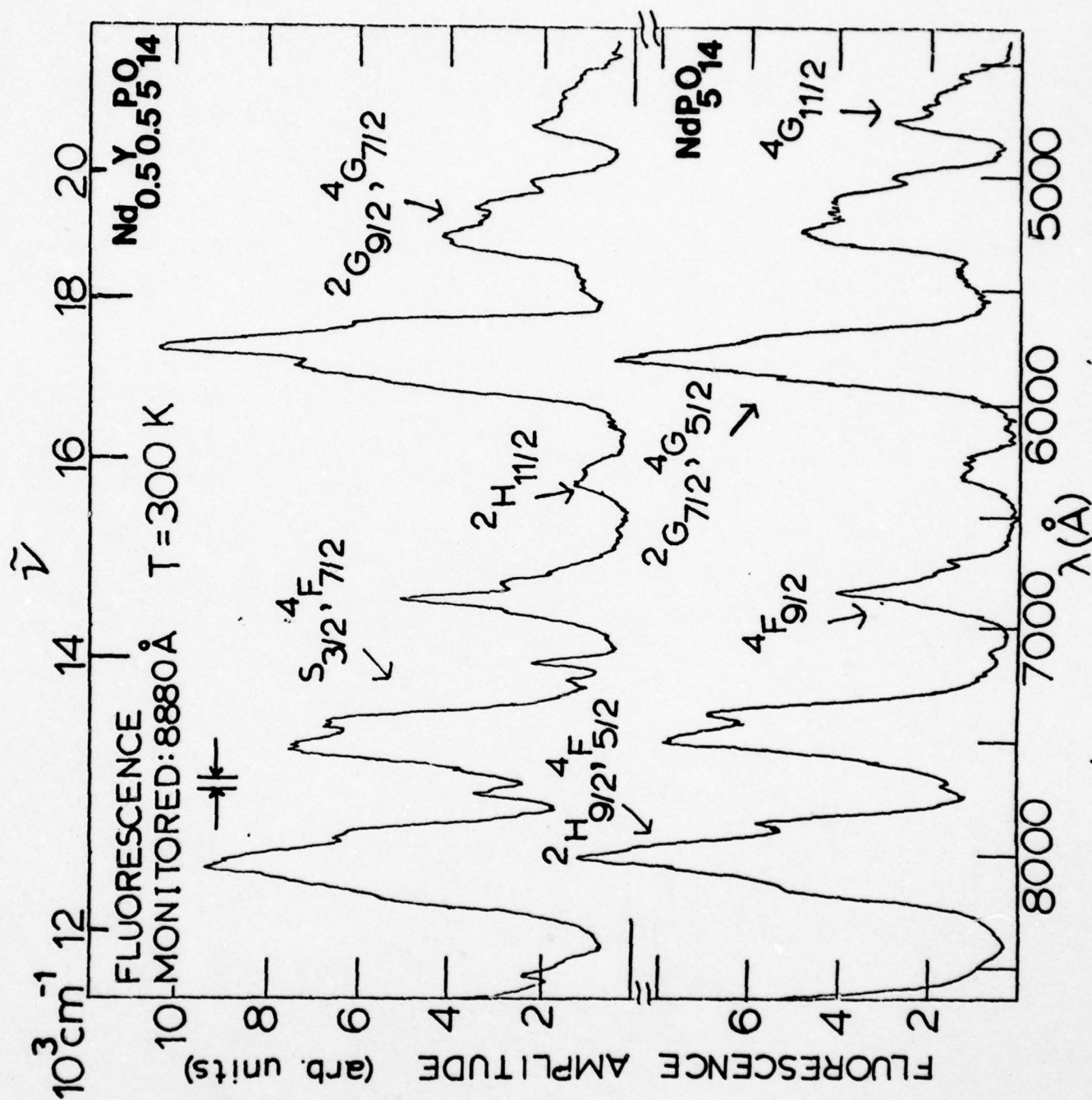


Fig. 2. Excitation Spectrum of  $^4F_{3/2}$  level in  $\text{Nd}_{0.5}\text{Y}_{0.5}\text{P}_5\text{O}_{14}$  and  $\text{NdP}_5\text{O}_{14}$  at 300K.



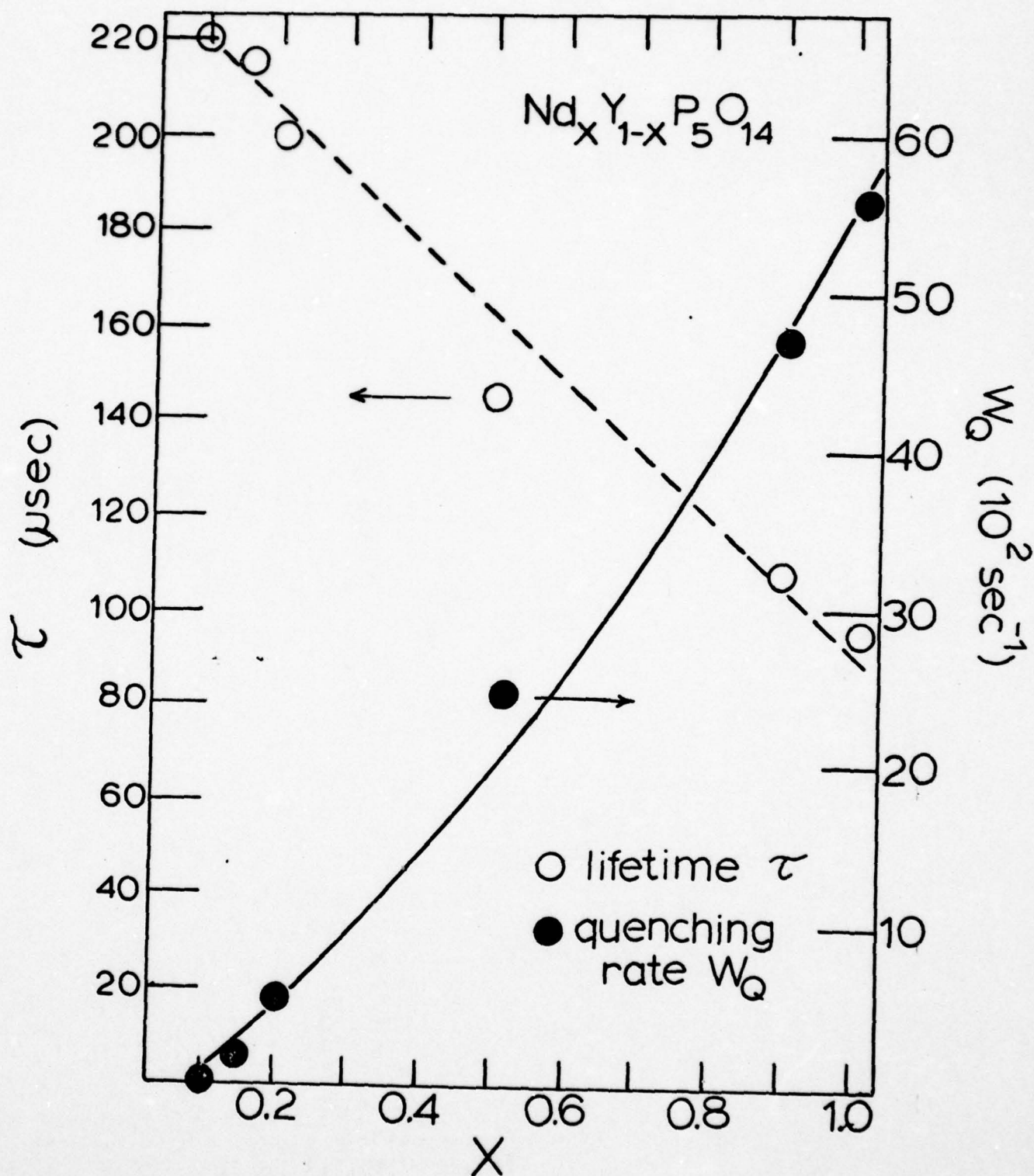


Fig. 3. Concentration dependence of the  ${}^4\text{F}_{3/2}$  fluorescence lifetime and quenching rate for  $\text{Nd}_x\text{Y}_{1-x}\text{P}_5\text{O}_{14}$  at 14K. See text for explanation of the theoretical line.

In particular, the excitation bands centered at  $\sim 8000\text{\AA}$  and  $\sim 5800\text{\AA}$  are comparable. The relative strength in the absorption spectrum of these two bands<sup>1</sup> correlated with the fact that the  $8000\text{\AA}$  excitation is approximately the same of less intense than the  $5800\text{\AA}$  band in the excitation spectrum suggests that the longer wavelength band is less efficient in contributing to  ${}^4F_{3/2}$  fluorescence than the shorter wavelength band.

Figure 3 shows the fluorescence lifetime of the  ${}^4F_{3/2}$  level at room temperature as a function of Nd concentration. The lifetime decreases from about  $220\mu\text{s}$  for the  $\text{Nd}_{0.1}\text{Y}_{0.9}\text{P}_5\text{O}_{14}$  sample to about  $95\mu\text{s}$  for  $\text{NdP}_5\text{O}_{14}$ . A concentration quenching rate can be defined as

$$w_Q = \tau^{-1} - \tau_0^{-1} \quad (1)$$

where  $\tau_0$  is the Nd fluorescence lifetime in the absence of any quenching interaction. This quenching rate is also plotted in Fig. 3 as a function of concentration. For an intrinsic lifetime of  $\sim 220\mu\text{s}$  the plot of the quenching rate varies approximately as  $x^{3/2}$ .

The fluorescence lifetime of the  ${}^4F_{3/2}$  level was measured with different wavelengths of excitation as a function of temperature between 14K and 300K. The fact that a significant variation in lifetime with excitation wavelength was observed is discussed in the next section. The temperature dependence of the fluorescence lifetime of  $\text{NdP}_5\text{O}_{14}$  for two different wavelengths of excitation is shown in Fig. 4. There is a small increase in lifetime between 14 and 300 K. A similar trend is observed for other samples and other excitation wavelengths.

#### D. Time-Resolved Site-Selection Spectroscopy Results

The optical spectral lines of impurity ions in solids all exhibit inhomogeneous broadening to some degree. This is due to the fact that imperfections

and internal strains give rise to non-equivalent crystal field sites for the impurity ions. In some cases the site differences are great enough that transitions from ions in different types of sites can be distinctly resolved. High resolution lasers have been used to selectively excite impurity ions in specific crystal field sites in glass and crystal hosts. By tuning the laser excitation through an inhomogeneously broadened absorption band, it has been possible to observe significant variations in fluorescence spectral parameters such as peak positions, intensities, and radiative and radiationless transition probabilities.<sup>14</sup> If pulsed lasers are used, time-resolved spectroscopy techniques allow the observation of fluorescence spectrum at specific times after the laser pulse. After selective excitation of ions in specific sites the fluorescence spectrum in some systems has been observed to evolve with time into spectra exhibited by ions in other types of sites. This implies that energy transfer is occurring between ions in different types of sites and the observed time dependence can be used to characterize the properties of the energy transfer and help in identifying the mechanism responsible for the transfer process.

For investigating site selection spectroscopy in the  $\text{Nd}_{x-1}\text{Y}_x\text{P}_5\text{O}_{14}$  system we pumped into the absorption band consisting of the unresolved  ${}^2\text{G}_{7/2}$  and  ${}^4\text{G}_{5/2}$  levels. The degree of site selection obtained with this pumping is somewhat surprising due to the number of overlapping levels and their homogeneous broadening resulting from radiationless relaxation processes. However these transitions are known to be "hypersensitive" to changes in the local environment of the ion<sup>11,15,16</sup> and for other systems such as Nd in mixed garnet crystals we found that pumping into this level resulted in easily observable site-selection and energy transfer.<sup>17</sup> The fluorescence was monitored from the  ${}^4\text{F}_{3/2}$  level to the various components of the  ${}^4\text{I}_{9/2}$  ground state manifold in order to minimize



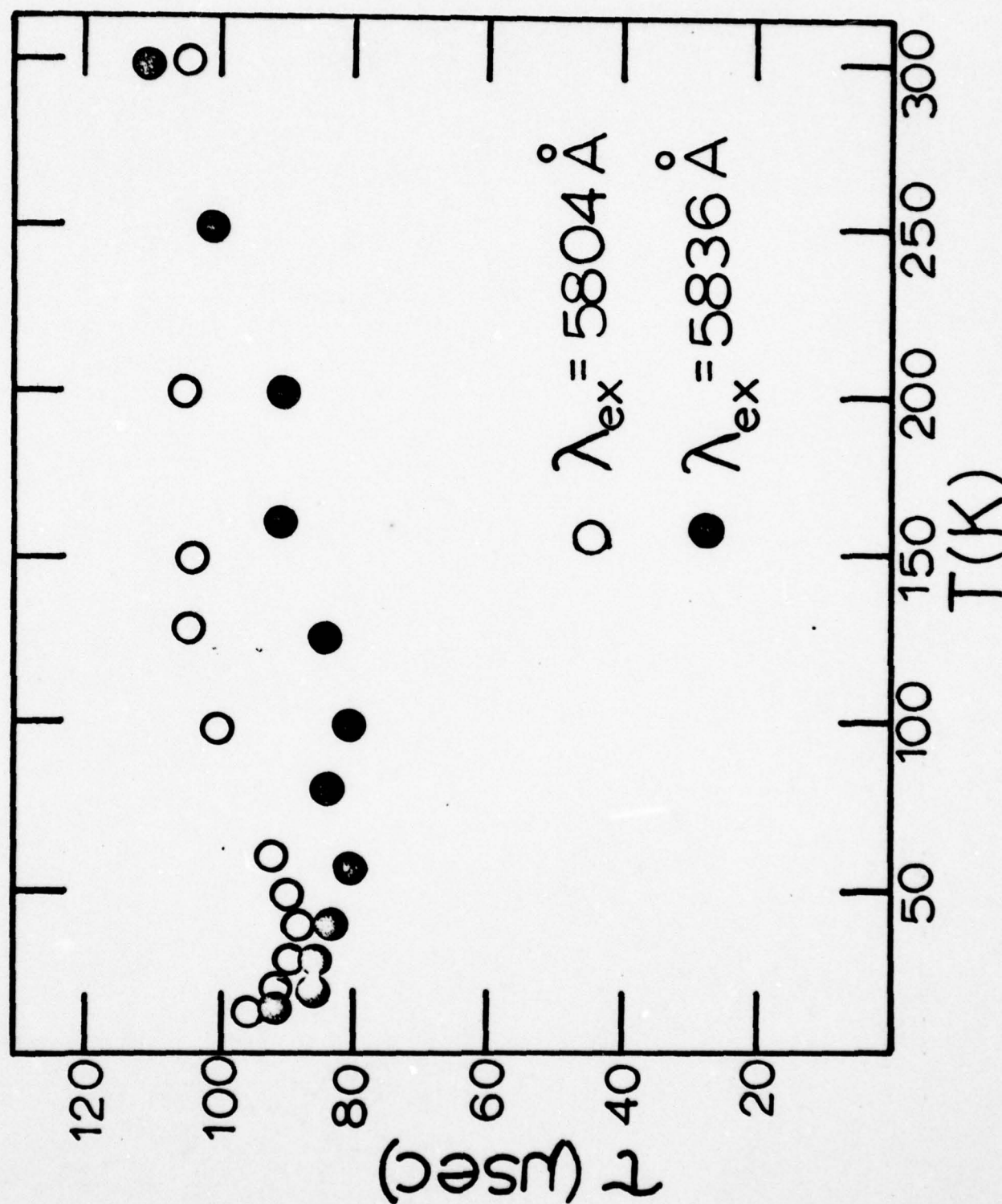


Fig. 4. Temperature dependence of the fluorescence lifetime of the  $^4F_{3/2}$  level in  $\text{NdPO}_5$  for laser excitation wavelengths of 5804 Å and 5836 Å.

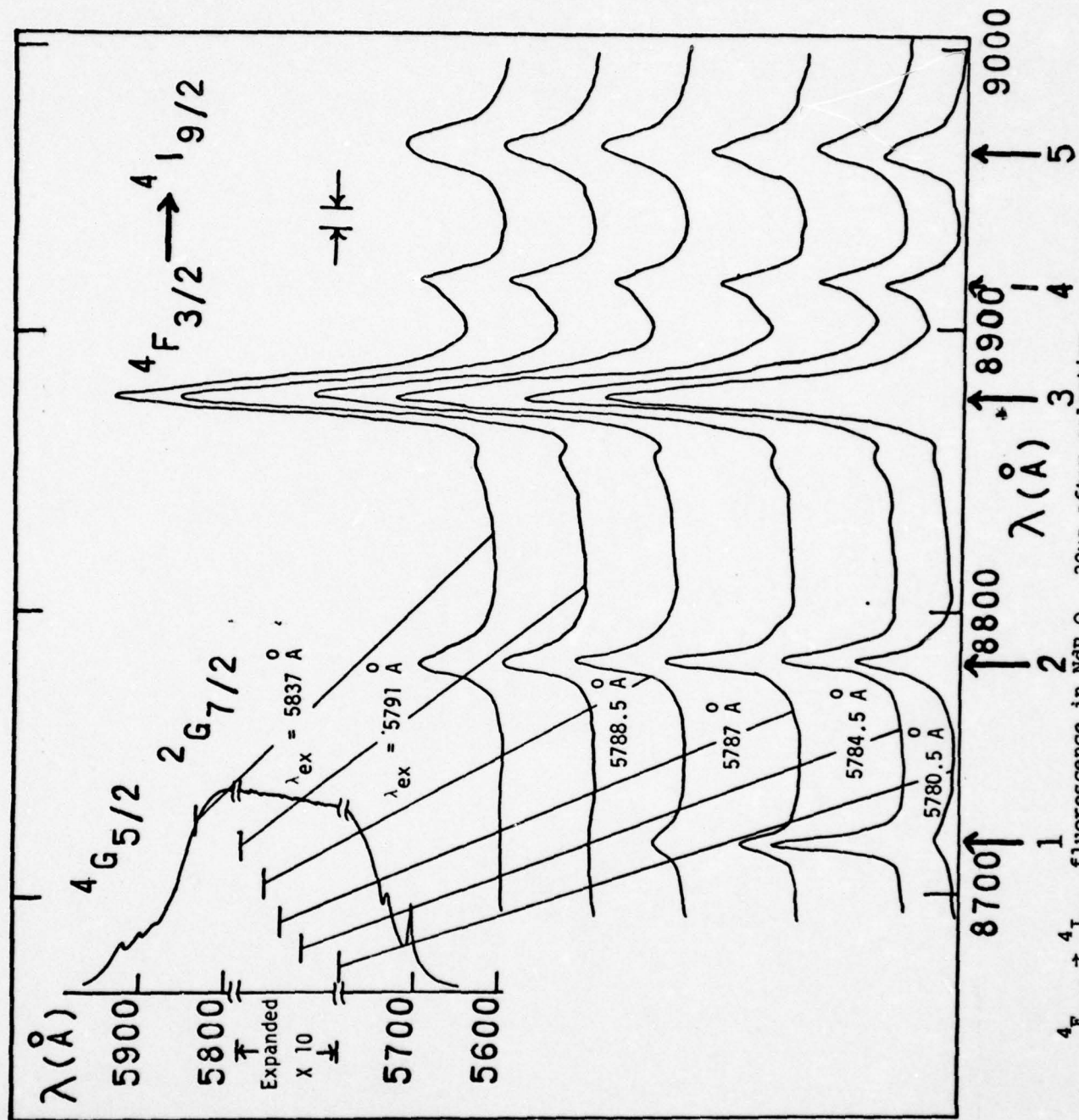


Fig. 5.  $^4F_{3/2} \rightarrow ^4I_{9/2}$  fluorescence in NdP<sub>5</sub>O<sub>14</sub> 20 $\mu$ s after selective excitation into different regions of the  $^2G_{7/2}$ ,  $^4G_{5/2}$  absorption band at 14K.

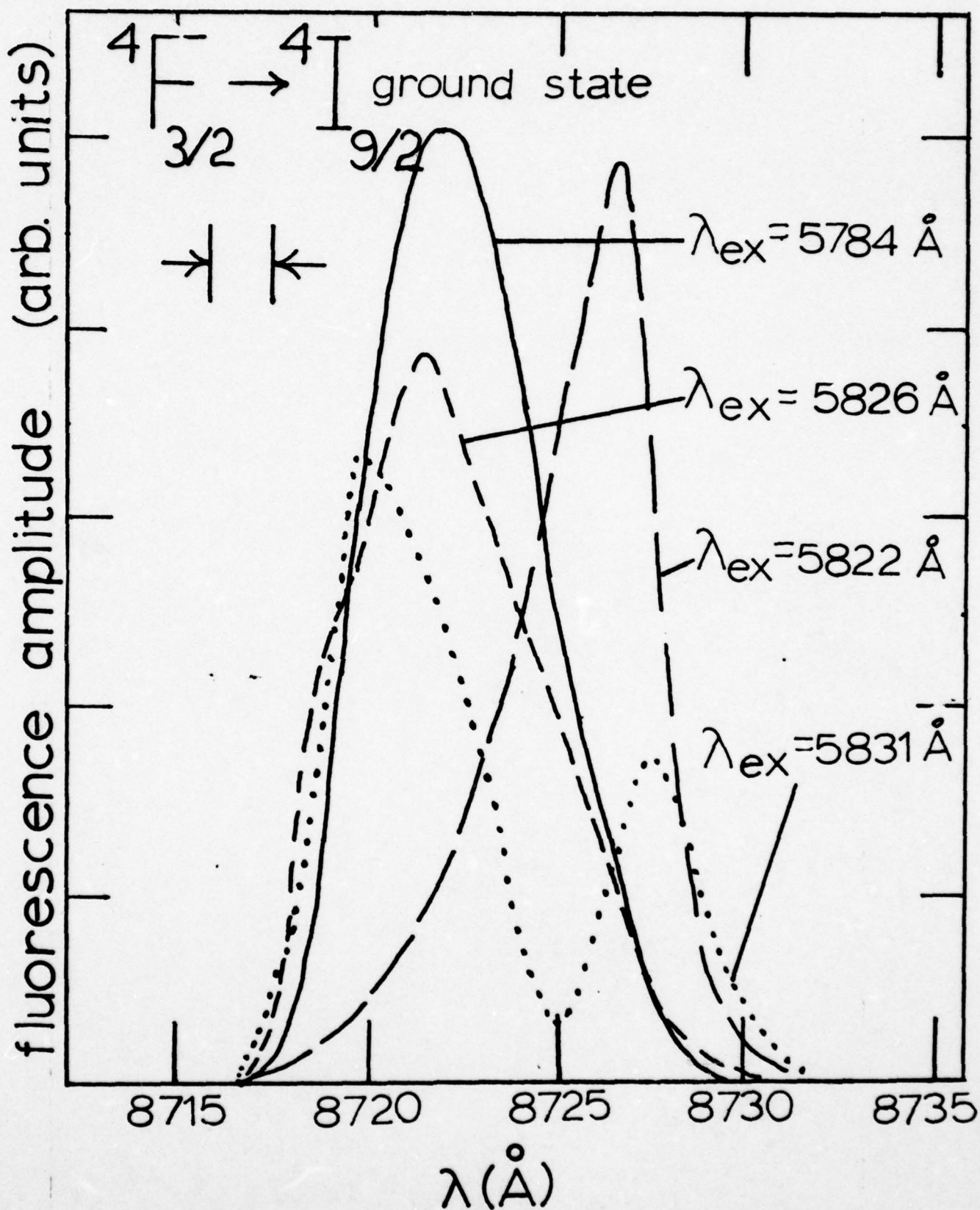


Fig. 6. Line 1 of  $4F_{3/2} \rightarrow 4I_{9/2}$  fluorescence in  $\text{Nd}_{0.5}\text{Y}_{0.5}\text{P}_5\text{O}_{14}$  after 20 $\mu\text{s}$  excitation at various wavelengths.



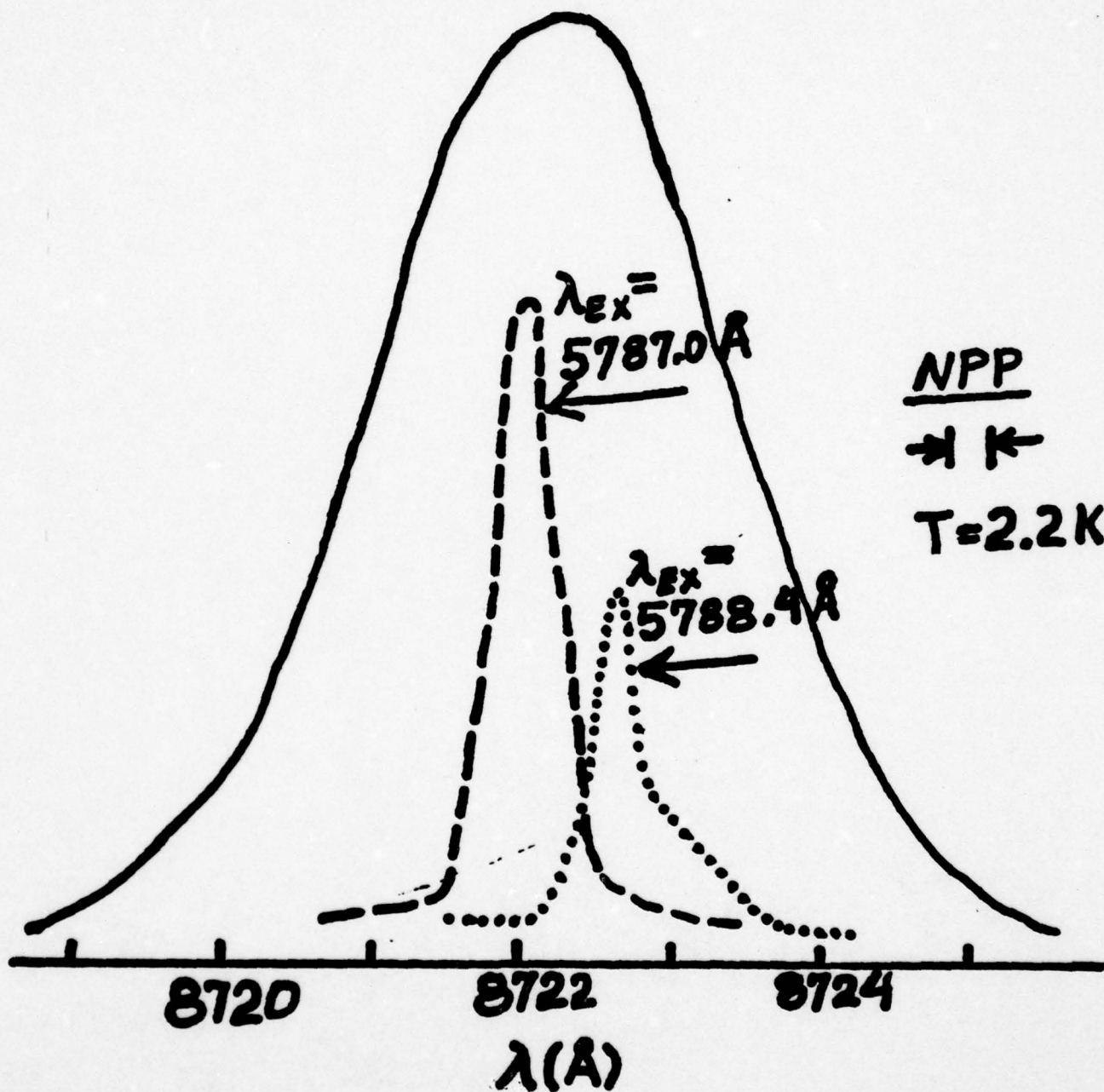


Fig. 7. Fluorescence line narrowing in Nd-pentaphosphate. The narrowed lines are constant as a function of time after the pulse.

homogeneous broadening of the transitions due to radiationless relaxation processes. As the narrow line laser excitation was scanned across the broad absorption band at low temperature, for all of the samples investigated, changes in the relative fluorescence peak intensities, peak positions, and lifetimes were observed. For example, for the  $\text{NdP}_{40}14$  sample at 14K the lifetimes ranged from 63  $\mu\text{s}$  to 105  $\mu\text{s}$  depending on the excitation wavelength whereas at 300K they varied between about 102 and 115  $\mu\text{s}$ . Figure 5 shows an example of the different fluorescence spectra which are obtained for the  $\text{NdP}_{50}14$  sample at 14K for pumping at different wavelengths. The distribution of the intensity among the five lines and the fluorescence lifetimes differ significantly. The lifetime is 67  $\mu\text{s}$  for 5785.5 $\text{\AA}$  excitation and 77  $\mu\text{s}$  for 5837 $\text{\AA}$  excitation. The highest energy line (labeled 1 in the figure) shows the greatest variation with pumping wavelength but there are relative changes in the intensities of all of the other lines also. Figure 6 shows an expanded picture of line 1 as a function of excitation wavelength as 14K for the  $\text{Nd}_{0.5}\text{Y}_{0.5}\text{P}_{50}14$  crystal. Here the changes in line shape and peak position are quite evident. For the 5831 $\text{\AA}$  excitation the line is resolved into two distinct peaks. Figure 7 shows fluorescence line narrowing results at very low temperatures for two excitation wavelengths.

The spectral as well as lifetime changes as a function of excitation wavelength can be attributed to the selective excitation of Nd ions in non-equivalent crystal field sites. If rapid energy migration occurs among the Nd ions, the spectra should evolve with time into some characteristic spectrum representing the average distribution of the energy among all of the ions in different types of sites. We attempted to observe this by monitoring the spectra as a function of time after the laser pulse in the range from 1 to 200  $\mu\text{s}$ . No significant time evolution of the spectra was detected in this range

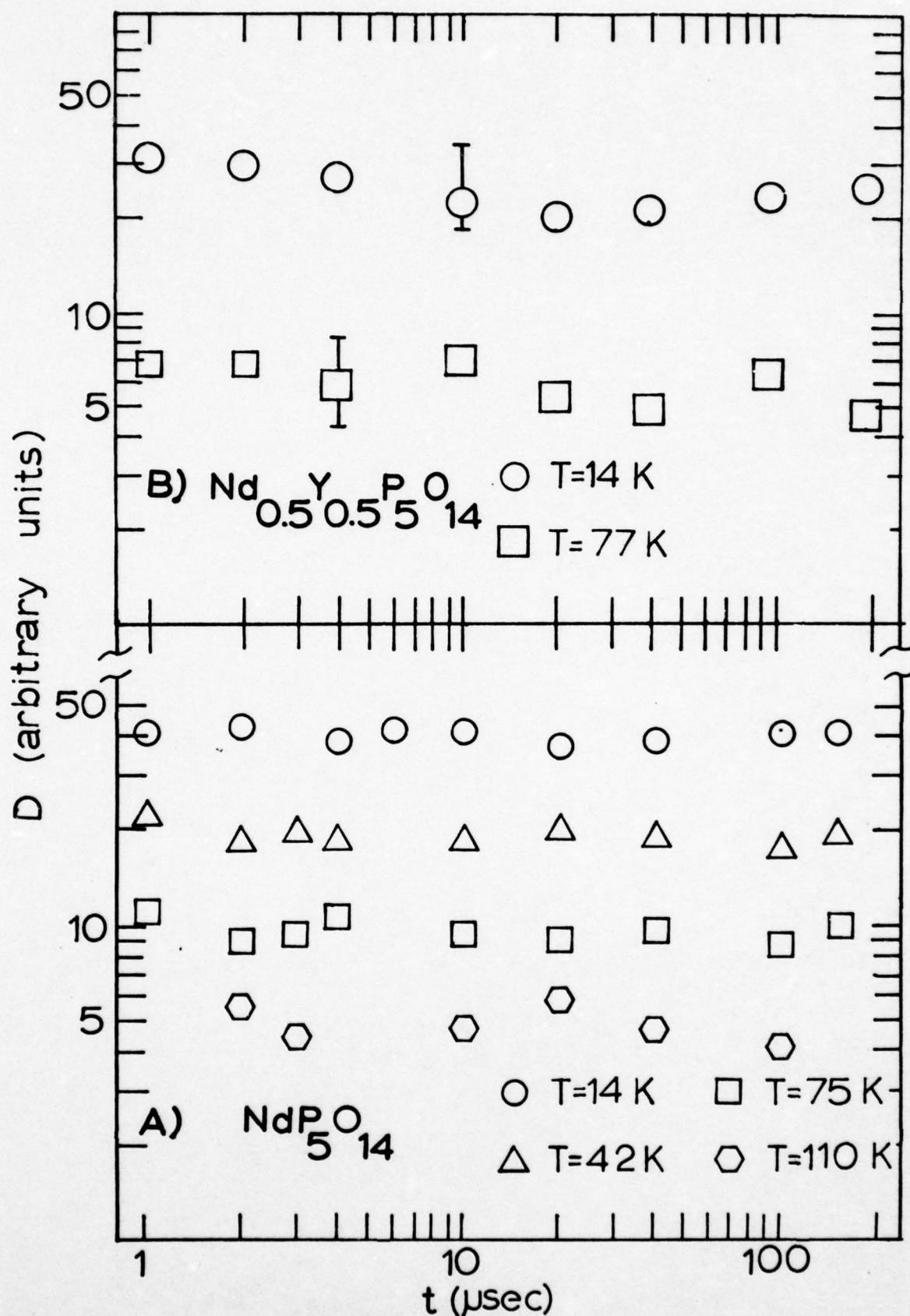


Fig. 8. A) Time dependence of the fluorescence deviation function after excitation at  $5784.5\text{\AA}$  and  $5837\text{\AA}$  in  $\text{NdP}_5\text{O}_{14}$ .  
 B) Time dependence of the fluorescence deviation function after excitation at  $5805.5\text{\AA}$  and  $5835\text{\AA}$  in  $\text{Nd}_{0.5}\text{Y}_{0.5}\text{P}_5\text{O}_{14}$ .



for either of the two samples investigated,  $\text{NdP}_{514}\text{O}_{14}$  and  $\text{Nd}_{0.5}\text{Y}_{0.5}\text{P}_{514}\text{O}_{14}$ , for any wavelength of excitation at any temperature. The FLN results in Fig. 7 were also found to be independent of time.

In order to quantitatively describe any time dependent relative changes in the spectra obtained for two different excitation wavelengths a fluorescence deviation function can be defined. The spectrum obtained for a given excitation wavelength is represented by a five component function, each component corresponding to the ratio of the integrated intensity of one of the lines of the  $^4\text{F}_{3/2} \rightarrow ^4\text{I}_{9/2}$  transitions to the total integrated intensity of all of the lines. Thus, each fluorescence spectrum can be characterized by a five component vector. Any correlation between the fluorescence spectra for different excitation wavelengths can be seen by forming the vector difference between the functions describing the spectra for each excitation wavelength. Figure 8 shows typical results for the fluorescence deviation as a function of time after the laser pulse for both the  $\text{NdP}_{514}\text{O}_{14}$  sample and the  $\text{Nd}_{0.5}\text{Y}_{0.5}\text{P}_{514}\text{O}_{14}$  at various temperatures. A value of D equal to 0 would indicate an identical distribution of relative intensities in the five spectral lines for the two excitation wavelengths. The presence of energy transfer between Nd ions in different types of sites should result in a time dependent decrease in D toward zero. Instead, for all cases investigated, D remains within experimental error constant with time indicating that no energy transfer is taking place between ions in non-equivalent sites.

The temperature dependence of the fluorescence deviation function for  $\text{NdP}_{514}\text{O}_{14}$  is shown in Fig. 9. The error bars indicate the spread in the values of D for measurements at different times after the laser pulse at each temperature. Since the decrease in D with temperature occurs without any associated time

dependence, this temperature dependence can be attributed to the reduced ability of the laser to selectively excite Nd ions in specific sites at high temperatures. This may be a result of homogeneous broadening of the absorption levels due to electron-phonon interactions.

The site-selection spectroscopy results presented above show that Nd ions in pentaphosphate hosts occupy different types of crystal field sites. Although the exact nature of these different sites is not known, they are probably due to differences in local strains resulting from structural imperfections and defects in the crystal. The fact that no energy transfer could be detected between ions in different types of sites is quite surprising in light of the fact that similar studies made on Nd ions in mixed garnet crystals show strong energy transfer between ions in non-equivalent sites.<sup>17</sup> It is important to note, however, that spatial energy transfer between Nd ions in equivalent sites may take place without spectral energy transfer to ions in different types of sites. This type of transfer would not be observable by the time-resolved site-selection spectroscopy techniques used here and is discussed further below.

A second experiment was performed in an attempt to determine the contribution to the fluorescence quenching due to energy migration to randomly distributed sinks. A sample of  $\text{Nd}_{0.9}\text{Y}_{0.1}\text{P}_5\text{O}_{14}$  was mounted in a dewar containing a hydraulically driven piston and immersed in liquid nitrogen. The sample was compressed along the a-axis and excited by a nitrogen laser pumped pulsed dye laser at  $5825\text{\AA}$ . The fluorescence lifetime was monitored at various levels of applied stress. The results are shown in Fig. 10. The application of extremely high levels of stress, up to 2000 psi, results in only an additional 10% quenching of the fluorescence lifetime.

Sinks for radiationless quenching of energy are generally associated with Nd ions located near crystal imperfections where local strains cause differences

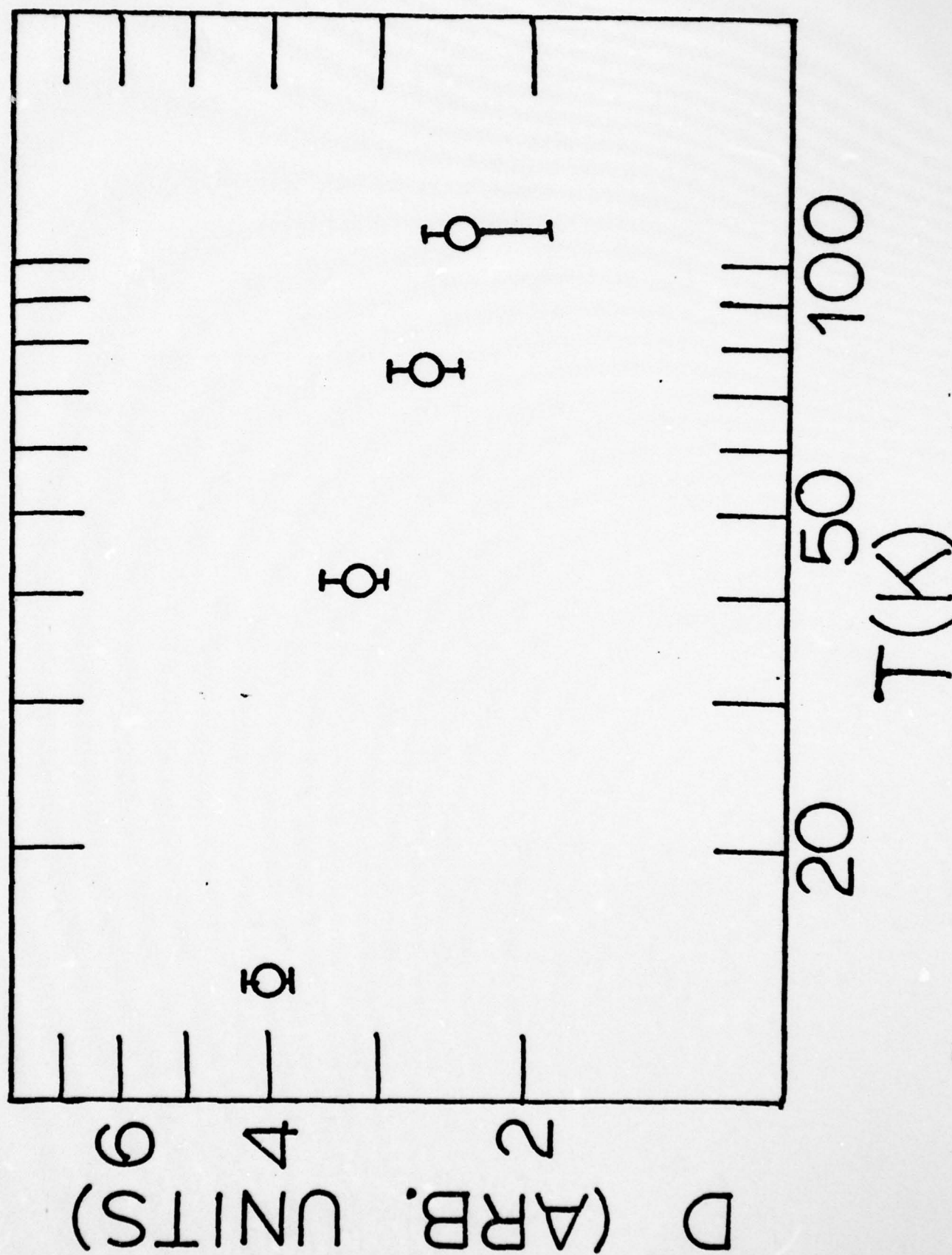


Fig. 9. Temperature dependence of the fluorescence duration function after excitation at 5784.5 Å and 5837 Å in  $\text{NdP}_2\text{O}_7$ .



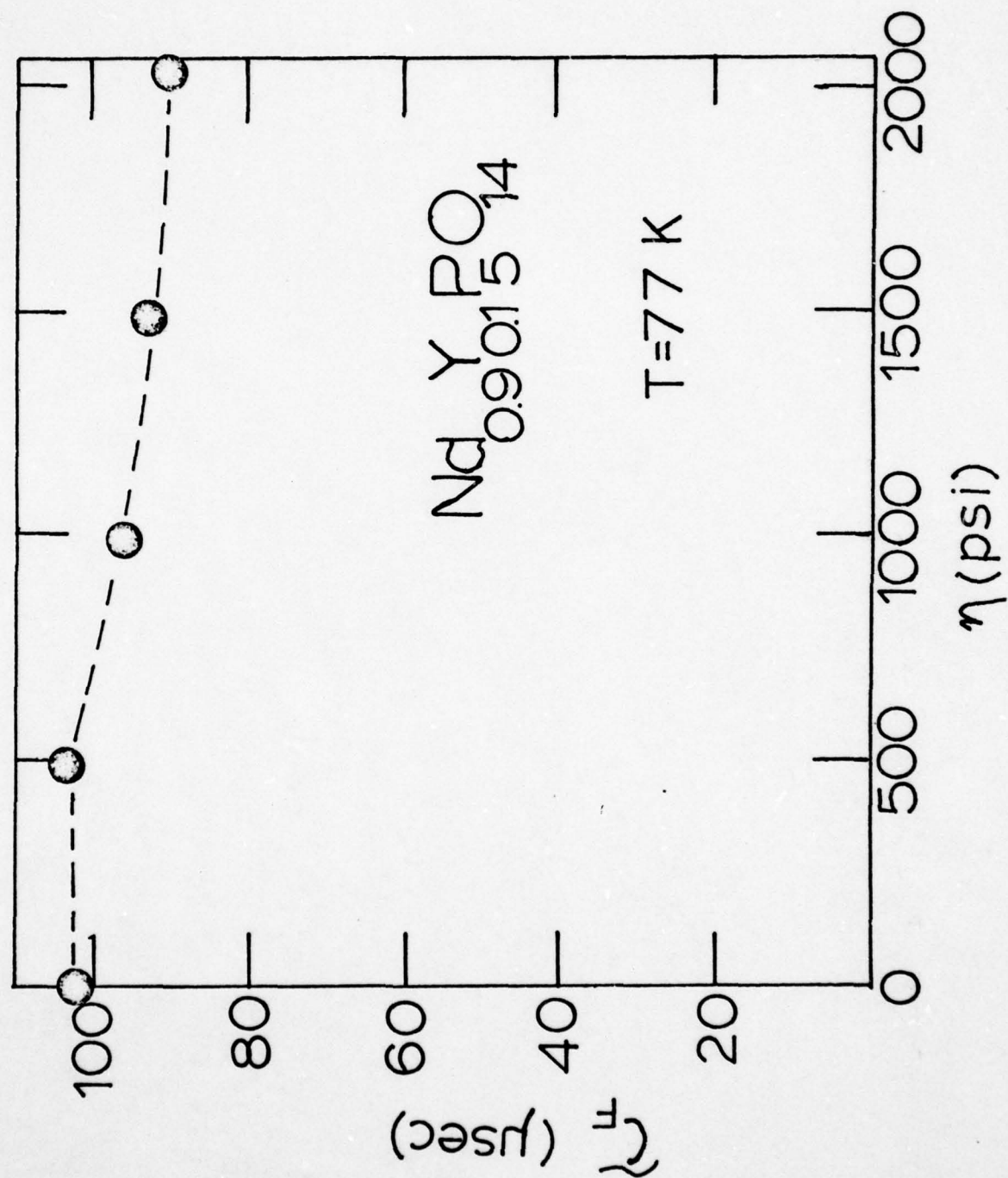


Fig. 10. Fluorescence lifetime of the  $^4F_{3/2}$  level at 77K as a function of uniaxial stress applied along the a-axis.

in the energy level structure allowing cross relaxation to occur. The application of external stress would be expected to introduce additional strains in the sample and, thus, increase the number of sink sites and, therefore, the radiationless quenching. It is well known that  $\text{NdP}_5\text{O}_{14}$  is a ferroelastic crystal and twin boundaries can be introduced into the crystal by very small forces. [31-33] Thus, the small increased lifetime quenching observed at very high external stresses implies that energy migration to randomly distributed sinks is not the dominant quenching mechanism in neodymium pentaphosphate. On the other hand, surface quenching of Nd excitons would be little effected by the application of external stress as observed.

#### E. Interpretation of Results

At this point it is worthwhile to summarize the experimental observations which must be explained by any viable model of concentration quenching in  $\text{Nd}_{x-1}\text{Y}_x\text{P}_5\text{O}_{14}$  and similar materials. The quenching rate must vary less than quadratically with Nd concentration. Also it must have a very weak dependence on temperature and it must be proportional to the absorption cross section. The quenching mechanism cannot lead to variations in oscillator strengths with Nd concentrations, cannot result in spectral energy transfer, and cannot lead to non-exponential fluorescence decays. These requirements along with quantitative theoretical predictions place very rigid restrictions on developing an acceptable model for concentration quenching in these materials. The mechanism responsible for concentration quenching of Nd fluorescence in other types of materials such as  $\text{Y}_3\text{Al}_5\text{O}_{12}:\text{Nd}^{3+}$  is cross-relaxation between pairs of closely spaced ions. This leads to a quadratic dependence of the quenching rate on Nd concentration which is contrary to the linear dependence observed for the pentaphosphate host. The other common mechanism for concentration quenching

which is observed in various materials is migration of the energy among the active ions until it reaches a sink where it is transferred to an ion which can dissipate the energy radiationlessly. This mechanism is not consistent with several of the requirements mentioned above. There is no dependence of the quenching rate on absorption cross section in this model and generally quenching by this mechanism has been found to lead to a strong temperature dependence. A quantitative estimate of the concentration of sinks necessary to give the observed quenching rate can be obtained in the fast diffusion limit from the expression  $W_Q = 4\pi D R_s C_s$  where  $D$  is the diffusion coefficient,  $R_s$  is the exciton trapping radius at the sink, and  $C_s$  is the sink concentration. For the case of neodymium pentaphosphate a sink concentration of only 10ppm of the Nd ions is necessary to cause the observed quenching rate whereas site-selection spectroscopy shows that significant numbers of Nd ions exist in sites of different local perturbations without resulting in energy transfer or quenching.

Since the normal models for concentration quenching do not appear to apply to stoichiometric laser materials, it is necessary to develop a new model. One model which appears to meet all of the requirements outlined above is based primarily on surface quenching of the excitation energy. In this model the Nd ions on the surface of the sample act as sinks where the energy is dissipated radiationlessly. This gives a high concentration of sink sites but only in a very small region and not distributed uniformly throughout the sample. This situation will result in effective quenching for concentrated materials where the excitation energy is deposited near to the sample surface whereas it will be much less effective in lightly doped materials where the energy is deposited more uniformly throughout the sample. Similarly for a given sample quenching will be more effective where the absorption of exciting light is stronger due



to the fact that more of the excited ions will reside closer to the surface. Weaker absorption bands will allow excitation energy to be deposited further into the crystal resulting in less effective quenching.

To determine whether or not a surface quenching model satisfies all of the necessary requirements for explaining the observed data, an expression for the quenching rate can be derived from simple geometric arguments based on the situation shown in Fig. 11. The incident light excites a Nd ions at a distance R from the surface of the crystal and the energy can as an exciton migrate out from this site to other Nd ions. According to standard diffusion theory, after a time equal to the intrinsic lifetime of the exciton the excitation energy will be found on one of the ions on the surface of a sphere of radius  $\ell$  is the diffusion length which is determined by

$$\ell = \sqrt{6D\tau_0} \quad (2)$$

where  $\tau_0$  is the intrinsic lifetime of the exciton. If it is assumed that only excitons which migrate far enough to reach the surface are quenched, the quenching rate for an excited ion at depth R is

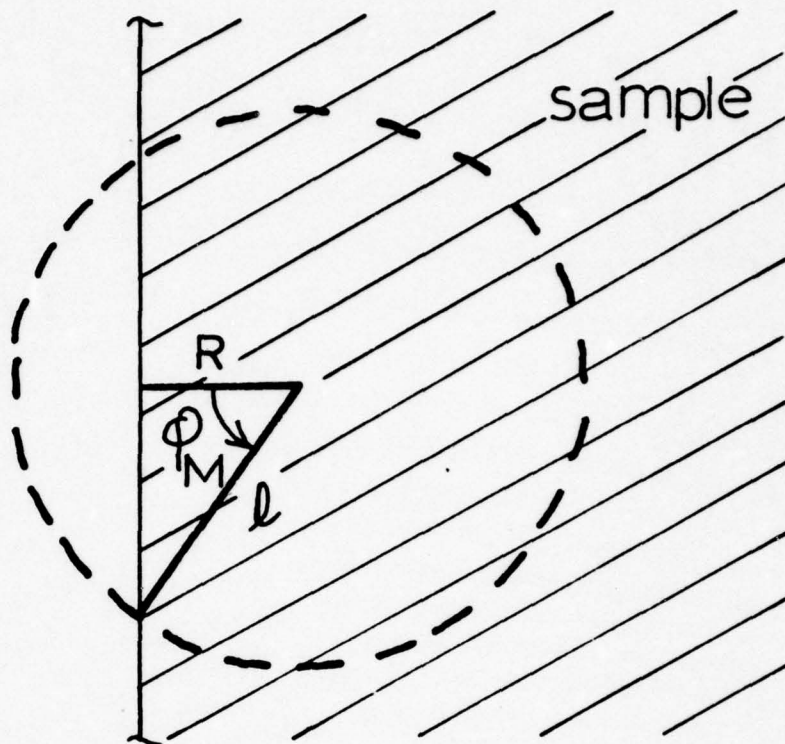
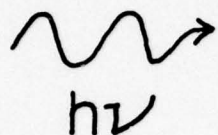
$$W_Q(R) = p\tau_0^{-1} (A'/A) \quad 0 \leq R \leq \ell \quad (3)$$

$$W_Q(R) = 0 \quad \ell < R \quad (4)$$

where A is the area of the sphere of radius  $\ell$ , A' is the part of the area of this sphere which is outside the sample surface, and p is a factor to account for the probability of energy being dissipated radiationlessly instead of radiatively when it reaches the surface. The fraction of the area outside the sample can be found from the double integration

$$\begin{aligned} A &= 2\ell \int_0^\phi \int_0^{\pi/2} d\phi \, 2\ell \sin \theta \, d\theta \\ &= 4\ell \sqrt{\ell^2 - R^2} \cos^{-1}(R/\ell). \end{aligned} \quad (5)$$

TOP  
VIEW



SIDE  
VIEW

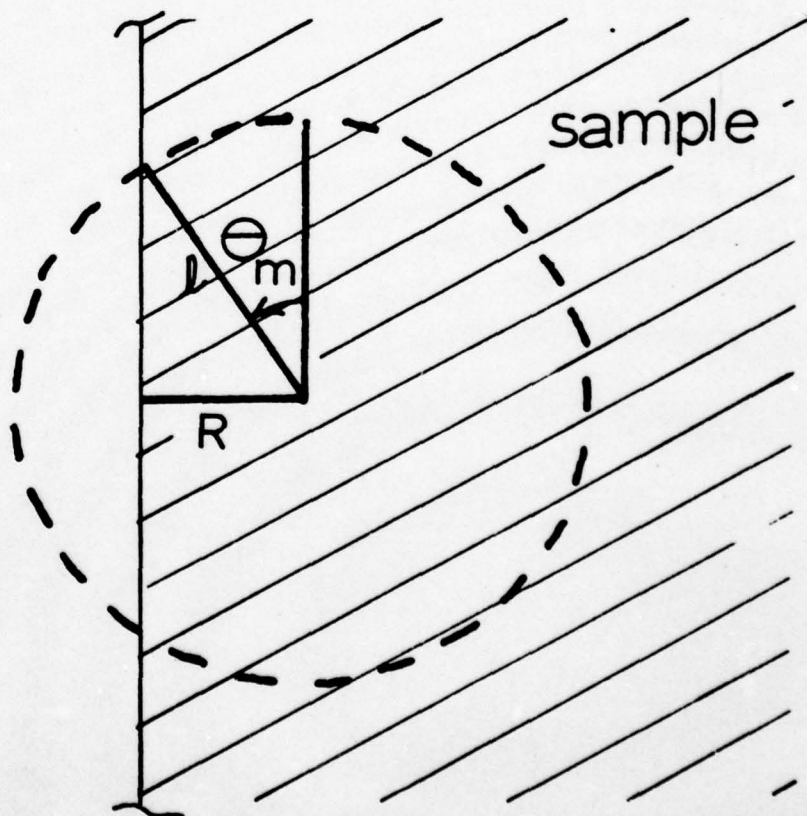
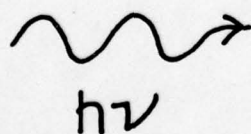


Fig. 11. Top and side view geometry for excitation energy migration in surface quenching model.

Thus, the first part of Eq. (4) becomes

$$W_Q(R) = p(\tau_0 \pi l)^{-1} \sqrt{l^2 - R^2} \cos^{-1}(R/l) \quad 0 \leq R \leq l. \quad (6)$$

The observed fluorescence intensity is proportional to the concentration of excited ions. At time  $t$  the remaining concentration of excited ions which were originally created at a depth  $R$  into the sample is given by the product of the probability of exciting an ion at that position multiplied by the exponential decay function for such ions

$$n_R^*(t) = \exp[-t(\tau_0^{-1} + W_Q(R))] I_0 \sigma C \exp(-\sigma C R) dR. \quad (7)$$

Here  $C$  is the concentration of Nd ions and  $\sigma$  is the absorption cross section and  $I_0$  is the intensity of the incident light. The total concentration of excited Nd ions is found by integrating this expression over the entire thickness of the crystal  $T$ . Using Eqs. (4) and (6) this becomes

$$n^*(t) = \sigma C I_0 e^{-t/\tau_0} \left[ \int_0^l \exp[-t p(\tau_0 \pi)^{-1} \sqrt{1 - (R/l)^2} \cos^{-1}(R/l)] dR + \int_l^T \exp[-\sigma C R] dR \right]. \quad (8)$$

Evaluation of this expression shows that in this model the time dependence of the fluorescence intensity is described by

$$I(t) = I(0) \exp[-t(\tau_0^{-1} + 0.226 p \sigma C l \tau_0^{-1})]. \quad (9)$$

Thus, the quenching rate is given by

$$W_Q = 0.226 p \sigma C l \tau_0^{-1}. \quad (10)$$

The results of these considerations show that a surface quenching model predicts exponential fluorescence decays and a quenching rate which varies linearly with absorption cross section. Since the ion-ion interaction



responsible for the migration is a resonant interaction, not thermal activation is necessary and only a weak temperature dependence is expected. The quenching rate should actually be somewhat greater at lower temperatures where there is less phonon scattering to limit the mean free path of the exciton. This appears to be verified by the lifetime data shown in Fig. 4. Quantitatively the experimentally observed quenching rate for neodymium pentaphosphate can be predicted by Eq. (10) if the thermal conversion probability for excitons reaching the surface ( $p$ ) is taken to be unity and the diffusion length is of the order of  $20\mu$ . Previous estimates of the diffusion length of excitons in this material have ranged from 360 to  $5,000\text{\AA}$ . A theoretical estimate for the diffusion coefficient can be obtained from the expression

$$D = |W_{\text{Nd-Nd}}|^2 R_{\text{nn}}^2 / \Delta v \quad (11)$$

where ion-ion interaction rate,  $R_{\text{nn}}$  is the nearest neighbor Nd separation and  $\Delta v$  is the exciton band widths. A rough estimate of the interaction rate can be found by assuming a nearest neighbor electric dipole-dipole interaction for two ions in exact resonance

$$W_{\text{Nd-Nd}} = \tau_0^{-1} (R_0/R_{\text{nn}})^6 (zC/C_T) \quad (12)$$

where  $z$  is the number of nearest neighbor Nd sites,  $C_T$  is the Nd concentration in the unmixed sample, and the critical interaction distance  $R_0$  is given by

$$R_0 = \left[ \frac{3e^4 f^2 \Omega \tau_0}{8\pi^2 m^2 c^2 n^4 \bar{\nu}} \right]^{1/6}. \quad (13)$$

Here  $f$  is the oscillator strength of the transition between the ground and metastable state.  $\bar{\nu}$  is the average wavenumber in the region of spectral

overlap, and  $\Omega$  is the spectral overlap integral. For two overlapping Lorentzian lines

$$\Omega = \frac{1}{\pi} \frac{\Delta\tilde{\nu}_1 + \Delta\tilde{\nu}_2}{(\Delta\tilde{\nu}_1 + \Delta\tilde{\nu}_2)^2 + (\tilde{\nu}_1^0 + \tilde{\nu}_2^0)^2} \quad (14)$$

where  $\tilde{\nu}^0$  is the peak position and  $\Delta\tilde{\nu}$  is the Lorentzian contribution to the line width. Thus, for perfect overlap  $\Omega$  is proportional to the inverse of the homogeneous contribution to the spectral line width. In most cases this is not possible to measure by normal spectroscopy methods when the transition terminates on the ground state and no significant contributions are present from relaxation processes. Saturation and coherent transient spectroscopy investigations have found homogeneous linewidths of transitions of this type to be of the order of  $10^7$  Hz.<sup>24</sup> This can be used in Eq. (13) which leads to a predicted value of  $51\text{\AA}$  for  $R_0$ . Then for transitions out to fifth nearest neighbors, a distance of  $7.4\text{\AA}$ , Eq. (12) predicts an ion-ion interaction rate of  $9.1 \times 10^9 \text{ sec}^{-1}$ . Substituting these numbers into Eq. (11) yields a predicted diffusion coefficient of  $3 \times 10^{-2} \text{ cm}^2 \text{ sec}^{-1}$ . Then substituting this result into Eq. (3) gives a predicted diffusion length of about  $63\mu$  which is consistent with the value needed to interpret the concentration quenching data with a surface quenching model.

Although each Nd ion has only one true nearest neighbor site in the  $\text{NdP}_5\text{O}_{14}$  lattice structure, there are eight Nd sites within an  $8\text{\AA}$  radius. Thus, for the high concentrations used here every Nd ion will always have other Nd ions close by for efficient energy transfer. Using Eqs. (2), (11) and (12) in Eq. (10) and accounting for the variation in homogeneous linewidth with concentration shown that the quenching rate should vary as  $C^{1.5}$ . This is consistent with experimental data as shown by the solid line in Fig. 3.

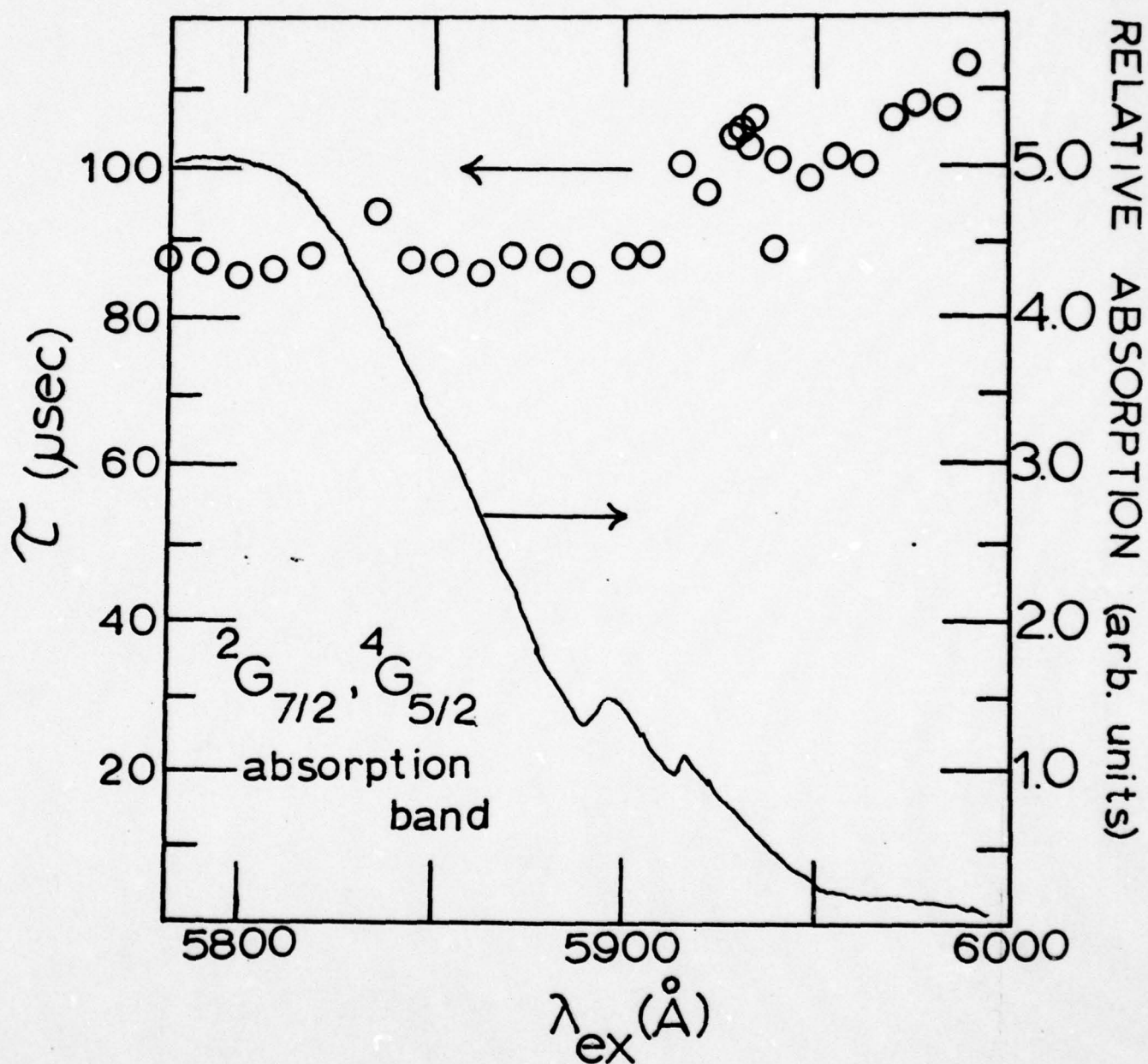


Fig. 12.  $^4F_{3/2}$  fluorescence lifetime vs. wavelength of laser excitation at 14K along with laser probed absorption band at 300K for  $\text{NdP}_5\text{O}_{14}$ .



An attempt was also made to fit the data with a surface quenching model in which the excitation energy did not diffuse but rather was transferred to the surface ions in a single step electric dipole-dipole process. The predictions of this model were not consistent with the observed results because they predicted a non-exponential decay time and quantitatively an unphysically large value for the interaction strength has to be assumed to give the correct magnitude for the quenching rate.

A direct check was made on the prediction that the quenching rate is proportional to the absorption cross section by monitoring the fluorescence lifetime as the laser excitation was scanned from the peak to the wings of the absorption band. The results obtained at 14K for the  $\text{NdP}_{514}\text{O}_{14}$  sample are shown in Fig. 12. There is an obvious increase in fluorescence lifetime and thus a decrease in the quenching rate as the excitation is scanned from the region of high absorption to one of small absorption as predicted. However, the dependence of  $W_Q$  on  $\sigma$  appears to be less than the linear dependence predicted by Eq. (10). There may be several reasons for this. First, it is difficult to change the laser wavelength without also altering its power and beam position. Thus, it is impossible to exactly repeat the experimental conditions from point to point in Fig. 12 and only the general trend of the data can be considered important. Also the theoretical derivation of Eq. (10) is based on the assumption that the number of photons absorbed from the incident beam at depth  $R$  is directly proportional to the absorption cross section. This is only true for small values of the absorption coefficient. The exact expression is

$$\begin{aligned} n &= n_0 [1 - \exp(-\sigma CR)] \\ &= n_0 \sigma CR [1 - \frac{1}{2}\sigma CR + \frac{1}{6}(\sigma CR)^2 - \dots] \end{aligned} \quad (15)$$

and, thus, for the high optical densities treated here the variation with absorption cross section should be less than linear. The linear approximation was made in deriving Eq. (10) only to simplify the calculations.

In order to determine whether the lifetime change shown in Fig. 12 is due to the change in absorption strength and not a result of selectively exciting ions in different sites having different energy transfer characteristics, we measured the decay time after pumping into the  ${}^4G_{11/2}$  band near  $4700\text{\AA}$ . The peak absorption strength of this band is significantly less than that of the  $5800\text{\AA}$  band and the lifetime is measured to be significantly greater, around  $100\mu$  sec. at  $14\text{K}$ . It was difficult to scan the excitation into the wings of this band and measure the lifetime change because of the much weaker fluorescence signal. However, the trend again appeared to be toward longer lifetimes on the band edge. No shorter lifetimes were detected. Thus, we conclude that the lifetime change in Fig. 12 is associated with the change in absorption strength and not just site selectivity.

There is still a question as to the exact mechanism for quenching after the exciton has migrated to the surface. The energy levels of the surface ions may be perturbed in such a way that they act as sinks or allow for cross-relaxation to occur with other Nd ions. A third possibility is that there is such a high density of excited Nd ions on the surface that bi-excitonic processes are responsible for the quenching. The latter possibility was investigated by monitoring the fluorescence lifetime as a function of laser power for the  $\text{NdP}_5\text{O}_{14}$  sample at  $14\text{K}$ . The excitation was near the peak of the  $5800\text{\AA}$  band and the power was decreased by a set of calibrated neutral density filters. The fluorescence lifetime was found to increase slightly with decreased laser intensity. This suggests that some amount of exciton-exciton interaction may be taking place. However, the dependence of  $W_Q$  on laser power does not appear to

be strong enough to account for all of the quenching and most probably several different mechanisms are taking place at the same time.

#### F. Photoacoustic Spectroscopy Results

Photoacoustic spectroscopy techniques have recently been developed to characterize radiationless decay processes of ions in crystals.<sup>18-21</sup> By comparing PAS results with fluorescence excitation spectra, it has been possible to determine dominant relaxation channels.<sup>20,21</sup> Low resolution photoacoustic spectra were obtained at room temperature on the concentrated neodymium pentaphosphate samples. The 1000 W tungsten-halogen lamp chopped at 110 Hz was used as an excitation source. Figure 13 shows the results obtained on the  $\text{NdP}_5\text{O}_{14}$  sample and the  $\text{Nd}_{0.9}\text{Y}_{0.1}\text{P}_5\text{O}_{14}$ . The signal to noise ratio on the more lightly doped samples was too poor to give meaningful results. Note that the relative peak heights of the major absorption bands in the PAS spectrum are comparable to those in the absorption and excitation spectra.

These PAS results are more difficult to interpret than those in the previous samples investigated.<sup>20-21</sup> The photoacoustic signal normalized for the energy of the incident light beam at phase angle  $\theta$  can be expressed as the sum over all the relaxation transitions which generate heat<sup>20</sup>

$$I_{\text{PAS}}(\theta) \propto N_a \sum_i \phi_{\text{nr}}(i) h\nu_i \cos(\alpha_i - \theta) / (N_o h\nu_o) \quad (16)$$

where  $N_a$  is the number of photons absorbed,  $\phi_{\text{nr}}(i)$  is the fraction of excited atoms relaxing via the  $i$ th type of radiationless transition,  $h\nu_i$  is the energy of the phonons emitted in the  $i$ th process, and  $\alpha_i$  is the phase angle at which the signal due to transitions from the initial state of the  $i$ th transition is maximum.  $N_o$  and  $h\nu_o$  are the number and energy of the photons in the excitation beam. For the case of  $\text{Nd}^{3+}$  ions the sum in Eq. (16) should include three



different types of radiationless decay processes which occur during the relaxation of the ions from the level excited by the incident light. First, phonons will be emitted during the decay from the absorption state to the  ${}^4F_{3/2}$  metastable level. Second, the  ${}^4F_{3/2}$  level does not have unit radiative quantum efficiency, and, thus, some amount of relaxation from this state to the ground state occurs radiationlessly. Third, the majority of the fluorescence transitions from the  ${}^4F_{3/2}$  state terminate on levels of the  ${}^4I_J$  multiplets other than the ground state and subsequent relaxation to the ground state occurs radiationlessly. Previous measurements have shown that there is virtually unit probability of relaxing to the metastable level after pumping into higher excited states.<sup>22</sup> The radiative quantum efficiency of the  ${}^4F_{3/2}$  levels is of the order of ~0.9 in the absence of quenching interactions.<sup>23</sup> Most of the emission terminates on either the  ${}^4I_{11/2}$  or the  ${}^4I_{9/2}$  multiplets. Thus, from these considerations and the energy level diagram shown in Fig. 1, it would seem that the higher lying absorption bands should be more intense in the PAS spectrum compared to the lower energy bands than in the absorption and excitation spectra due to the first type of decay processes listed above. This is the type of behavior observed in other samples.<sup>20,21</sup> Figure 10 shows that this is not the case here as exemplified by the fact that the 8000Å band is equal or greater in intensity than the 5800Å band.

This comparison of the absorption, excitation, and photoacoustic spectra indicates that there is relatively more radiationless quenching occurring after excitation into the 8000Å band than after excitation into the 5800Å band. Since the absorption coefficients of these two bands are different, a different spatial distribution of excited ions will occur after excitation into each band. For such heavily concentrated systems as those considered here, the high absorption

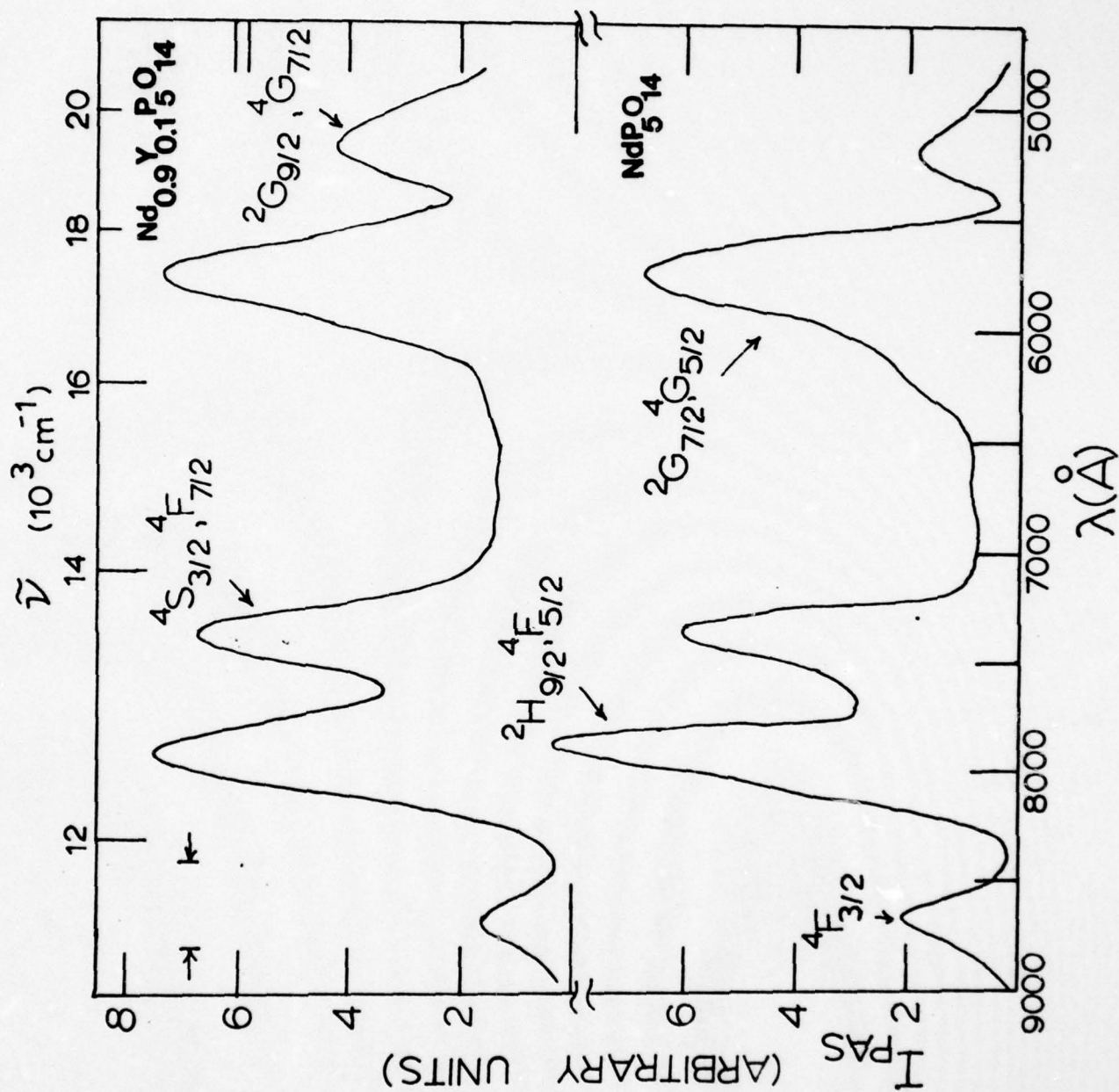


Fig. 13. Photoacoustic Spectra of  $\text{Nd}_{0.9}\text{Y}_{0.1}\text{P}_5\text{O}_{14}$  and  $\text{NdP}_5\text{O}_{14}$  at 300K.

coefficient of the  $8000\text{\AA}$  band will result in a significant fraction of the excited Nd ions being located close to the surface of the crystal. The somewhat smaller absorption coefficient for the  $5800\text{\AA}$  band allows for more the the excited ions to be located farther into the bulk of the crystal. One mechanism to explain the spectral properties reported here is surface quenching which is discussed in detail in the previous section.

We also measured the intensity of the photoacoustic signal as a function of chopping frequency between 110 and 2000 Hz. The  $5145\text{\AA}$  line of an argon ion laser was used for excitation and the rest of the experimental apparatus is the same as described previously.[5] The laser power was maintained at 1 W for all measurements. This excitation wavelength pumps the band consisting of the unresolved levels of the  $^2G_{9/2}$  and  $^4G_{7/2}$  states. The phase of the lock-in amplifier was adjusted for maximum intensity at each chopping frequency for each sample and the PAS intensity normalized to the maximum signal detected for each sample. The S/N ratio was between 50/1 and 100/1 for these measurements.

The results of these measurements are inconclusive at the present time due to cell wall effects and they are now being repeated. However, in all cases the PAS signal was found to exhibit a weaker variation with chopping frequency than predicted theoretically. This is consistent with the predictions of a surface quenching model.

#### G. Discussion and Conclusions

The surface quenching model is consistent with all of the results obtained in this investigation. It also appears to be consistent with data reported by other workers. Similar surface quenching effects have also been observed in other types of materials with high absorption coefficients such as aromatic hydrocarbon crystals.<sup>25</sup>



For crystals with high absorption coefficients radiative reabsorption effects should be expected. We attempted to determine the extent of such effects by observing the fluorescence lifetime as a function of sample alignment. The lifetime appeared to lengthen slightly in going from front face illumination to minimize radiative reabsorption effects.

It should be pointed out that there is a possible alternative explanation for the fact that the relaxation processes in the excited states do not appear to contribute to the PAS signal. This would be true if the decay occurred radiatively instead of radiationlessly. There has been some weak fluorescence observed between 1.4 and 1.7  $\mu\text{m}$  which has not been explained.<sup>7</sup> However, this was observed only at a high level of excitation and only at room temperature and, thus, can not generally account for all of the observed quenching characteristics.

It is still not clear exactly why the fluorescence quenching rate is so much less in  $\text{NdP}_5\text{O}_{14}$  than in YAG:Nd. One obvious difference is that there is less resonance between the  $^4\text{F}_{3/2} \rightarrow ^4\text{I}_{15/2}$  emission transitions and the  $^4\text{I}_{9/2} \rightarrow ^4\text{I}_{15/2}$  absorption. Also a distinguishing feature of the pentaphosphate host is that the Nd ions are fairly isolated from each other and do not share the same oxygen ion.<sup>4</sup> Another interesting observation is that the quenching of Nd fluorescence in phosphate glass hosts is also significantly less than for other glasses.<sup>26</sup> Which of these features is most important in determining the quenching characteristics is not evident. It is known that hydrogen and other impurity ions are very effective in quenching the fluorescence in these materials.<sup>27</sup> These impurities may perturb the energy levels of neighboring Nd ions to allow stronger quenching interactions to occur. The energy levels of surface ions may similarly be perturbed.

The diffusion coefficient of the order of  $\sim 10^{-2} \text{ cm}^2 \text{ sec}^{-1}$  determined for  $\text{NdP}_5\text{O}_{14}$  is significantly greater than the typical values of D which range

between  $10^{-9}$  to  $10^{-14}$   $\text{cm}^2 \text{sec}^{-1}$  for energy migration among other systems of rare earth ions in solids.<sup>28</sup> The reason for this primarily the higher concentration of Nd ions. In other highly concentrated systems exciton diffusion coefficients of this magnitude have been found.<sup>25,29,30</sup> This results in efficient spatial diffusion without spectral diffusion. As the excitation energy migrates near to a spectrally different site there are always a significant number of ions nearby in equivalent sites that favor transfer. Only at the surface is there a significant concentration of perturbed ions to cause effective quenching. The fact that the exciton diffusion length is greater than the effective thermal diffusion length<sup>19</sup> minimized the contribution of excited state relaxation phonons to the photoacoustic signal and enhances the contribution of the radiationless quenching at the surface.

The experiments described here do not provide conclusive proof for the mechanism of fluorescence quenching in neodymium pentaphosphate crystals. However, they are not consistent with the predictions of a model of energy migration to randomly distributed sinks whereas the experiments are in agreement with the predictions of a model based on the surface quenching of excitons with a large diffusion length. It is also interesting to note that quenching and PAS studies made by Auzel, et. al.<sup>34</sup> on powdered neodymium pentaphosphate with an  $80\mu\text{m}$  grain size exhibited substantially greater fluorescence quenching than our single crystal samples. This is also consistent with a surface quenching model involving excitons with long diffusion lengths.

A final attempt to substantiate our surface quenching model was made by making a measurement of the fluorescence lifetime of a sample of  $\text{NdP}_5\text{O}_{14}$  covered with an epitaxial layer of  $\text{Gd}_{0.5}\text{La}_{0.46}\text{P}_5\text{O}_{14}$ . A 10% increase in lifetime was observed. Although a lifetime increase would be predicted by the surface

quenching model, the small observed increase is not sufficient to unambiguously substantiate the model. We plan to continue investigating the effect of different surface environments on the lifetime of these samples.

#### REFERENCES

- [1] S. R. Chinn, H. Y-P. Hong and J. W. Pierce, *Laser Focus* 12, (May), 64 (1976).
- [2] H. G. Danielmeyer and H. P. Weber, *IEEE J. Quantum Elect.* 8, 805 (1972).
- [3] H. G. Danielmeyer, in *Festkörperprobleme (Advances in Solid State Physics)*, ed H. J. Quieser (Pergamon/Vieweg, Braunschweig, 1975) vol. 15, p. 253.
- [4] H. P. Weber, *Opt. and Quantum Elect.* 7, 431 (1975).
- [5] S. Singh, D. C. Miller, J. R. Potopowicz and L. K. Shick, *J. Appl. Phys.* 46, 1191 (1975).
- [6] W. Strek, C. Szafranski, E. Lukowiak, Z. Mazurak and B. Jezowska-Trzebiatowska, *Phys. Stat. Sol. A* 41, 547 (1977).
- [7] M. Blätte, H. G. Danielmeyer, and R. Ulrich, *Appl. Phys.* 1, 275 (1973).
- [8] B. C. Tofield, H. P. Weber, T. C. Damen and P. F. Liao, *J. Solid State Chem.* 12, 207 (1975).
- [9] A. Lempicki, *Optics Comm.* 23, 376 (1977).
- [10] H. G. Danielmeyer, *J. Lumin.* 12/13, 179 (1976).
- [11] F. Auzel, *IEEE J. Quantum Elect.* 12, 258 (1976).
- [12] P. P. Liao, H. P. Weber, and B. C. Tofield, *Solid State Comm.* 16, 881 (1973).
- [13] J. M. Flaherty and R. C. Powell. *Solid State Comm.*, to be published, (1978).
- [14] C. Brecher, L. A. Riseberg, and M. J. Wever, *Appl. Phys. Lett.* 30, 475 (1977); C. Brecher and L. A. Riseberg, *Phys. Rev. B* 13, 81 (1976); M. D. Kurz and J. C. Wright, *J. Lumin.* 15, 169 (1977); R. K. Watts and W. C. Holton,



- J. Appl. Phys. 45, 873 (1974); C. Hsu and R. C. Powell, Phys. Rev. Letters 35, 734 (1975); C. Hsu and R. C. Powell, J. Phys. C 9, 2467 (1976); G. E. Venikouas and R. C. Powell, Phys. Rev. B. to be published, (1978); R. Flach, D. S. Hamilton, P. S. Selzer, and W. M. Yen, Phys. Rev. B 15, 2348 (1977); P. M. Selzer, D. S. Hamilton and W. M. Yen, Phys. Rev. Letters 38, 858 (1977); J. Koo, L. R. Walker, and S. Geschwind, Phys. Rev. Letters 35, 1609 (1975); N. Motegi and S. Shionoya, J. Luminescence 8, 1 (1973); and L. A. Kiseberg and W. C. Holton, Optics Comm. 9, 298 (1973).
- [15] F. Auzel. Ann. Telecommun. 4, 199 (1969).
- [16] B. K. Judd, Phys. Rev. 127, 750 (1962).
- [17] M. Zokai and R. C. Powell, Bull. American Phys. Soc. 23, 202 (1978).
- [18] A. Rosencwaig. Opt. Commun. 7, 305 (1975); Anal. Chem. 47, 593 (1975).
- [19] H. C. Murpny and L. C. Aamodt, J. Appl. Phys. 48, 3502 (1977); L. C. Aamodt, J. C. Murpny and J. G. Parker, J. Appl. Phys. 48, 927 (1977).
- [20] L. D. Merkle and R. C. Powell, Chem. Phys. 46, 303 (1977).
- [21] R. G. Peterson and R. C. Powell, Chem. Phys. Letters 53, 366 (1978).
- [22] H. P. Weber and B. C. Tofield, IEEE J. Quantum Elect. 11, 368 (1975).
- [23] H. P. Weber, P. F. Liao and B. C. Tofield, IEEE J. Quantum Elect. 10, 563 (1974).
- [24] A. Z. Genack, R. M. Macfarlane and R. G. Brewer, Phys. Rev. Lett. 37, 1078 (1976); A Szabo, Phys. Rev. Lett. 25, 924 (1970); L. E. Erickson, Phys. Rev. B 16, 4731 (1977).
- [25] R. C. Powell and Z. G. Soos, J. Luminescence 11, 1 (1975).
- [26] M. J. Weber, Private Communications.
- [27] B. C. Tofield, H. P. Weber, T. C. Damen and G. A. Pasteur, Mat. Res. Bull. 9, 435 (1974).

- [28] R. K. Watts, in "Optical Properties of Ions in Solids", edited by B. DiBartolo (Plenum Press, New York, 1975).
- [29] F. J. Himpsel, V. Saile, N. Schwentner, M. Skibowski, E. E. Koch and J. Jortner, J. Chem. Phys. 65, 5226 (1976).
- [30] C. E. Bleil and I. Broser, J. Phys. Chem. Solids 25, 11 (1964).
- [31] H. P. Wever, B. C. Tofield, and P. F. Liao, Phys. Rev. B11 (1975) 1152.
- [32] J. P. Budin, A. Milatos-Roufos, N. D. Chinh, and G. Le Roux, J. Appl. Phys. 46 (1975) 2867.
- [33] T. Kobayashi, T. Sawada, H. Ikeo, K. Muto and J. Kai, J. Phys. Soc. Japan 40 (1976) 595.
- [34] F. Auzel, D. Meichenin and J. C. Michel, presented at the International Conference on Luminescence, Paris, July 17-21, 1978.

## VII. RESULTS ON THE CHARACTERIZATION OF RADIATIONLESS PROCESSES

### VII.1 Radiationless Processes in $\text{KCl:Eu}^{2+}$

#### A. Introduction

There has been significant interest in divalent europium in various hosts for use as a phosphor material (Reisfeld and Glasner 1964, Chase 1970, Loh 1968, Kisliuk et. al. 1968, Weakliem 1972, Nasu et. al. 1974, Kaplyanskii and Feofilov 1962, Blasse 1973, Basse and Brill 1968, 1970, Blasse et. al. 1971, 1968a, b, Krüger 1948, Butement 1948, Freed and Katcoff 1948, Waite 1974, Karel and Mares 1973). However, there are still many aspects of the optical properties of  $\text{Eu}^{2+}$  ion which are not well characterized. We report here the results of a study of the spectroscopic properties of divalent europium in potassium chloride single crystals. The investigation centers around the characterization of three different types of physical processes: energy transfer, vibronic emission, and radiationless transitions. Along with standard optical spectroscopy methods, special techniques of laser time-resolved spectroscopy and photoacoustic spectroscopy were utilised.

The crystal structure of KCl is face centered cubic with lattice constant  $6.29\text{\AA}$ . The  $\text{K}^+$ -atom, for which the  $\text{Eu}^{2+}$  impurity substitutes, has an octahedral site symmetry, point group  $O_h$ , with six nearest neighbor  $\text{Cl}^-$  ions. Due to the double positive charge of the europium, charge compensation occurs in the form of  $\text{K}^+$  vacancy. It is expected that this vacancy will usually reside at one of the  $\text{K}^+$  sites nearest the  $\text{Eu}^{2+}$ , lowering the symmetry of the  $\text{Eu}^{2+}$  site to  $C_{2v}$ . The crystal structure around such a site is depicted in Fig. 1.

The previous work on  $\text{Eu}^{2+}$  ions in various crystal hosts has demonstrated the existence of two strong broad absorption bands in the near ultraviolet region of the spectrum. This is attributed to transitions from the  $^8S_{7/2}$  ground state of the  $4f^7$  configuration to the crystal field splitting of the d electron into  $e_g$  and  $t_{2g}$  states. In KCl crystals the  $\text{Eu}^{2+}$  ions enter the lattice substitutionally for  $\text{K}^+$  ions and due to the resultant six-fold coordination of nearest-neighbour anions the  $t_{2g}$  level lies below the  $e_g$  level. Under high resolution at low temperature structure can be observed on the  $t_{2g}$  band which has been attributed to the electronstatic and spin-orbit interactions between the electron and the six f electrons. The fluorescence spectrum of  $\text{Eu}^{2+}$  varies greatly in different hosts, depending on whether the excited states of the  $4f^7$  configuration lie above or below the lowest  $4f^65d$  level. In potassium chloride crystals the  $t_{2g}$  level of the  $4f^65d$  configuration has been found to be the fluorescing level. At low temperatures this appears as a sharp zero-phonon line with a broad, low-energy vibronic sideband.

In this study we investigated several aspects of the optical spectra which have not been well characterized in the past. The first is the effect of annealing on the fluorescence spectrum which shows that there is a tendency for the europium ions to form aggregates due to charge compensation problems as reported in §2. Radiationless energy transfer between ions in different types



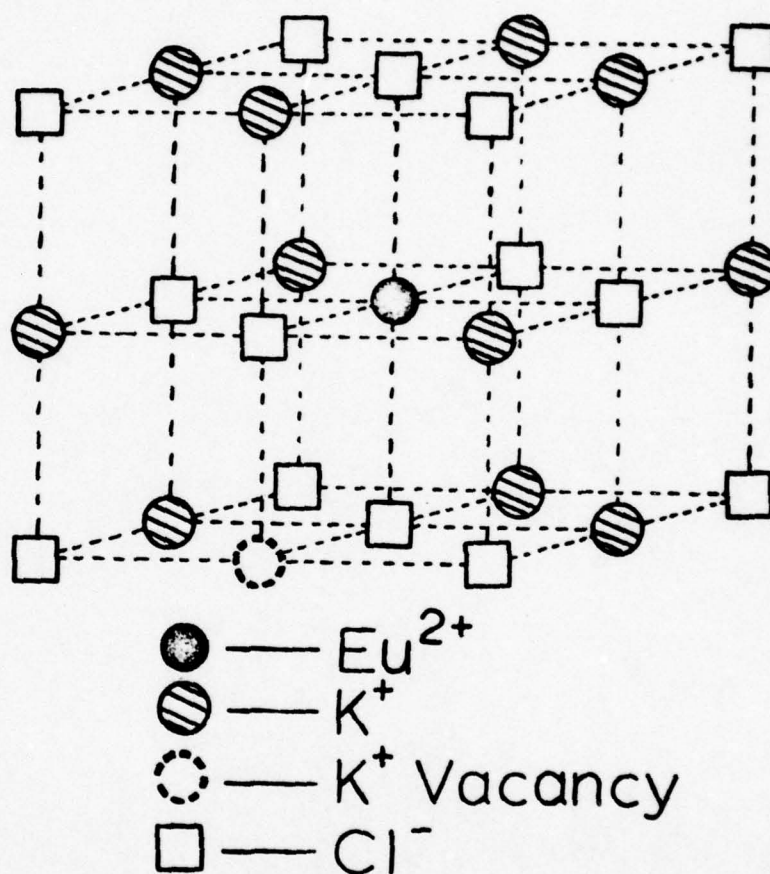


Fig. 1.  $\text{Eu}^{2+}$ - $\text{K}^{+}$  Vacancy Site in KCl

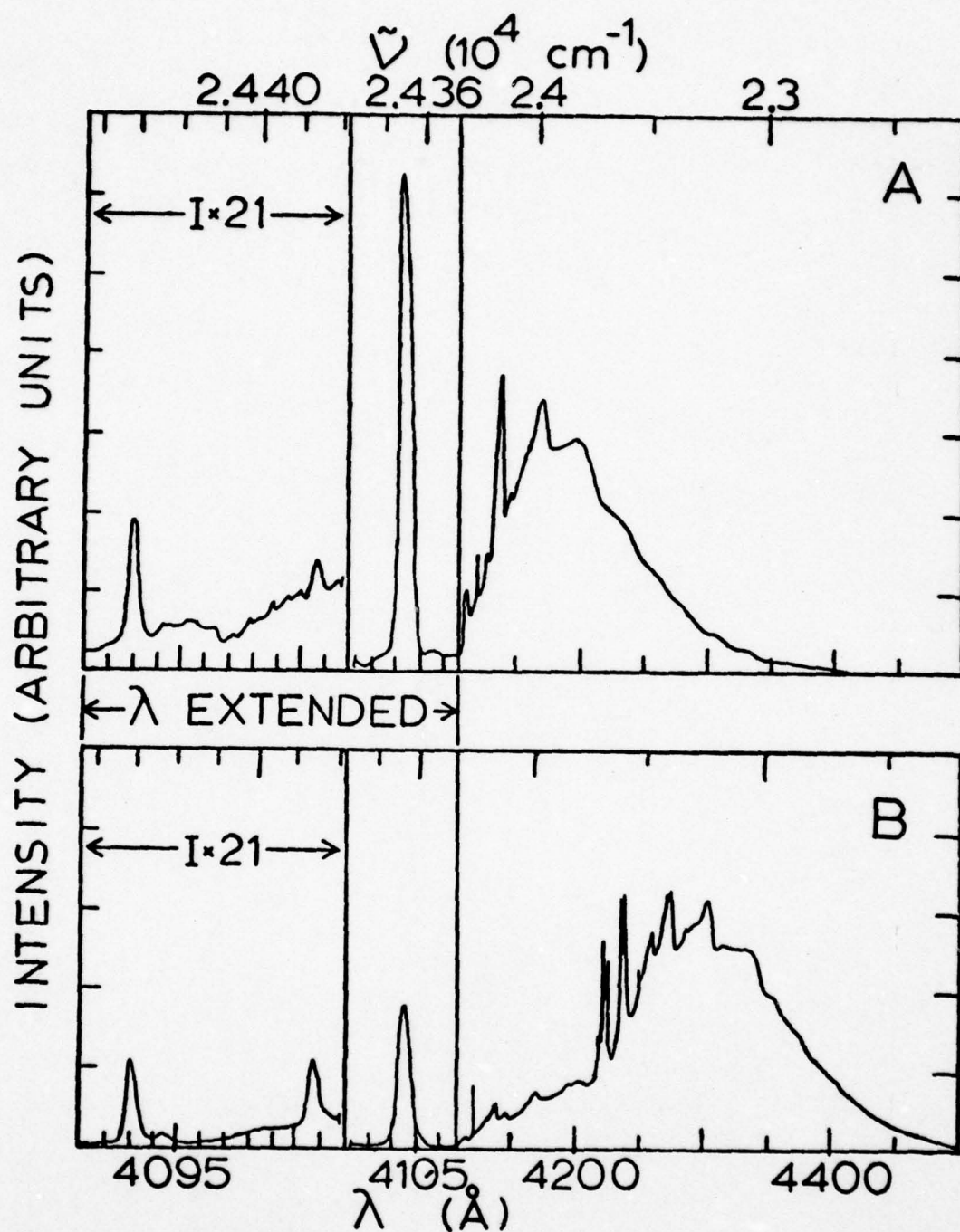


Fig. 2. KCl:Eu Fluorescence at 13 K  
 A: Briefly Annealed Sample  
 B: Unannealed Sample

of aggregate sites was then characterized as described in §3. Section 4 describes a computer analysis of the vibronic emission band. The one-phonon effective density of states obtained from this work is used to interpret the temperature dependence of the width and position of the major zero-phonon line described in §5. It is found that only low-frequency modes contribute strongly to these effects. Finally the radiationless decay processes from the excited  $e_g$  and  $t_{2g}$  levels are investigated and it is found that a slow decay takes place from the higher level which is attributed to the participation of an excited state of the  $4f^7$  configuration in the relaxation process. This is discussed in §6.

#### B. Sample Growth and Properties

The samples used in this work were grown in the Oklahoma State University crystal growth facility. The starting materials were purified in a Bridgman-Stockbarger furnace by a reactive-atmosphere processing technique with slow refreezing of the melt. Single crystals were pulled from the melt of this starting material using previously grown seeds. The samples used in this work were cleaved from boules containing 275 ppm (atomic) of europium.

The  $\text{Eu}^{2+}$  ions replace  $\text{K}^+$  ions in the lattice and charge compensation is provided by the presence of potassium ion vacancies. Previous studies by Fong et al (1969, 1970) have shown that the charge compensation is primarily local with the vacancy probably residing at a cation site which is a nearest neighbour to a  $\text{Eu}^{2+}$  ion. The presence of vacancies facilitates the migration of the europium ions and Sill and Martin (1977), Sill et. al. (1977) have observed a strong thermal-treatment dependence of the formation of aggregates of  $\text{Eu}^{2+}$ -vacancy pairs. Their flow stress measurements indicate that after annealing at temperatures near the KCl melting point and quenching to room temperature isolated



$\text{Eu}^{2+}$ -vacancy pairs dominate the distribution of defects whereas after a few days at room temperature aggregates of these pairs are found. After many months at room temperature precipitation of the pairs into very large aggregates is observed.

The optical absorption spectrum is not affected by heat treating the sample but the fluorescence spectrum shows significant changes due to aggregation of defects. At room temperature the fluorescence band for an annealed sample is narrower and peaks at higher energy compared to the band in an unannealed sample. The low-temperature fluorescence spectra for partially annealed (900K for one half hour) and unannealed samples are shown in Fig. 2. Two distinct differences are seen. The first is that the unannealed sample exhibits a major zero-phonon line at  $4104.5\text{\AA}$  as well as three minor lines at  $4093.0$ ,  $4094.4$ , and  $4100.7\text{\AA}$ , whereas in the partially annealed sample the minor lines are greatly reduced in intensity. In a sample thoroughly annealed for 24 hours at 1000K the minor lines are not observed at all. These four zero-phonon lines are attributed to fluorescence from europium ions in different types of crystal field environments. The major line appears to be associated with isolated  $\text{Eu}^{2+}$ -vacancy pairs whereas the weaker, higher energy lines appear to come from europium ions in aggregated sites. The fluorescence lifetime of the major zero-phonon line is  $1.1\text{ }\mu\text{s}$  whereas the lifetimes of the smaller lines are between  $0.8$  and  $0.9\text{ }\mu\text{s}$ .

The second type of evidence for the effects of aggregation of defects can be seen in the broad band emissions shown in figure 1. In the annealed sample the broad band emission is the vibronic sideband of the major zero-phonon line and is similar in appearance to divalent europium emission reported by other workers. These features are much weaker in the spectrum of the unannealed sample and most of the fluorescence intensity appears in a new, longer wavelength

band which peaks at about  $4300\text{\AA}$ . This emission grows in intensity very slowly as a function of time and is prominent only after the sample has been kept at room temperature for several months. Because of this characteristic the  $4300\text{\AA}$  band is attributed to emission from europium ions in regions of the crystal in which precipitation of defect aggregates has occurred. The fluorescence lifetime of this band is measured to be  $1.3\text{ }\mu\text{s}$ .

### C. Energy Transfer Between $\text{Eu}^{2+}$ Ions

Energy transfer between europium ions having different types of local crystalline environments was investigated by monitoring the relative time dependences of the various zero-phonon lines in both the partially annealed and the unannealed samples (Merkle and Powell 1977a). The samples were mounted on the cold finger of a cryogenic refrigerator capable of varying the temperature from about 10 K to room temperature. They were excited by pumping into the  $t_{2g}(4f^65d)$  excited level using a pulsed nitrogen laser having a 10 ns pulse of about 350 kW peak power. The fluorescence was analysed by a 1-m Czerny-Turner monochromator and detected by a cooled RCA C31034 photomultiplier tube. A boxcar integrator was used for signal averaging. The time-variable aperture on the boxcar was used to obtain both the time-resolved fluorescence spectra and the fluorescence decay times.

The ratios of the integrated fluorescence intensities of the  $4104.5\text{\AA}$  line to the  $4093\text{\AA}$  line are shown in Fig. 3 as a function of time after the laser excitation pulse for both the unannealed and partially annealed samples at 13 and 35 K. The data are listed in Table I. In general there is a decrease, or only a slight increase, in these intensity ratios at early times and a strong increase at later times. Two sources can contribute to these observed time dependences. The first is the difference in fluorescence decay times between

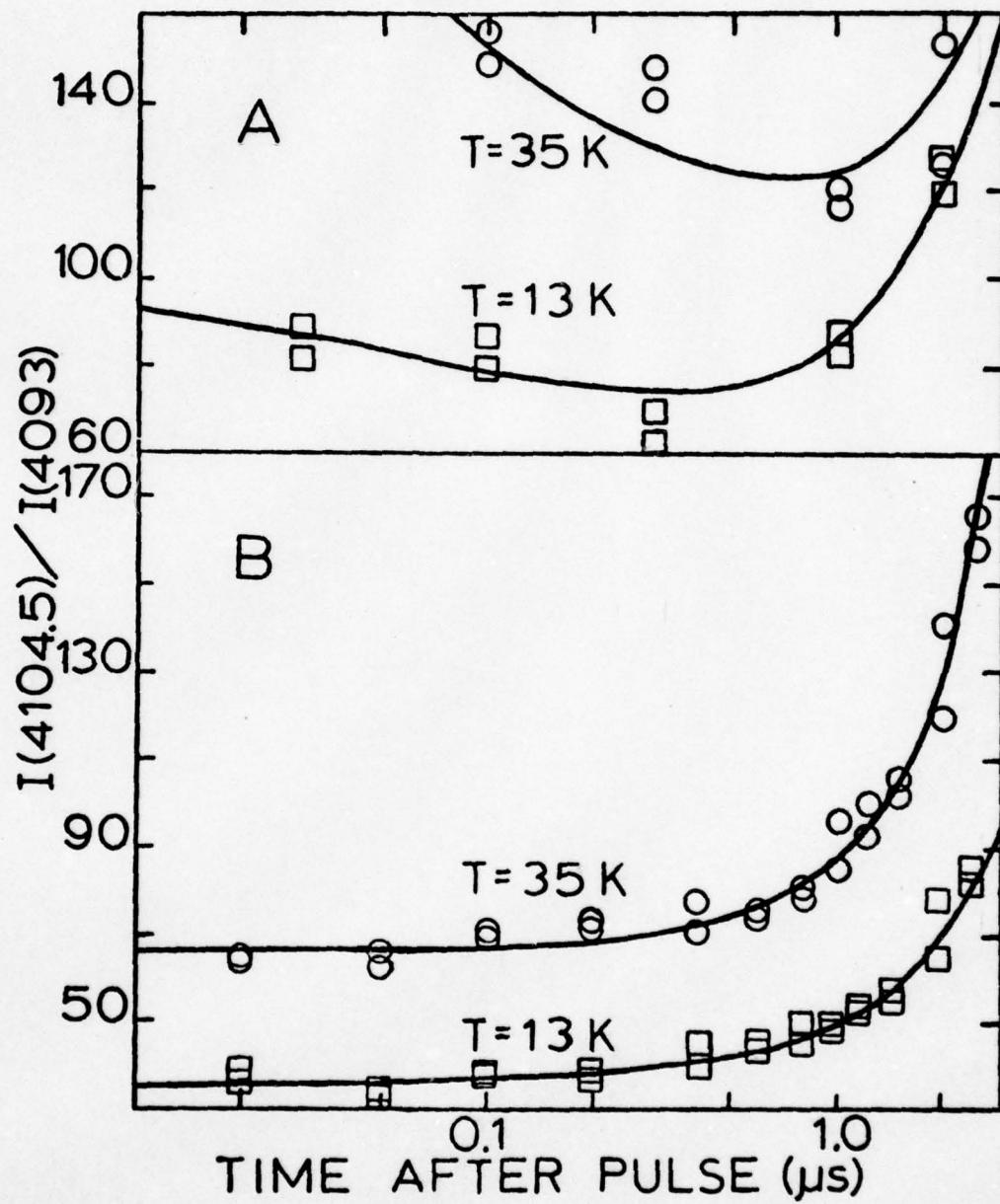


Fig. 3. . KCl:Eu TRS Intensity Ratios  
 A: Briefly Annealed Sample  
 B: Unannealed Sample



TABLE I  
INTEGRATED FLUORESCENCE INTENSITIES FOR 4093.0 Å AND 4104.5 Å  
LINES OF KCl:Eu<sup>2+</sup> (ARBITRARY UNITS)

(μsec)	T = 13K			T = 35K		
	I <sub>4093.0</sub>	I <sub>4104.5</sub>	$\frac{I_{4104.5}}{I_{4093.0}}$	I <sub>4093.0</sub>	I <sub>4104.5</sub>	$\frac{I_{4104.5}}{I_{4093.0}}$
0.02	0.23	8.82	38.3	0.19	12.18	64.1
	0.23	8.40	36.5	0.19	12.18	64.1
0.05	0.29	9.45	32.6	0.21	13.23	63.0
	0.26	8.61	33.1	0.20	13.23	66.2
0.1	0.25	9.45	37.8	0.20	14.07	70.4
	0.24	9.24	38.5	0.19	13.44	70.7
0.2	0.24	8.82	36.8	0.19	14.07	74.1
	0.23	8.82	38.3	0.20	14.28	71.4
0.4	0.26	10.08	38.8	0.18	12.81	71.2
	0.22	10.08	45.8	0.15	11.76	78.4
0.6	0.19	8.40	44.2	0.17	12.81	75.4
	0.20	8.40	42.0	0.17	12.81	75.4
0.8	0.20	9.87	49.4	0.16	12.39	77.4
	0.21	9.45	45.0	0.16	12.60	78.8
1.0	0.17	7.98	46.9	0.14	13.44	96.0
	0.16	7.98	49.9	0.15	12.81	85.4
1.2	0.15	7.77	51.8	0.14	13.02	93.0
	0.15	7.77	51.8	0.13	13.02	100.2
1.5	0.15	8.19	54.6	0.12	12.60	105.0
	0.14	7.98	57.0	0.12	12.18	101.5
2.0	0.12	7.77	64.8	0.11	13.23	120.3
	0.10	7.77	77.7	0.10	14.07	140.7
2.5	0.09	7.56	84.0	0.07	11.13	159.0
	0.09	7.35	81.7	0.07	11.55	165.0

the two types of emitting centres and the second is energy transfer between the centres. The energy transfer process itself can have an intrinsic time dependence associated with it depending on such factors as the mechanism for the interaction and the spatial distribution of defect centres. Many different kinetic models were formulated in an attempt to explain the results shown in Fig. 3. The only model which gave a good, consistent fit to the data was one based on a resonant electric dipole-dipole interaction process between randomly distributed ions with no back-transfer taking place as described below.

The rate equations describing the time dependences of the populations of the excited states of ions in the two different types of sites are

$$\dot{n}(t) = W - Bn(t) - \frac{1}{2}n(t) \omega t^{-\frac{1}{2}} \quad (1)$$

$$\dot{n}'(t) = W' - B'n'(t) + \frac{1}{2}n(t) \omega t^{-\frac{1}{2}} \quad (2)$$

where  $n$  and  $n'$  refer to the excited state populations of ions in sites emitting the 4104.5Å and 4093.0Å lines, respectively. The  $W$ 's and  $B$ 's represent the pumping rates and the fluorescence decay rates of the ions in the two sites. The energy transfer rate is  $\omega/t^{\frac{1}{2}}$  where the time dependence of electric dipole-dipole interaction is expressed explicitly. For the short laser pulse the pumping rates can be considered to be delta functions and equations (1) and (2) solved to give the fluorescence intensity ratios

$$\frac{I(t)}{I'(t)} = \frac{B_r n(t)}{B'_r n'(t)} = \frac{B_r}{B'_r} \frac{\exp[(B' - B)t - \omega t^{\frac{1}{2}}]}{[n'(0)/n(0)] + \omega \int_0^t \exp[B' - B)x^2 - \omega x] dx} \quad (3)$$

where  $B_r$  and  $B'_r$  are the radiative decay rates.

TABLE II  
KCl:Eu<sup>2+</sup> ENERGY TRANSFER PARAMETERS

Parameter	Briefly Annealed Sample		Unannealed Sample	
	T = 13K	T = 35K	T = 13K	T = 35K
$\tau/\tau'$	1.33	1.33	1.43	1.43
$n'(o)/n(o)$	140	140	52.6	52.6
K	0	0.0055	0	0.0120
$B'-B(\mu s^{-1})$	0.9	0.4	0.32	0.20
$\omega_{fit}(\mu s^{-1})$	0.010	0.007	-0	0.001
$\omega_{theory}(\mu s^{-1})$	0.004	0.004	0.0006	0.0007
$R_{o_{fit}}(\text{\AA})$	35.0	31.1	-0	30.1
$R_{o_{theory}}(\text{\AA})$	25.6	26.8	25.6	26.8



The expression in equation (3) can be used to fit the low-temperature data treating the energy transfer rate as an adjustable parameter. The ratio of radiative decay times is taken to be the same as the ratio of measured fluorescence decay times which is a good approximation for these allowed transitions. The best fits to the results are shown as solid lines in Fig. 3 and the magnitudes of the transfer rates which are used to obtain these fits are listed in Table II. At high temperatures part of the I' intensity may be obscured by the vibronic sideband and an additional adjustable parameter K must be included in the theoretical expression used to fit the data.

This analysis indicates that the decrease in the intensity ratios at short times can be attributed to energy transfer from ions in sites giving rise to the 4104.5Å emission to ions in sites emitting at 4093.0Å whereas the increase at long times is associated with the lifetime differences between the ions in the two different sites. The transfer rate can be predicted theoretically from the expression (Eisenthal and Siegel 1964)

$$\omega = \frac{4}{3}\pi^{3/2} R_0^3 C_a \tau_s^{-1/2} \quad (4)$$

where  $C_a$  is the concentration of activator ions,  $\tau_s$  is the intrinsic lifetime of the sensitiser ions, and  $R_0$  is the critical interaction distance given by (Förster 1948, Dexter 1953)

$$R_0^6 = \frac{e^2}{mc^2} \frac{3\phi_s f_a}{4(2\pi n \bar{\nu}_{sa})^4} \int G_s(\bar{\nu}) g_a(\bar{\nu}) d\bar{\nu}. \quad (5)$$

Here  $f_a$  is the oscillator strength of the activation transition,  $\phi_s$  is the quantum efficiency of the sensitiser,  $\bar{\nu}_{sa}$  is the average wavenumber in the region of spectral overlap, and the overlap integral is given in terms of normalised

lineshape functions for the sensitiser and activator transitions. The index of refraction for KCl is  $n = 1.52$ , the activator oscillator strength is estimated from the  $t_{2g}$  absorption band to be 0.02, and the sensitiser quantum efficiency is taken to be 0.6 as will be discussed in §5. The overlap integral can be roughly approximated by that of two Lorentzian lines

$$\int G_s(\tilde{\nu})g_a(\tilde{\nu})d\tilde{\nu} \approx \frac{1}{\pi} \frac{\Delta\tilde{\nu}_s + \Delta\tilde{\nu}_a}{(\Delta\tilde{\nu}_s + \Delta\tilde{\nu}_a)^2 + (\tilde{\nu}_s^0 - \tilde{\nu}_a^0)^2} \quad (6)$$

Although local strains causing inhomogeneous broadening may alter the exact overlap of a specific sensitiser-activator pair, equation (6) provides a reasonable average value for the overlap. This is especially true since it is used in equation (5) to obtain an estimate for  $R_0$ . In this equation all parameters are taken to the 1/6 power and thus large deviation in the parameters are required to cause significant changes in  $R_0$ . Using a Voigt profile analysis of the observed lineshapes (Posener 1959), the Lorentzian widths are found to be about  $1.5 \text{ cm}^{-1}$  at 13 K and  $2.4 \text{ cm}^{-1}$  at 35 K. The theoretical values predicted in this way for  $R_0$  are listed in Table II.

The qualitative fit to the data with this model is quite good. The slight change of  $R_0$  with temperature is consistent with the assumption of a resonant interaction process where the temperature dependence of the interaction is contained in the spectral overlap integral as opposed to a phonon-assisted process with a stronger, activation-energy type of temperature dependence. The quantitative fit to the data with this model is also acceptable. The values of  $R_0$  predicted by (5) and (6) are somewhat smaller than those obtained from fitting the data using (3) and (4). However, this is relatively good agreement considering

the estimates of parameters which had to be made in obtaining both the experimental and theoretical values of  $R_0$ .

One of the sources of error in determining values of  $R_0$  from equation (6) is the estimate of the concentration of  $\text{Eu}^{2+}$  ions in activator sites. Comparison of laser-excited and broad-excited fluorescence spectra indicates that no selective excitation occurs. Therefore, the ratios of the fluorescence intensities of the lines observed immediately after the laser pulse are proportional to the ratios of the concentration of europium ions in the different types of sites. For the partially annealed sample this information was used in estimating values of  $C_a$  for determining  $R_0$  from equation (6). For the unannealed sample the situation is more complicated because of the presence of the broad band associated with emission from large aggregate centres. Since many of the  $\text{Eu}^{2+}$  ions in the sample will be in these aggregate centres, the concentration of ions in activator sites will be greatly reduced. Relative intensity measurements indicate that  $C_a = 0.0011 C_{\text{Eu}}$  in this case.

#### D. Analysis of the Vibronic Spectrum of $\text{Eu}^{2+}$ in KCl

The broad band fluorescence emission shown in figure 1 originates from the simultaneous emission of one or more phonons concurrently with the photon emission. The structure of this vibronic band has been analysed by Nasu et. al. (1974) by projecting the phonon density of states at different parts of the Brillouin zone onto the normal vibrational modes of the Eu-vacancy defect centre complex. They identify two of the sharp peaks on the sideband structure as being associated with local modes of the defect centre. We describe in this section a different type of analysis of this sideband in which a computer iteration fitting process is used to deconvolute the observed band into one-phonon and multi-phonon contributions.



The peaks in the observed vibronic emission band should occur at energies where there is a high density of phonon states and where selection rules allow the phonons having these energies to take place in vibronic emission processes. The selection rules for vibronic emission processes can be determined from group theory considerations. Phonons which can take part in vibronic emission processes are those which transform according to irreducible representations of the initial and final electronic states and the electric-dipole-moment operator

$$\Gamma_i^{\text{el}} \times \Gamma_{\text{ed}} \times \Gamma_f^{\text{el}} \subset \Gamma_{\text{ph}}. \quad (7)$$

Assuming  $O_h$  symmetry for the crystallographic point group, group theory analysis shows that all gerade phonon modes at all points in the Brillouin zone are allowed to take place in the vibronic emission processes in  $\text{KCl:Eu}^{2+}$ . With local charge compensation the site symmetry is lowered to  $C_{2v}$  and no phonon modes are forbidden by selection rules to participate in vibronic transitions.

The theoretical derivation of the equation and the computer program used to fit these data were described previously (Mostoller et. al. 1971, Kim et. al. 1975). The expression for the sideband of an allowed electric dipole transition can be expressed as

$$P_{ab} = C\omega^3 |M_{ab}|^2 G_B(ab;\omega) \quad (8)$$

where  $C$  is a constant,  $M_{ab}$  is the matrix element for the electronic transition between state  $a$  and state  $b$ , and  $G_B(ab;\omega)$  is the spectral distribution function which is given by

$$G_B(ab;\omega) = \sum_{m=1}^{\infty} G_m(ab;\omega) \quad (9)$$

where  $m$  is the order of the phonon process, In this calculation the one-phonon spectrum  $G_1(ab;\omega)$  for emission at  $T = 0$  was represented by a series of evenly spaced  $\delta$ -function spikes,

$$G_1(ab;\omega) = 2\pi e^{-S} \sum_q S_q \delta[(\omega_0 - \omega) - \omega_q], \quad (10)$$

where  $S_q$  gives the individual mode Huang-Rhys factor for the  $q$  phonon mode, and  $S$  is the total Huang-Rhys factor for the system. The function  $G_m$  is represented as a convolution of  $G_1$  and  $G_{m-1}$

$$G_m(ab;\omega) = \frac{e^S}{2\pi m} \int_{-\infty}^{\infty} d\omega' G_1(ab;\omega') G_{m-1}(ab;\omega_0 - \omega' - \omega). \quad (11)$$

An original 'guess' at the one-phonon contribution to the sideband is needed as input to the computer program to initiate its iteration process, but the final fitting is not very sensitive to the initial estimate chosen.

The results of this fitting procedure are shown in Fig. 4. Part (a) compares the experimental sideband  $G_{exp}$  with the best fit obtained from the iteration process  $G_{tot}$ . This fit was obtained using the measured sideband up to about 0.03 eV as the initial input for the estimated  $G_1$  and a value of 3.72 as the total Huang-Rhys factor. The latter is a measure of the strength of the electron-phonon coupling. This can be estimated from the ratio of the integrated intensities of the zero-phonon line and the vibronic sideband and is found to be 3.65 which is in close agreement with the value of  $S_{tot}$  needed to obtain the best fit. As seen in figure 3(a), this procedure gives an excellent fit to the data with only the structure beyond 0.09 eV missing. Since this structure has also been observed by other investigators (Bron and Wagner 1966), it cannot be simply attributed to noise. Such high-energy structure has been shown in other materials to be associated with quadratic coupling effects

(Kim et. al. 1975). However, in this case it is more likely due to the presence of some aggregate centres since the peaks in this structure are similar to those seen in the aggregate band in Fig. 1.

Fig. 4(b) shows the deconvolution of the predicted total sideband into its n-phonon contributions. Vibronic processes involving up to nine phonons appear to make non-negligible contributions to the band. The structure appearing in the one-phonon part of the sideband can be understood qualitatively by comparing  $G_1$  with the phonon dispersion curves of pur KCl obtained from neutron scattering experiments by Copley et. al. (1969).

Consideration of symmetry properties imposes selection rules upon a vibronic transition. The transition matrix element for an electric dipole electronic transition and for electron-phonon interaction given by  $V_q^\mu$  may be expressed as proportional to

$$\langle \psi_f | \underline{r} \cdot \underline{\pi}_k^\lambda | \psi_j \rangle \langle \psi_j | V_q^\mu | \psi_i \rangle \quad (12)$$

where  $\psi_i$ ,  $\psi_f$  and  $\psi_j$  represent the initial, final and intermediate electronic state wave functions, respectively. Since the wave functions are seldom well known these matrix elements cannot be evaluated precisely, so that use of symmetry to predict which transitions are possible becomes valuable. This may be accomplished by means of group theory. Since the impurity ion under study destroys the translational symmetry of the crystal the relevant group is the point group of the impurity site symmetry. The total matrix element of Eq. (12) may be non-zero only if it transforms as a scalar under the operations of the symmetry group. This will be the case if  $\Gamma_i \times \Gamma_v \times \Gamma_{ed}$  contains  $\Gamma_f$  or equivalently if  $\Gamma_i \times \Gamma_{ed} \times \Gamma_f$  contains  $\Gamma_v$ , where  $\Gamma_i$ ,  $\Gamma_f$ ,  $\Gamma_{ed}$ , and  $\Gamma_v$  are the irreducible representations of the transformation properties of  $\psi_i$ ,  $\psi_f$ , the



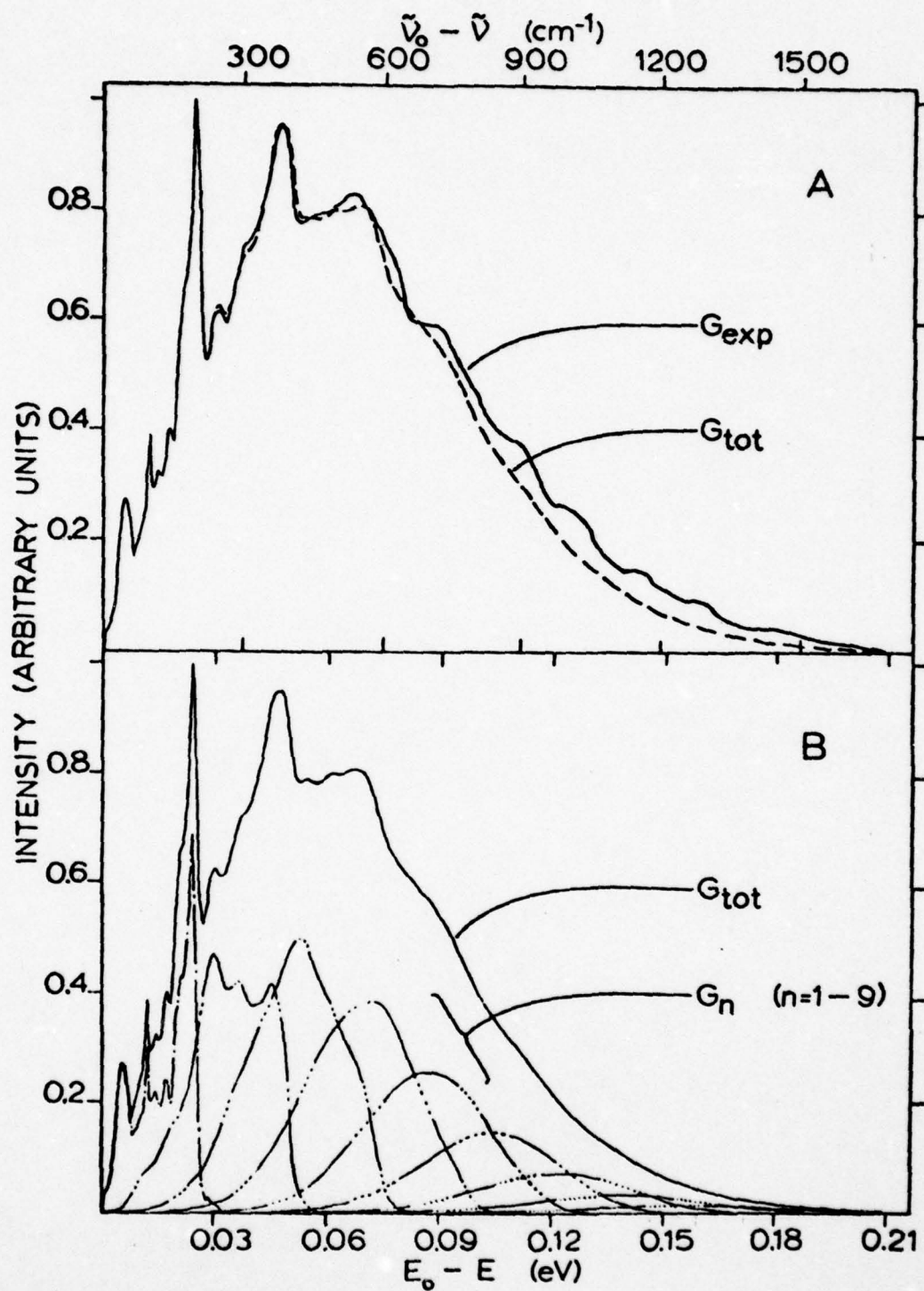


Fig. 4. Comparison of Experimental and Calculated KCl:Eu Vibronic Band

electric dipole operator and the vibrational interaction operator, respectively. Since  $V_q^\mu = (\partial V / \partial Q_q^\mu)$  and since the potential  $V$  possesses the symmetry of the impurity  $Q_q^\mu = 0$  site,  $\Gamma_v$  is just the irreducible representation according to which the phonon mode  $Q_q^\mu$  transforms.

The  $\text{Eu}^{2+}$  ion in KCl occupies a  $\text{K}^+$  site, which has octahedral symmetry. A charge compensating vacancy at a nearest neighbor  $\text{K}^+$  site lowers the site symmetry to point group  $C_{2v}$ , but it is possible to treat the ion first in cubic symmetry, than to consider the effect of the lowered symmetry. In  $O_h$  symmetry all three components of  $\underline{r}$  transform according to the irreducible representation  $\Gamma_{ed} = T_{1u}$ . Due to the half-integral spin of the seven  $\text{Eu}^{2+}$  electrons not in closed shells, the cubic double group must be used in determining  $\Gamma_i$  and  $\Gamma_f$ . The photon emitting level, the lowest level of the  $4f^6 5d(t_{2g})$  state, is expected to have irreducible representation  $\Gamma_i = \Gamma_{8g}$ , whereas the crystal field levels of the  $4f^7(^8S_{7/2})$  ground state may transform as  $\Gamma_f = \Gamma_{6u}, \Gamma_{7u}$  or  $\Gamma_{8u}$ , it being uncertain which is lowest in energy. The direct product  $\Gamma_i \times \Gamma_{ed} \times \Gamma_f$  is formed by multiplying the characters of each for each class in the symmetry group. Due to the multiplication of  $\Gamma_i$  by  $\Gamma_f$  the double valuedness of these due to their half-integral spins will be cancelled, so that we may use  $O_h$  rather than its double group. Table III shows the character table for the point group  $O_h$ , the direct product characters, and the irreducible representation into which  $\Gamma_i \times \Gamma_{ed} \times \Gamma_f$  reduces. Regardless of terminal level all gerade phonons, and no ungerade phonons, are allowed to participate in vibronic transitions assuming  $O_h$  symmetry.

In general it would now be necessary to project the phonons at all points in the first Brillouin zone onto the point were of the allowed representation, or were forbidden. The present case is much simpler, however, due to the symmetry reduction to  $C_{2v}$  required. This symmetry group does not contain the inversion

TABLE III  
CHARACTER TABLES OF  $O_h$  and  $C_{2v}$  WITH REDUCTIONS OF  $\Gamma_i \times \Gamma_{ed} \times \Gamma_f$

Representation	E	$8C_3$	$6C_2$	$6C_4$	$3C_4^2$	I	$8S_6$	$6\sigma_d$	$6S_4$	$3\sigma_h$	Reduction
$O_h$ :											
$A_{1g}$	1	1	1	1	1	1	1	1	1	1	
$A_{2g}$	1	1	-1	-1	1	1	1	-1	-1	1	
$E_g$	2	-1	0	0	2	2	-1	0	0	2	
$T_{1g}$	3	0	-1	1	-1	3	0	-1	1	-1	
$T_{2g}$	3	0	1	-1	-1	3	0	1	-1	-1	
$A_{1u}$	1	1	1	1	1	-1	-1	-1	-1	-1	
$A_{2u}$	1	1	-1	-1	1	-1	-1	1	1	-1	
$E_u$	2	-1	0	0	2	-2	1	0	0	-2	
$T_{1u}$	3	0	-1	1	-1	-3	0	1	-1	1	
$T_{2u}$	3	0	1	-1	-1	-3	0	-1	1	1	
$\Gamma_i \times \Gamma_{ed} \times \Gamma_f$ :											
$\Gamma_{8g} \times \Gamma_{1u} \times \Gamma_{6u}$	24	0	0	0	0	24	0	0	0	0	$A_{1g} + A_{2g} + 2E_g + 3T_{1g} + 3T_{2g}$
$\Gamma_{8g} \times \Gamma_{1u} \times \Gamma_{7u}$	24	0	0	0	0	24	0	0	0	0	$A_{1g} + A_{2g} + 2E_g + 3T_{1g} + 3T_{2g}$
$\Gamma_{8g} \times \Gamma_{1u} \times \Gamma_{8u}$	48	0	0	0	0	24	0	0	0	0	$2A_{1g} + 2A_{2g} + 4E_g + 6T_{1g} + 6T_{2g}$



TABLE III (Continued)

Representation	E	$8C_3$	$6C_2$	$6C_4$	$3C_4^2$	i	$8S_6$	$6\sigma_d$	$6S_4$	$3\sigma_h$	Reduction
$C_{2v}$											
$A_1$	1	1						1		1	
$A_2$	1	1						-1		-1	
$B_1$	1	-1						-1		1	
$B_2$	1	-1						1		-1	

operator so that the identification of representations as gerade or ungerade is no longer meaningful, suggesting that since all gerade phonons are allowed in  $O_h$  symmetry, all phonons should be allowed in  $C_{2v}$ . Indeed, Table III also shows the characters of  $C_{2v}$  in the columns to which the various operation correspond. It is clear that reduction of each of the direct products in terms of  $C_{2v}$  gives all four  $C_{2v}$  representations, so that indeed phonons of all possible representations in  $C_{2v}$  symmetry are allowed for vibronic transitions. Therefore no further consideration of selection rules need be given. In view of the previous symmetry discussion, the sideband peaks in  $G_1$  should correlate directly with regions of high density of states of the phonons. These regions should occur where the dispersion curves shown in Fig. 5 have a zero slope.

Although some correlation between the vibronic structure and the dispersion curves can be seen in Fig. 5, it is obviously not exact. The reason for these discrepancies is that the dispersion curves are obtained for an undoped crystal while the vibronic sideband is associated with an impurity in the crystal. The presence of the  $Eu^{2+}$  impurity ion causes two effects. The first is that it alters the interatomic force constants which results in slight changes in the frequencies of the phonon modes. The second is that local modes involving the impurity ion can occur which are not present in the pure crystal. The two dominant features of  $G_1$  are peaks occurring at 0.0063 eV and 0.0247 eV which do not correlate well with the phonon dispersion curves and thus are attributed to local vibrational modes.

#### E. Width and Position of the Zero-Phonon Line

The width and position of the fluorescence zero-phonon line of the annealed sample were monitored as a function of temperature and the results are shown in Figure 6 and listed in Table IV. The error bars are indicated by the spread

of data points at 15 K. The large spread for  $\delta\tilde{\nu}$  is due to the slack in the gears of the spectrometer scanning mechanism. Above 65 K the zero-phonon line becomes too small to measure accurately.

Two types of processes are generally found to contribute to the increase of the linewidth with temperature: single-phonon direct absorption or emission processes, and two-phonon Raman scattering processes. Since there are no observed levels lying just below either the initial or final state of the zero-phonon transition in this case, Raman processes should dominate the line broadening. This effect can be described by the expression (Mostoller et. al. 1971, Kim et. al. 1975)

$$\Delta\tilde{\nu}(\text{cm}^{-1}) = \pi \sum_{q,q'} V_{qq'}^2 n(\omega_q) [n(\omega_q) + 1] \delta(\hbar\omega_q - \hbar\omega_{q'}) \quad (13)$$

where  $V_{qq'}$  is the quadratic coupling constant for the  $q$  and  $q'$  phonons. This can be expressed in terms of the individual mode Huang-Rhys factors and an arbitrary constant  $\alpha_2$

$$\begin{aligned} \Delta\tilde{\nu}(\text{cm}^{-1}) = & \pi [\alpha_2 / \hbar\omega_D]^2 \sum_{q,q'} [(\hbar\omega_q)^2 S_q] [(\hbar\omega_{q'})^2 S_{q'}] n(\omega_q) \\ & \times [n(\omega_{q'}) + 1] \delta(\hbar\omega_q - \hbar\omega_{q'}). \end{aligned} \quad (14)$$

The dashed line in Fig. 4 represents the best fit to the linewidth data using Eq. (14) with the values of the  $S_q$ 's taken from  $G_1(\omega)$  projected from the computer analysis of the vibronic sideband as described in the preceding section and treating  $\alpha_2$  as an adjustable parameter. We have also used the approximation

$$\Delta\tilde{\nu}_{\text{total}} \approx [(\Delta\tilde{\nu}_{\text{homo}})^2 + (\Delta\tilde{\nu}_{\text{inhomo}})^2]^{\frac{1}{2}} \quad (15)$$



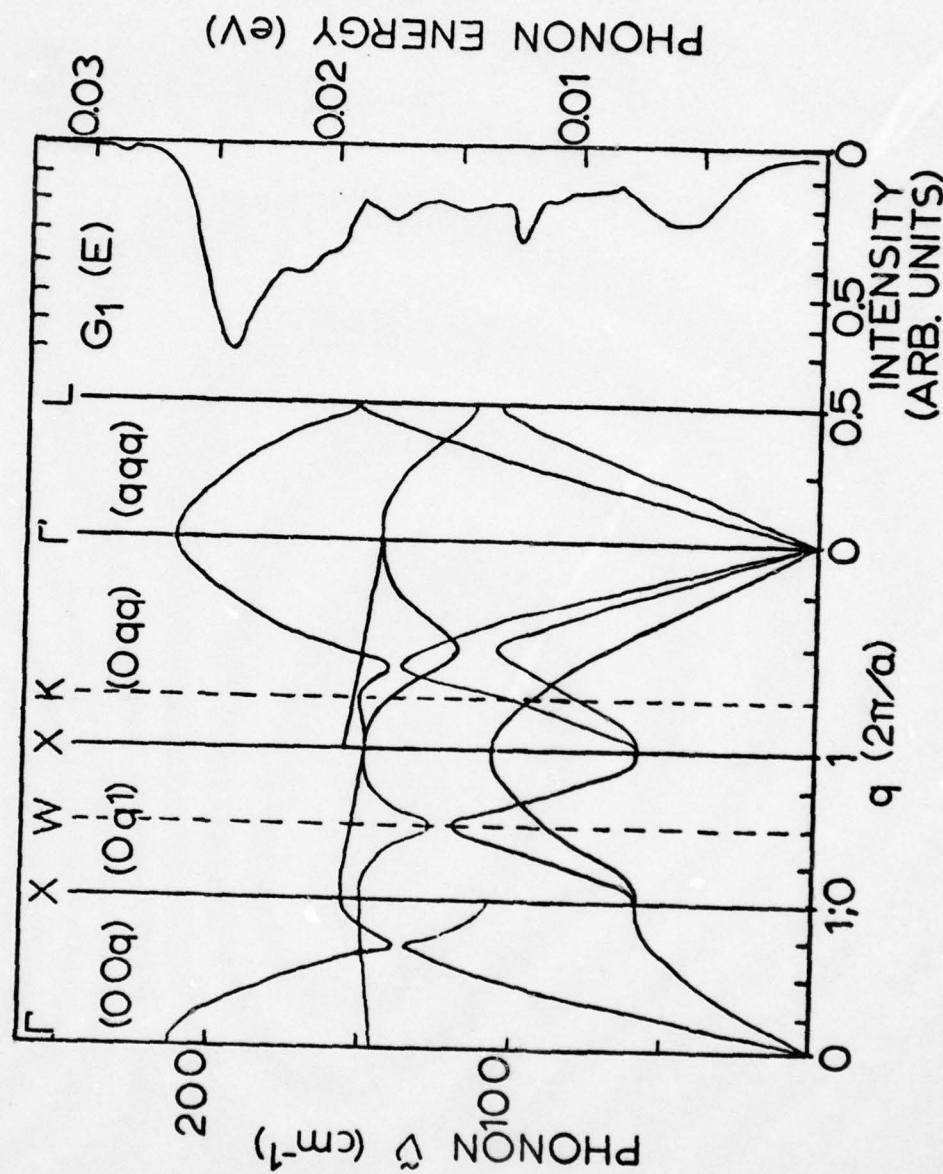


Fig. 5. Comparison of One-Phonon KCl:Eu Vibronic Band from Fitting with Published Dispersion Curves

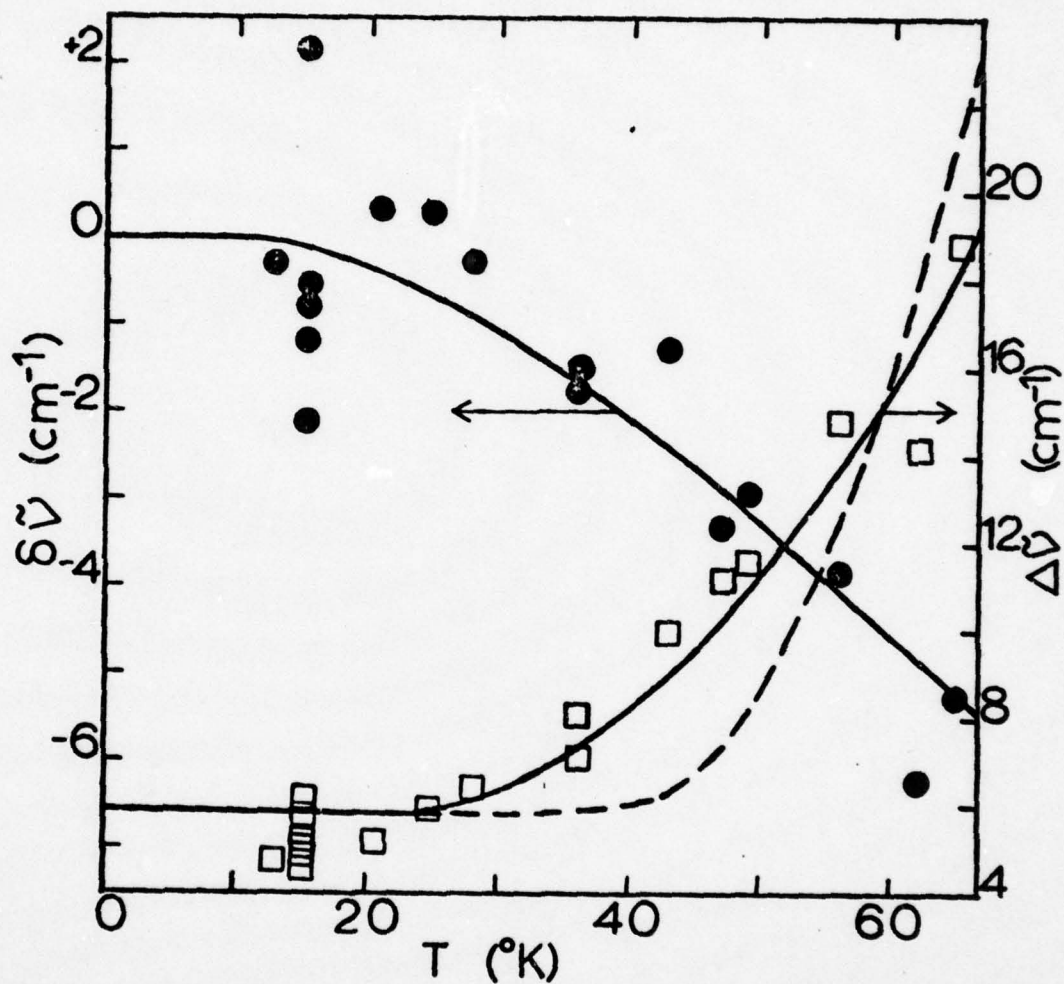


Fig. 6. KCl:Eu Lineshift (Circles) and Linewidth (Squares) Versus Temperature

TABLE IV  
KCl:Eu<sup>2+</sup> ZERO PHONON LINE WIDTH AND SHIFT VERSUS TEMPERATURE

T (K)	$\delta\nu = \nu(T) - \nu(13K)$ (cm <sup>-1</sup> )	$\Delta\nu$ (cm <sup>-1</sup> )
13	0.0	4.7
15	-0.89	4.93
	0.25	5.05
	0.02	5.16
	2.43	6.19
	-1.81	5.74
		4.59
21	0.60	5.16
25	0.6	5.9
28	0.02	6.42
36	1.2	7.1
	1.47	8.03
43	-1.01	9.98
47	-3.0	11.2
49	-2.61	11.5
56	-3.53	14.8
62	-5.9	14.2
65	-4.91	18.9



where the homogeneous contribution to the linewidth is due to the phonon processes and the inhomogeneous contribution is due to microscopic strains. The fit to the data obtained in this way is very poor. The only way in which a good fit to the data could be obtained was by considering only the low-frequency portion of the phonon density of states where the major contribution comes from the low-frequency local mode. The solid line in Fig. 6 was obtained with the parameters  $\hbar\omega_D = 0.0171$  eV and  $\alpha_2 = 6.25$ . This gives a good fit to the data.

A similar analysis can be made of the lineshift data where the temperature dependence is primarily due to the continual absorption and emission of phonons of the same frequency (Mostoller et. al. 1971, Kim et. al. 1975)

$$\delta\tilde{\nu} = [\alpha_1/2\hbar\omega_D] \sum_q (\hbar\omega_q)^2 S_q [2n_q(\omega_q) + 1] \quad (16)$$

where  $\alpha_1$  is another arbitrary coupling constant. Again the best fit to the data is obtained by considering coupling to only the low-frequency modes with  $\hbar\omega_D = 0.0171$  eV and  $\alpha_1 = -0.093$ . However, the large error bars in the data prevent this fit from being as exact as in the case of the linewidth.

An alternative interpretation of the thermal variation of the zero-phonon line involves the radiationless transitions to excited states lying just above the metastable level. Although no such levels are observed in the optical spectra, it is known that excited states of the  $4f^7$  configuration lie in this region. Since transitions involving these levels and the ground state are parity forbidden, they are difficult to observe optically except in host crystals in which one of them lies below the lowest  $4f^6 5d$  state. Thermal effects due to phonon absorption to these levels can be described by

$$\Delta\bar{\nu} = \sum_f \beta_{if} n(\omega_{if}) \omega_{if}^2 S_{if} \quad (17)$$

$$\delta\bar{\nu} = \sum_f \beta'_{if} n(\omega_{if}) \omega_{if}^2 S_{if} \frac{\Delta E_{ij}}{\Delta E_{ij}^2 - (\hbar\omega_{ij})^2} \quad (18)$$

where  $\beta_{if}$  and  $\beta'_{if}$  are arbitrary coupling parameters and  $\Delta E_{ij}$  is the activation energy for the phonons involved in the transitions.

The solid lines shown in Fig. 6 can also be obtained as the best fit to the linewidth and lineshift data using Eqs. (7) and (8) and assuming only a single phonon absorption process with an activation energy of about  $66 \text{ cm}^{-1}$  and a coupling parameter of about 60.

Thus, either Raman scattering or direct phonon absorption processes can predict the observed temperature dependences of the width and position of the zero-phonon line. Probably both of these types of processes make contributions to the thermal changes, but it is difficult to determine the extent of the different contributions due to the number of adjustable parameters involved.

#### F. Radiationless Relaxation

The radiationless relaxation of  $\text{Eu}^{2+}$  ions in KCl crystals at room temperature was studied by photoacoustic spectroscopy (Merkle and Powell 1977b). This is a technique which is commonly applied to the study of gases which has only recently been used on solid samples (Rosencwaig 1973). The sample is mounted in an acoustical cavity containing a microphone and is illuminated by a periodic source of light. If the light is absorbed and some of the energy is dissipated by radiationless relaxation, a periodic heating of the gas occurs at the surface of the sample and this is detected by the microphone as a periodic variation in cell pressure. The photoacoustic spectrum obtained in this way can be compared

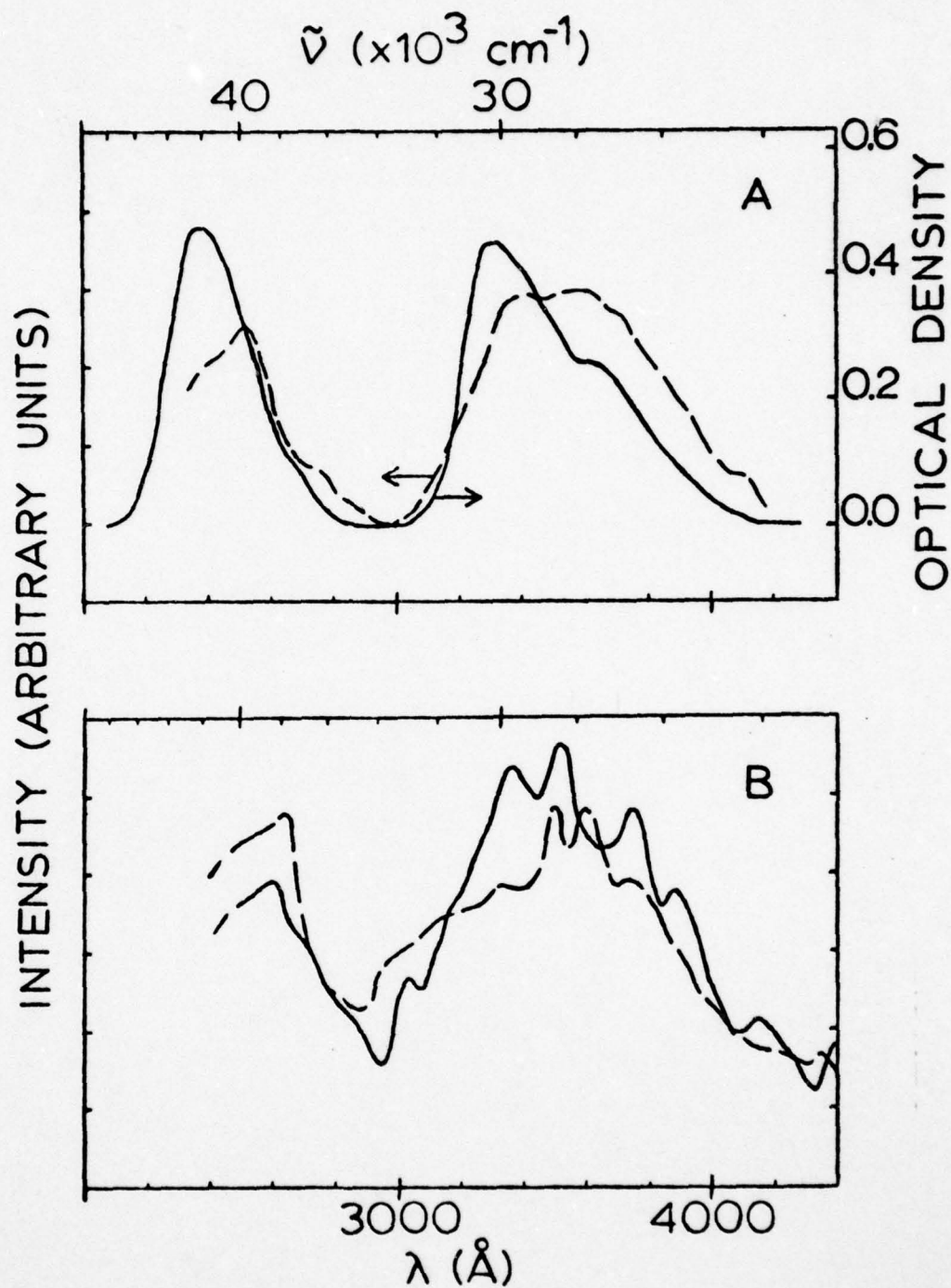


Fig. 7. KCl:Eu Absorption, Excitation and Photoacoustic Spectra  
 A: Optical Absorption of a 0.67 mm Thick Sample (Solid Line), Fluorescence Excitation Monitored at  $4350 \text{ \AA}$  (Dashed Line).  
 B: PAS Spectra Monitored at Phases  $-15^\circ$  (Solid) and  $+30^\circ$  (Dashed)



with absorption and fluorescence excitation spectra to determine the relative fractions of the absorbed light which are converted into heat and emitted light. The absorption measurements were made on a Cary 14 spectrophotometer. The incident light for photoacoustic and fluorescence excitation spectra was supplied by a 1000 W high-pressure mercury lamp which was passed through a quarter-meter monochromator having a  $200\text{\AA}$  bandpass. This light was chopped at 100 Hz and focused onto the sample. The fluorescence was analysed by a one-meter monochromator and cooled RCA C31034 photomultiplier tube. The photoacoustic signal was analysed by a 1/2 inch electret microphone. In both cases the signals were amplified by a lock-in amplifier receiving a reference signal from the chopper. The spectra were normalised to the photoacoustic spectra of charcoal to account for fluctuations in incident light intensity.

The absorption and fluorescence excitation spectra at room temperature are shown in Fig. 7(a). The two broad bands are due to transitions to the  $t_{2g}$  and  $e_g$  states of the  $4f^65d$  configuration with the crystal field splitting being about  $12000\text{ cm}^{-1}$ . The fact that fluorescence occurs from the  $t_{2g}$  level after pumping into the  $e_g$  level demonstrates the occurrence of radiationless relaxation from the upper to the lower level. The phase sensitive detector indicates maximum signal for zero degree phase shift for both excitation bands. The phase-angle measurement is accurate to within about  $5^\circ$ . The lifetime of the excited state is related to the phase of the signal  $\alpha$  and chopping frequency of the exciting light by the relationship

$$\tau = (\tan\alpha)/(2\pi\nu_c). \quad (19)$$

This indicates that the lifetimes of both levels are less than  $100\text{ }\mu\text{s}$ . This is consistent with the observed fluorescence lifetime of  $1.1\text{ }\mu\text{s}$  for the  $t_{2g}$  level. Since the transitions are electric dipole, the radiative decay rates

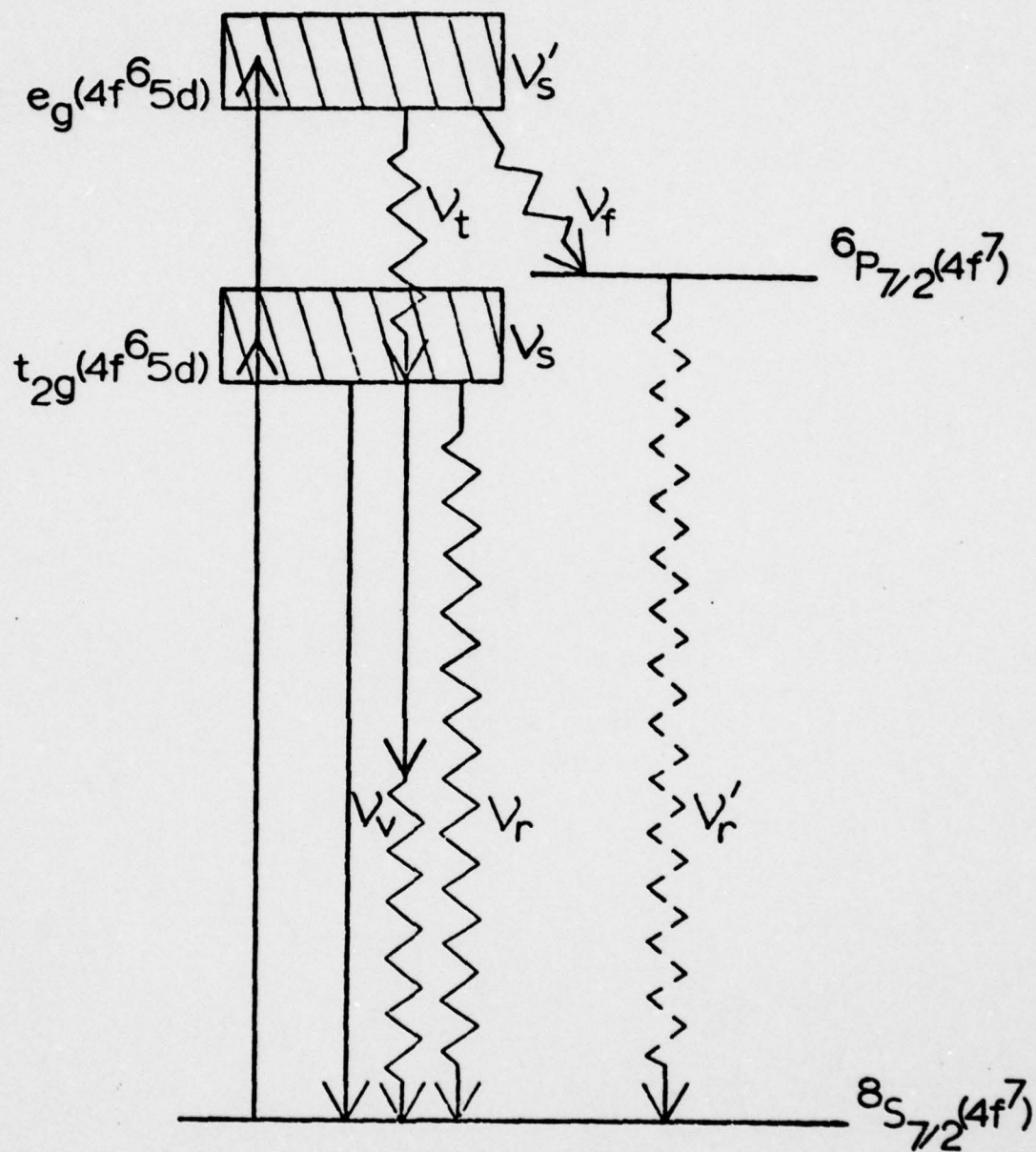


Fig. 8. Radiationless Relaxation Model for KCl:Eu

can be estimated from (Fowler and Dexter 1962)

$$\tau_{if}^{\text{rad}} = \frac{[\xi_{\text{eff}}(\nu_{fi})/\xi_{\text{eff}}(\nu_{if})]^2 \nu_{fi} (2J_i + 1) \langle r_{fi} \rangle^2}{8\pi C \eta(\nu_{if}) \eta(\nu_{fi}) \int \sigma(\nu) d\nu \nu_{if}^3 (2J_f + 1) \langle r_{fi} \rangle^2} \quad (20)$$

The effective field and the ratio of the matrix elements can both be assumed to be unity. The integrated absorption band is measured to be  $\int \sigma_{eg}(\nu) d\nu = 2.08 \times 10^{-14} \text{ cm}$ ,  $\nu_{eg}^{\text{abs}} \approx 42000 \text{ cm}^{-1}$ ,  $\nu_{eg}^{\text{em}} \approx 38000 \text{ cm}^{-1}$ ,  $\eta(\nu_{fi}) = \eta(\nu_{if}) = 1.5$ ,  $J_f = 7/2$  and  $J_i = 1/2$ . Using these values the radiative decay time of the  $e_g$  level is estimated to be of the order of a microsecond and thus the fluorescence decay time of this state will be much less than 100  $\mu\text{s}$  as indicated by the phase shift of the fluorescence emission.

The photoacoustic spectra were measured at several different phase shift settings two of which as shown in Fig. 7(b). It was found that the  $t_{2g}$  band has a maximum photoacoustic signal for zero phase shift but the  $e_g$  band is maximum for about  $35^\circ$  phase shift. The former result is consistent with optical measurements but the latter predicts a lifetime of the  $e_g$  state of the order of 1.1 ms which does not agree with optical results.

This apparent discrepancy between the PAS and fluorescence excitation results can be resolved by interpreting the results using the model shown in Fig. 8. The most important feature of this model is the role played by the excited state of the  $4f^7$  configuration. Actually there are several such levels in this region and only the lowest one is shown for simplicity. The photoacoustic signal at phase  $\theta$  due to excitation by photons of energy  $h\nu_0$  can be expressed as the sum over all of the relaxation transitions which generate heat,



$$I_{PAS}(\theta) \propto N_a \sum_i \sum_j \phi_{ji}^{nr} h\nu_{ji} \cos(\alpha_j - \theta) / (N_o h\nu_o). \quad (21)$$

Here  $N_a$  is the number of photons absorbed,  $\phi_{ji}^{nr}$  is the fraction of excited ions decaying via the  $i$ th type of radiationless transition from the  $j$ th level,  $h\nu_{ji}$  is the thermal energy emitted in the  $i$ th transition from the  $j$ th level, and  $\alpha_j$  is the phase shift of the signal from the  $j$ th level. Division by  $(N_o h\nu_o)$  represents normalising the results for variations in the energy of the exciting light. The PAS spectrum of charcoal was used for this purpose.

For the model shown in Fig. 8 three terms contribute to the PAS signal from the  $t_{2g}$  state: relaxation within the  $t_{2g}$  band characterised by  $\nu_s$ , radiationless decay to the ground state characterised by  $\phi_r^{nr} \nu_r$ , and vibronic decay which may be represented by  $(1 - \phi_r^{nr}) \nu_v$  since the zero-phonon fluorescence is negligible at room temperature. In this case, Eq. (21) can be written explicitly as

$$I_{t_{2g}}(\theta) \propto (N_a/N_o) [1/\nu_o(t_{2g})] [\nu_s + (1 - \phi_r^{nr}) \nu_v + \phi_r^{nr} \nu_r] \cos \theta \quad (22)$$

where  $\alpha_{t_{2g}}$  has been set equal to zero to be consistent with experimental results.

The PAS signal resulting from excitation of the  $e_g$  band is more complex. It has contributions arising from relaxation of the ions within the  $e_g$  band characterised by  $\nu'_s$ , relaxation of the fraction  $\phi_t^{nr}$  of the ions to the  $t_{2g}$  state represented by  $\nu_t$ , and subsequently relaxation to the ground state as before, and relaxation of the fraction  $\phi_f^{nr} = (1 - \phi_t^{nr})$  to the excited  $4f^7$  state. Finally, the radiationless decay of the  $4f^7$  excited state is characterised by  $\phi_{r'}^{nr} \nu_{r'}$ . Thus

$$I_{e_g}(\theta) \propto [N'_a/N'_o][1/v_o(e_g)]\{[v'_s + \phi_t^{nr}v_t + (1 - \phi_r^{nr})\phi_t^{nr}v_\eta + \phi_n^r\phi_r^{nr}v_r + \phi_f^{nr}v_f]\cos\theta + \phi_f^{nr}\phi_r^{nr}v'_r\cos(\alpha_f - \theta)\}. \quad (23)$$

Again to be consistent with experimental data, terms arising from either the  $e_g$  or  $t_{2g}$  levels are assigned phase shifts of zero while the phase shift of the signal from the  $4f^7$  level is shown explicitly as  $\alpha_f$ .

Equations (22) and (23) can be used to fit the photoacoustic data obtained at different phases. Some of the parameters appearing in these expressions can be estimated from observed spectral data and the others are treated as adjustable parameters with only estimates of limiting values available. The values of the parameters which were found to give the best fit to the data are listed in Table V. The adjustable parameters are determined by requiring that the ratios of Eqs. (22) and (23) be consistent with the observed ratios of the integrated photoacoustic signals from the  $e_g$  and  $t_{2g}$  bands at different phases and the requirement that  $dI_{e_g}/d\theta|_{\theta=35^\circ}=0$ . Although there are no independent measurements available to check the accuracy of the fitting parameters listed in Table V, none of them appear to be physically unrealistic. The value of  $\alpha_f$  of  $67^\circ$  implies a lifetime of  $4f^7$  excited state of about 4 ms. This value of the non-radiative decay time is consistent with the measured value of  $4f^7$  fluorescence decay times in host lattices where emission can be observed.

#### G. Discussion and Conclusions

In summary, the results of the spectroscopic investigation of  $KCl:Eu^{2+}$  presented here demonstrate relatively strong interactions both among the europium ions and between the  $Eu^{2+}$  ions and the host lattice.

TABLE V  
KCl:Eu<sup>2+</sup> PAS MODEL FITTING PARAMETERS

Estimated From Spectra	Estimated From Fitting
$\nu_o(t_{2g}) = 29,000 \text{ cm}^{-1}$	$\nu_f = 5,000 \text{ cm}^{-1}$
$\nu_o(e_g) = 42,000 \text{ cm}^{-1}$	$\nu'_r = 32,000 \text{ cm}^{-1}$
$\nu_r = 24,500 \text{ cm}^{-1}$	$\phi_t^{nr} = 0.3$
$\nu_t = 12,500 \text{ cm}^{-1}$	$\phi_r^{nr} = 0.4$
$\nu_s = 4,000 \text{ cm}^{-1}$	$\phi_f^{nr} = 0.7$
$\nu'_s = 5,000 \text{ cm}^{-1}$	$\phi_{r'}^{nr} = 1.0$
$\nu_v = 1,000 \text{ cm}^{-1}$	$\alpha_f^{r'} = 60^\circ$



One interesting aspect of the energy transfer results is that they show energy transfer to be taking place from ions with lower energy levels to ions with higher energy levels. In this case for either resonant or phonon-assisted interaction, the back transfer of energy from activator to sensitiser ions would be expected to be at least as efficient as the energy transfer process, but it was found that the results could be fitted only with a kinetic model which assumed negligible back transfer. The reason for this apparent discrepancy appears to be associated with the nature of the activator centre which is not a single ion but rather two or more  $\text{Eu}^{2+}$ -vacancy pairs close together as shown by the annealing results described in §2. When the sensitiser transfers its energy to one of the  $\text{Eu}^{2+}$  ions in the activator complex, there will be approximately an equal rate of back transfer to the isolated  $\text{Eu}^{2+}$ -vacancy site. However, there will be a much higher rate of transfer to another  $\text{Eu}^{2+}$  ion within the activator complex since the transfer rate varies as the inverse sixth-power of the ion-ion separation. As the energy is transferred among the ions of the complex, the average distance from the sensitiser may be greater than that of the activator ion originally receiving the energy, which is probably the one closest to the sensitiser. Due to the inverse sixth-power separation dependence, a small increase in average separation may reduce back transfer probability significantly. The emission from different ions in the activator complex is essentially equivalent and can not be resolved. Spectroscopic evidence for defect clustering has been observed in other systems (Sundberg et al. 1975, Fenn et al. 1973) and it has been found previously that energy transfer is more efficient between ions within a cluster than more distant ions (Tallant and Wright 1975, Tallant et al. 1976).

Although the analysis of the vibronic emission band was done in a different way from the approach used by Nasu et al. (1974), our results agree quite well

with theirs as well as being in agreement with the results of neutron scattering data. Comparison of the spectra in Fig. 2 indicate that aggregated centres may be responsible for the weak structure on the long-wavelength tail of the vibronic band and may contribute to the sharp peak at about  $4121\text{\AA}$ . The vibronic analysis and the thermal variation of the zero-phonon lines both indicate the importance of a low-frequency local vibrational mode in determining the optical properties of this system.

The most important result of the photoacoustic investigation in that PAS techniques can yield information on the dynamics of the radiationless processes which can not be obtained by standard optical methods. Both PAS results and the temperature dependences of the zero-phonon linewidth and position indicate that the excited levels of the  $4f^7$  configuration play an important part in determining the optical properties of the sample. These levels are consistent with the positions of the excited  $4f$  levels when they have been observed by techniques such as two-photon absorption (Fritzler and Schaack 1976). Tyner and Drickamer (1977) have recently published results of an investigation of the effects of high pressure on the luminescence properties of divalent europium phosphors. They also find it necessary for several systems to postulate the existence of additional excited states which take part in the relaxation processes of  $\text{Eu}^{2+}$ . Their results indicate that the activation energy for luminescence quenching via these states is of the order of  $73\text{ cm}^{-1}$  which is close to the activation energy needed to explain the zero-phonon linewidth and position temperature dependence by direct phonon absorption processes. They feel that the extra level is another  $4f^6 5d$  state.

In conclusion, it is important to emphasize that the sample history of crystal growth and thermal treatment is critically important in establishing

AD-A066 086

OKLAHOMA STATE UNIV STILLWATER DEPT OF PHYSICS  
MULTISTEP ENERGY MIGRATION AND RADIATIONLESS RELAXATION PROCESS--ETC(U)  
DEC 78 R C POWELL

F/G 20/5

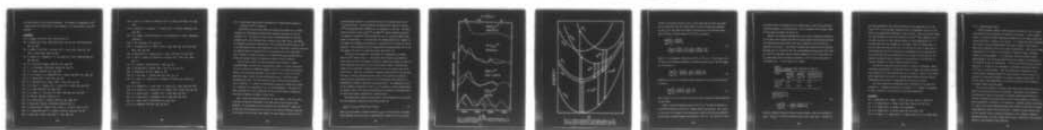
DAA629-76-G-0099

UNCLASSIFIED

ARO-13318.8-P

NL

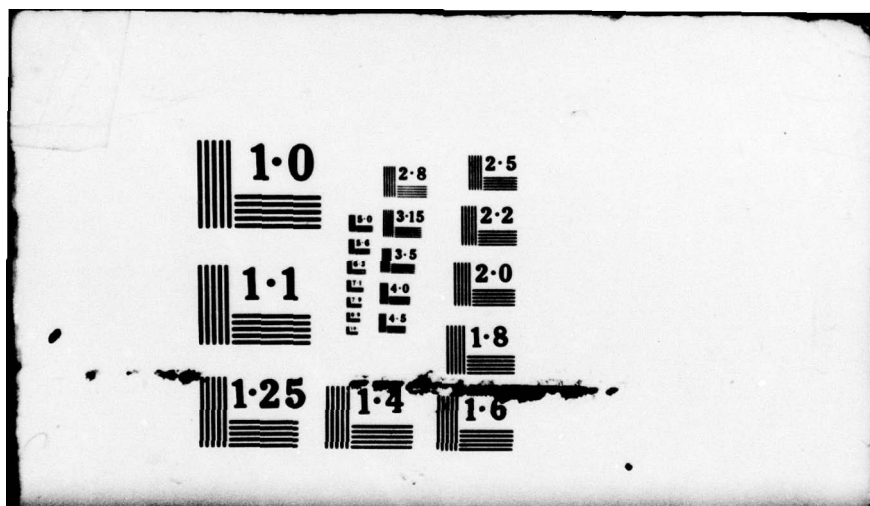
4 OF 4  
ADA  
066086



END  
DATE  
FILMED

5-79  
DDC





the exact details of its optical properties. The presence of aggregates of  $\text{Eu}^{2+}$ -vacancy pairs of various sizes is very apparent in the spectroscopy of  $\text{KCl:Eu}^{2+}$  crystals.

#### REFERENCES

- [1] G. Blasse, 1973 Phys. Stat. Solidi B 55 K 131.
- [2] G. Balisse and A. Brill, 1968 Philips Res. Rep. 23, 201; 1970 Philips Tech. Rev. 31, 304.
- [3] G. Blasse, A. Brill and J. De Vries, 1971 J. Inorg. Nucl. Chem. 31, 568; 1971 J. Inorg. Nucl. Chem. 31, 568.
- [4] G. Balisse, W. L. Wanmaker, J. W. ter Vrugt and A. Brill, 1968b Philips Res. Rep. 23, 189.
- [5] W. E. Bron and M. Wagner, 1966 Phys. Rev. 145, 689.
- [6] F. D. S. Butement, 1948 Trans. Faraday Soc. 44, 617.
- [7] L. L. Chase, 1970 Phys. Rev. B2, 2308.
- [8] J. R. D. Copley, R. W. Macpherson and T. Timusk, 1969 Phys. Rev. 182, 965.
- [9] D. L. Dexter, 1953 J. Chem. Phys. 21, 836.
- [10] K. B. Eisenthal and S. Siegel, 1964 J. Chem. Phys. 41, 652.
- [11] J. B. Fenn, J. C. Wright and F. K. Fong, 1973 J. Chem. Phys. 59, 5591.
- [12] F. K. Fong, 1969 Phys. Rev. 187, 1099.
- [13] F. K. Fong, R. L. Ford and R. H. Heist, 1970 Phys. Rev. B2, 4202.
- [14] Th. Förster, 1948 Ann. Physik 2, 55.
- [15] W. B. Fowler and D. L. Dexter, 1962 Phys. Rev. 128, 2154.
- [16] S. Freed and S. Katcoff, 1948 Physica (Utrecht) 14, 17.
- [17] U. Fritzler and G. Schaack, 1976 J. Phys. C: Solid St. Phys. 9, L23.
- [18] A. A. Kaplyanskii and P. P. Feofilov, 1962 Opt. Spectros. 13, 129.
- [19] F. Karel and J. Mares, 1973 Czech. J. Phys. B23, 652.

- [20] Q. Kim, R. C. Powell, M. Mostoller and T. M. Wilson, 1975 Phys. Rev. B12, 5627.
- [21] P. Kisliuk, H. H. Tippins, C. A. Moore and S. A. Pollack, 1968 Phys. Rev. 171, 336.
- [22] F. A. Kröger, 1948 Some Aspects of the Luminescence of Solids, (Amsterdam: Elsevier).
- [23] E. Loh, 1968 Phys. Rev. 175, 533.
- [24] L. D. Merkle and R. C. Powell, 1977a J. Chem. Phys. 67, 371; 1977b Chem. Phys. Lett. 46, 303.
- [25] M. Mostoller, B. N. Ganguly and R. F. Wood, 1971 Phys. Rev. B4, 2015.
- [26] K. Nasu, A. Tamura, K. Kojima and T. Kojima, 1974 J. Phys. Soc. Japan 36, 55.
- [27] D. W. Posener, 1959 Australian J. Phys. 12, 184.
- [28] R. Reisfeld and A. Glasner, 1964 J. Opt. Soc. Am. 54, 331.
- [29] A. Rosencwaig, 1973 Opt. Commun. 7, 305.
- [30] E. L. Sill and J. J. Martin, May. Res. Bull. 12, 127.
- [31] E. L. Sill, J. J. Martin and Z. Al Shaieb, 1977 Phys. Stat. Solidi (a) 39, K 131.
- [32] M. N. Sundberg, H. V. Lauer and F. K. Fong, 1975 J. Chem. Phys. 62, 1853.
- [33] D. R. Tallant, M. P. Miller and J. C. Wright, 1976 J. Chem. Phys. 65, 510.
- [34] D. R. Tallant and J. C. Wright, 1975 J. Chem. Phys. 63, 2074.
- [35] C. E. Tyner and H. G. Drickamer, 1977 J. Chem. Phys. 67, 4116.
- [36] M. S. Waite, 1974 J. Electrochem. Soc. 121, 1122.
- [37] H. A. Weakliem, 1972 Phys. Rev. B6, 2743.



## VII.2 Photoacoustic Spectroscopy Investigation of Radiationless Relaxation Processes of $\text{Cr}^{3+}$ In Crystals

Photoacoustic spectroscopy (PAS) has recently been shown to be a useful technique for investigating radiationless relaxation processes of ions in crystals [1-3]. We report here the results of PAS experiments on trivalent chromium ions in four different host crystals;  $\text{Al}_2\text{O}_3$ ,  $\text{MgO}$ ,  $\text{SrTiO}_3$ , and  $\text{BaTiO}_3$ . By comparing the relative intensities of the two broad absorption bands of  $\text{Cr}^{3+}$  in the PAS spectrum with their intensities in the fluorescence excitation spectrum, the dominant mode of relaxation back to the ground state can be determined. This is shown to be quite different for chromium doped  $\text{Al}_2\text{O}_3$  and  $\text{MgO}$  while in  $\text{SrTiO}_3$  and probably  $\text{BaTiO}_3$  the signals are masked by host absorption.

The excitation light for these experiments was provided by a 1000-W tungsten/halogen "sun gun" after being passed through a 1/4-meter monochromator with a resolution of  $200\text{\AA}$  and chopped at 100 Hz. For obtaining excitation spectra, the fluorescence emission in the region of the R lines of  $\text{Cr}^{3+}$  was monitored using a second 1/4-meter monochromator and a cooled RCA C31034 photomultiplier tube. The spectra were recorded after being processed by a lock-in amplifier. To obtain the photoacoustic spectra the samples were placed in a acoustical cell containing a 1-in. electret microphone. The signal was again processed by a lock-in amplifier and in this case signal averaging was also used to improve the signal to noise ratio.

Fig. 1 shows the spectra obtained for the four samples. These have been corrected for spectral variations in the light source and excitation monochromator. No fluorescence could be observed for the  $\text{BaTiO}_3:\text{Cr}^{3+}$  sample and in this case the PAS spectrum is very close to the optical absorption spectrum. In the spectra for the other three samples the most dominant features are the

broad absorption bands due to transitions from the  $^4A_2$  ground state to the  $^4T_2$  excited states. In the excitation and photoacoustic spectra of  $SrTiO_3:Cr^{3+}$  the strong band below  $4500\text{\AA}$  is due to absorption in the host. The photoacoustic spectra of both  $Al_2O_3:Cr^{3+}$  and  $MgO:Cr^{3+}$  exhibit absorption peaks in the regions of the R and B lines although the very low resolution makes these appear as broad bands. It was found that the maximum photoacoustic signal for all bands in all samples was obtained for a phase shift of  $0^\circ$  with the lock-in amplifier. This indicates that the radiationless processes giving rise to the PAS signals all occur on a time scale faster than  $100\text{ }\mu\text{s}$  [2].

The data can be analyzed by considering the configuration coordinate model for  $Cr^{3+}$  shown in Fig. 2. The general level positions and predicted decay rates are taken from Fonger and Struck's theoretical analysis of ruby [4]. After absorption into either of the excited quartet levels, a photoacoustic signal will be generated by phonons given off as the ion relaxes back to the ground state. There are two different relaxation paths which the ion may take. The first is direct radiationless decay back to the ground state while the second involves radiationless decay to the  $^2E$  metastable level which has a predominantly radiative relaxation to the ground state. By comparing the ratio of the integrated intensities of the  $^4T_1$  to  $^4T_2$  bands in the PAS spectrum with the similar ratio in the excitation spectrum it is possible to determine which of these decay modes is dominant for a specific host.

The photoacoustic signal at phase angle  $\theta$  can be expressed as the sum over all the relaxation transitions which generate heat [2]

$$I_{PAS}(\theta) \propto N_a \sum_i \phi_{nr}(i) h\nu_i \cos(\alpha_i - \theta) / N_o h\nu_o, \quad (1)$$

where  $N_a$  is the number of photons absorbed,  $\phi_{nr}(i)$  is the fraction of excited atoms relaxing via the  $i$ th type of radiationless transition,  $h\nu_i$  is the total



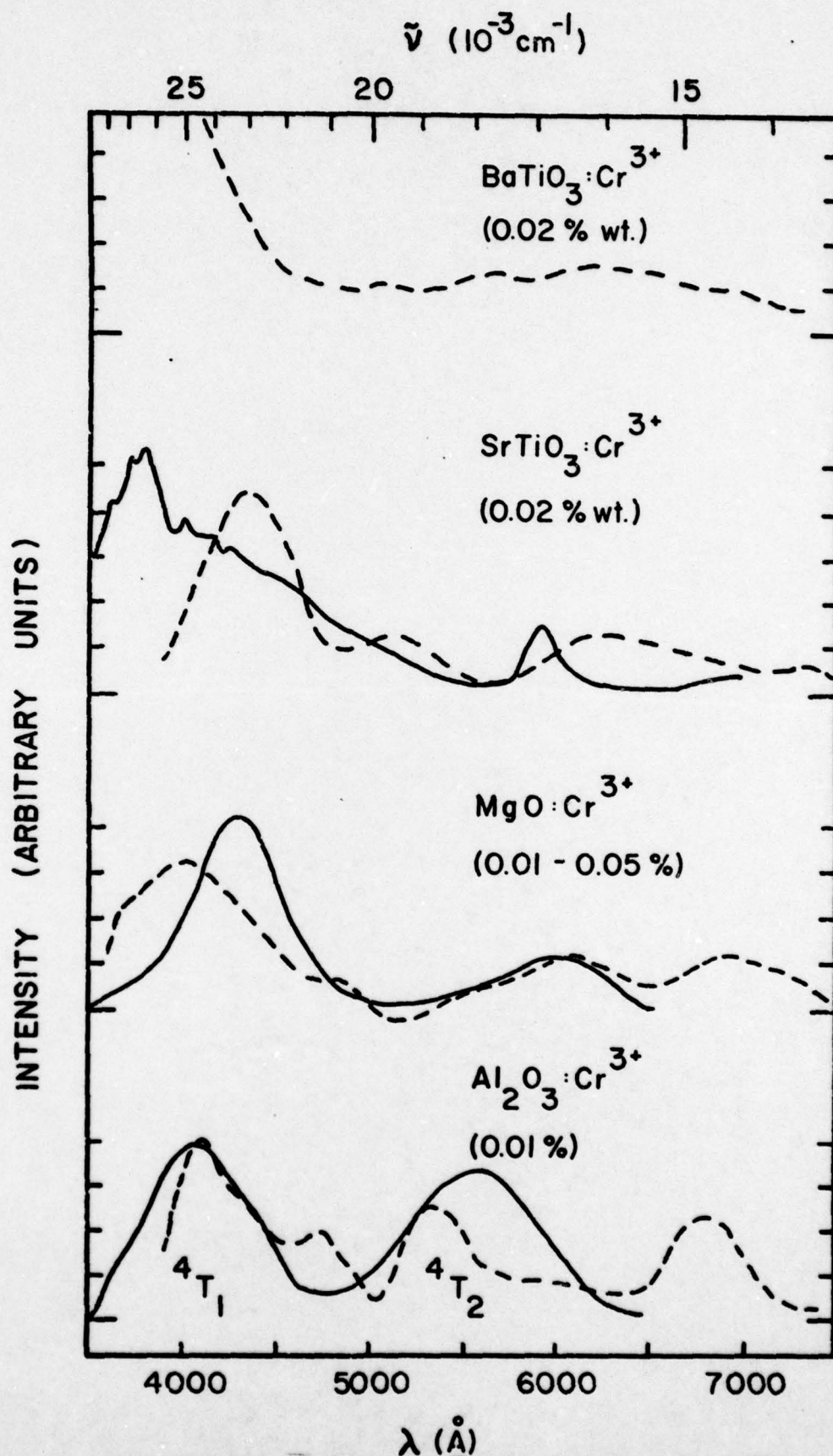


Fig. 1. Unpolarized, room temperature photoacoustic (---) and fluorescence excitation (—) spectra of  $\text{Cr}^{3+}$  ions in different host crystals.



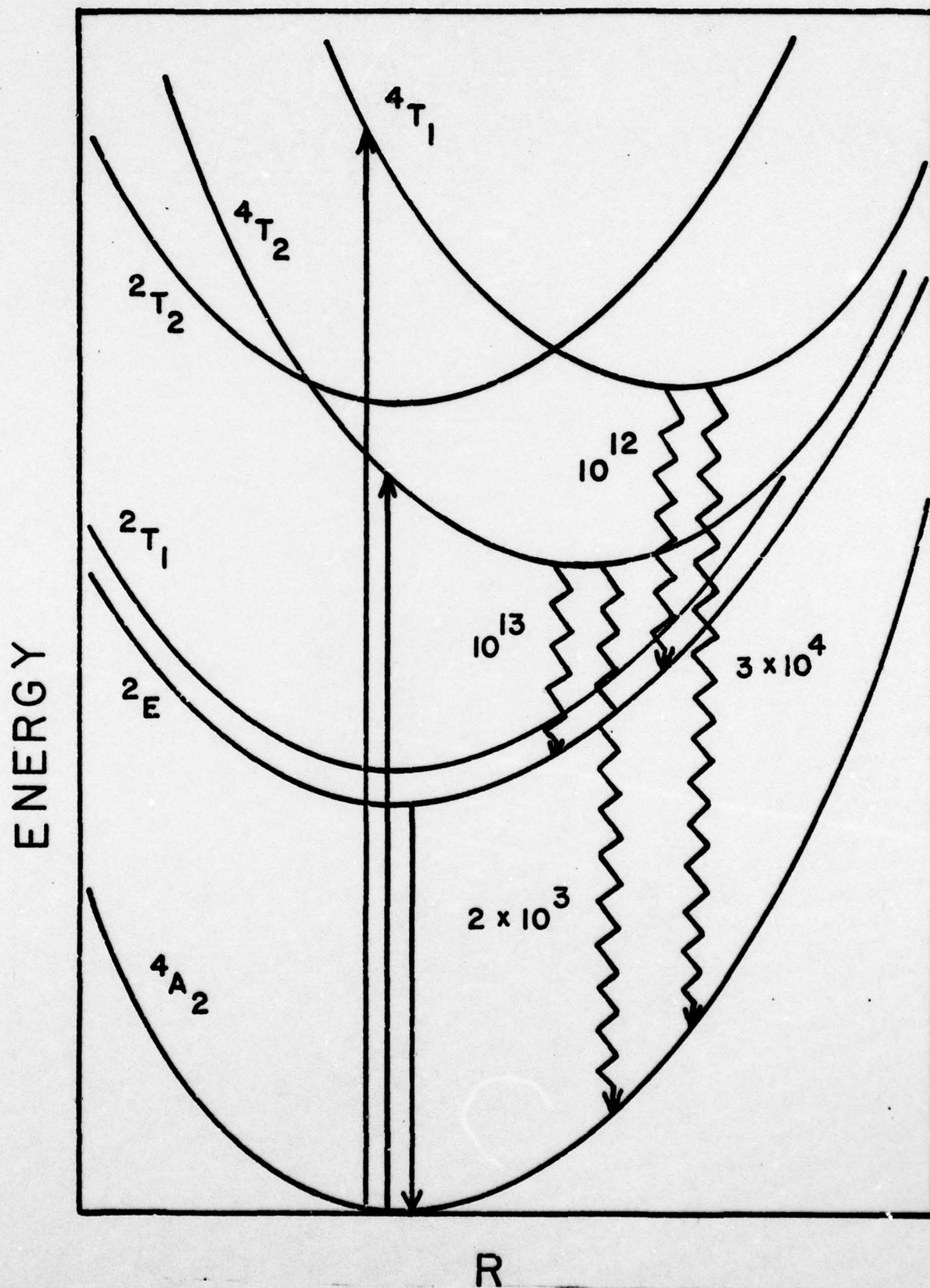


Fig. 2. Typical configuration coordinante model for  $\text{Cr}^{3+}$  in cubic crystal field site. The radiationless relaxation rates which are listed are predicted for ruby in ref. [4].

energy of the phonons emitted, and  $\alpha_1$  is the phase angle at which the signal due to transitions from the initial state of the  $i$ th transition is maximum.

$N_0$  and  $h\nu_0$  are the number and energy of the photons in the excitation beam.

Thus the ratio of the PAS bands for  $\text{Cr}^{3+}$  ions is given by

$$\frac{I_{\text{PAS}}(^4T_1)}{I_{\text{PAS}}(^4T_2)} = \frac{N_a(1)h\nu_2}{N_a(2)h\nu_1} \times \frac{[\phi_{\text{nr}}(1-E)h\nu(1-E) + \phi_{\text{nr}}(1-A)h\nu(1-A)]}{[\phi_{\text{nr}}(2-E)h\nu(2-E) + \phi_{\text{nr}}(2-A)h\nu(2-A)]}, \quad (2)$$

where  $(1-E)$  designates a transition from  $^4T_1$  to  $^2E$ , etc. If the decay to the  $^2E$  level is the dominant mechanism of relaxation giving rise to the PAS signal, Eq. (2) reduces to

$$\frac{I_{\text{PAS}}(^4T_1)}{I_{\text{PAS}}(^4T_2)} \sim \frac{N_a(1)h\nu_2}{N_a(2)h\nu_1} \frac{\phi_{\text{nr}}(1-E)h\nu(1-E)}{\phi_{\text{nr}}(2-E)h\nu(2-E)}. \quad (3)$$

Similarly, the ratio of integrated band intensities in the excitation spectra is given by

$$\frac{I_{\text{EXS}}(^4T_1)}{I_{\text{EXS}}(^4T_2)} = \frac{N_a(1)h\nu_2}{N_a(2)h\nu_1} \frac{\phi_{\text{nr}}(1-E)}{\phi_{\text{nr}}(2-E)}. \quad (4)$$

Note the Eqs. (3) and (4) differ only in the ratio of phonon energies appearing in the former.

Table 1 lists the measured ratios of the  $^4T_1$  to  $^4T_2$  band as observed in the PAS and excitation spectra for chromium doped  $\text{Al}_2\text{O}_3$  and  $\text{MgO}$ . Also listed is the ratio of the bands in the photoacoustic spectra after being multiplied by the ratio of phonon energies as indicated in Eq. (3). For the case of ruby,



the dominant mode of relaxation is the cascade decay of the  $^2E$  level and then radiative emission to the ground state. This is expected from the decay rates for ruby given by Fonger and Struck [4].

However, for chromium doped MgO there is an order of magnitude difference in the band ratios obtained from PAS and those obtained from excitation spectra. This indicates that decay modes other than relaxation to the  $^2E$  level are important in this case. One possible situation which would cause the adjusted PAS band ratio to be smaller than the corresponding excitation band ratio would be if the  $^4T_1$  band decays mainly through relaxation to the  $^2E$  level while the  $^4T_2$  band decays both by relaxation processes to the  $^2E$  level and directly to the ground state. In this case Eq. (2) becomes

Table 1  
Ratios of integrated band intensities in PAS and excitation spectra

Sample	$I_{\text{EXS}}(^4T_1)$	$I_{\text{PAS}}(^4T_1)$	$I_{\text{PAS}}(^4T_1)h\nu(2-E)$
	$I_{\text{EXS}}(^4T_2)$	$I_{\text{PAS}}(^4T_2)$	$I_{\text{PAS}}(^4T_2)h\nu(1-E)$
$\text{Al}_2\text{O}_3:\text{Cr}^{3+}$	0.69	1.12	0.53
$\text{MgO}:\text{Cr}^{3+}$	0.36	0.21	0.04

$$\frac{I_{\text{PAS}}(^4T_1)h\nu(2-E)}{I_{\text{PAS}}(^4T_2)h\nu(1-E)}$$

(5)

$$= \frac{I_{\text{EXS}}(^4T_1)}{I_{\text{EXS}}(^4T_2)} \left( 1 + \frac{\phi_{\text{nr}}(2-A)h\nu(2-A)}{\phi_{\text{nr}}(2-E)h\nu(A-E)} - 1 \right)$$

Using the observed PAS and excitation spectra results, this can be solved for  $\phi_{\text{nr}}(2-A)/\phi_{\text{nr}}(2-E)$  which is found to have a ratio near unity. Initially it



may seem surprizing to have such very different decay properties for the  ${}^4T_2$  band of  $Cr^{3+}$  in ruby and MgO, especially since the Huang-Rhys factor for this band is not significantly different in the two hosts. Most probably the reason for this difference is that more than half of the  $Cr^{3+}$  ions in MgO will be in non-cubic sites due to local defects needed for charge compensation [5]. It has been shown that for chromium ions in rhombic sites the relaxed state of the  ${}^4T_2$  level lies below the  ${}^2E$  level [5] and thus for ions in these types of sites relaxation from the  ${}^4T_2$  band will be predominantly to the ground state. In the work described here chromium ions in all types of sites were and the observed relaxation effects represent the superposition of the different relaxation processes for ions in different types of sites.

The spectra reported here must certainly be taken as preliminary results indicating the importance of having PAS spectra of higher resolution and faster time capabilities so more detailed data can be obtained. However, this investigation demonstrates the ability of distinguishing between different possible radiationless decay modes by comparing PAS and excitation spectra.

The authors gratefully acknowledge useful discussion of this work with Professor G. F. Imbusch and also wish to thank Dr. J. C. Murphy for supplying us with a preprint of his PAS work on ruby before publication.

#### REFERENCES

- [1] A. Rosencwaig, Opt. Commun. 7 (1973) 305; Anal. Chem. 47 (1975) 593.
- [2] L. D. Merkle and R. C. Powell, Chem. Phys. Letters 46 (1977) 303.
- [3] J. C. Murphy and L. C. Aamodt, to be published.
- [4] W. H. Fonger and C. W. Struck, Phys. Rev. B11 (1975) 3251.
- [5] M. O. Henry, J. P. Larkin and G. F. Imbusch, Phys. Rev. B 13 (1976) 1893.

#### VIII. Miscellaneous Studies

Several secondary research efforts have been initiated to try to clarify some specific points concerning the materials of interest. A joint research project to study the thermal luminescence properties of our  $\text{CaWO}_4$  crystals was started with Prof. E. Kohnke of our faculty. It is hoped that this investigation will lead to a better understanding of the defect centers in this material which play an important role in our energy transfer model. Also we are collaborating with Prof. W. Unruh of the University of Kansas in light scattering studies of our  $\text{YVO}_4$  samples. It is hoped that this will provide a better understanding of the scattering centers which have limited the usefulness of this material in optical applications. A third joint effort has been started with Prof. B. Ackerson of our department on antistokes excitation studies of  $\text{Er}^{3+}$  ions in our  $\text{YVO}_4$  samples. This work should yield information on the electron-phonon coupling parameter for this system so it will not have to be treated as an adjustable parameter in fitting our energy transfer data. So far the results have been difficult to interpret because of the interference of resonant Raman scattering peaks.

The last four months of this grant period were spent working with Prof. A. Zewail at California Institute of Technology. During this time information was obtained on using the techniques of transient grating spectroscopy and coherent transient spectroscopy and we are now in the processes of setting up these experimental techniques in our laboratory. Transient grating spectroscopy is a type of four wave mixing spectroscopy which allows the detection of spatial energy migration without spectral diffusion. Coherent transient methods such as free induction decay can provide information on the coherence lengths of migrating excitons. We plan to apply both of these techniques to our characterization of stoichiometric laser materials.